POLYCARBONATE-SILSESQUIOXANE AND POLYCARBONATE-SILOXANE NANOCOMPOSITES: SYNTHESIS, CHARACTERIZATION, AND APPLICATION IN THE FABRICATION OF POROUS INORGANIC FILMS

A Dissertation
Presented to
The Academic Faculty

by

Jassem Abdallah

In Partial Fulfillment
of the Requirements for the Degree
Doctor of Philosophy in the
School of Chemical and Biomolecular Engineering

Georgia Institute of Technology
December, 2009

POLYCARBONATE-SILSESQUIOXANE AND POLYCARBONATE-SILOXANE NANOCOMPOSITES: SYNTHESIS, CHARACTERIZATION, AND APPLICATION IN THE FABRICATION OF POROUS INORGANIC FILMS

Approved by:

Dr. Cliff Henderson, Advisor
School of Chemical and Biomolecular Engineering
Georgia Institute of Technology

Dr. Sankar Nair
School of Chemical and Biomolecular Engineering
Georgia Institute of Technology

Dr. Amyn Teja
School of Chemical and Biomolecular Engineering
Georgia Institute of Technology

Dr. Haskell Beckham
School of Polymer, Textile, and Fiber Engineering
Georgia Institute of Technology

Dr. Dennis Hess
School of Chemical and Biomolecular Engineering
Georgia Institute of Technology

Date Approved: August 18, 2009

DEDICATION

Dedicated to those without whose support I would not have come this far.

ACKNOWLEDGEMENTS

I would like to thank my family and friends for the encouragement and advice that they continually provided. I would also like to thank my advisor, members of my committee, and members of their respective research groups for providing me with guidance and assistance throughout my research. Janice Whatley and Gloria Beale of the School of Chemical Engineering and all of the advisors at the Office of International Education deserve special mention for going out of their way to facilitate my progress. Dr. Teresita Marzialetti was instrumental in gaining me access to equipment necessary for some of my synthesis experiments and film processing, as well as assisting me with their experimental setup. Marshall Silver played a pivotal role in preliminary work, specifically in the assistance he gave me in the design of a basic process for producing direct-write porosity.[1, 2] I would like to thank Dr. Takashi Okada, a visiting scientist from JSR, for synthesizing and purifying the N-methyl nifidepine photobase generator (PBG), and verifying its structure using 1H-NMR analysis. I would also like to thank Professor Seth Marder in the Department of Chemistry for offering advice in the synthesis of photobase generators. Dr. Yueming Hua, Dr. Michael Romeo, and Richard Lawson provided me with extensive training that I needed to design and perform synthesis, purification, and characterization procedures used in my studies.

All of the solid-state 29Si NMR experiments were performed by Dr. Johannes Liesen of the Nuclear Magnetic Resonance (NMR) Center. All elemental analyses were performed by Atlantic Microlab. I would like to acknowledge the guidance received from both Dr. Leslie Gelbaum and Mariefel Valenzue-Olarte in optimizing solution-state

29Si NMR studies. I would like to thank Murtaza Askari, Hua-Wei Chu, and Dr. David Noga for taking part in the fabrication of silicon wafers containing free-standing ultrathin silicon nitride membranes, which were used for through-plane TEM imaging of films. Both the osmium tetraoxide (OsO4) vapor staining and through-plane TEM imaging of films coated on the silicon nitride membrane substrates were performed by Jeanette Taylor at the Robert P. Apkarian Integrated Electron Microscopy Core at Emory University. Electron-lucent, ultrathin cross-sections of films were milled by Dr. Martin Brucherseifer using focused gallium ion beams (FIB) at the FIB2 Center. In-plane TEM analyses of these cross-sections were performed by Yolande Berta using the facilities at the Center of Nanostructure Characterization and Fabrication (CNCF).

I would like to thank Ryan Kincer and Andrew Zappas for performing all the Gel Permeation Chromatography (GPC) measurements. Additionally, Ryan Kincer also provided me with training and general guidance in Differential Scanning Calorimetry (DSC). I would like to thank Dr. Marcus Foston and Kate McFadden for the training and guidance that they provided me in Dynamic Light Scattering (DLS) analyses. AFM analyses were performed by Dr. Dhananjay Bhusari and Dr. Xiaohong Zhang using the facilities located in the cleanroom of the Microelectronics Research Center (MiRC). I would like to acknowledge the assistance and guidance that I received from Gary Spinner, the MiRC cleanroom staff, and numerous cleanroom users while performing work in the cleanroom. Samples of the **PNC1-ROP** sacrificial polymer and FOx-1x® resin samples were donated by Promerus LLC and Dow Corning Corporation, respectively.

TABLE OF CONTENTS

LIST OF TABLES

LIST OF FIGURES

LIST OF SYMBOLS

R	The electrical resistance in units of Ohms (Ω)
C	The capacitance in units of Farads (F)
C_H	The intralevel (horizontal plane) capacitance
C_V	The interlevel (vertical plane) capacitance
ρ	Resistivity of a material in units of Ohm-meters (Ω-m)
ε_0	Permittivity of free-space (8.85×10^{-12} Farads per meter)
k	The value of the relative dielectric constant of a material; equivalent to ε_r
P	The pitch or spacing between signal lines
H_w	The height of a signal line
L_w	The length a signal line
δ	Chemical shift of an nuclear magnetic resonance (NMR) peak relative to a reference peak position (typically reported in units of ppm)
^1H	The hydrogen-1 or proton isotope, or a substance's NMR properties relating to this isotope
^{13}C	The carbon-13 isotope, or a substance's NMR properties relating to this isotope
$^{13}C\{^1H\}$	Proton-decoupled, carbon-13 NMR analysis

^{29}Si	The silicon-29 isotope, or a substance's NMR properties relating to this isotope
$^{29}Si\{^{1}H\}$	Proton-decoupled, silicon-29 NMR analysis
^{o}C	Degrees Celsius
%C	Relative atomic abundance (in percent) of carbon observed by elemental analysis
%H	Relative atomic abundance (in percent) of hydrogen observed by elemental analysis
%O	Relative atomic abundance (in percent) of oxygen observed by elemental analysis
A	Amperes; a unit of current
cm^{-1}	Reciprocal centimeters; a unit of measuring wavenumbers in FTIR spectra
E_r	Reduced Modulus of indented films reported in units of giga-pascals (GPa)
T_d	Temperature at which thermal degradation begins; at the T_d of a PAG, acid is thermally released without any prior irradiation
T_g	Glass transition temperature
ϕ_2	Volume fraction occupied by air in a porous film, i.e. the induced porosity
ϕ_1	Volume fraction occupied by host matrix in porous film ($1-\phi_2$)
n_2	Refractive index of air ($1.0003 \cong 1$)

n_{12}	Effective bulk refractive index of a mixed-component film
n_1	Refractive index of host matrix in a porous film, same value as the non-porous control sample
ε_{12}	Effective bulk dielectric constant of a porous film
ε_1	Relative dielectric constant of host matrix in a porous film, same value as that of the non-porous control sample
ε_2	Relative dielectric constant of air, equal to unity
g	grams
n	Degree of polymerization
1	**PNC1**
2	**PNC2**
3	**PNC3**
4	5-Norbornene-2-carboxyaldehyde
5	5-Norbornene–2 endo, 2 exo–dimethanol
6	Norbornane-2 endo, 2 exo-dimethanol
7	5-Norbornene-2,3 cis endo-dicarboxylic acid anhydride
8	5-Norbornene-2,3 cis exo-dicarboxylic acid anhydride
9	5-Norbornene-2, 3 cis exo-dimethanol

10	Norbornane-2, 3 cis exo-dimethanol
11	5-Norbornene-2, 3 cis endo-dimethanol
12	Norbornane-2, 3 cis endo-dimethanol
13	Spiro[bicyclo[2.2.1]heptane-2,5'-[1,3]dioxan]-2'-one. The IUPAC name for Norbornane-5,5-cyclic carbonate
M_n	Number-average molecular weight of an ensemble of polymer chains
M_w	Weight-average molecular weight of an ensemble of polymer chains
L	Length of a single repeat unit
$\langle r^2 \rangle^{1/2}$	Root mean square end-to-end distance of an ensemble of linear polymer chains
N_A	Avogadro's constant (6.022×10^{23} per mole)
$V_{H,\,m}$	Hydrodynamic volume of one mole of polymer chains in solution
V_H	Hydrodynamic volume of a single polymer chain in solution
R_H	Hydrodynamic radius of a polymer chain
$R_{H,\eta}$	Viscosity-derived hydrodynamic radius of a polymer chain
$R_{H,D}$	Diffusion-derived hydrodynamic radius of a polymer chain
$R_{H,\theta}$	Hydrodynamic radius of a polymer chain in its unperturbed (theta) state
D_0	The translational diffusion coefficient of the chains at infinite dilution

η_0	The viscosity of a solute-free solvent
T	The absolute temperature in Kelvin (K)
K	Kelvin; unit of absolute temperature
k_B	Boltzmann's constant (1.381×10^{-23} Joules per Kelvin)
^oC/min	Degrees Celsius per minute
T_d	Onset temperature for decomposition
T_{d10}	Temperature at which a sacrificial polymer exhibits 10 wt% loss under a constant dynamic heating rate
T_{d50}	Temperature at which a sacrificial polymer exhibits 50 wt% loss under a constant dynamic heating rate
t	Time variable in units of seconds
k_0	The pre-exponential rate constant in units of reciprocal seconds (sec^{-1})
E_A	The activation energy in units of joules per mole ($J\ mol^{-1}$)
C	The constant heating rate of a dynamic TGA run in units of Kelvin per second ($K\ sec^{-1}$), which is equivalent to ^oC/second
R	Universal gas constant (8.314 Joules per mole per Kelvin)
T_0	Initial absolute temperature in units of Kelvin
T_8^H	Octahydridosilsesquioxane; an HSQ cage
D_4^H	Tetramethyl-tetrasiloxane

M	The trimethylsilyl end-group or its silicon atom ($\underline{Si}Me_3$)
M^H	The dimethylsilane end-group or its silicon atom ($\underline{Si}Me_2H$)
M^{OH}	The dimethylsilanol end-group or its silicon atom ($\underline{Si}Me_2OH$)
M^{CH2}	The dimethylsiloxy-methylene group or its silicon atom ($O\underline{Si}Me_2CH_2$). This group is formed when M^H groups undergo hydrosilylation reactions with vinyl-containing organic groups
D	The dimethylsiloxy group or its silicon atom ($O\underline{Si}Me_2$)
D^H	The methyl-hydrosiloxy group or its silicon atom ($O\underline{Si}HMe$)
D^{OH}	The methyl-hydroxysiloxy group or its silicon atom ($O\underline{Si}(OH)Me$)
T	The methyl-trisiloxy end-group or its central silicon atom ($Me\underline{Si}(OSi)_3$)
T^H	The hydro-trisiloxy end-group or its central silicon atom $H\underline{Si}(OSi)_3$)
T^{OH}	The silanol-trisiloxy end-group or its central silicon atom ($HO\underline{Si}(OSi)_3$). In organosilicon literature, the terms Q_3 and T^{OH} are synonymous.
T^{CH2}	The trisiloxysilyl-methylene group or its silicon atom ($(SiO)_3\underline{Si}Me_2CH_2$). This group is formed when T^H groups undergo hydrosilylation reactions with vinyl-containing organic groups
Q	The quartenary siloxane group or its silicon center ($\underline{Si}(OSi)_4$). In organosilicon literature, the Q abbreviation is also referred to as Q_4.
Q_3	The silanol-trisiloxy end-group or its central silicon atom ($HO\underline{Si}(OSi)_3$). In organosilicon literature, the terms Q_3 and T^{OH} are synonymous.

LIST OF ABBREVIATIONS

SOG	Spin-on glass
low-k	Low dielectric constant material (has a dielectric constant < 4.0).
Ultra low-k	Material with a dielectric constant < 2.0. Materials usually achieve such low dielectric constants via the incorporation of porosity within the films
HSQ	Hydrogen silsesquioxane
MSQ	Methyl silsesquioxane
NMR	Nuclear Magnetic Resonance
Hz	Hertz; unit of measuring frequency and angular velocity
FT	Fourier transform
ppm	Parts per million
kHz	Kilohertz (1000 Hz)
MHz	Megahertz (10^6 Hz)
DP-MAS	Direct-polarization magic-angle-spinning
DSS	3-(trimethylsilyl)-1-propane sulfonic acid sodium salt
Elem. Anal	Elemental analyses
amu	Atomic mass units

GPC	Gel Permeation Chromatography
POSS	Polyhedral oligomeric silsesquioxane structure
Me	A methyl group (CH_3)
OH	The hydroxyl group
TMAH	Tetra-methyl ammonium hydroxide
SiO_2	Silicon dioxide
CMOS	Complimentary metal-oxide-semiconductor
XLK	Tradename for porous HSQ films made using Dow Corning's patented process
TEOS	Tetra-ethoxy silane
PECVD	Plasma-enhanced chemical vapor deposition
Si:O:C:H	An organosilicate or organosilica film. Also known as carbon-doped silica or silicon-oxycarbide
MIBK	Methyl isobutyl ketone
FOx-1x®	Flowable oxide (a commercial resin of HSQ in MIBK solvent)
nm	Nanometer (10^{-9} meters)
μm	Micrometer (10^{-6} meters)
mm	Millimeter (10^{-3} meters)
μL	Microliter (10^{-6} liters)

mL	Milliliter (10^{-3} liters)
mA	Milliamperes; a unit of current equivalent to 10^{-3} amperes
$Cr(acac)_3$	Chromium acetylacetonate
CF_4	Tetrafluoromethane
H_2O_2	Hydrogen peroxide
H_2SO_4	Sulfuric acid
HCl	Hydrochloric acid
TMS	Tetramethylsilane
THF	Tetrahydrofuran
M_w	Weight-average molecular weight
M_n	Number-average molecular weights
PDI	Polydispersity index
DLS	Dynamic light scattering
QELS	Quasi-elastic light scattering
PNC	Poly(norbornane carbonate)
PNC1	A PNC chain with the carbonate linkage at the 2-endo, 2-exo positions of the bicyclo[2.2.1]heptane ring
PNC2	A PNC chain with the carbonate linkage at the 2-exo, 3-exo positions of the bicyclo[2.2.1]heptane ring

PNC3	A PNC chain with the carbonate linkage at the 2-endo, 3-endo position of the bicyclo[2.2.1]heptane ring
ROP	Ring-opening polymerization
PNC1-ROP	A **PNC1** chain synthesized by ROP
PNC1-OH	Hydroxyl-terminated **PNC1** chains
PNC2-OH	Hydroxyl-terminated **PNC2** chains
PNC3-OH	Hydroxyl-terminated **PNC3** chains
PNC3v	Vinyl-terminated **PNC3** chains
TGA	Thermogravimmetric analysis
TGA-MS	Combined thermogravimmetric-mass spectrometry analyses
MS	Mass spectrometry
PAG	Photoacid generator (a photoinitiator that releases an acid when excited by radiation)
HTPFPB	Hydrogen tetrakis(perflourophenyl)borate
TTBPS-Tf	tris(tert-butyl phenyl)sulfonium triflate
TTBPS-Nf	tris(tert-butyl phenyl)sulfonium nonaflate
PBG	Photobase generator (a photoinitiator that releases a base when excited by radiation)
CTS	N-cyclohexl-*p*-toluene sulfonamide

NBC	*o*-nitrobenzyl cyclohexylcarbamate
FTIR	Fourier transform infrared spectroscopy
ATR	The attenuated total reflectance mode of FTIR analysis
S_ni-Si	A mechanism that describes how silane bonds are hydrolyzed to form silanol bonds
c/n	The ratio of the areas underneath the FTIR peaks corresponding to cage-type siloxane and network-type siloxane, respectively
GPA	Giga-pascals (10^9 pascals)
DUV	Deep ultraviolet radiation
PEB	Post-exposure bake
EMA	Effective medium Approximation, an optical or dielectric models used to predict the effective properties of multi-component materials
DSC	Differential scanning calorimetry
IDE	Interdigitated electrodes
UV-VIS	Ultraviolet-visible light spectroscopy
FIB	Focused ion beam
SEM	Scanning electron microscope
TEM	Transmission electron microscope
kV	Kilovolts (10^3 volts)

Si_xN_y	Low-stress (non-stoichiometric) silicon nitride
DSP	Double-sided polished
LPCVD	Low-pressure chemical vapor deposition
ICP	Inductively-coupled plasma
DI	De-ionized water
PTFE	polytetrafluoroethylene
KOH	Potassium hydroxide
IPA	Isopropyl alcohol
rpm	Revolutions per minute; a unit of angular velocity equivalent to 1/60 Hz
AFM	Atomic force microscopy
rms	Root mean square, the value of the standard deviation of a distribution
PC	Propylene Carbonate
NMP	N-Methyl-2-pyrrolidinone
GBL	Gamma-butyrolactone
sccm	Standard cm^3 per minute; a unit of measuring volumetric flowrates of gases
DCM	Dichloromethane
TMCS	Trimethylchlorosilane

$MgSO_4$	Magnesium sulfate
$NaHCO_3$	Sodium hydrogen carbonate
K_2CO_3	Potassium Carbonate
$LiAlH_4$	Lithium aluminum hydride
TEA	Triethylamine
Et_3N	Alternative abbreviation for triethylamine
MeOH	Methanol
EtAc	Ethyl acetate
EtOH	Ethanol
CDI	Carbonyldiimidazole
DMAP	4-dimethylaminopyridine
H_2	Hydrogen gas
N_2	Nitrogen gas
mmoles	Millimoles (10^{-3} moles)
$HOCH_2OH$	Oxymethylene glycol
$(CH_2O)_n$	Poly(oxymethylene glycol) or Paraformaldehyde oligomers
$(CH_2O)_3$	Trioxymethylene or trioxane; a cyclic trimer of oxymethylene glycol

NaCl	Sodium chloride
Pd/C	10% Palladium supported on activated carbon
NaOMe	Sodium methoxide
sec-BuLi	Sec-butyllithium
BF_3OEt_2	Boron trifluoride diethoxide
DBU	1,8-diazabicyclo[5.4.0]undec-7-ene
MHS	Mark-Houwink-Sakurada constants
PBAC	Poly(bisphenol-A-carbonate)
PDMSH	Silane-terrminated polydimethylsiloxane
$Q8M8^H$	Octa(dimethyl siloxy)silsesquioxane
Pt(dvtms)	Platinum divinyl-tetramethylsiloxane complex
CTS	N-cyclohexl-*para*-toluene sulfonamide (CTS)
NBC	*Ortho*-nitrobenzyl cyclohexylcarbamate (NBC)

SUMMARY

Three types of poly(bicycle[2.2.1]heptane carbonate) or poly(norbornane carbonate) or PNC oligomers were synthesized and characterized via spectroscopic methods and elemental analyses to validate their chemical structures. End-group analyses were used to estimate the degree of polymerization of the oligomers via the use of proton nuclear magnetic resonance (^{1}H NMR) results. Random-coil and rigid-rod models were used to estimate the sizes of individual PNC chains based on the degrees of polymerization calculated from NMR data. Due to the small sizes of the PNC chains, dynamic light scattering (DLS) was incapable of measuring the hydrodynamic radii, R_H, of individual chains. Attempts at using gel permeation chromatography (GPC) data to estimate the hydrodynamic radii of individual chains consistently provided values that were an order of magnitude smaller than the estimated sizes of individual chains based on random-coil calculations. The thermal properties of PNCs were determined via differential scanning calorimetry (DSC) and thermogravimetric analyses (TGAs). All three types of PNC structures were both thermally-labile and acidolytically-labile, allowing them to be used as sacrificial materials in both direct-write and thermally-processed template systems. TGA data was used to determine the kinetic parameters for the thermolytic decomposition reactions and evolved-gas analysis via mass spectrometry (TGA-MS) was used to validate the mechanisms for polycarbonate thermolysis reactions that have been previously proposed in literature.

PNC oligomers were freely-mixed with hydrogen silsesquioxane (HSQ) to form solutions that were spin-coated to form templated films. Ellipsometry and dielectric

measurements were used to track the changes in the optical and dielectric properties of templated films and effective medium approximations were used to estimate the level of porosity incorporated within each porous film. Transmission electron microscopy (TEM) showed that the free-mixing of PNCs with HSQ resulted in the agglomeration of the porogen molecules during the spincoating step. This phase-segregation led to the formation of domains with dimensions much larger than those of the individual chains, and during decomposition large pores were produced. To combat the phase segregation, hydrosilylation reactions were used to covalently bond vinyl end-capped PNC chains to silane-functionalized siloxane and silsesquioxane molecules. These matrix-like materials served as compatibilizers in order to improve the phase-compatibility of the sacrificial polymers in HSQ films. NMR and GPC analyses showed that the solids recovered from the hydrosilylation reactions were binary mixtures of hybrid nanocomposite molecules and residual ungrafted chains. All attempts at isolating the hybrid molecules proved to be unsuccessful and the solids were templated as blends in HSQ films.

TEM imaging showed that the domains in these nanocomposite films had bimodal size distributions due to the presence of two components in the mixtures. The hybrid molecules produced pores ranging in size from about 6-13 nm as a result of improvements in the phase-compatibility of the grafted oligomers. However, the residual ungrafted oligomers in the blends produced larger domains measuring 30-40 nm. Although the siloxane and silsesquioxane molecules were shown to fulfill the stated goal of compatibilizing the PNC chains with HSQ and the hybrid molecules produced domain sizes comparable to those of templated films reported in literature, the difficulty in isolating the hybrid molecules from the ungrafted oligomers limits the benefits of using

these blends as porogen materials. It is believed that separation difficulties can be avoided if the physical and chemical conditions used in the vinyl termination reactions can be adjusted to ensure 100% conversion of all the terminal hydroxyl groups to vinyl groups. Doing so would allow all PNC chains to be grafted during hydrosilylation reaction; thus, avoiding the recovery of ungrafted oligomers. The recovery of pure hydrosilylation products would allow monodisperse domains with sizes ranging from 6-13 nm to be produced in templated films. Additionally, improvements can still be made in the morphology of hybrid films by successfully grafting polycarbonate chains directly to HSQ prior to spincoating thin films. Although all attempts at performing this reaction using PNC chains were unsuccessful, it is expected that another polycarbonate with a less sterically-hindered chemical structure may be successfully bonded to HSQ. Based on literature data, such a template system can be expected to produce pores as small as the individual polycarbonate chains, which is an ideal morphology for low-k applications.

CHAPTER 1

INTRODUCTION[†]

1.1 Motivation for Investigating Porosity in Thin Films

The incorporation of porosity in a material potentially results in changes in its electrical, mechanical and optical properties (eg. lowering of dielectric constant, enhancement in flexibility and crack-resistance, the lowering in refractive index, etc), and has generated much interest by researchers.[3] Porous thin films have found wide use in the microelectronics industry due to their low dielectric constant properties, which allow them to replace silicon dioxide as an intralevel dielectric material. The development of new techniques for producing porosity in thin films may prove advantageous if they lead to a decrease in processing complexity, or a relaxation of processing constraints by widening the window of compatible physical conditions, or an improvement in the final properties of the porous materials. The final physical properties of porous films are dependent on the pore structure characteristics, such as the total amount of porosity induced, the sizes of the pore, the pore size distribution, and presence or absence of pore interconnectivity.[3] The differences in the morphology of the final pore structure are a result of variations in the physical and chemical environment that each film is exposed to during its fabrication. Important factors include the type of porogen used, the porogen

---

[†] Portions of the material presented in this dissertation appear in previous publications.[1, 2]

loading, phase compatibility between the porogen and the surrounding matrix, and the processing temperatures required.[4]

1.2 Dielectric Materials

1.2.1 General Considerations for Dielectric Applications

As the dimensions of complimentary metal-oxide-semiconductor (CMOS) transistors in integrated circuits (ICs) have continued to shrink to obtain higher performance, the gate switching time has been surpassed by the signal propagation time as the timescale limiting the overall speed of micro-processors.[3-5] This is because although the transistor switching time has scaled down with the decreasing feature sizes, the global and semi-global RC delay time has *increased*.[6] The increase in the RC delay time is a product of two factors: the increase in resistance (R) that is produced by the decreased width of electrical interconnects, and the increased capacitance (C) that is produced by decreases in the line-to-line spacing (pitch) between interconnects and height of interconnects.[3, 6] The mathematical relationships relating signal line dimensions to the electrical resistance, overall capacitance, and RC delay are shown in Equation (1.1), Equation (1.2), and Equation (1.3), respectively. [6]

$$R = \frac{2\rho L_W}{PH_w} \tag{1.1}$$

$$C = 2(C_H + C_v) = 2k\varepsilon_0\left(\frac{2L_wH_W}{P} + \frac{L_wP}{2H_W}\right) \tag{1.2}$$

$$RC = 2k\varepsilon_0 L_w{}^2\left(\frac{4}{P^2} + \frac{1}{H_W{}^2}\right) \tag{1.3}$$

The symbols ρ, ε_0, k, P, H_w, and L_w, refer to the resistivity, permittivity of free-space, relative dielectric constant, pitch, height and length of the wires, respectively. The symbols C_H and C_V refer to the intralevel (horizontal plane) capacitance and the interlevel (vertical plane) capacitance, respectively. Figure 1.1 shows a cross-sectional view of a typical interconnect wiring level, complete with annotations for the dimensions of the electrical interconnects, and the contributions of each dielectric area towards C_H and C_V.

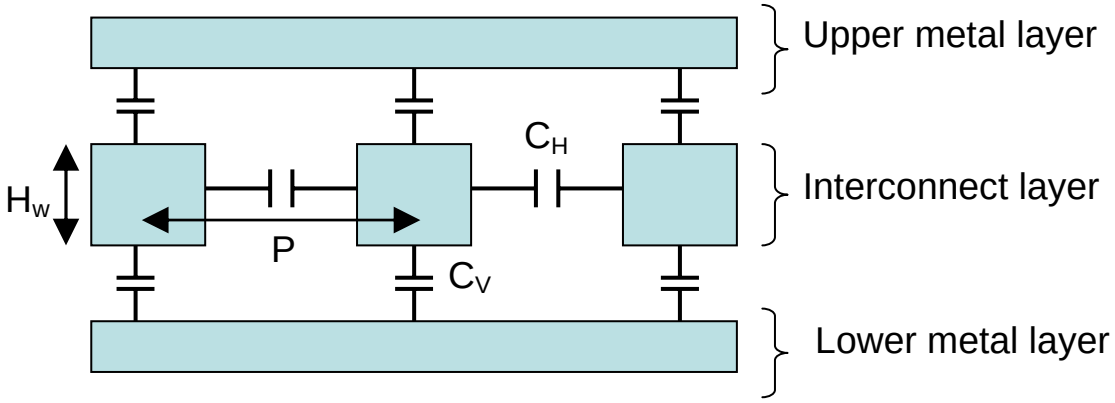

Figure 1.1 – Cross-section of a typical interconnect wiring level

Thus reductions in transistor dimensions (P and H_w) do not guarantee reductions in micro-processing times since switching times are no longer the dominate timescale that dictates the overall delay time of ICs. Silicon dioxide (SiO_2), which is the current and traditional dielectric material, must be replaced by alternative materials that have lower dielectric constants in order to ensure that that the RC delay remains low.[3, 5, 7]

1.2.2 Low-k Materials and General Processing Methods

Low-k materials, which are defined as materials with dielectric constants (k) lower than 4.0, exhibit lower polarizabilities than SiO_2 when subjected to electrical

fields.[3-5] The substitution of SiO_2 with a low-k film leads to decreases in the capacitance of the intralevel dielectric material, thus decreasing the RC delay.[4, 8, 15-33] However, the IC industry has placed stringent requirements for low-k materials to be considered compatible with IC processing. Namely, the low-k materials should have $k < 4.0$, have high breakdown voltages, allow low leakage currents, have good mechanical properties, have good adhesion properties to IC substrate materials, have high thermal stability, and be resistant to the chemicals used in wet-processing of ICs.[3, 5, 7-10] Additionally, low-k materials should not be hydrophilic since any moisture uptake would result in (a) large increases in both the dielectric constant and the leakage current and (b) a decrease in the breakdown voltage. Each of these phenomena would detrimentally affect the performance of an integrated circuit.[3, 5, 7, 11-19] Over several years, a multitude of low-k materials have been investigated, including silsesquioxanes, polymers, and films deposited by plasma-enhanced chemical vapor deposition (PECVD) to determine if the final material properties and the processing conditions are compatible with standard CMOS processing.[3, 9, 18, 20] A general description of the low-k materials and their processing methods are outlined below.

1.2.2.1 Low-k Films via PECVD

PECVD is frequently used to deposit thin films owing to the ease of operation of a PECVD tool (ie. a single-step process), the excellent uniformity of deposited films, the superior mechanical properties of PECVD films due to low internal stresses both during and after deposition, and the highly repeatable results when all of the processing parameters are kept invariant.[3, 5] Since most of the reactions essential for film

deposition occur in the gaseous phase, all the chemical precursors used in PECVD must be volatile so that they can be swept into the reaction chamber by a carrier gas.[5] Additionally, in order to obtain a uniform film deposition, the processing parameters (temperature, frequency, etc) in the reaction chamber must be appropriate for the formation of a stable plasma.[4, 8, 10-12, 17-20, 22, 33, 35, 37-55] Owing to the extra processing constraints imposed on PECVD processing in comparison to the greater flexibility enjoyed of wet-chemical methods, the number of low-k and ultra low-k ($k < 2.0$) films produced via PECVD are far fewer than those produced via wet-processing.[3, 9, 18, 20] To decrease the polarizability of the deposited low-k film below that of pure silica, the chemical structures of the precursors are chosen to substitute some of the polarizable siloxane bonds in the silica structure with either silicon-methyl (Si-CH_3 or Si-Me) or silicon-fluorine (Si-F) bonds.[3] The substitution of Si-O with either Si-Me or Si-F leads to an increase in the interatomic distances between atoms, thus leading to a lower density and larger free volume within the C-doped or F-doped silica structure.[3] The increased void space is an inherent type of microporosity (pores < 2 nm) within the matrix and typically constitutes about 5-15% of the total film volume.[3, 9, 10, 18, 20] The resultant dielectric constant depends on the degree of substitution (ie. the ratio of the different elements in the structure), but typical k values for carbon-doped or silicon-oxycarbide (Si:O:C:H) PECVD films are between 2.6 and 3.0, which is well below that of pure silica (4.0) even though no sacrificial pore generators are used.[3, 5, 7]

1.2.2.2 Low-k Films via Wet-Processing Methods

Although numerous polymeric materials posses low dielectric constants due to their natural hydrophobicity, their organic nature makes them thermally unstable. Most polymers degrade when exposed to the high temperature (> 500 C) conditions that are commonly used in CMOS processing.[3, 5, 7] Thus, for practical reasons, most of the polymeric low-k candidates first proposed as replacements for silicon dioxide have since been abandoned as viable intralevel low-k materials.[3, 14-16, 19, 21, 22] However, inorganic glasses (eg. HSQ) and inorganic-organic hybrid glasses (eg. methyl-silsesquioxane or MSQ) have been shown to posses both good dielectric properties and high thermal stability due to their silica-like internal bonding structure.[14, 15, 17] HSQ is a purely inorganic spin-on glasses (SOG) with the general formula $HSiO_{1.5}$, and it is spin-coated prior to being thermally cured in a nitrogen-purged furnace to form a rigid SiO2-like structure.[11, 13] The thermal cure reactions of HSQ occur over a wide range of temperatures (200-800^{o}C), and the final dielectric and optical properties of HSQ films depend on the cure process (ie. time and temperature profile) used.[3, 23, 24] At optimal processing conditions for low-k applications (under low oxygen content atmosphere at 350-400^{o}C), HSQ has a dielectric constant of 2.7-2.8 that is stable at ambient humidity for extended periods of storage.[25, 26]

A major disadvantage of using HSQ as a low-k film is that it has poor resistance to chemical attack, leading to degradation when exposed to polar liquids, plasma conditions, and ashing conditions.[5, 8, 10, 27] In the presence of bases, the hydrophobic silane bonds in HSQ films undergo hydrolysis resulting in their conversion to hydrophilic

silanol bonds. Silanols bonds cause the low-k films to absorb moisture, leading to increases in their dielectric constant and leakage current, and decreases in their breakdown voltage.[3] Since aqueous bases, such as tetra-methyl ammonium hydroxide (TMAH), are frequently used as developers during photolithography, exposure of films to such media cannot be avoided during IC processing.[20] Non-porous inorganic-organic hybrid SOGs, such as MSQ have an inherently hydrophobic structure, which gives them a better chemical resistance than HSQ and silica to hydrolytic degradation by polar liquids and oxygen plasma during short-term exposures.[3, 19, 21, 22, 26, 28-32] For this reason, organosilicon SOGs have generated much interest as materials for low-k applications.[3, 8-10, 33]

However, no low-k material is immune to degradation during long-term exposure to aggressive chemical conditions.[34] To avoid film degradation, the surfaces of low-k films are modified in one of two ways: (1) the first method employs silanization agents to convert any silanol bonds to highly hydrophobic trimethylsilyl sites (ie. $Si(CH_3)_3$ or $SiMe_3$) that repel water molecules;[3, 35-42] and (2) the second method, which is more effective and more widely used, protects films from environmental effects via the deposition of hermetic diffusion barriers using either PECVD or sputtering deposition.[3, 8, 10, 25, 26, 28, 29, 35, 43-45]

1.2.3 Porous Films as Ultra low-k Materials

Since porosity is known to decrease the polarizability of materials, several porous films have been investigated as potential ultra low-k ($k < 2.0$) candidates. Among the potential ultra low-k materials, porous PECVD films, porous silica, and porous

silsesquioxanes (eg. XLK and porous MSQ) have been widely reported.[3, 25, 26, 35, 43] XLK is a porous version of HSQ and its pores are induced by the volatilization of entrapped solvent, as described in a later section.[3, 25, 26, 35, 43] Depending on the processing conditions used, XLK can have a dielectric constant as low as 1.5, induced-porosities as high as 60%, pore sizes ranging from 2-4 nanometers (nm), fair mechanical integrity and fairly stable dielectric properties even when left uncapped at ambient conditions.[3, 19, 35, 42, 44-49] However, both XLK and porous silica films have an interconnected open- pore structure, which makes them vulnerable to absorption of both gaseous and liquid contaminants during subsequent exposure of films to humid atmosphere or aggressive chemical environments that are frequently encountered in CMOS processing. [3, 8, 28, 29, 31, 32, 50]

Because of their overall qualities, porous MSQ films have attracted a great deal of interest from the IC industry and it remains one of the leading candidates for use as an ultra low-k material.[3, 8, 19, 28-32, 38, 40, 41] Porous MSQ films, formed via the decomposition of templated sacrificial polymers, have been shown to possess tunable dielectric constants as low as 2.2, pore sizes comparable to XLK films, and superior chemical resistance properties.[8, 9, 32] However, researchers have also shown that both porous MSQ films and porous PECVD films absorb moisture if left uncapped.[4, 11, 17, 21, 34, 35, 45, 47, 54, 57-61] Hence, all the ultra low-k films reported have a tendency towards moisture uptake, and to overcome this problem, porous thin films must either be capped with barrier layers or have their surface sites chemically modified to avoid degradation of their ultra low-k qualities upon exposure to reactive environments.[3, 25, 26, 35, 43] Although the porous films presented in this dissertation

are all based on the HSQ host matrix, their processing methods and their final film properties are all different from those of XLK films developed by Dow Corning. [1, 2]

1.3 Methods of Inducing Porosity in Thin Films

A variety of methods have been reported in literature for producing porosity in PECVD and spun-coated thin films.[3, 9, 20] The processing methods for producing porosity in spun films can be broadly categorized under two main categories, namely those that employ sacrificial polymers to serve as templates for pores after their decomposition and those that use solvents to generate the pores. The following subsections summarize each of the processing methods used to form porous thin films.

1.3.1 Mesoporous PECVD Films

As stated earlier, constitutive microporosity in the form of increased free volume can be incorporated in silica by substituting siloxane bonds with Si-Me, Si-F bonds since their interatomic distances are larger. To generate even more porosity, thermally unstable organic species can be embedded into doped-silica via the gas-phase mixing of the organosilicate precursors with thermally labile organic precursors prior to formation of reactive intermediates and film deposition.[3, 9, 20] After deposition, the hybrid films are then annealed at high temperatures to decompose the sacrificial organic constituents and, depending on the ratio of mixed precursors, porosities as high as 30-40% and k values as low as 2.05 may be achieved. [3, 9, 20] Although the level of porosity and the sizes of the mesopores produced are interdependent, the pore sizes always remain below 5 nm. [3]

As an alternative to thermal decomposition of the organic phase, the sacrificial component can be removed via a selective chemical etch with a dilute hydrofluoric acid (HF) can be used to remove after chemical vapor deposition. [3] The porosity and pore sizes depend on the concentration of the HF acid (affects etch rate) and the etching time, with the porosity ranging from 10-55% and the pore sizes ranging from 1-11 nm.[3] Similar to the first method for producing mesoporosity in PECVD films, the level of porosity and the sizes of the pore cannot be independently adjusted. The etching method for porous PECVD films is similar in principal to a process for producing porosity in spun-on polymer films called solvent leaching and selective dissolution, which is discussed in the following section.

1.3.2 Solvent Leaching and Particle Dissolution in Spun Polymer Films

A wet-processing method by which solvents have been used to generate porosity is via dissolution of soluble particles or co-polymer segments dispersed within films. [3] This method is called a subtractive method due to the removal of the pore-generator via dissolution by solvents.[3, 51, 52] In this processing method, coated films are leached with appropriate solvents that are able to swell an insoluble matrix and also dissolve the dispersed sacrificial solid material. Following this leach and dissolution step, the solvents and the dissolved particles) are removed, and the films are then dried to produce pores in place of the particles.[7] Polymers are used as the insoluble host matrix materials since a large number of polymer films are easily penetrated solvents and can be chemically bonded with soluble co-polymer segments or sacrificial particles to ensure that the resultant pore structure is homogenous.[3, 51, 52] The pore sizes are highly

dependent on the sizes of the sacrificial solids that are originally dispersed within the matrix. The sacrificial co-polymer segments and colloidal particles that have been reported to be used are fairly large, producing pores ranging in size from several hundred nanometers (nm) to hundreds of micrometers (μm). [3, 5, 7, 53, 54] Given the large sizes of the pores and the tendency of porous polymeric films to quickly absorb atmospheric moisture due to the high permeability of water in polymers compared to inorganic glasses, these leaching methods have not been adopted by the IC industry for producing porous dielectrics.[3]

1.3.3 Porosity Induced via Volatilization of Encapsulated Solvent

An alternative method for producing porous films is to volatilize encapsulated solvents from rigid, spun films. Although a wide selection of solvents are available that can be mixed into spinnable formulations and later boiled off from matrix materials, solvents must be carefully selected to ensure that they are chemically compatible with the host matrix used (i.e. the solvent must not dissolve or otherwise degrade the bulk material that is meant to host the pores nor volatilize before the matrix has been fully vitrified).[7] The methods of crosslinking the films prior to solvent removal depend on the nature of the matrix material. Many organic materials (i.e. polymers) can be thermally cured at moderate temperatures, where some high boiling point solvents will not prematurely be removed.[3, 7, 55-57] Alternatively, polymers may be crosslinked at low temperature via radical-, cationic-, or anionic-catalysis.[46] Researchers have produced solvent-induced porosity in poly(aryl ethers) via a process of phase separation and evaporation.[3] The pores produced were about 3 nm in size but the processing times were long because of

the extensive mixing times required (over 24 hours) to ensure that the degree of phase segregation was sufficient prior to spin-coating.

Spinnable inorganic materials are sol-gel based, and their thermal cure reactions take place at such high temperatures that few solvent molecules would remain trapped within a thermally cured matrix.[3, 25, 35, 36, 38, 41, 44, 45, 58, 59] To overcome this constraint, the crosslinking reactions of sol-gel films are catalyzed at low temperatures via the use of acids or bases to induce silanol condensation in order to allow all of the solvent molecules to be encapsulated and ensure high induced porosities when they are removed. A multitude of inorganic materials have been successfully incorporated with solvent-induced pores, such as silica (aeorgels, xerogels) and silsesquioxane-based matrices (e.g. XLK, which is Dow Corning's porous version of HSQ).[3, 44, 45, 58-61] Porous silica films are produced by spin-coating resins of silica-precursors, such as tetra-ethoxy silane (TEOS), and then crosslinking them via exposure to bases under tightly controlled conditions (pH, temperature, water content, alcohol content, etc) prior to removal of entrapped solvents.[3]

Aerogels and xerogels are both produced by "aging" a sol-gel film to form a "wet gel" framework, thermal curing to form a rigid network, then the volatilization of internal solvents either via evaporation (xerogels) or by supercritical drying (aerogels).[3] Although aerogels may have porosities as high as 98%, it requires supercritical drying to achieve these high porosities, leading to the requirement of a solvent exchange step between the original solvent and carbon dioxide.[3, 44, 45, 58-61] The processing of Xerogel is less restrictive since the internal solvent is evaporated by conventional means at moderate temperatures (100-200 C); however, the final porosities of xerogels are much

lower (50-80%).[35, 36, 42] During the processing of XLK, films are spin-coated from a resin that already contains the porogen, and then these films are crosslinked using aqueous ammonia for 30-60 seconds at ambient temperature.[3, 35-38, 41, 42] The ammonia soak step is used to initiate base-catalyzed gelation, which makes the matrix rigid enough to support porosity. Finally, the films are baked on a 150^{o}C hotplate for 1 minute and subsequently in a 450^{o}C furnace for an hour to completely volatilize solvents trapped within the rigid film structure.[4] XLK films have high levels of porosity (> 50%), very low dielectric constants (1.5 - 2.2), and small pores (< 4 nm), making them very attractive dielectric materials.[3]

Although aerogels and xerogels have relatively high porosities, film-to-film reproducibility is poor since several environmental parameters affect the rate of both gelation and volatilization steps resulting in large differences in both the degree of both film shrinkage and pore formation.[3] Additionally, the "aging" step that they both require do not allow independent control of both pore size and porosity, and it has been observed that the sizes of their pores tends to increase as their porosity increases, leading to poor mechanical integrity and high susceptibility to moisture uptake.[3, 19, 35, 42, 46-49] Lastly, the volatilization of solvent from xerogels and aerogels produces an interconnected open- pore structure, making them vulnerable to absorption of both gaseous and liquid contaminants to the chemical environments that are frequently encountered in CMOS processing.[3, 35-42] This necessitates the hermetic sealing of their pore structure with a diffusion barrier, as detailed in a previous section.[3, 25, 26, 35, 43]

1.3.4 Thermal Decomposition of Templated Sacrificial Polymers

The traditional template technique for fabricating a porous thin film makes use of a porogen (thermally decomposable polymer or volatile solvent) distributed in a crosslinkable matrix.[54] During processing, the matrix is cured to instill mechanical integrity, before the film is heated to high temperatures to decompose and volatilize the templated polymer.[1, 2, 28-31, 53, 54, 62-64] As the decomposition by-products diffuse out of the films, air diffuses in to replace the porogen, resulting in the formation of air pockets in-place of the sacrificial polymer chains. The total processing time for the template technique may be several hours because of the necessity of thermally setting the matrix as well as decomposing the polymer via a slow ramp in temperature to the decomposition point of the porogen and a dwell time to ensure the removal of all of the porogen.[1, 2, 28, 30, 62]

Additionally, films must be allowed to cool slowly prior to removal from furnaces to avoid the buildup of internal stresses and subsequent formation of cracks arising from the thermal shock of exposing hot films to ambient conditions.[1, 2, 28, 30, 62] A further disadvantage of producing porosity via the thermal decomposition of a porogen is that most organic materials cannot be used as substrates owing to their degradation at the high temperatures required to decompose the templated polymers.[7] Finally, the high temperatures required to thermally decompose polymers encourage phase segregation and agglomeration of the macromolecules prior to decomposition thus producing large, non-uniformly dispersed pores that may produce undesirable final properties in the porous films.[1, 2] To avoid phase-segregation during thermal processing, sacrificial

polymers chains must be chemically bonded to the matrix backbone to prevent their movement at high temperatures.[28, 53, 54, 62-64]

1.3.5 Porosity via Self-Assembly: Zeolites

Researchers have shown that, zeolites, which are aluminosilicate sol-gel frameworks, can self-assemble into well-ordered, monodisperse microporous (pores < 2 nm) crystallites, and if these zeolites are mixed with labile surfactants, then mesoporous (pores sizes from 2-50 nm) silicates can be produced.[3] Unlike xerogel and aerogel processing, self-assembly approaches afford precise control over the pore sizes as well as the pore size distribution within the porous silica.[3, 65-67] This is because both the size of the mesopores and their size distribution are determined by the size of the surfactant molecules templated in the zeolite network.[28-31, 53, 54, 64] This morphological dependence on the porogen size is similar to those of porous film techniques discussed earlier that use sacrificial polymers as the templated porogen.[3, 65-67] The sizes of zeolitic mesopores reported in literature (10 nm to above 50 nm) are also comparable to the pores produced from sacrificial polymers. The pores of zeolites have a narrow size distribution and are ordered periodically in their matrix due to the specific packing arrangement of the aluminosilicate crystallites.[3, 65-67] Mesoporous zeolites have interconnected pore structures, and the widths of their pore channels are larger than those of xerogels and aerogels.[3, 19, 35, 42, 46-49, 65-67] Although this makes mesoporous zeolites ideal for use as membranes and catalysts owing to the ease of diffusion of species to and from the pore-sidewalls, these open-pore structures favor significant moisture uptake, which is undesirable for dielectric applications, as discussed previously.[68-77]

1.3.6 Photobleaching Method via Photocleavable Polysilanes

Polysilanes are susceptible to photocleavage of the main chain and thus direct decomposition via photolytic reactions (photobleaching).[70]. Researchers have made use of the photocleavable nature of Si-Si bonds in the structure of polysilanes to UV-induce porosity in hybrid films composed of methacrylate-polysilane copolymers (MPS) chemically bonded to inorganic sol-gel matrix materials.[70] Miura and co-workers. reported that when an MPS-titania film with 50 wt% MPS was exposed for 10 seconds to 248 nm UV radiation having an intensity of 105 mW cm^{-2}, the refractive index of the film dropped by 0.18 while a MPS-silica film with 50 wt% MPS had a refractive index drop of 0.16.[78] These decreases in refractive indices were due to the incorporation of air within the matrix materials since air has a refractive index of only 1.0003.[71] While investigating the use of poly(methyl phenylsilane) (PMPS) films in the formation of phase masks, Nagayama and co-workers. reported that 0.3 μm PMPS films exposed to 308 nm light had a refractive index drop from 1.70 to 1.63 while films exposed to 254 nm light showed a drop in refractive index from 1.70 to 1.58 due to photodecomposition of the PMPS.[69] Mimura and co-workers. reported that when a MPS-silica (24wt% MPS) hybrid film was exposed to UV radiation, the refractive index of the film dropped from 1.60 to 1.53 before rinsing with hexane, and dropped further to 1.40 after the hexane rinse leading them to conclude that all of the polysilane had decomposed.[1, 2]

1.3.7 Novel Methods for Producing Porosity in HSQ Films below its Tg

Although a variety of methods exist for producing porous films, the majority of these techniques require high processing temperatures to crosslink the host matrix prior to pore formation and/or to remove the pore generator (porogen). As an alternative to the traditional processing methods, two new techniques were developed to produce porosity in thin dielectric films at temperatures below the glass transition temperature of the host matrix.[1] These glassy-regime processing methods rely on the susceptibility of hydrogen silsesquioxane to gelation when exposed to polar substances.

1.3.7.1 Direct-Write Porosity via Photodefinable Polycarbonates

The polysilane-based photobleaching system described previously relies on the direct photosensitivity of polysilane and will only work for polymers that can be directly decomposed by radiation. Aromatic and aliphatic polycarbonates, although not directly photocleavable, may be indirectly decomposed via UV-initiation due to their vulnerability to acid-catalyzed decomposition.[1, 2, 79-87] By mixing bulk polycarbonate films with photoacid generator (PAG) photoinitiators, the polymers molecules have been selectively decomposed via the UV-generation of acids under a photomask thus enabling their use as UV-patternable, positive-tone photoresist materials.[79-85] The general mechanisms for the thermolytic and acidolytic de-polymerization of both aromatic and aliphatic polycarbonates have been reported by several researchers.[79, 86-92]

The radiation-based (direct-write) process developed as part of my research also relied on PAG/polycarbonate chemistry, but instead of dispersing PAG molecules in a bulk polycarbonate film, both PAG and polycarbonate molecules were templated within a crosslinkable HSQ matrix.[1, 2] The basic sequence of steps in the direct-write process is shown in Figure 1.2. Prior to acid-induced decomposition of the polycarbonate chains, the matrix was hardened to allow it to mechanically support porosity. UV-exposure and a post-exposure bake (PEB) were used to drive the acidolysis of the sacrificial polymer, resulting in the production of porosity and the lowering of the refractive index.[93]

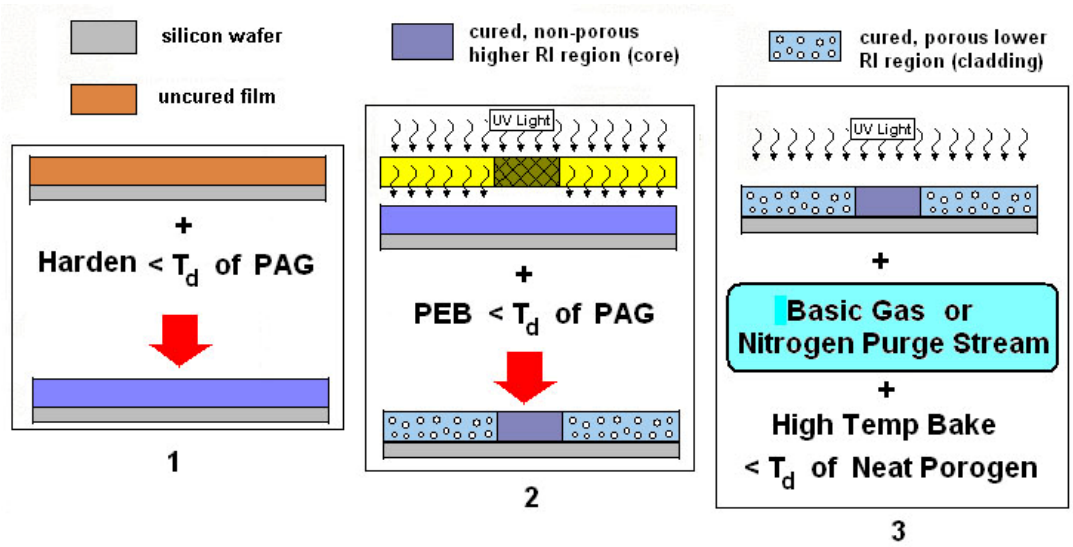

Figure 1.2 – Basic sequence for lateral patterning of direct-write porosity. T_d refers to the temperature at which thermal degradation begins.

By performing irradiation through a photomask, porous regions (cladding) and non-porous regions (cores) were laterally-patterned to create refractive index profiles within the processed films. To prevent acid-catalyzed decomposition of the polycarbonate molecules in non-porous regions, a blanket UV-irradiation was used to

generate acids before their neutralization via the diffusion of a basic gas through the film. As an alternative to using a basic gas to neutralize the acid molecules, a vacuum environment or a high purge flowrate to sweep away volatile acid molecules after their photogeneration were both found to be effective methods to remove photoacids from the films.

This radiation-based (direct-write) method of decomposing photodefinable polymers had several advantages over the traditional method of thermally decomposing templated sacrificial polymers at high temperature.[2, 54] By using radiation to induce the decomposition of templated polymer chains, the processing temperature required to produce porosity was decreased, which led to a decrease in the overall processing time since there was no need to ramp a furnace to a high temperature to initiate polymer decomposition. Lower processing temperatures potentially allow organic substrates to be used as well as reduce tendency for polymers to phase segregate during the procedure.[7] Furthermore, UV-induced decomposition enables the patterning of porosity in selective areas of the exposed films i.e. lateral patterning of porosity. This patterning capability may be used to make interesting devices in which functionality is dependent on the level of porosity present (eg. phase masks, or lateral confinement in waveguides due induced refractive index profiles).[1, 69-71, 73, 74, 76, 77, 94]

1.3.7.2 Glass-State Processing via a Mixed-Solvent (Gelator/Porogen) System

The second glassy-state processing method for producing porous films made use of non-protic organic co-solvent mixtures to serve both as a gelation catalysts and a pore-generators.[1, 2] The development of this technique was motivated by the discovery that,

in addition to aqueous bases, non-protic organic solvents with strong dipoles were efficient catalysts for the low-temperature sol-gel crosslinking of HSQ. Among the advantages of using this processing method, the processing conditions were flexible enough to allow HSQ to be highly crosslinked at temperatures as low as ambient, while still being able to easily remove them from the rigid films by using a single heating step to form pores. Owing to the complete miscibility of the co-solvents, this technique potentially allows wide ranges of porosities to be produced; hence, enabling the properties of the porous films to be tuned by varying the composition of the gelator-porogen mixed solvent system.

The dual use of the co-solvents as both crosslinking agents and as placeholders for air pockets decreased the processing complexity relative to other xerogel solvent-processing techniques, since the need for a separate crosslinking catalyst was eliminated and there was no need for supercritical drying of solvent, as done with aerogel processing.[1, 2] Additionally, this technique had all of the processing advantages of other solvent-processing methods for porous films, such as relatively short processing times (about 50 minutes), and low processing temperatures (120-150^{o}C). In contrast, porosity methods that use thermal decomposition of sacrificial polymers usually require processing times of at least 2 hours and temperatures well above 250^{o}C in order to decompose the porogen.[1, 2] However, all porosity methods that rely on the volatilization of solvent (eg. xerogels, aerogels, etc) invariably produce an interconnected open- pore structure, making them vulnerable to absorption of both gaseous and liquid contaminants to the chemical environments that are frequently encountered in CMOS

processing.[3, 5, 10, 33] Thus the porous films must be hermetic sealed via the use of a diffusion barrier, as detailed in a earlier section.[3, 37-41, 43, 48]

1.4 Phase Compatibility in Templated Films

The ideal internal structure of a porous dielectric film is of uniformly-distributed, monodisperse small-sized (< 10 nm) pores, which are not interconnected. Although the templated sacrificial polymer technique produces closed mesopores with independently tunable pore sizes and pore size distributions, ungrafted templated macromolecules tend to phase-segregate and agglomerate either during spincoating or during thermal treatments prior to decomposition.[1, 2] If this occurs, the resultant pore structure contains macro-voids that may span hundreds of nanometers from end-to-end, and lead to non-uniform properties throughout the films.[2] Earlier investigations of the use of freely-mixed polycarbonate chains in HSQ resins showed that porous films were produced with poor internal and surface morphologies.[2] These characteristics, which are summarized below, removed the incentive for using the novel direct-write process to make useful porous films unless phase-segregation issues were first addressed. These undesirable features of the porous films included: non-uniform placement of pores throughout the films due to a lack of control over the dispersion of the polymer chains during spin-coating, large pore sizes and pore-size distributions possibly as a result of coalescence of unevenly spaced-pores, and a significant degree of surface roughness due to the macro-sized pores beneath the surface of the porous films.[2]

Researchers have shown that the movement of sacrificial polymers can be prevented by tethering them covalently to their surrounding immobile matrix, resulting in

the production of ideal pore morphologies.[28, 30, 53, 54, 62-64] The covalent bonding of porogens to thermally-stable polyimide chains, produces porous spun films free of phase-segregation, with pore sizes of about 10-15 nm, porosities as high as 24%, and *initial* dielectric constants as low as 2.3.[53, 54, 64] However, although polyimides have high thermal stability, they are hydrophilic and begin to absorb ambient moisture as soon as porosity is formed.[7] For this reason, the porous polyimide films have been abandoned by the IC community in favor of inorganic and organosilicate materials as viable candidates to meet the requirements of ultra low-k applications.[3, 5] When thermally-labile organic molecules are grafted to thermally-stable HSQ resins, the mesopores produced are closed and evenly distributed throughout the matrix, the tunable pore sizes can be as low as 2-3 nm, the porosity levels higher than 30%, and dielectric constants as low as 1.8 and remain fairly stable.[95, 96] Additionally, inorganic and organosilicate materials are less prone to moisture uptake compared to polyimide films, and their low-k properties are effectively maintained via post-deposition of hermetic barrier layers, as described previously. [3, 37-41, 43, 48]

Hence, in eliminating phase-segregation through the synthesis and templating of composite porogen-matrix precursor molecules it is preferable to select a sol-gel precursor as the thermally-stable component in order to produce either silica or silica-like polyhedral oligomeric silsesquioxane (POSS) films after thermal curing. Thus, we anticipated that if polycarbonates were covalently bonded to either the HSQ matrix backbone (immobilization) or a matrix-like compatibilizer (to make the polymer more miscible with the surrounding inorganic material), then the final pore structure of both the thermally-induced and UV-induced (direct-written) films would have a uniform

placement of pores with smaller sizes and narrower size-distributions. Thus the focus of the research presented the improvement of the structural properties of the porous HSQ films made using templated polycarbonates via syntheses of new polycarbonate-siloxane and polycarbonate-silsesquioxane nanocomposites.

CHAPTER 2

ANALYTICAL METHODS

2.1 Materials Used during Sample Preparations

A micropipette was purchased from Eppendorf with a volumetric range of 2-20 microliter (μL), and an error of about 6%. Sterile 20 μL-capacity micropipette tips, 37.5% hydrochloric acid (HCl), anhydrous pellets of potassium hydroxide (KOH), type-3A (4-8 mesh) molecular sieves, and spectroscopic-grade chloroform-D ($CDCl_3$) were all purchased from Fisher Scientific. $CDCl_3$ was stored in a refrigerator over the molecular sieves to avoid moisture uptake. Reagent-grade chloroform, isopropyl alcohol (IPA), 98% sulfuric acid (H_2SO_4), and 30% hydrogen peroxide (H_2O_2) were obtained from VWR and used without further purification. Disposable 30 milliliter (ml) capacity Nalgene storage vials, disposable polypropylene-casing Luer-lock type syringes, polytetrafluoroethylene (PTFE) membrane syringe filters with 0.2 μm pore sizes, and PTFE-coated stirrer bars were also purchased from VWR. Standard 5 millimeter (mm) nuclear magnetic resonance (NMR) tubes made of ASTM Type 1 Class B glass and PTFE were obtained from Norell. Cleanroom quality (lint-free, woven fabric) wipes were purchased from ITW Texwipe. Chromium acetylacetonate or $Cr(acac)_3$ was obtained from Sigma Aldrich, and Shipley 1813P phororesist was obtained from Rohm & Haas Co. Batches of prime-grade, single-sided polished (SSP) and double-sided polished (DSP) n-type silicon wafers (wafer diameters of 100 mm and nominal thicknesses of about 0.4 mm) were obtained supplied from Wacker Siltronic AG and Nova Electronic

Materials, respectively. 200 mesh copper transmission electron microscopy (TEM) grids were purchased from Electron Microscopy Services.

2.2 NMR Studies

Solution-state, proton (^{1}H) Nuclear Magnetic Resonance (NMR) samples were made by dissolving 10-20 mg of the substance to be analyzed in about 0.5 ml of dry $CDCl_3$ and adding 4 μL of tetramethylsilane (TMS) as the internal standard. The ^{1}H NMR samples were pipetted into glass NMR tubes and analyzed using a Varian Mercury-Vx400. Quantitative ^{1}H NMR data was acquired using a frequency of 400 MHz, a recycle delay of 6 seconds, a pulse angle of 37.5 degrees, an acquisition time of 1.993 seconds, a spectral width of 6006 Hz, and a Fourier transform (FT) data set of 32768 data points. Chemical shifts (δ) were referenced to the TMS peak (set to 0.00 ppm).

Solution-state, proton-decoupled carbon-13 or $^{13}C\{^{1}H\}$ NMR samples were prepared by dissolving at least 100 mg of the substance to be analyzed in about 1.0 ml of $CDCl_3$, with the deuterated solvent serving as the internal standard (set to 77.0 ppm). The $^{13}C\{^{1}H\}$ NMR samples were pipetted into glass NMR tubes and analyzed using a Varian Mercury-Vx400. Qualitative $^{13}C\{^{1}H\}$ NMR spectra were obtained using the following parameters: a ^{13}C detection frequency of 100 MHz with a proton-decoupling frequency of 400 MHz, a recycle delay of 6 seconds, a pulse angle of 46.3 degrees, a spectral width of 25000 Hz, and an FT data set of 65536 data points. Chemical shifts (δ) were referenced to the central peak of the $CDCl_3$ triplet (set to 77.0 ppm).

$Cr(acac)_3$ was used as a relaxation agent in solution-state, proton-decoupled silicon-29 ($^{29}Si\{^{1}H\}$) NMR analyses. Solid $Cr(acac)_3$ was dissolved to form a saturated

solution in $CDCl_3$, then this solution was filtered through 0.2 um PTFE syringe filters and used to make $^{29}Si\{^1H\}$ NMR samples, as described below. $^{29}Si\{^1H\}$ NMR samples were prepared by adding at least 100 mg of the substances to be analyzed to Nalgene vials containing 60μL of pre-filtered, saturated solutions of $Cr(acac)_3$ in $CDCl_3$. The solids were dissolved in about 1.0 ml of $CDCl_3$, and 8 μL of TMS was added to the solution as the internal standard. The NMR samples were then pipetted into PTFE NMR tubes to avoid the influence of glass NMR tubes on the observed ^{29}Si signal intensities. A Bruker DMX-400 was used to record proton-decoupled silicon-29 or $^{29}Si\{^1H\}$ NMR spectra using the following parameters: a ^{29}Si detection frequency of 79.5 MHz with a proton-decoupling frequency of 400 MHz, a recycle delay of 4 seconds, a pulse angle of 30 degrees, an inverse-gated proton-decoupling pulse-program, a spectral width of 31746 Hz, and an FT data set of 65536 data points. All δ were referenced to the TMS peak (set to 0.00 ppm)

Solid-state $^{29}Si\{^1H\}$ samples were prepared by carefully packing the dry substances being analyzed in a 4 mm zironia rotor with before sealing the rotor with a KeL-F rotor cap. Quantitative $^{29}Si\{^1H\}$ spectra were captured using Bruker DSX-400 under direct-polarization magic-angle-spinning (DP-MAS). The NMR equipment was operated using a ^{29}Si observation frequency of 79.4 MHz, a proton-decoupling frequency of 400 MHz, a recycle delay of 210 seconds, a pulse angle of 30 degrees, a spectra width of 41667 Hz, a rotor speed of 10 kHz, and an FT data set of 2048. The external reference was 3-(trimethylsilyl)-1-propane sulfonic acid sodium salt (DSS), which was set to 0.00 ppm. All δ were referenced to this DSS peak.

2.3 Elemental Analyses

After spectroscopic studies were performed, samples of each of the synthesized oligomers were sent to Atlantic Microlab for elemental analyses (elem. anal.) to determine their respective atomic compositions of carbon (%C), hydrogen (%H), and oxygen (%O). The chemical structures of the oligomers predicted by NMR data were validated by comparing the atomic compositions predicted from theoretical calculations with those observed by Atlanic Microlab.

2.4 Gel Permeation Chromatography (GPC)

Gel permeation chromatography (GPC) was used to determine the size distribution of PNC oligomers. The number-average molecular weights (M_n) and weight-average molecular weight (M_w), and the polydispersity index (PDI) were all reported to three significant figures. For GPC studies in which tetrahydrofuran (THF) was used as the eluent, a Waters 2690 Separations Module was used with a Waters styragel THF column (depending on the eluent used), and a Waters 410 refractive index detector. For GPC analyses in chloroform, a Shimadzu LC-10ATvp liquid chromatograph separation module was used with a Waters styragel chloroform column, and a Shimadzu SPD-10Avp detector.

2.5 Dynamic Light Scattering (DLS)

A Wyatt Technology DAWN EOS light scattering photometer, equipped with a Quasi-elastic light scattering (QELS) sensor was to perform dynamic light scattering

(DLS) experiments. Prior to performing a DLS experiment, a scintillation vial was first cleaned by soaking it overnight in 30% HCL, followed by successive rinses using copious DI water, then Acetone. Finally, the vial was wiped clean using cleanroom-quality wipes, and then air-dried. Multiple solutions were made of PNC oligomers in chloroform from ranging in concentration from 10-50 mg/ml and then stirred overnight using PTFE-coated magnetic stirrer bars in clean scintillation vials. These solutions were then filtered through PTFE membrane syringe filters (0.2 μm pores) into separate clean vials, labeled, and inserted into the DLS. A QELS correlation function was used to compute the distributions of hydrodynamic radii (R_H) of the oligomeric chains in chloroform.[97]

2.6 Differential scanning calorimetry (DSC)

A Seiko TG/DTA 320 was used to perform differential scanning calorimetry (DSC) experiments. Prior to performing a DSC experiment, a 5-15 mg dry sample of a substance was placed in a tared aluminum pan before it was covered and permanently sealed using a hand-press. The general procedure for performing each DSC analysis was as follows: a DSC pan was placed inside the instrument, the temperature of the system was allowed to stabilize for 15 min, then the DSC pan was heated at a rate of 10^{o}C per minute to an upper temperature limit determined by the particular thermal characteristics of each material, then the samples were cooled using liquid nitrogen to ambient temperature, after allowing system to remain at ambient temperature for 1 min, the pan was reheated using the same ramp rate and final temperature to check for reversibility of any transitions. The glass transition temperature (Tg) of material was recorded as the

midpoint of the slope between the two points of inflexion of a step-type reversible phase transition. The melting points were defined as the minima of reversible endotherms.

2.7 Thermogravimmetric Analyses (TGAs)

Thermogravimmetric analyses (TGAs) were carried out using either a TA Instruments Q500 or Seiko TG/DTA 320. TGA studies were used to analyze the thermal behavior of ungrafted poly(norbornane carbonate) or PNC sacrificial polymers, siloxane and silsesquioxane precursors, PNC-siloxane, and PNC-silsesquioxane nanocomposite molecules. Additionally, TGA experiments proved useful in investigating the kinetics of thermally-induced and acid-catalyzed decomposition of PNC chains via the use of both isothermal TGA and dynamic TGA (non-isothermal TGAs performed with constant ramp rates) analyses.[98-100] PNC/photoacid generator blends were also analyzed via TGA so as to compare the relative thermal stabilities of different photoinitiators to determine the optimal PAG structures to use in the direct-write process shown in Figure 1.2. PNC/PAG mixtures were made by a similar method to that reported by Jayachandran and co-workers.[89]

Separate solutions of PNC and each PAG were made using methyl isobutyl ketone (MIBK) solvent. These PNC and PAG solutions were then mixed such that the mass of dry PAG solids was 3 wt% with respect to the mass of dry PNC solids in the blend. The PAG/PNC mixtures were pipetted onto aluminum dishes and dried at about 110^{o}C for 1-2 hours in a vacuum oven prior to each TGA run in order to avoid the influence of solvent volatilization on the TGA results. Dynamic TGA plots were obtained by tracking changes in the weights of tared dry samples as the TGA furnace was

heated at 3°C per minute from ambient to a final temperature of at least 325°C. Isothermal TGAs were performed by first heating the TGA (at 20°C per minute) to the desired dwell temperature and waiting for the temperature of the furnace to stabilize before tracking the weight of the sample against time. All TGA runs were performed with nitrogen purge flowrates of 50 cm^3 per minute or lower to avoid the effect of photoacid volatilization on the rate of acid-catalyzed PNC decomposition.

2.8 Mass Spectrometry (MS) and TGA-MS Analyses

A Pfeiffer Vacuum Omnistar GSD 301C gas analysis system was used to perform mass spectrometry (MS) and thermogravimetric-mass spectrometry (TGA-MS) analyses of the gases evolved from a TA Instruments Q500 TGA furnace, which was attached via a meter-long capillary containing a 20 μm wide orifice. Inert nitrogen or argon carrier gases were used to sweep the volatile products from the exhaust of the TGA furnace through the capillary orifice to the MS system. Electronic bombardment was used to ionize and fragment the inlet gases, and the electron emission source was a tungsten filament with a controlled emission current setting of 1 milliampere (mA). The ionized gases were detected using a quadrupole mass detector, and the MS system had a mass detection range of 1-300 atomic mass units (amu). To perform simultaneous TGA-MS analyses, the communication (COM) ports of the TGA and MS hardware were connected a COM link, and the TGA software was used to simultaneously trigger the collection of the MS data at the same instant that the TGA data collection was initiated. The recorded transient times were used to correlate the MS data to the TGA data, thus allowing MS peaks to be tracked against all of the following variables: time elapsed since the TGA-

MS experiment was initiated, MS cycle number, TGA furnace temperature, or changes in sample weight during heating.

2.9 Fourier Transform Infrared Spectroscopy (FTIR) Studies

A Thermo-Nicolet 520 spectrophotometer was used to perform Fourier transform infrared spectroscopy (FTIR) studies of HSQ films using attenuated total reflectance (ATR) mode. The HSQ films, which were spun-coated to thicknesses of 0.7-1.2 μm, were analyzed both before and after chemical and thermal treatments to investigate the changes in their chemical structures. The wavenumber values of FTIR peaks were reported in units of reciprocal centimeters (cm^{-1}) and identified via literature sources. In accordance with methods used in literature, the bond transformations within HSQ were tracked by recording the ratio of the areas underneath the FTIR stretch peaks corresponding to cage-type siloxanes and network-type siloxane stretch peaks.[16, 17] This variable was referred to as the c/n ratio, and its significance is discussed in greater detail later sections of this thesis.

2.10 Nanoindentation Analysis

After FITR analyses were performed, a Hysitron Triboindenter® was used to nanoindent each of the gelled or thermally-cured HSQ films in order to quantify the mechanical rigidities induced by the crosslinking reactions. During nanoindentation, each of the films was probed multiple times using a Berkovich tip according to the method outlined by Oliver and Pharr.[101] After nanoindentation the reduced moduli, E_r, of the films were compared with their c/n ratios (obtained from FTIR data) so as to

correlate the interdependence of the chemical and mechanical changes within the internal structure of the HSQ matrix.

2.11 Characterization of Refractive Indices

A J.A. Woollam M2000 VI spectroscopic ellipsometer was used together with a Cauchy model to find the refractive index values of porous and non-porous films during processing. All refractive indices reported in this thesis are for a wavelength of 632 nm and when necessary, the extinction coefficients of the processed thin films were also fit using ellipsometry software. To track the refractive index differences between porous and non-porous areas of direct-written samples, one half of each sample was covered with a polished wafer during the UV-exposure step so as to prevent any UV-induced decomposition of polymer in the covered half. For all other steps, the entire direct-write film underwent identical processing conditions.

2.12 Characterization of Dielectric Constants

In order to determine the intralevel or in-plane dielectric constant (refer to Figure 1.1) of porous films and their non-porous controls samples, interdigitated electrodes (IDEs) were fabricated on oxidized silicon wafers, such as the one shown in Figure 2.1. Each IDE had 200 comb-like fingers connected to each bond pad with a 1 cm overlap length between adjacent comb fingers to give an overall field length of 4 m. Using the lift-off technique (photolithography followed by metal deposition onto patterned photoresist, followed by photoresist removal), the IDEs were patterned with 5 μm wide metal lines and 5 μm wide gap spacing between each metal line. An e-beam evaporator

was used to deposit 10-15 nm of titanium followed by 200 nm of gold at high vacuum onto least 10 μm thick PECVD SiO_2. A Tencor KLA profilometer and calibrated microscope were used to measure the actual dimensions of the IDEs and a Nanospec refractometer was used to measure the thickness of the PECVD oxide layer.

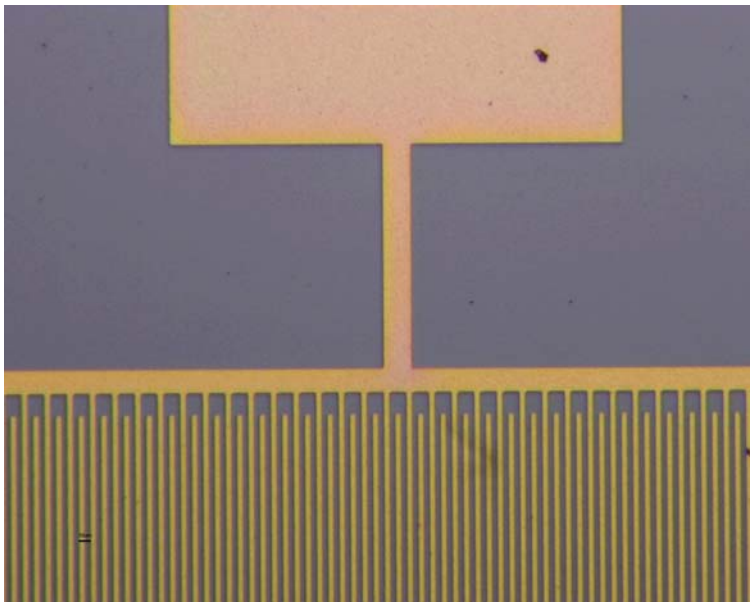

Figure 2.1 – Microscope image showing the top down view of an IDE.

An HP 4253 LCR meter and Karl Suss PM5 probe system were used to measure the capacitances of multiple IDEs at a frequency of 100 kHz both before and after spin-coating the silicon wafers with films. After spin-coating films onto the IDEs, portions of the films were removed by scraping to allow film thickness measurements to be performed by the profilometer. Both the thicknesses of the coated films and the capacitances of the coated IDEs were re-measured after each processing step to track changes in polarizability during processing. By utilizing the measured dimensions of the IDEs, and the measured thicknesses of the oxide and coated films, electrostatic

simulations of the electric fields in the dielectric layers were modeled using Ansoft's Maxwell software. The dielectric constants of the low-k films were empirically determined by adjusting the material properties of the modeled dielectric layers until the simulated capacitance values of the IDEs matched the experimentally observed capacitance values.[3]

To determine the interlevel or through-plane dielectric constants (refer to Figure 1.1) of porous films and their non-porous controls samples, area capacitors were fabricated according to well-established methods.[3, 8, 10, 29, 62, 102] A silicon wafer was sputter-deposited with successive layers of 15 nm of titanium, 200 nm of gold, and another 15 nm of titanium as an adhesion layer. These conductive metal layers collectively served as the bottom electrode for the area capacitors. A low-k film was then spun-coated on the metalized wafer to completely cover the bottom electrode and this film was processed and its thickness was measured using an ellipsometer. Finally multiple top electrodes were deposited above the dielectric films via the use of an electron-beam evaporator and a shadow mask containing several circular holes measuring 2 mm in diameter. The thicknesses of the metal layers of the top electrode were 15 nm for the lower titanium layer and 200 nm for the upper layer of copper or gold. Figure 2.2 shows a top-down view of a typical wafer piece after the complete fabrication of area capacitors.

A dilute solution of hydrofluoric acid (HF) was used to etch away a small area of the low-k film in order to expose the underlying metal layer ie. the bottom electrode. A probe station and LCR meter were used to measure the capacitances of multiple capacitors. The measured dimensions of the metal and dielectric layers were substituted

into Maxwell software to build electrostatic models of the capacitors. The interlevel dielectric constants were determined empirically by adjusting the assumed values of the dielectric constants for the low-k layers in the modeled capacitors until the simulated capacitance matched the experimental value of the average capacitance measured.[3]

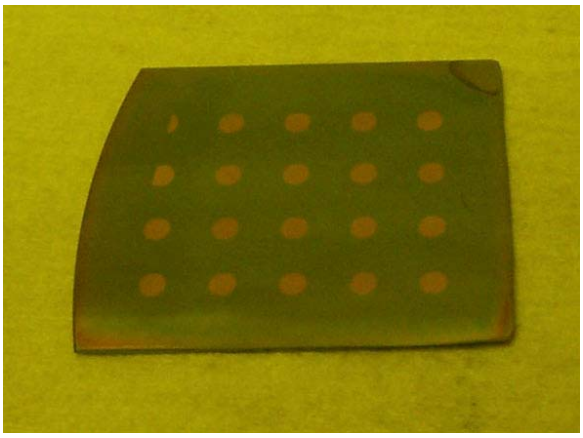

Figure 2.2 – A top-down view of a wafer chip containing multiple area capacitors

2.13 The Use of Mixing Rules to Estimate Porosity

Effective medium approximations (EMAs) or refractive index and dielectric mixing rules are a widely used method of estimating porosity within thin films.[93, 103-105] In order to do this, the refractive indices (n) and/or dielectric constants (ε) of porous films are compared with those of a non-porous control samples and the EMAs are then used to solve for the relative porosity induced in the porous films.[1-3, 54, 64, 106]

2.13.1 Porosity Estimates via the Lorentz-Lorenz Mixing Rule

After using spectroscopic ellipsometry to determine the refractive indices of porous films, pure HSQ films were processed in a similar manner to their porous

counterparts and their refractive indices were recorded. The Lorentz-Lorenz equation, shown in equation (2.1), was used then to model the effective refractive index, n_{12}, of a porous film.[93] Since the refractive index of air (n_2 = 1.0003)[78] is approximately equal to 1, the second term on the right hand side of the Lorentz-Lorenz equation was eliminated. The resultant expression was then rearranged to explicitly solve for the volume fraction of air, ϕ_2, in a porous film, as shown in equation (2.2).[3] The refractive index values of the non-porous control samples (n_1) and their porous counterparts (n_{12}) were then substituted into equation (2.2) to solve for the porosity, ϕ_2, of each porous film.[1-3, 54, 64, 106]

$$\frac{{n_{12}}^2 - 1}{{n_{12}}^2 + 2} = \phi_1 \left(\frac{{n_1}^2 - 1}{{n_1}^2 + 2} \right) + \phi_2 \left(\frac{{n_2}^2 - 1}{{n_2}^2 + 2} \right) \tag{2.1}$$

$$\phi_2 = (1 - \phi_1) = 1 - \left(\left[\frac{{n_{12}}^2 - 1}{{n_{12}}^2 + 2} \right] \Big/ \left[\frac{{n_1}^2 - 1}{{n_1}^2 + 2} \right] \right) \tag{2.2}$$

The symbols ϕ_1 and ϕ_2 are the volume fractions occupied by the host matrix and air pockets, respectively. The symbol n_{12} refers to the effective refractive index of the bulk porous film, while n_1 and n_2 are the refractive indices of the non-porous control film and air, respectively.[3]

2.13.2 Porosity Estimates via the Maxwell-Garnett Mixing Rule

After determining the intralevel dielectric constants (ε) of the porous films using IDEs, pure HSQ films were coated on bare IDEs and processed and characterized in a similar manner to their porous counterparts and their non-porous control ε values were

recorded. The Maxwell-Garnett mixing rule, equation (2.3), was then used to model the effective relative dielectric constant, n_{12}, of a porous film.[103] In order to estimate the level of induced porosity from the dielectric constant data, equation (2.3) was then rearranged to explicitly solve for the volume fraction of air, $(1-\phi_1)$, in a porous film, as shown in equation (2.4).[3] The ε values of air, ε_2 the non-porous control samples (ε_1) and their porous counterparts (ε_2) were then substituted into equation (2.4) to solve for the level of porosity induced within the porous films.[1-3, 54, 64, 106]

$$\frac{{\varepsilon_{12}}^2 - \varepsilon_2}{{\varepsilon_{12}}^2 + 2\varepsilon_2} = \phi_1 \left(\frac{{\varepsilon_1}^2 - \varepsilon_2}{{\varepsilon_1}^2 + 2\varepsilon_2} \right) \tag{2.3}$$

$$\phi_2 = (1 - \phi_1) = 1 - \left(\left[\frac{\varepsilon_{12} - \varepsilon_2}{\varepsilon_{12} + 2\varepsilon_2} \right] \Big/ \left[\frac{\varepsilon_1 - \varepsilon_2}{\varepsilon_1 + 2\varepsilon_2} \right] \right) \tag{2.4}$$

Similar to equation (2.2), the symbols ϕ_1 and ϕ_2 are the volume fractions occupied by the host matrix and the pores, respectively.[3] The symbol ε_{12} refers to the effective dielectric constant of the porous film, and ε_1 and ε_2 refer to the relative dielectric constants of the host matrix and air, respectively.[3] Since ε_2 is equal to unity for air, and since the square of the refractive index of any component is equal to its relative dielectric constant value, equations (2.2) and (2.4) are mathematically equivalent for a porous film. This indicates that theoretically, the porosities that were estimated using experimental data and Lorentz-Lorenz and Maxwell Garnett rules should have matched. To test for consistencies of the porosity estimations the calculated using optical experimental data were compared with those calculated from experimental dielectric constant data and any discrepancies were noted. As an additional method of validating

the porosity estimates, comparison were made between the EMA results and films porosities reported in literature for similar sacrificial polymer loadings.

2.14 TEM Sample Preparations and Analyses

2.14.1 Focused Ion Beams (FIB) Preparation of Ultrathin Cross-sections

Using a Nova 200 focused ion beam (FIB) system, ultrathin (< 100 nm thick) cross-sections of porous films and their silicon substrates were milled by FIB after first sputtering each of these samples with protective gold and platinum layers to prevent implantation of the gallium ions during FIB bombardment.[62] The Kleindiek micromanipulator and scanning electron microscope (SEM) features of the Nova 200 were used in tandem to mount the cross-sections onto 200 mesh copper transmission electron microscopy (TEM) grids. Figure 2.3 and Figure 2.4 show SEM images of FIB-prepared wafer cross-sections before and after being mounted unto a TEM grid by the Kleindiek micromanipulator tip. As shown in Figure 2.5, the sides of each cross-section were kept thick enough to allowing for welding to, and movement by the micromanipulator without risk of fracturing the wafer. The central regions of each cross-section, which accounted for about half of the total length, were below 100 nm in width in order to be electron-lucent. Hence, only the porous layers located these central regions were viewable by TEMs.

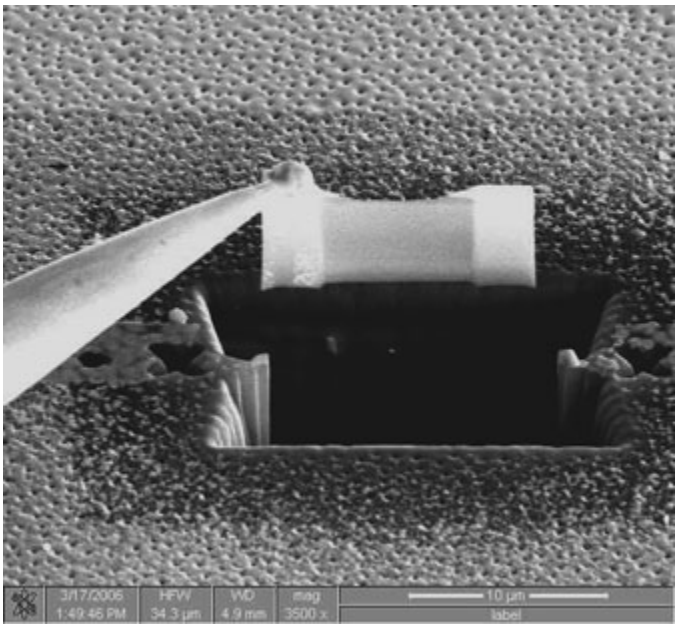

Figure 2.3 – An SEM image of an FIB-milled cross-section just after it has been welded to, and lifted by, a micromanipulator tip but prior to attachment to a TEM grid.

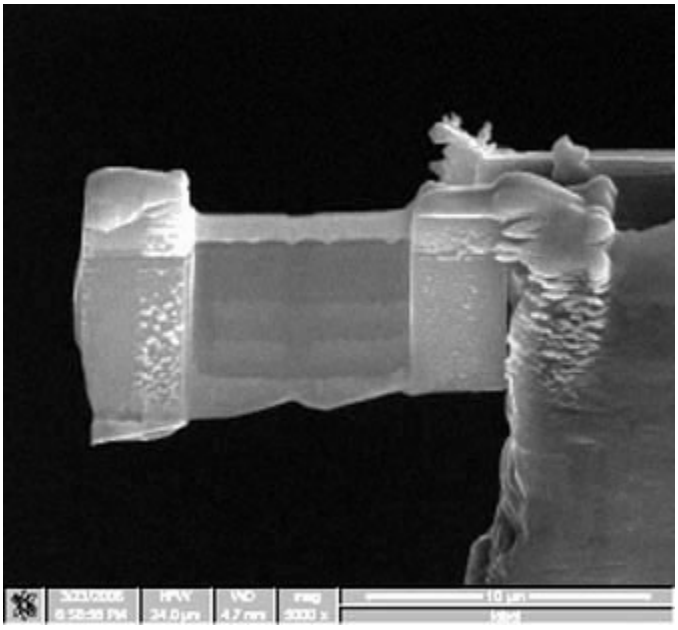
Figure 2.4 – An SEM image of an FIB-milled cross-section that has been mounted on to a TEM grid.

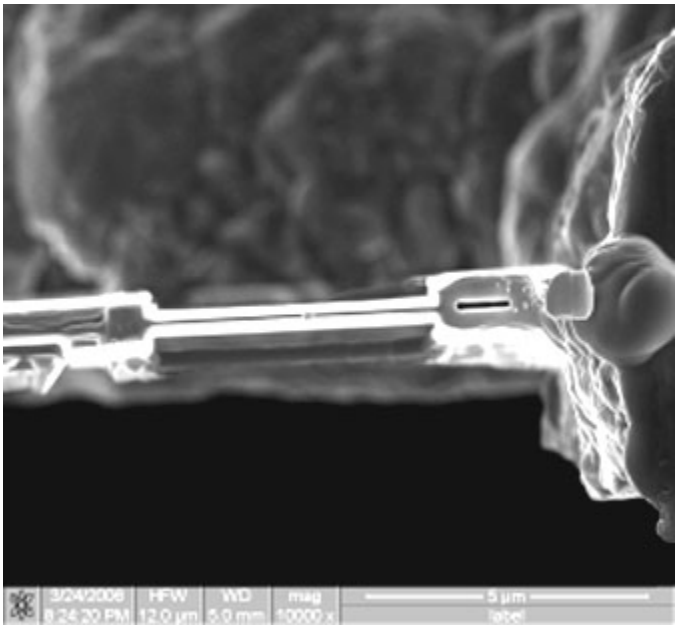

Figure 2.5 – An SEM image (top-down view) of an FIB-milled cross-section illustrating the relatively large differences in the widths of the ultrathin central regions and the thicker side outer areas

2.14.2 In-plane TEM Analyses

Then internal structures of the ultrathin cross-sections of porous films prepared by FIB and mounted on TEM grids were analyzed using a Hitachi HF-2000 TEM. The TEM was operated using an accelerating voltage of 200 kilovolts (kV) and images were recorded at magnifications of 1 x 10^5 and 2 x 10^5.

2.14.3 Preparation of Ultrathin, Low-Stress Silicon Nitride (Si_xN_y) Membranes

Ultrathin, low-stress (non-stoichiometric) silicon nitride (Si_xN_y) free-standing membranes were prepared according to the method reported by Cheng-Tsung Lee and co-workers.[107, 108] Double-sided polished (DSP) <100> orientated silicon wafers with thicknesses ranging from 360-380 μm were cleaned of traces of organic residue by immersing them in a preheated, 120^{o}C Piranha bath (a 70:30 volumetric ratio of 96%

H_2SO_4 and 30% H_2O_2) for 10 minutes. Afterwards, the wafers were rinsed with de-ionized (DI) water, and then immersed in 2% hydrofluoric acid (HF) for about 10 seconds to strip away the native SiO2 layers from the silicon surfaces. After another rinse with DI water, the wafers were spray-dried using dry nitrogen, and then spun-dried using a Semitool Spin-Rinse Dryer to remove all traces of moisture.

A Tystar TYTAN Furnace was used to deposit about 50 nm of low-stress silicon nitride (Si_xN_y) on both sides of the DSP silicon wafers using low-pressure chemical vapor deposition (LPCVD). The chemical precursors used for the deposition reactions were dichlorosilane and ammonia, which were flowed into the reaction chamber at 17 standard cubic centimeters per minute (sccm) and 100 sccm, respectively. The deposition was carried out at 850^{o}C, and the deposition time was 10 min.[107, 108]

After SixNy deposition, one side of each wafer was spun-coated with a 1.3 μm thick layer of a positive-tone photoresist (Shipley 1813P). Then, using photolithography, twenty, 6x7 arrays of squares were patterned across the whole wafer to selectively expose only the Si_xN_y layers that were underneath these openings. Using a Plasma-Therm Inductively-coupled plasma (ICP) and tetrafluoromethane (CF_4) as the etchant gases, the exposed Si_xN_y regions were removed via an anisotropic plasma dry-etch to reveal their underlying silicon surface. The upper photoresist layer on each ICP-etched wafer was then removed by immersing the wafer in a preheated, 100^{o}C Piranha bath for 10 minutes, followed by a DI rinse to clean the wafer. The resultant wafer had one side (membrane side) with an unpatterned, blanket Si_xN_y film, and the other side (back-etch side) with a patterned Si_xN_y layer containing arrays of silicon-exposed windows with vertical sidewalls, as shown in Figure 2.6.[107, 108]

Each wafer was then clamped between two annular ringed-spacers made of polytetrafluoroethylene (PTFE), and then immersed in a preheated, 100^{o}C alkaline bath of the following composition: 40wt% KOH, 15% IPA, and a balance of DI water. The wafers were kept in the hot KOH baths for at least 4-6 hours to completely etch through the entire thickness of exposed silicon on the back-etch side of the wafer, and stopping at the Si_xN_y layer of the membrane side of the DSP wafers.[107-109] The preferential attack of <100> and <110> crystal planes of the exposed silicon substrates in comparison to the relatively slow attack of the close-packed <111> crystal planes produced angled window sidewalls (the exposed <111> crystal faces) as shown in Figure 2.7.[109]

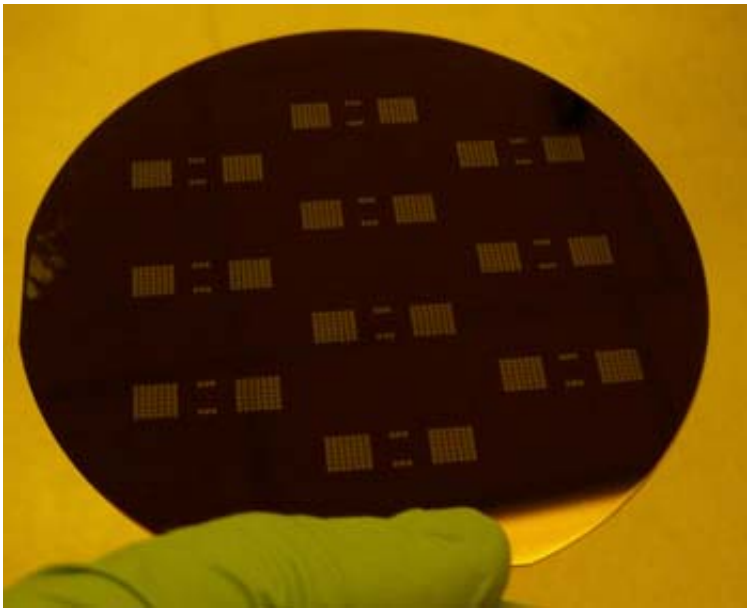

Figure 2.6 – A picture of a dry-etched of silicon nitride surface showing arrays of windows with the silicon substrate exposed.

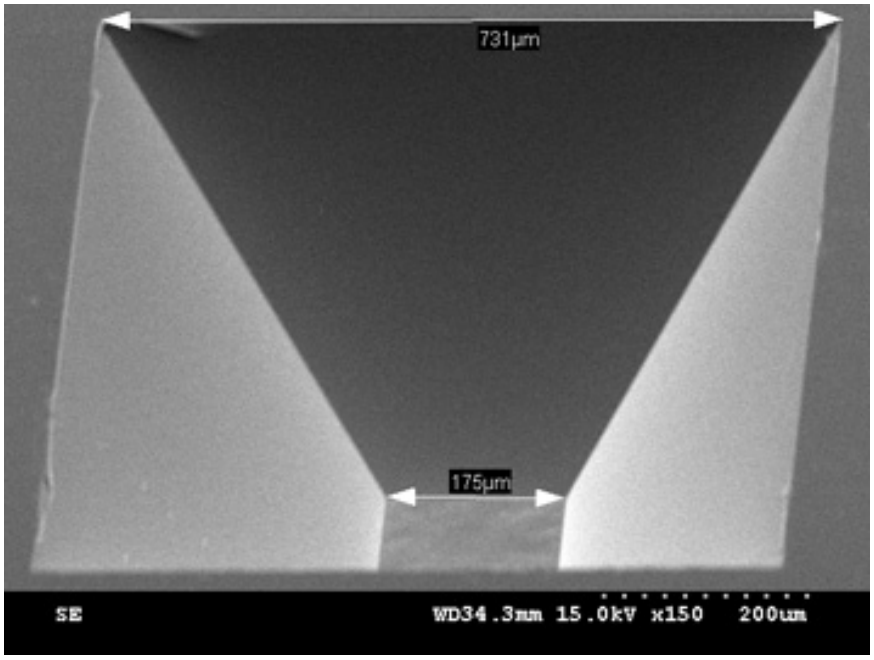

Figure 2.7 – SEM image showing the isometric view of an individual silicon window after the complete wet-etching of the exposed <100> silicon crystal face, leaving only the <111> silicon crystal planes and the free-standing Si_xN_y membranes.

After alkaline etch, the wafers were thoroughly rinsed with DI water, and then immersed in preheated, 100^{o}C piranha baths for 10 minutes to remove all traces of IPA and other organic residues from their surfaces. A final DI rinse, followed by an acetone rinse and a spray-drying step using dry nitrogen left the DSP wafers clean of all traces of chemicals. Figure 2.8 shows the final appearance of the membrane side of a DSP wafer after all fabrication and cleaning steps had been performed. Depending on their wafer thicknesses, the final free-standing SixNy square membranes on each wafer measured between 160 µm and 190 µm on each side, with a center-to-center pitch of about 910 µm between adjacent membranes.[107, 108]

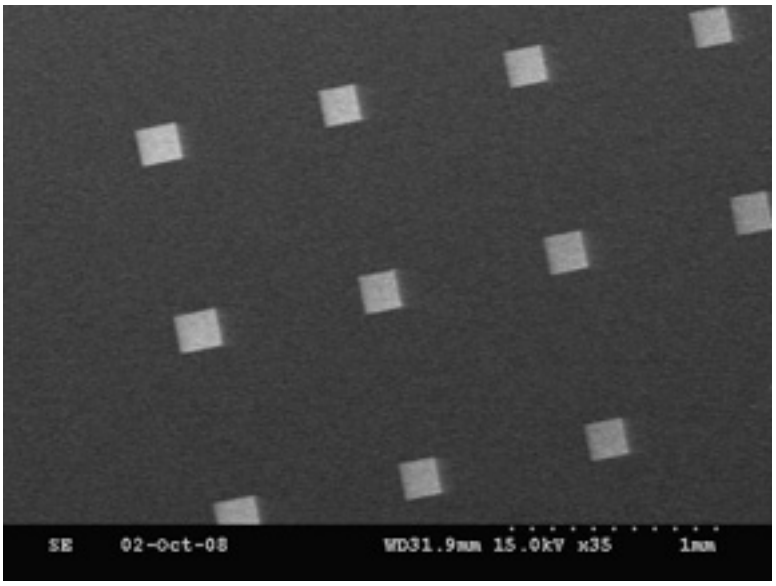

Figure 2.8 – An SEM image showing an array of free-standing SixNy membranes viewed from the smooth (not etched) side of the DSP wafer.

Although silicon nitride is naturally hydrophobic, multiple contact-angle measurements of the final Si_xN_y films showed that water droplets wet the surfaces with contact angles of 36-40 degrees, which indicated that the alkaline and piranha treatments made the fully processed DSP wafers very hydrophilic, probably due to the formation of silanol groups on the surfaces. When droplets of HSQ resins were placed on the DSP wafers, these too showed excellent wetting of the surfaces, which was an encouraging result since good wetting properties are essential for spincoating uniform films on any substrate. Prior to spincoating films, the DSP wafers were cleaved into smaller chip pieces containing individual 6x7 arrays of free-standing membranes. Since the ultrathin membranes were too fragile to withstand the forces of a vacuum chuck, the back-etched sides of the DSP chips were adhered to thick silicon pieces free of membranes using double-sided tape. These underlying protective wafer pieces were then placed directly on vacuum chucks to facilitate the spincoating of films on to the upper DSP chips. To

ensure that the films that were coated on the DSP chips were electron-lucent, their formulations were kept to dilutions of 0.8 wt% HSQ in solution and spincoating was performed at 2000 rpm. Although the membranes were only 50 nm thick, the low internal stresses within the Si_xN_y layers allowed the membranes to survive all of the thermal treatments of curing HSQ films (two hour bake steps at 200^{o}C) and decomposing the templated porogen within the HSQ films (dynamic heating up to 325^{o}C followed by a 30 minutes dwell step). The detailed procedures for the processing templated HSQ films are outlined in later chapters.

2.14.4 Osmium Tetraoxide Staining, and Through-plane TEM Analyses

Multiple DSP chips with spun templated films were analyzed after each of the processing steps ("as spun" samples were not processed further after spincoating, the "as cured" samples were only spun-coated and thermally cured at 200^{o}C for 2 hours, and "decomp" samples were fully processed to form porosity). To enhance the otherwise poor contrast of TEM images of non-porous films ("as spun" and "as cured" samples), the HSQ matrix phases of the non-porous films were selectively post-stained with heavy atoms to increase their electron scattering density relative to the dispersed phase.[110-126] Using modified form of Kato's method,[120] each non-porous TEM sample was stained by placing it in a petri dish containing a few drops of a 1% aqueous solution of osmium tetraoxide (OsO_4), and then covering the petri dish and allowing the OsO_4 vapor to diffuse into the non-porous film for 15 minutes.[111, 118, 119, 122] Unstained porous films were observed to have superior TEM image contrast to non-porous films that were selectively stained, hence, porous films did not require any OsO_4 vapor treatment prior to

TEM imaging. Since standard TEM grid holders were unable to accept samples wider than 3 mm, the spun-coated DSP chips were cleaved again into smaller square pieces (measuring about 1 mm across) containing individual membranes. These millimeter-wide chips were then secured within folding-type TEM grids in order to fit into a standard TEM grid holder. A JEOL JEM-1210 TEM was used to image the through-plane structures of the films above the free-standing Si_xN_y membranes that were discussed earlier. Optimal image contrasts were obtained using accelerating voltages of 80 kV. Images were taken at multiple magnifications between 2.5×10^4 and 2×10^5.

2.15 Characterization of Surface Morphology via AFM

In order to determine the surface profiles of porous films, they were analyzed using either a Veeco Dimension 3100 atomic force microscope (AFM) or a Molecular Imaging Picoplus AFM. The AFM analyses were operated under intermittent contact mode using silicon nitride tips, which had radii of curvature of about 7 nm. 512 raster scans were used to generate each AFM image and the sizes of the scanned areas ranged from 2 μm by 2 μm to 10 μm by 10 μm. The root mean square (rms) roughness values of the films surfaces were recorded along with the dimensions of surface anomalies such as depressions.

CHAPTER 3

SYNTHESIS AND CHARACTERIZATION OF POLY(NORBORNANE CARBONATE) OLIGOMERS

3.1 Materials Used in Syntheses and Purifications

5-Norbornene-2,3 cis exo-dimethanol (**9**), anhydrous magnesium sulfate ($MgSO_4$) in powder form, sodium chloride crystals (NaCl), potassium carbonate (K_2CO_3), sodium hydrogen carbonate ($NaHCO_3$), anhydrous triphosgene, anhydrous 4-nitrophenyl chloroformate, a 1.0M solution of lithium aluminum hydride ($LiAlH_4$) dissolved in anhydrous THF and sealed under inert atmosphere, and 18-crown-6 ether were obtained from Sigma Aldrich. Saturated aqueous solutions of NaCl and $NaHCO_3$ were separately made in DI water. 37.5% HCl and anhydrous KOH pellets were both purchased from Fischer Scientific. The concentrated HCL was diluted to 5% using DI water prior to use in any purification scheme. Anhydrous dichloromethane (DCM), anhydrous allyl chloroformate, reagent-grade triethylamine (Et_3N or TEA), anhydrous trimethylchlorosilane (TMCS), $CDCl_3$, and type-3A (4-8 mesh) molecular sieves were also purchased from Fisher Scientific. TMS was obtained from Sigma Aldrich and NMR samples were prepared via the methods outlined in chapter 2. TMS, $CDCl_3$, anhydrous triphosgene, anhydrous 4-nitrophenyl chloroformate, anhydrous allyl chloroformate, and anhydrous TMCS were all stored in a freezer to maintain their stability.

The following solvents and reagents, all of reagent-grade purity or higher, were purchased from VWR: 5-Norbornene-2-carboxyaldehyde (**4**), 5-Norbornene-2,3 cis endo-

dicarboxylic acid anhydride (**7**), a 38% aqueous solution of formaldehyde solution (stabilized with 15% methanol), anhydrous carbonyl diimidazole (CDI), a 50% wet water paste of 10% palladium catalyst on activated carbon support (Pd/C), 4-dimethylaminopyridine (DMAP), chloroform, THF, ethyl acetate (EtAc), methanol (MeOH), absolute ethanol (EtOH), acetone, hexane, and toluene. The Pd/C catalyst was stored in a dark cabinet and all reactions were carried out under filtered yellow lighting to avoid photo-oxidation of the catalyst. MeOH, THF, acetone, and chloroform were kept dry via storage over molecular sieves in sealed vessels. DCM, Ethyl acetate, hexane, and toluene were stored over anhydrous $MgSO_4$. CDI was kept stable via storage in a refrigerator. Grade-410 fine porosity (with 1.0 μm nominal pore sizes) filter paper, disposable polypropylene-casing Luer-lock type syringes, polytetrafluoroethylene (PTFE) membrane syringe filters with 0.2 μm pores, and PTFE-coated stirrer bars were also purchased from VWR. All glassware was obtained from Chemglass, and was silanized using TMCS prior to the use in moisture-sensitive reactions and purifications. Gas cylinders of ultra-high purity nitrogen (N_2) and hydrogen (H_2) were supplied by Airgas.

3.2 General Chemical Structures of Polycarbonate Oligomers

The general chemical structures of the three types of poly(norbornane carbonate) or PNC sacrificial polymers investigated in this study are shown in Figure 3.1. Numerals **1**, **2**, and **3**, correspond to **PNC1**, **PNC2**, and **PNC3**, main chain structures, respectively. **PNC1** has its carbonate linkage at the 2-endo and 2-exo positions of the bicycle[2.2.1]heptane or Norbornane ring. **PNC2** has its carbonate linkage at the 2-exo

and 3-exo positions of the Norbornane ring. **PNC3** has its carbonate linkage at the 2-endo and 3-endo positions of the Norbornane ring, but with both of its linkages having an endo orientation.

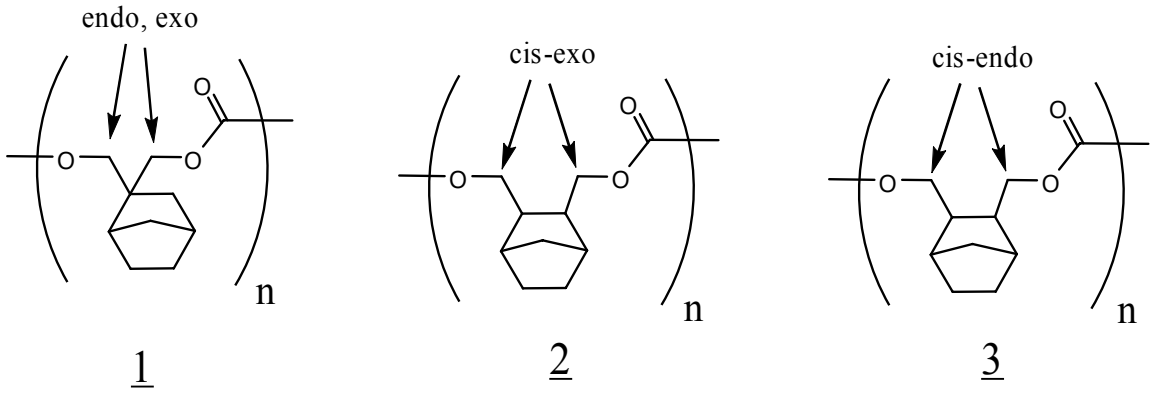

Figure 3.1 – Structures of the repeat units of **PNC1**, **PNC2**, and **PNC3**, respectively.

3.3 Syntheses of PNC Precursors

3.3.1 Synthesis of PNC1 Precursors

The **PNC1**'s diol precursors 5-Norbornene–2 endo, 2 exo–dimethanol (**5**), and Norbornane–2 endo, 2 exo–dimethanol (**6)**, were synthesized and purified according to procedures cited in literature, as outlined in the following sections.[127-130]

3.3.1.1 Synthesis of 5-Norbornene-2 endo, 2 exo-dimethanol (**5**)

Figure 3.2 shows the general scheme by which **5** was synthesized. Using a modified form of the procedure outlined by Hino and co-workers,[128] 20.316g (166.5 millimoles or mmoles) of 5–Norbornene– 2–carboxyaldehyde was pipetted into a tared, 500 ml 3-neck flask. 44.453g of a 38wt% aqueous solution of formaldehyde (stabilized in 15% methanol) was then added to the flask as excess reagent. In aqueous media,

formaldehyde molecules exist in the hydrated form of oxymethylene glycol, which has the chemical formula $HOCH_2OH$.[131, 132] Oxymethylene glycol molecules are highly reactive, and have a tendency to self-react to form poly(oxymethylene glycol) or paraformaldehyde oligomers of general structure $(CH_2O)_n$. [132] The 3-neck flask was sealed and immersed into an ice bath was to promote the formation of paraformaldehyde oligomers such as the reactive trimer $(CH_2O)_3$, which is called trioxymethylene or trioxane.[128, 131]

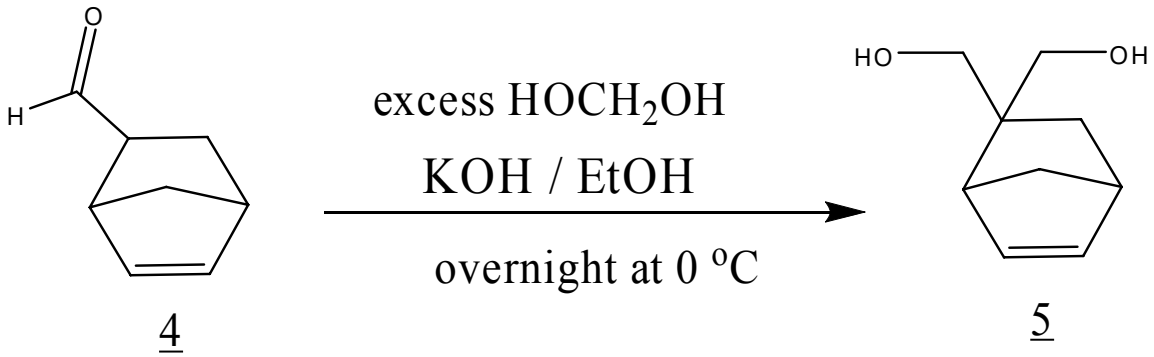

Figure 3.2 – Scheme for the synthesis of 5-Norbornene-2 endo, 2 exo-dimethanol (**5**)

To a tared beaker was added 16.088g of anhydrous KOH pellets and then 80 ml of a pre-mixed, 95% ethanol solution. The KOH pellets were dissolved by stirring the mixture vigorously for one hour before transferring the alkaline solution to an addition funnel. The addition funnel was connected to the 3-neck flask, and the KOH solution was added dropwise to the reaction mixture over a period of 4 hours under continuous stirring, while maintaining the reaction mixture's temperature below 5 ^oC throughout the addition.[128] The alkali promoted hydrolysis of trioxane, which released methylene hydroxide ($^+CH_2OH$) species, leading to insertion of a methanol group in structure **4,** a

key step in its conversion to and produced the product **5**.[128] After the addition was completed, the reaction mixture was stirred overnight in a fresh ice-bath, to promote reaction completion.

The reaction mixture was then transferred to a round boiling flask and all the alcohols were evaporated using a rotary evaporator. The concentrated residue was composed of two phases, a deep red liquid above a clear-colored liquid. After allowing the liquids to cool to ambient temperature, 300 ml of DCM and a PTFE-coated stirrer bar were added to the flask, and the contents were stirred vigorously. The flask was connected to a reflux condenser and immersed in a hold oil bath to reflux the DCM and promote extraction of the diol into the organic phase. After an hour of heating, the flask was then cooled to ambient under continuous stirring, before its contents were poured into a separatory funnel, agitated, and allowed to stand for several hours. The aqueous layer was discarded, and the organic layer was washed once with 50 ml of saturated NaCl solution. The organic layer was recovered and dried over anhydrous $MgSO_4$, before being filtered into a pre-weighed round flask. The filtrate was then evaporated to dryness using a rotary evaporator, to obtain 25g of solids. A sample of the solids was analyzed by ^1H NMR to confirm that the reaction had proceeded to completion – the disappearance of the aldehyde proton peak (δ = 8.44 ppm) being indicative of 100% conversion of reactant **4** to product **5**.

250 ml of toluene was added to the flask and then heated the mixture above 80 ^oC to dissolve all the solids. Using, a rotary evaporator, the solution was concentrated by distilling off 155 ml of the original toluene. Without allowing the round flask to cool, it was transferred to a preheated, oven held at 85^oC. After allowing the flask to thermally

equilibrate for 15 minutes, the oven was turned off to gradually cool the insulated system to ambient over a period of several hours in order to promote recrystallization.[128] The resultant mixture was vacuum filtered to recover the first batch of crystals, which were dried overnight under high vacuum in at 85^{o}C to recover 16.598g of purified product. The second batch of crystals were formed by was concentrating the filtrate further, and gradually cooling the residual solution, as done with the first batch of crystals. After vacuum filtration, and an overnight drying step, 2.40g of a second set of crystals was recovered. Subsequent attempts at recrystallization of more crystals were unsuccessful, thus, the total amount of purified product recovered was 18.998g (123.4 mmoles or 74% yield). The experimentally observed yield of **5** crystals (74%) was comparable to yields reported in literature, which range from 68-76%. [127-130] The structure of synthesized product **5** was validated by comparing its ^{1}H NMR spectrum to the spectroscopic results of the literature sources,[128-130] as well as to the ^{1}H NMR spectra of a commercially sample purchased from Aldrich. Peak assignments were made using the spectroscopic predictions of ChemDraw Ultra (Cambridge Soft) software.

^{1}H NMR: 0.67-0.71 ppm (1H, doublet), 1.25-1.29 ppm (1H, doublet), 1.43-1.55 ppm (2H, two doublets), 2.80 ppm (1H, singlet), 2.95 ppm (1H, singlet), 3.1-3.3 ppm (2H, broad singlet), 3.46-3.60 ppm (2H, two doublets), 3.81-3.87 ppm (2H, two doublets), 6.14 ppm (2H, singlet)

^{13}C{^{1}H} NMR: 32.8 ppm (singlet), 41.9 ppm (singlet), 44.5 ppm (singlet), 46.8 ppm (singlet), 48.5 ppm (singlet), 70.0 ppm (singlet), 70.9 ppm (singlet), 135.0 ppm (singlet), 137.0 ppm (singlet)

3.3.1.2 Synthesis of Norbornane-2 endo, 2 exo-dimethanol (**6**)

Figure 3.3 shows the general scheme by which **6** was synthesized. A batch of 5-Norbornene– 2 endo, 2 exo –dimethanol was synthesized and purified using a modified version of the one reported by Nemoto and co-workers.[130] 10.500g (68.2 mmoles) of **5** and 2.511g of a wet water paste of Pd/C containing approximately 0.103g of palladium (1.0 wt% palladium metal loading with respect to weight of **5**) was added to a tared 500 ml, 3-neck flask. The unsaturated diol was then dissolved in 350 ml of MeOH and the flask was sealed with two stoppers and a 2-way valve, which was left in the closed position.

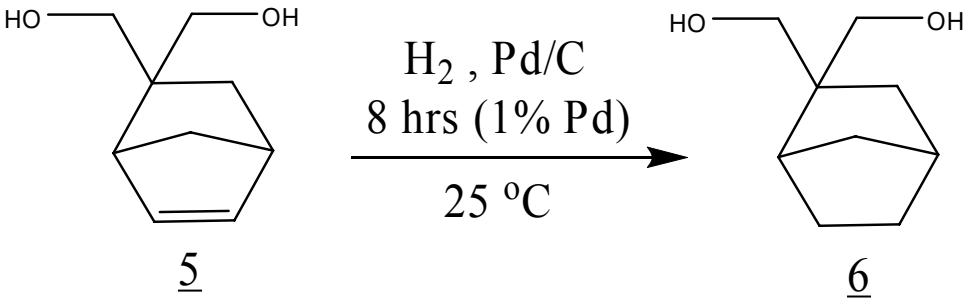

5 6

Figure 3.3 – Scheme for the synthesis of Norbornane-2 endo, 2 exo-dimethanol (**6**)

A balloon was inflated with H_2, and then attached to the closed 2-way valve. The flask was then evacuated under high vacuum and then backfilled with hydrogen from the balloon. The cycle of evacuating and backfilling of the reaction flask with H_2 was repeated at least five times to enrich the flask with an H_2 atmosphere and remove any traces of air. The 2-way valve was left closed while the balloon was re-inflated one last time to a volume of approximately 9 liters, corresponding to 375 mmoles of H_2 at

ambient conditions. The 2-way valve was then opened one last time to ensure that H_2 remained in excess of **5** throughout the hydrogenation reaction. The flask was kept under yellow lighting to prevent UV degradation of the catalyst, and the reaction mixture was vigorously stirred at room temperature for 8 hours.

After the reaction was complete, the flask was evacuated and backfilled with inert N_2. The evacuation and N_2-backfilling cycle was repeated multiple times to remove to remove all the H_2 from both the gas and solid (catalyst) phases within the flask. The reaction mixture was then filtered several times through fine filter paper to recover a quantitative amount of the original catalyst. The filteration residue was was several times with copious MeOH to improve the yield of **5**, then the catalyst was dried and stored in a dark drawer for use in future hydrogenation reactions. The combined filtrate was transferred to a pre-weighed round flask and then all the solvent was removed using a rotary evaporator. The solids were redissolved in a copious amount of absolute EtOH, and then the alcohol was distilled to remove remaining traces of water via azeotropic distillation. 52 ml of EtAc was then added to the flask, which was reheated to 70 ^{o}C, to redissolve all the solids. Then EtAc was slowly evaporated under high vacuum to promote evaporative recrystallization, as done by Nemoto and co-workers.[130] A set of pure white crystals was produced weighing a total of 10.37g (67.3 mmoles or 97% yield).

The recovered product was analyzed by ^{1}H NMR to confirm that the reaction had proceeded to completion – disappearance of the vinyl group's proton peak (δ = 6.14 ppm) was indicative of complete conversion of all the unsaturated bonds. In agreement with observations in literature, the required reaction time for complete hydrogenation using Pd/C scaled inversely proportionally with the wt% of palladium metal with respect to the

unsaturated diol (loadings of 0.5, 1.0, and 2.0 wt% required reaction times of 16, 8, and 4 hours, respectively).[130, 133, 134] The experimentally observed yield (95%) was comparable to the quantitative yield reported by Nemoto and co-workers.[130] ^{1}H NMR was used to confirm that the desired diol was formed by comparing the spectroscopic results to those cited in literature sources.[130] Peak assignments were made via the use of the spectroscopic predictions of ChemDraw Ultra (Cambridge Soft) software.

^{1}H NMR: 0.68-0.71 ppm (1H, doublet), 1.03-1.12 ppm (2H, multiplet), 1.21-1.23 ppm (1H, doublet), 1.44-1.64 ppm (4H, broad quartet), 2.21 ppm (1H, singlet) , 2.38 ppm (1H, singlet), 2.8-3.2 ppm (2H, broad singlet), 3.47-3.50 ppm (1H, doublet), 3.63-3.65 ppm (2H, doublet), 3.76-3.79 ppm (1H, doublet).

^{13}C{^{1}H} NMR: 24.4 ppm (singlet), 28.6 ppm (singlet), 36.3 ppm (singlet), 37.2 ppm (singlet), 37.7 ppm (singlet), 39.1 ppm (singlet), 46.2 ppm (singlet), 68.7 ppm (singlet), 69.9 ppm (singlet)

3.3.2 Synthesis of PNC2 Precursors

3.3.2.1 Synthesis of 5-Norbornene-2, 3 cis exo-dimethanol (**9**)

According to literature sources, the general scheme of synthesizing Norbornene-2, 3 cis exo-dimethanol (**9**) is shown in Figure 3.4. The first step, involves the heat isomerization of 5-Norbornene-2,3 cis endo-dicarboxylic acid anhydride (**7**) above its melting point into a mixture of its exo (**8**) and endo (**7**) isomers, followed by the isolation of the exo form via successive recrystallizations in selective solvents.[133, 135-137] The second step of synthesizing **8**, involves the reduction of **8** by lithium aluminum hydride.[133, 136-139] Owing to multiple unsuccessful attempts to separate isomers **7**

and **8** after the heat isomerization step shown in Figure 3.4, laboratory synthesis of **9** was abandoned. Instead, **9** was purchased from a commercial vendor and used as received after spectroscopic characterization. Peak assignments were made via the use of the spectroscopic predictions of ChemDraw Ultra (Cambridge Soft) software.

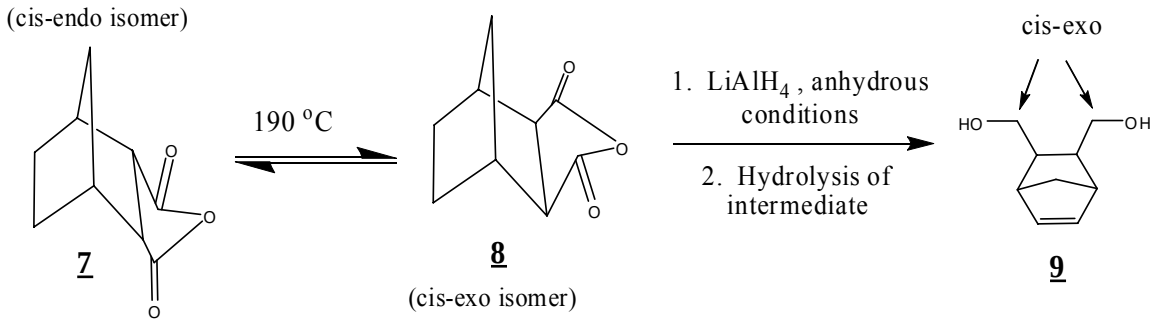

Figure 3.4 – General Scheme for synthesizing Norbornene-2,3-cis exo-dimethanol (**9**)

^{1}H NMR: 1.19-1.21 ppm (1H, doublet), 1.30-1.32 ppm (1H, doublet), 1.73-1.80 ppm (2H, multiplet), 2.48-2.49 ppm (2H, doublet), 3.66-3.67 ppm (4H, doublet), 4.85 ppm (2H, singlet), 6.14 ppm (2H, singlet).

^{13}C{^{1}H} NMR: 43.2 ppm (singlet), 43.7 ppm (singlet), 45.5 ppm (singlet), 63.1 ppm (singlet), 64.5 ppm (singlet), 137.3 ppm (singlet)

3.3.2.1 Synthesis of Norbornane-2, 3 cis exo-dimethanol (**10**)

Norbornane-2, 3 cis exo-dimethanol (**10**) was synthesized and purified using procedures similar to those used to obtain Norbornane-2 endo, 2 exo-dimethanol (**6**), except **10** could not be recrystallized; instead an oil was recovered in quantitative yield.[130, 133, 134, 136] ^{1}H NMR was used to confirm complete conversion of all vinyl groups to unsaturated bonds, as done with the synthesis of **6**. The structure of **10**

was validated by comparing its experimentally observed spectroscopic data to that cited in literature.[136, 137] Peak assignments were made via the use of the spectroscopic predictions of ChemDraw Ultra (Cambridge Soft) software.

^{1}H NMR: 0.96-0.99 ppm (1H, doublet), 1.18-1.28 ppm (3H, broad multiplet), 1.92 ppm (4H, singlet), 3.53-3.65 ppm (4H, broad quartet), 4.74 ppm (2H, singlet)

^{13}C{^{1}H} NMR: 29.5 ppm (singlet), 34.6 ppm (singlet), 40.3 ppm (singlet), 48.3 ppm (singlet), 63.3 ppm (singlet)

3.3.3 Synthesis of PNC3 Precursors

3.3.3.1 Synthesis of 5-Norbornene-2, 3 cis endo-dimethanol (**11**)

Similar to procedures cited by other researchers, 5-Norbornene-2, 3 cis endo-dimethanol (**11**) was synthesized by reducing **7** using lithium aluminum hydride (LiAlH4), as shown in Figure 3.5.[133, 136, 137, 140]

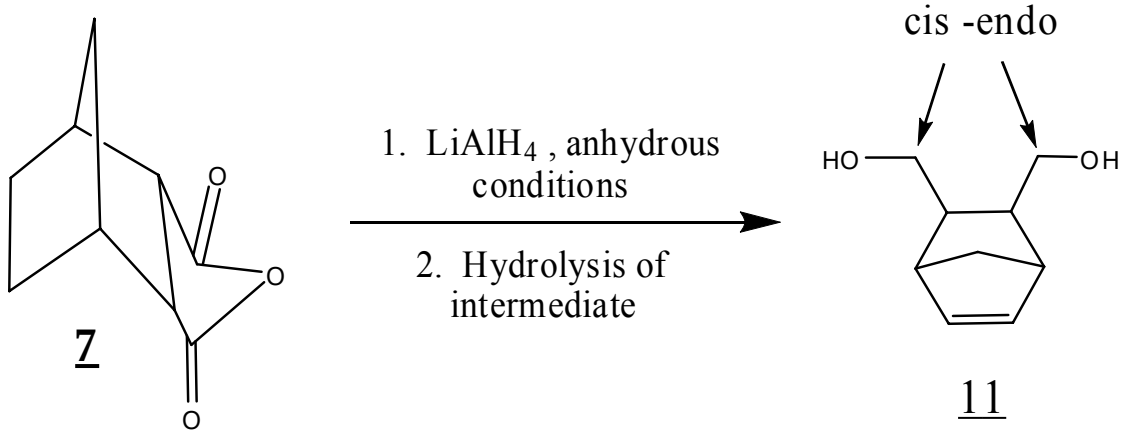

Figure 3.5 – Reaction scheme for synthesizing Norbornene-2,3-cis endo-dimethanol (**11**)

One batch of **11** was synthesized and purified according to the following details: Prior to adding reactants, a pre-silanized, 500 ml 3-neck flask was heated > 100 ^{o}C, while under high vacuum conditions to desorb any moisture from its sidewalls. Then the flask was backfilled with dry N_2 gas and allowed to cool to ambient under the inert atmosphere. The flask was then tared and then an nitrogen-purged cannular was used to transfer 192.24g of a 1.0M solution of $LiAlH_4$ in anhydrous THF (217 ml of solution or 217 mmoles of LiAlH4 reactant added) to the flask. The flask was then immediately sealed and evacuated until the bubble point of the solvent was reached. Then the flask was backfilled with N2 gas, and the cycle of evacuation and N_2-backfill was repeated at least 5 times to remove all traces of moisture from the system. A separate solution was made of 15.504g (94.5 mmoles) of 7 crystals dissolved in 100 ml of dry THF and then transferred to an addition funnel. The addition funnel was attached to the 3-neck flask, and the evacuation and N_2-backfill cycles were repeated 5 more times to fill the reaction system with inert atmosphere. I connected a silicone bubbler and an N_2 purge line to the 3-neck flask, and began dropwise addition of **7** to the excess LiAlH4 under vigourous stirring and a constant purge of inert gas. The dropwise addition was completed after 5 hours, and the addition funnel was replaced by a reflux condenser, which had been pre-silanized and pre-vacuum dried.

The reaction mixture was refluxed overnight under inert atmosphere to promote the formation of the metal alcoholate intermediate.[133, 136-139] The reaction mixture was then allowed to cool to ambient under an inert atmosphere, and the reflux condenser was replaced by a clean addition funnel. The 3-neck flask was then immersed in an ice bath and allowed to cool for at least an hour before water was dropwise added to the ice-

cold mixture under vigorous stirring. The addition of water produced a highly exothermic reaction, which caused the reaction mixture to begin boiling even while immersed in the ice bath. A total of 60 ml of water was added to completely convert all of the reactive intermediate molecules to **11** while producing a thick slurry composed of **11** and a white precipitate (by-product). The resultant mixture was diluted using 400 ml of EtAc and then vacuum filtered to remove the insoluble byproduct. The filtrate was combined and transferred to a boiling flask, before being concentrated to approximately 250 ml.

The organic solution was washed with 75 ml of saturated NaCl solution, and then dried over anhydrous $MgSO_4$. The mixture was filtered into a pre-weighed boiling flask and then all the solvent was removed using a rotary evaporator. The solid residue was dried under high vacuum condition at 80 ^{o}C (slight sublimation observed). A set of white, needle-like crystals formed as the solids slowly cooled to ambient. The weight of crystals recovered was 14.04g (91.2 mmoles or 96% yield). The structure of **11** was validated by comparing its experimentally observed spectroscopic data to that cited in literature.[136, 137, 140] Peak assignments were made via the use of the spectroscopic predictions of ChemDraw Ultra (Cambridge Soft) software.

^{1}H NMR: 1.32-1.39 ppm (2H, quartet), 2.43-2.50 ppm (2H, doublet), 2.75 ppm (2H, singlet), 3.26-3.35 ppm (2H, triplet), 3.54-3.58 ppm (2H, doublet), 4.73 ppm (2H, broad singlet), 5.98-5.99 ppm (2H, doublet)

^{13}C{^{1}H} NMR: 44.8 ppm (singlet), 46.3 ppm (singlet), 49.8 ppm (singlet), 63.1 ppm (singlet), 134.7 ppm (singlet)

3.3.3.2 Synthesis of Norbornane-2, 3 cis endo-dimethanol (**12**)

Norbornane-2, 3 cis endo-dimethanol (**12**) was synthesized and purified using procedures similar to those used to obtain Norbornane-2 endo, 2 exo-dimethanol (**6**), except an overnight cooling of the **12** in an ice-bath was needed to initiate nucleation of crystals from EtAc; Hexane and EtOH served as alternative solvents for EtAc.[133] White crystals were recovered in quantitative yield. ^{1}H NMR was used to confirm complete conversion of all vinyl groups to unsaturated bonds, as done with the syntheses of **6** and **10**. The structure of **12** was validated by comparing its experimentally observed spectroscopic data to that cited in literature.[136] Peak assignments were made using the spectroscopic predictions of ChemDraw Ultra (Cambridge Soft) software.

^{1}H NMR: 1.28-1.30 ppm (5H, multiplet), 1.44-1.47 (1H, doublet), 2.18-2.25 ppm (4H, multiplet), 3.59-3.62 ppm (2H, doublet), 3.88-3.93 ppm (2H, doublet), 4.32 ppm (2H, broad singlet).

^{13}C{^{1}H} NMR: 22.5-22.8 ppm (doublet), 39.9-40.5 ppm (triplet), 42.2 ppm (singlet), 42.9 ppm (singlet), 45.6 ppm (singlet), 61.4 ppm (singlet)

3.4 Synthesis of Polycarbonates

3.4.1 Ring-Opening Polymerization (ROP) of Polycarbonates

Polycarbonate macromolecules may be synthesized via the ring-opening polymerization (ROP) of cyclic carbonate monomers using either anionic or cationic initiators, as shown in Figure 3.6.[106, 129, 130, 141-163] Although ROP has been successfully used to synthesize a wide variety of polycarbonate structures, the

macromolecular products tend to be large with the molecular weights of the products ranging from 10,000 to > 100, 000 due to the "living chain" nature of ROP.[130, 141-149] Large chain sizes are problematic for sacrificial polymers since they would produce large domains when templated in spun inorganic films and thus large pore sizes, as well as exhibiting phase-segregation due to poor miscibility. Thus, the M_w of any synthesized polycarbonate chains must be kept as small as possible to ensure that their domain sizes would be small prior to decomposition and also that, after grafting them to siloxane and silsesquioxane structures, they would be phase-compatible with HSQ.

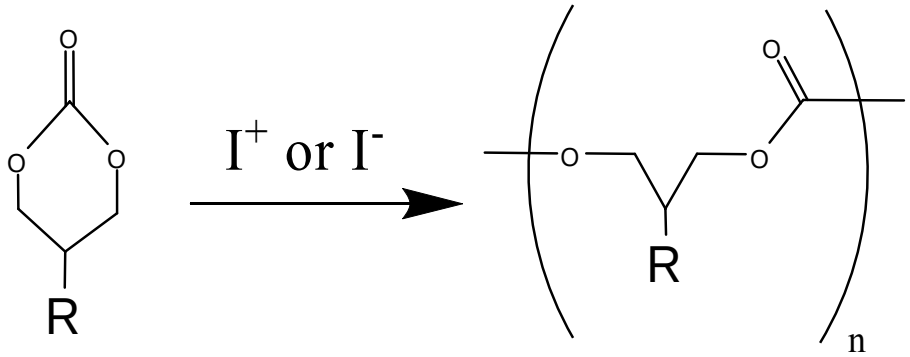

Figure 3.6 – General scheme showing the synthesis of a linear polycarbonate chain via the ROP of a cyclic carbonate monomer. Where I^- and I^+ denote anionic and cationic initiators, respectively

An additional issue with ROP is that each initiator has its own specifications for initiating ROP (eg. specific mechanism, specific thermal activation temperature, specific loading levels requirements with respect to monomers, etc). [150, 151] This leads to large differences in the reported properties (yield, chain length, polydispersity, presence or absence of ether links due to backbiting during ROP, etc) of polycarbonate chains

synthesized from identical monomers when either the initiator or any of the physiochemical conditions of the ROP reaction are varied.[145, 146, 152-155]

Cationic initiators have a tendency to produce polycarbonate chains of low M_w, but in relatively low yields and also to cause the formation of ether links in the polycarbonate chains, with the amount of ether linkages depending on numerous factors including: specific chemical structures of initiator and monomer, loading level of initiator, reaction time, reaction temperature, etc.[141, 145, 151-158] Since ether links have high stability towards acid attack, they would interfere with the acid-catalyzed decomposition reactions that are necessary for the direct-write porosity process shown in Figure 1.2. In general, anionic initiators produce polycarbonate chains of larger M_w in higher yields than cationic initiators, and anionic initiators also have a lower tendency towards backbiting reactions during ROP, thus producing chains with fewer and sometimes no ether links.[142-144, 147, 148, 150, 151, 154, 157, 159]

Finally, the end-groups of the polycarbonate chains are dependent on the chemical structure and nature (anionic or cationic) of the initiators used to produce them; hence, two polycarbonate chains produced from two different initiators may have different properties (eg. solubility) even if their main chain characteristics are identical. [145, 146, 152-155]

3.4.2 Synthesis via Copolymerization of Epoxides with Carbon Dioxide

Polycarbonate homopolymers have been successfully produced in high yields via the catalyzed copolymerization of carbon dioxide (CO_2) with cyclic ethers (epoxides), as shown in Figure 3.7.[160-166] According to the reported mechanisms for these types of

reactions, during the initiation step the metal catalysts promote the opening of the epoxides rings to form reactive metal-ether intermediates, the intermediates are then carboxylated to form carbonate linkages, followed by propagation of the "living chain".[160, 161] Most of the polycarbonate chains synthesized via this technique tend to be large (M_w ranging from 20,000 to > 100,000), which is an undesirable property for a templated sacrificial polymer films as discussed in the previous section.[162-164]

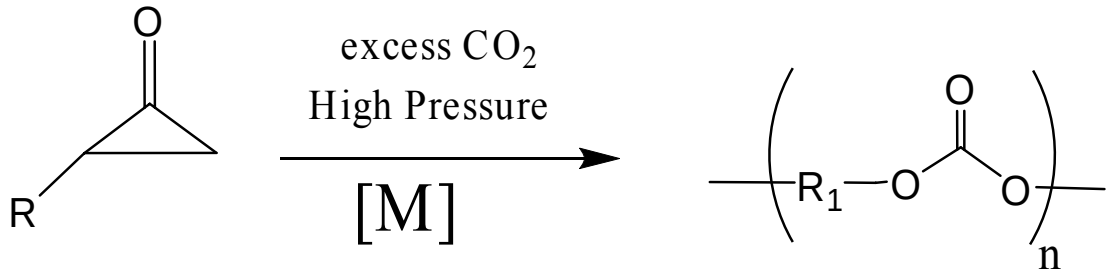

Figure 3.7 – General scheme for the synthesis of polycarbonates via the co-reaction of CO_2 and epoxides. M denotes a catalyst

There have been reports of low molecular weight (2,000 < M_w 4,000) polycarbonate being formed when CO_2-soluble catalysts are used, but all the polycarbonate chains produced by the co-reaction of epoxides and CO_2 invariably contain numerous ether links.[160, 164-166] As stated earlier, the presence of ether bonds in the polycarbonate chains would hinder their acid-catalyzed decomposition, making them unsuitable for use in the direct-write porosity process shown in Figure 1.2. An additional disadvantage of using this synthesis method to produce polycarbonates is that it requires very high pressures (400-2000 pounds per square inch) to promote the reactivity of CO_2, thus limiting its applicability in small-scale laboratory syntheses.[163-166]

3.4.3 Synthesis via Polycondensation

Homo-polycarbonate and co-polycarbonate chains may be synthesized via the polycondensation of diols (glycols) with carbonyl-containing co-reactants such as CO_2, CDI, phosgene, and triphosphegene.[79-82, 84, 85, 88, 98, 99, 167-171] The general scheme for synthesizing homopolymers via polycondensation is shown in Figure 3.8.

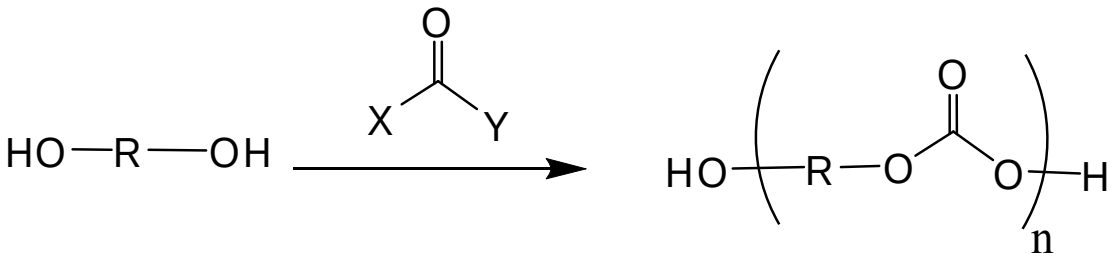

Figure 3.8 - General scheme for synthesizing a polycarbonate homopolymer via polycondensation. X and Y denote good leaving groups

Polycondensation is an advantageous synthesis route for producing the polycarbonate chains for uses as templated sacrificial polymers. The reaction rates of polycondensation reactions are easier to control, unlike the methods with "living reactions" (ROP and the co-reaction of epoxides with CO_2), resulting in high batch-to-batch reproducibility of final polymer characteristics. Since polycondensation reactions rates are low when one of the co-reactants is in excess of the other and chain propagation is terminated when the limiting reactant is depleted, polycondensation lends itself to the formation of low M_w oligomers (2000-6000).[56, 79-82, 84, 85, 88, 98, 168, 169] The production of oligomers is advantageous because small templated chains would produce small pores in the matrix of a spun film if phase-segregation can be avoided.

Furthermore, the end-groups of the oligomers are easily controlled by adjusting the stoichiometry of the co-reactants; the reactant that is in excess will produce the end-groups in the final chain after propagation has been terminated (eg. if the diol in Figure 3.8 is an excess reactant, then the homopolymer will have hydroxyl end-groups).[79-82, 84, 85, 88, 98, 167-169] Both hydroxyl groups and the common end-groups used in polycondensation (e. imidazoles, chlorofomates, etc) are highly reactive, affording further reactions that may be used to graft the polycarbonate chains to inorganic or organosilicon molecules that may serve as compatibilizers to increase the miscibility of the sacrificial chains with HSQ.[98, 168, 169]

3.4.4 Annotations for ^{1}H and $^{13}C\{^{1}H\}$ NMR Spectra of Synthesized PNCs

Figure 3.9 shows the annotated chemical structure of the hydroxyl-terminated **PNC1** chains. And Figure 3.10 shows the annotations for both the hydroxyl-terminated and vinyl-terminated chains of **PNC2** and **PNC3** oligomers.

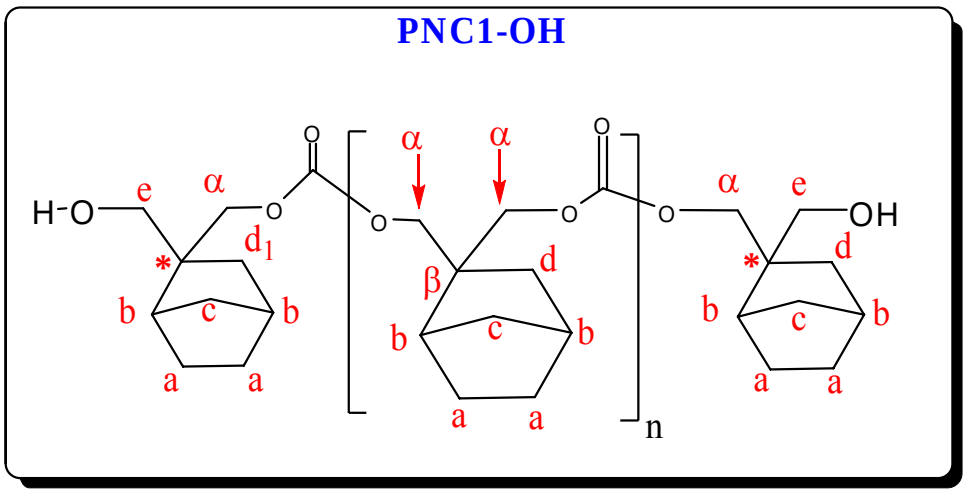

Figure 3.9 – Annotated chemical structure of hydroxyl-terminated **PNC1** oligomers

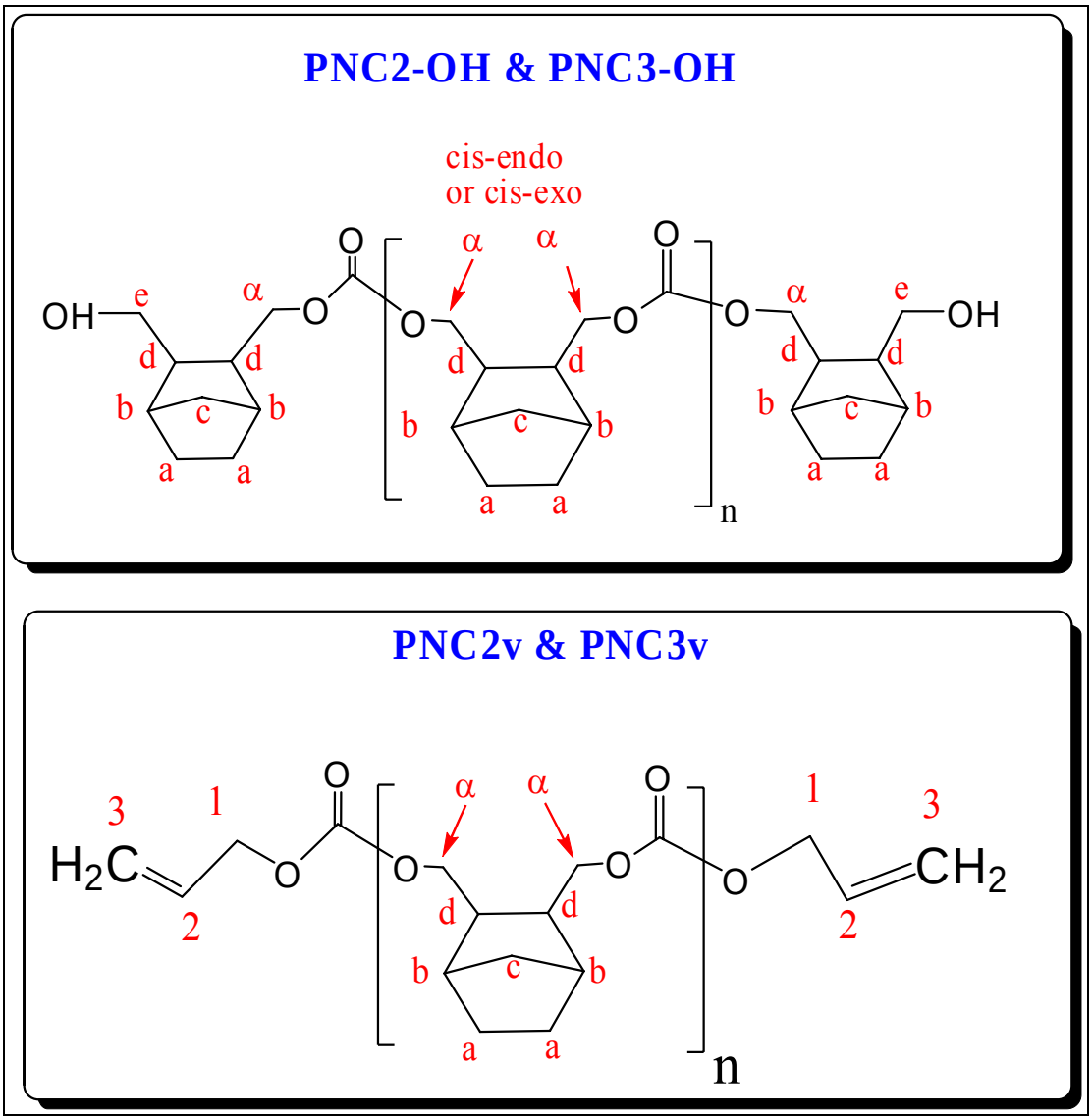

Figure 3.10 – Annotated chemical structures of hydroxyl-terminated and vinyl-terminated **PNC2** and **PNC3** oligomers

The annotations shown in Figure 3.9 and Figure 3.10 were used to identify the ^{1}H NMR peaks and $^{13}C\{^{1}H\}$ NMR peaks in the sections that immediately follow the detailed procedures for synthesizing and purifying each oligomer.

3.4.5 Synthesis of PNC1-ROP via Ring Opening Polymerization (ROP)

Literature sources show that ROP-synthesized **PNC1** (**PNC1-ROP**) chains can be synthesized by either the anionic or cationic-initiated ROP of spiro[bicyclo[2.2.1]heptane-2,5'-[1,3]dioxan]-2'-one (**13**), as shown in Figure 3.11, using any of the following initiators: sodium methoxide (NaOMe), sec-butyllithium (sec-BuLi), boron trifluoride diethoxide (BF_3OEt_2), or 1,8-diazabicyclo[5.4.0]undec-7-ene (DBU). [129, 151, 159]

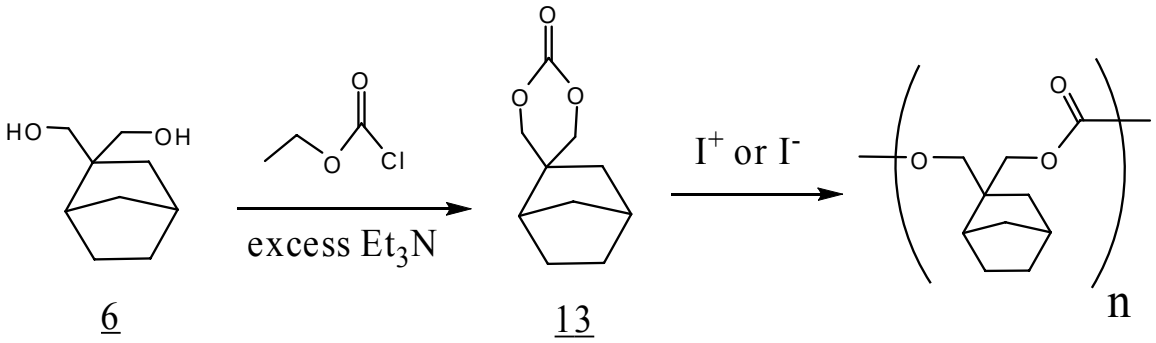

Figure 3.11 – General reaction scheme for the ROP synthesis of **PNC1-ROP** cited in literature. Where I^- and I^+ denote an anionic and cationic initiator, respectively

However, owing to the complexity of successfully tailoring ROP conditions to produce polycarbonate chains with specific properties, the ROP of **13** and the purification of the **PNC1-ROP** chains produced were both performed by experienced polymer chemists at Promerus LLC. The details for the ROP synthesis and purification procedures were kept confidential by the company, but they managed to produce and recover over 15g of **PNC1-ROP** product. Prior to shipment of product to Georgia Institute of Technology, Promerus LLC validated the structure of the **PNC1-ROP**chains, by comparing their experimental NMR results to spectroscopic data cited reported in

literature.[129] Although the exact structures of the end-groups of the **PNC1-ROP** chains synthesized by ROP were not divulged, they were known to be chemically inert. Hence, the **PNC1-ROP** chains synthesized by Promerus LLC could not be grafted to compatibilizers to form nanocomposites, which would be phase-compatible with HSQ. GPC analyses of the purified **PNC1-ROP** chains were also performed by Promerus LLC, and the results are discussed in a later section.

3.4.6 Synthesis of PNC1-OH via Polycondensation

Low M_w, hydroxyl-terminated **PNC1** oligomers (**PNC1-OH**) were synthesized in low yields via a modified form of the phase-transfer catalyzed polycondensation procedure developed by Frechet and co-workers for the synthesis of co-polycarbonates.[79, 80, 88, 167] The details of the polycondensation reaction, shown in Figure 3.12, and purification procedure are as follows: 5.830g (37.4 mmoles) of diol **5**, 6.372g (39.3 mmoles) of CDI, 5.827g (42.2 mmoles) of K_2CO_3, and 0.296g (1.12 mmoles) of 18-crown-6 ether were added to an empty 250 ml 3-neck flask. The solids were dissolved in 70 ml of anhydrous DCM, and the flask was sealed with 2-way valves. The top of a pre-silanized and pre-dried reflux condenser was connected to a silicon-oil bubbler through a 2-way valve, while the bottom of the condenser was attached to the 3-neck flask. The apparatus was purged with a stream of dry N_2 for at least 15 minutes, and then the 3-neck flask was immersed in a hot oil bath to induce boiling of the DCM solvent.

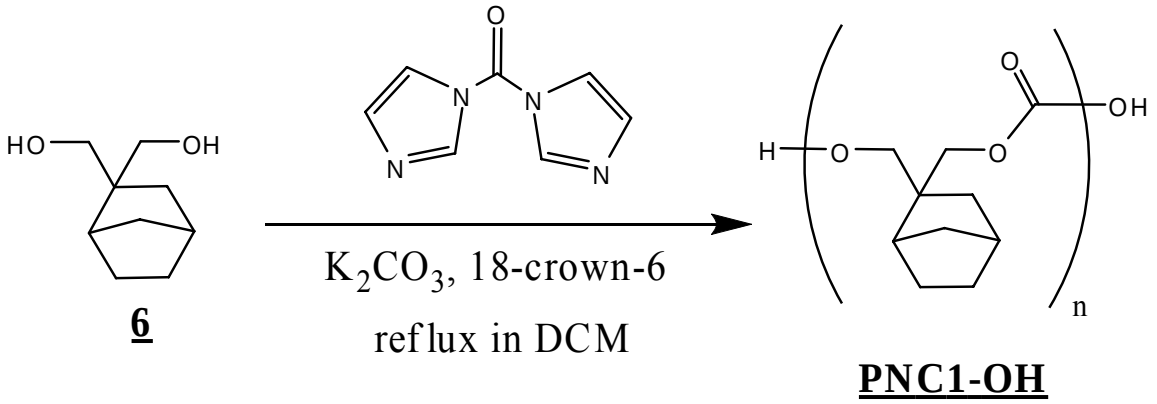

Figure 3.12 – Synthesis scheme for hydroxyl-terminated **PNC1** oligomers (**PNC1-OH**) via phase-transfer catalyzed polycondensation

The reaction mixture was refluxed for 71 hours under inert atmosphere and vigorous stirring, and then allowed to cool to ambient. The mixture was then diluted with 140 ml DCM, and then filtered to remove the insoluble K_2CO_3 solids. The filtrate was divided into two parts, and each part was transferred to a different separatory funnel and washed three times with equal volumes of fresh DI water. The organic layers were then combined and dried over anhydrous $MgSO_4$ for several hours, before being filtered and transferred into a pre-weighed round flask. The solution was concentrated to approximately 7 ml using a rotary evaporator, and then pipetted dropwise into an ice-cold beaker containing 100 ml of MeOH to induce selective precipitation of polymer chains. The insoluble product was recovered by filtration, and the filtrate was collected, concentrated to 3 ml, and a second batch of solids were precipitated into fresh MeOH. Similar to purification procedures published in literature, the cycle of filtration, concentration of filtrate, and further precipitation was repeated multiple times to increase the yield of recovered solids.[56, 79-82, 84, 85, 88, 98, 167, 168] Finally, the solids in the filtration residue were dried overnight at 80^{o}C under high vacuum conditions. The

weight of **PNC1-OH** oligomers recovered was 0.626g (corresponded to a yield of 9% based on the theoretical mass of oligomers if all of **6** molecules were polycondensed to **PNC1-OH** chains).

Although the polycondensation conditions were varied by the use of other reactants (triphosgene, 4-nitrophenyl chloroformate, etc), activated diol intermediates, and higher reaction temperatures (via the use of a pressure vessel), the product yield could not be improved beyond the yield shown above.[81, 82, 84, 85, 88, 98, 99, 168] The low yield for **PNC1-OH** was due to the tendency of diols **5** and **6** tend to form cyclic carbonate molecules such as **13** during condensation, instead of linear polycarbonate chains.[128-130] The structural properties of the recovered **PNC1-OH** chains were analyzed by spectroscopic methods, elemental analysis, and GPC. NMR Peak assignments were made using the spectroscopic predictions of ChemDraw Ultra (Cambridge Soft) software. DSC and TGA-MS were used to elucidate the thermal behavior of the oligomeric **PNC1** chains. The NMR (the underlined annotations are identified in Figure 3.9), DSC, and elemental analysis data for **PNC1-OH** chains are summarized below. GPC and TGA-MS data for **PNC1** oligomers are discussed later.

^{1}H NMR: 0.77-0.87 ppm (1H, singlet, 1d), 0.99-1.62 (7H, overlapping multiplets, 4a + 2b + 1d), 2.20 ppm (1H, singlet, 1c), 2.29 ppm (1H, singlet, 1c), 3.41-3.73 ppm (0.5H, multiplet, e of endgroups), 3.88-4.31 ppm (4H, broad quartet, 4C_{α}), 7.46 ppm (0.1H, singlet, traces of imidazole), 7.65 ppm (0.1H, singlet, traces of imidazole)

$^{13}C\{^{1}H\}$ NMR: 23.3 ppm (singlet, a), 27.7 ppm (singlet, a), 35.9-40.1 ppm (multiple overalapping singlets, β & b & c & d), 67.5 ppm (singlet, 1e), 73.5 ppm (singlet, C_{α}), 75.7 ppm (singlet, C_{α}), 128.3 ppm (singlet, traces of imidazole), 131.9 ppm

(singlet, traces of imidazole), 148.4 ppm (singlet, cyclic carbonate), 155.5 (trace singlet, linear carbonate)

Elem. Anal. Results: Experimental (66.33 %C, 8.10 %H, 25.53 %O), Theory (66.23 %C, 7.99 %H, 25.77 %O)

DSC: semi-crystalline solid with melting point at 109-110^{o}C

3.4.7 Synthesis of PNC2-OH via Polycondensation

Low M_w, hydroxyl-terminated **PNC2** oligomers (**PNC2-OH**) were synthesized from diol **10** via a procedure similar to that used to obtain **PNC1-OH** oligomers.[79-82, 84, 85, 88, 98, 99, 167-171] The purification procedure for **PNC2-OH** oligomers was slightly different to that used to obtain **PNC1-OH** oligomers: during liquid-liquid extraction steps, the organic layer was sequentially washed twice with 5% HCl, once with saturated $NaHCO_3$, twice with DI water, and once with saturated NaCl solution. The subsequent purification steps were identical to those used to isolate **PNC1** oligomers. The polycondensation of 1.867g of diol **10** produced 1.648g of **PNC2-OH** oligomers (corresponded to a yield of 76% based on the theoretical mass of oligomers if all of **12** molecules were polycondensed to **PNC2-OH** chains). The high yield of **PNC2-OH** relative to **PNC1-OH** was due to the low tendency of diols **9-12** to form cyclic carbonates instead of linear oligomers during condensation, unlike diols **5** and **6**.[128-130] The structural properties of the recovered **PNC2** chains were analyzed by spectroscopic methods, elemental analysis, and GPC. NMR Peak assignments were made using the spectroscopic predictions of ChemDraw Ultra (Cambridge Soft) software. DSC and TGA were used to elucidate the thermal behavior of the oligomeric **PNC2**

chains. The NMR (the underlined annotations are identified in Figure 3.10), DSC, and elemental analysis data for **PNC2-OH** chains are summarized below. GPC and TGA-MS data for **PNC2** oligomers are discussed later.

^{1}H NMR: 1.04-1.51 ppm (6H, multiplet, 4a + 2b), 1.96 ppm (2H, singlet, 2c + trace d), 2.14 ppm (2H, singlet, 4β), 3.39-3.58 ppm (0.3H, two triplets, e), 3.72-4.40 ppm (4H, broad quartet, 4C_{α})

$^{13}C\{^{1}H\}$ NMR: 29.1-29.4 ppm (multiple overlapping peaks, a), 39.3-39.4 ppm (multiple overlapping peaks, b), 44.0-44.2 ppm (singlet, β), 47.9 ppm (singlet, d), 62.3-62.4 ppm (doublet, e), 67.5-68.1 ppm (broad singlet, C_{α}), 155.0 ppm (singlet, carbonate)

Elem. Anal. Results: Experimental (66.42 %C, 8.19 %H, 25.63 %O), Theory (66.23 %C, 7.99 %H, 25.77 %O)

DSC: amorphous solid with T_g at 46.5^{o}C and no melting point prior to decomposition.

3.4.8 Synthesis of PNC3-OH via Polycondensation

Low M_w, hydroxyl-terminated **PNC3** chains (**PNC3-OH**) were synthesized from diol **12** via a procedure similar to that used to obtain **PNC1-OH** oligomers. [79-82, 84, 85, 88, 98, 99, 167-171] The purification procedure for **PNC3-OH** oligomers was identical to that used to obtain **PNC2-OH** oligomers. The polycondensation of 4.100g of diol **12** produced 2.820g of **PNC3-OH** oligomers (corresponded to a yield of 69% based on the theoretical mass of oligomers if all of **12** molecules were polycondensed to **PNC3-OH** chains). The high yield of **PNC3-OH** oligomers relative to **PNC1-OH** oligomers

was due to the low tendency of diols **9-12** to form cyclic carbonates instead of linear oligomers during condensation, unlike diols **5** and **6**. [128-130]

The structural properties of the recovered **PNC3-OH** chains were analyzed by spectroscopic methods, elemental analysis, and GPC. NMR Peak assignments were made using the spectroscopic predictions of ChemDraw Ultra (Cambridge Soft) software. DSC and TGA were used to elucidate the thermal behavior of the oligomeric **PNC3** chains. The NMR (the underlined annotations are identified in Figure 3.10), DSC, and elemental analysis data for **PNC3-OH** chains are summarized below. GPC and TGA-MS data for **PNC3** oligomers are discussed later.

^{1}H NMR: 1.38-1.46 ppm (6H, doublet, 4a + 2b), 2.33 ppm (4H, singlet, 2β + 2c), 3.61-3.63 ppm (0.05H, two triplets, e of endgroups), 3.80-4.55 ppm (4H, broad quartet, 4C_{α})

$^{13}C\{^{1}H\}$ NMR: 22.1 ppm (singlet, a), 38.9-39.6 ppm (multiple overlapping singlets, β & b & c), 42.8 ppm (singlet, d), 60.6 ppm (singlet, e), 62.6 ppm (singlet, e), 66.1 ppm (singlet, C_{α}), 66.7 ppm (singlet, C_{α})

Elem. Anal. Results: Experimental (65.94 %C, 7.88 %H, 26.00 %O), Theory (66.07 %C, 7.87 %H, 26.06 %O)

DSC: semi-crystalline solid with T_g at 57^{o}C and melting point at 115^{o}C

3.4.9 Synthesis of PNC3v via Vinyl End-capping of PNC3-OH Oligomers

Low M_w, vinyl-terminated **PNC3** chains (**PNC3v**) were synthesized by end-capping **PNC3-OH** oligomers with vinyl end-groups, as shown in Figure 3.13. During a typical end-capping experiment, a pre-silanized 3-neck flask was evacuated and heated

above 100 °C to desorb any moisture from the sidewalls. The flask was backfilled with dry N_2 gas and allowed to cool to ambient under the inert atmosphere. Then 1.445g (approximately 0.45 mmoles of chains with M_n of 3,190) of **PNC3-OH**, 2.799g (22.9 mmoles) of DMAP, and 15 ml of anhydrous DCM were added to the 3-neck flask. While being purged with dry N_2 gas, the flask was immersed in an ice-water bath for over 30 minutes, while the contents were stirred to dissolve all the solids in the cold solvent. 2.300g (19.1 mmoles) of allyl chloroformate and 15 ml of anhydrous DCM were added to a separate pre-silanized 100 ml one-neck flask, and then the flask was sealed. The contents of the second flask were swirled to ensure good mixing of the liquid contents, and then cooled in an ice-water batch for 30 minutes to prevent volatilization of the allyl chloroformate.

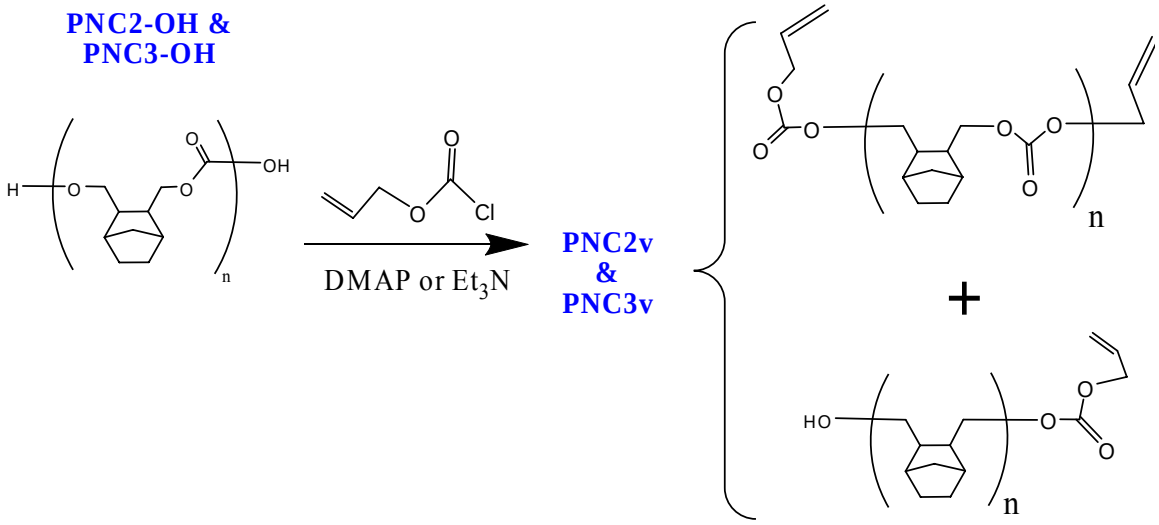

Figure 3.13 – General scheme for end-capping **PNC2-OH** and **PNC3-OH** chains with vinyl groups to produce **PNC2v** and **PNC3v** oligomers, respectively

After 30 minutes of cooling, the second solution was transferred to a pre-silanized addition funnel, and 10 ml of extra DCM was used to wash any residual solution out of

the one-neck flask into the addition funnel. The addition funnel was attached to the 3-neck flask, and a silicone-oil bath, and the entire apparatus was continuously purged with dry N_2 gas. The allyl chloroformate solution was added dropwise to the ice-cold solution in the 3-neck flask while vigorously stirring the reaction mixture and continuously purging the apparatus to remove the HCl gas by-product and promote the forward reaction. After 85 minutes of dropwise addition, all the allyl chloroformate had been added, and the reaction mixture was stirred overnight, under a continuous nitrogen purge. The reaction mixture was then sequentially washed twice with 5% HCl, once with saturated $NaHCO_3$, twice with DI water, and once with saturated NaCl solution. The organic layer was then dried over anhydrous $MgSO_4$ for several hours, before the mixture was filtered into a pre-weighed round flask.

The filtrate was concentrated to about 3g (solution contained approximately 2.5 ml of DCM solvent) using a rotary evaporator, and then it was pipetted dropwise into an excess amount (100 ml) of dry acetone to selectively precipitate the oligomers. The cloudy suspension was filtered through a fine-porosity fritted-glass filter, and the filter cake was washed with fresh acetone that had been warmed to 50^{o}C to remove any entrapped DMAP. The second filtrate was collected, concentrated as before, and dropwise added to fresh acetone to selectively precipitate more oligomers. The cycle of filtration, concentration of filtrate, and selective precipitation was repeated several times to increase the yield of **PNC3v** solids recovered. Finally, the solids were dried overnight in an 80^{o}C oven under high vacuum conditions. The weight of dry product recovered was 0.960g (corresponded to a yield of 66% based on the theoretical mass of **PNC3v** product if all of the hydroxyl end-groups of the **PNC3-OH** chains were converted to

vinyl end-groups). Spectroscopic analyses of several batches of vinyl end-capping reactions showed that the actual conversion of hydroxyl groups varied from 60-72% when the dropwise addition and overnight reaction were both performed near 0^{o}C. Since the OH conversion was over 50% but less than 100%, the recovered **PNC3v** product contained a mixture of chains that were double terminated with vinyl groups, those that had only one vinyl termination (mono end-capped), and probably some with no vinyl-terminations.

Attempts were made to increase the conversion of the hydroxyl end-groups by varying the reaction conditions. Although other strong nucleophiles were used in place of DMAP as reagents for the reaction, DMAP was found to be the most efficient at promoting the conversion of OH end-groups. When temperature was varied it was found that the OH conversion decreased as the temperature was increased (6% OH conversion at at ambient temperature, 0% OH conversion at reflux ie. 40^{o}C). Low temperatures promoted the forward reaction for two reasons: (i) the forward reaction was exothermic hence, the position of equilibrium shifted to the right to counteract the cooling effect of the ice bath, as predicted by Le Chatelier's principle; (ii) secondly, allyl chloroformate is highly volatile and boils at 27^{o}C hence cold temperatures keep the majority of this reactant in the liquid phase, which promotes the forward reaction. If an alternative cooling system to ice-water were used to cool the reaction mixture below 0^{o}C (eg. ethylene glycol or methanol liquid that is cooled below 0^{o}C via the use of either excess amounts of dry-ice or a refrigeration unit), it may be possible to achieve 100% conversion of OH end-groups.

The structural properties of the recovered **PNC3v** chains were analyzed by spectroscopic methods, elemental analysis, and GPC. NMR Peak assignments were made using the spectroscopic predictions of ChemDraw Ultra (Cambridge Soft) software. To quantify the %conversion of OH groups in the **PNC3-OH** chains, the ^{1}H NMR spectra of **PNC3v** (Figure 3.15) was compared to the batch of **PNC3-OH** (Figure 3.14) oligomers used to synthesize it. The %conversion of OH was calculated as the fractional drop in the ratio of the integrals of the peaks labeled (C_α) and (e) in the two spectra.

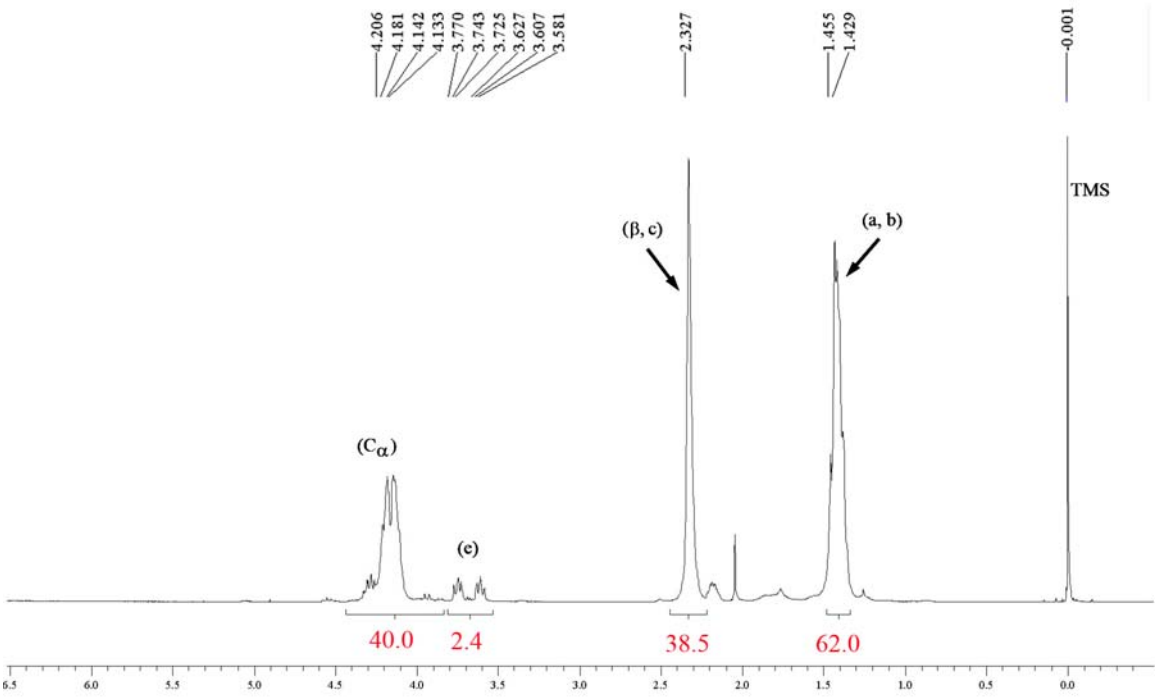

Figure 3.14 – An annotated ^{1}H NMR spectrum for a batch of **PNC3-OH** oligomers

From a comparison of the two ^{1}H NMR spectra, we observe that the %conversion of OH was (2.4-0.8)/2.4*100 = 67%. An alternative method of calculating the conversion is to use the ratio of the $C\underline{H_2}O$ peak (e) in Figure 3.15 to the peaks from the

allyl (#1) or the vinyl groups peaks (#2 and #3). The calculated result using the second method is also 67%, since the final **PNC3v** solids have half as many OH groups as vinyl groups.

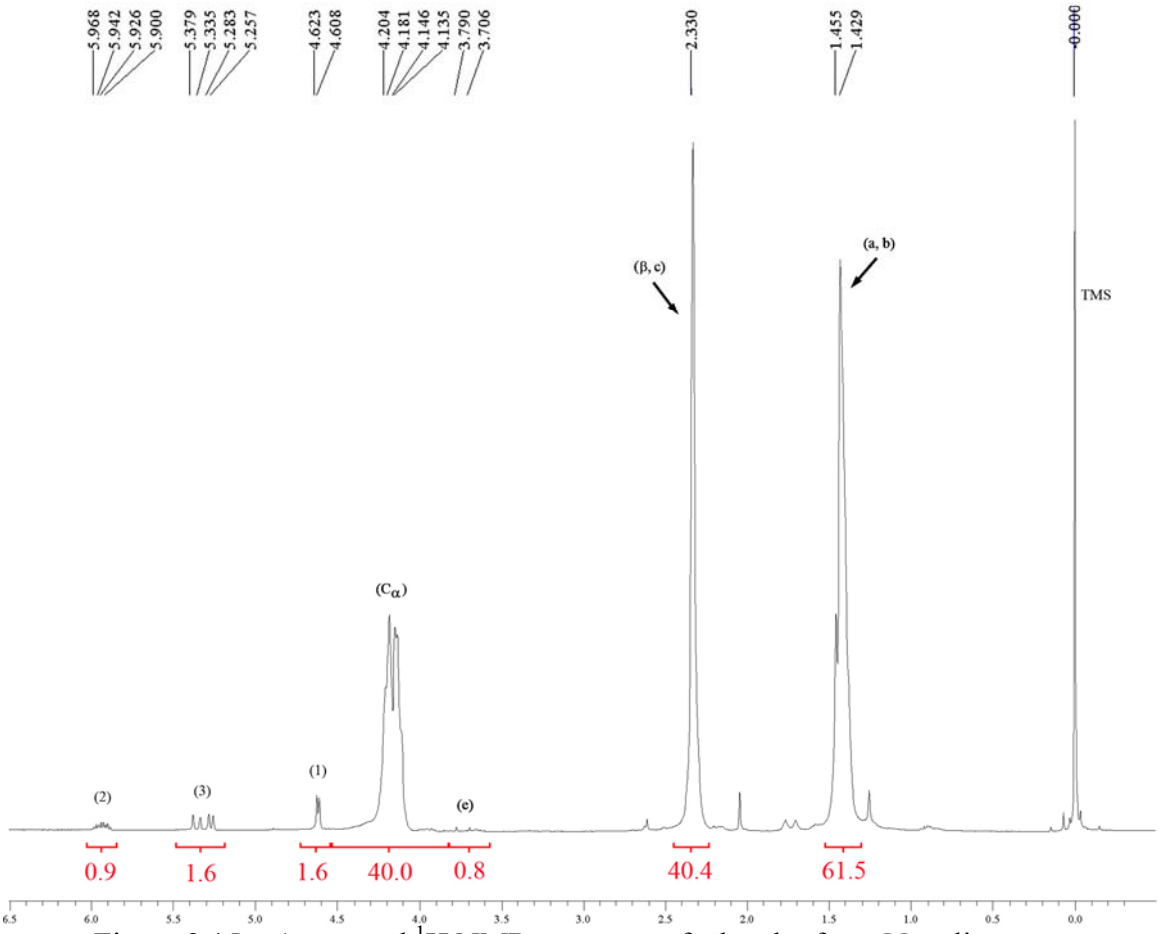

Figure 3.15 – Annotated ^{1}H NMR spectrum of a batch of **PNC3v** oligomers

Although hydroxyl groups are not active towards hydrosilylation, researchers have been able to successfully graft OH-terminated groups to silanes via alcohol silanization reactions (also called silane alcoholysis or de-hydrogenative coupling or O-silylation).[172-177] However, the silyl-ether bonds produced from O-silylation are

hydrolytically unstable, meaning that even if grafting was successful the bonds could be broken prior to decomposition of templated PNC segments.[60, 175, 178-183] Thus, the presence of hydroxyl groups in **PNC3v** was deemed highly undesirable. Several attempts were made at isolating the **PNC3v** chains with vinyl end-groups but adequate separation could not be achieved due to the similarity of the properties of all the chains in the blends (similar solubilities, similar movement up a TLC plate, negligible weight and size differences, etc). Due to inability to purify the **PNC3v** chains any further, the **PNC3v** oligomers used in the hydrosilylation reactions (described later in chapter 6) were actually a mixture of **PNC3** chains that were (i) double vinyl end-capped, (ii) mono vinyl end-capped, and (iii) double OH-terminated chains, such that two-thirds of all end-groups were vinyl groups. Below is a summary of the spectroscopic data pertaining to **PNC3v** using the annotations shown in Figure 3.10.

^{1}H NMR: 1.38-1.46 ppm (6H, doublet, 4a + 2b), 2.33 ppm (4H, singlet, 2β + 2c), 3.50-3.80 ppm (0.06H, two triplets, e from residual OH end-groups), 3.82-4.50 ppm (4H, broad quartet, 4C_{α}), 4.61-4.63 ppm (0.14H, doublet, two #1 protons from allyl group), 5.26-5.38 (.15H, quartet, #3 proton from vinyl end-group), 5.90-5.94 (.08H, quartet, two #2 protons from vinyl end-group)

$^{13}C\{^{1}H\}$ NMR: 22.2 ppm (singlet, a), 39.0-39.6 (multiple overlapping peaks, β & b & c), 41.1 ppm (singlet, d from residual OH end-groups), 62.6 ppm (singlet, e from residual OH end-groups), 66.0 ppm (singlet, C_{α}), 68.3 ppm (singlet, #1 from ally group), 118.8 ppm (singlet, #3 from vinyl end-group), 131.5 ppm (singlet, #2 from vinyl end-group), 154.9 ppm (singlet, carbonate)

3.4.10 Synthesis of PNC2v via Vinyl End-capping of PNC2-OH Oligomers

Low M_w, vinyl-terminated **PNC2** chains (**PNC2v**) were synthesized and purified via procedures similar to those used to obtain **PNC3v** oligomers except dry hexane was used in place of dry acetone to precipitate the vinyl-terminated oligomers. The end-capping of 2.173g of **PNC2-OH** afforded 1.312g of **PNC2v** product (corresponded to a yield of 60% based on the theoretical mass of **PNC2v** product if all of the hydroxyl end-groups of the **PNC2-OH** chains were converted to vinyl groups). The structural properties of the recovered **PNC2v** chains were analyzed by ^{1}H NMR and $^{13}C\{^{1}H\}$ NMR and the peak assignments were made using the spectroscopic predictions of ChemDraw Ultra (Cambridge Soft) software. The OH %conversion of the end-capping of **PNC2** chains was calculated using an identical method to the one described above for **PNC3v** oligomers. Although similar reaction conditions were used to end-cap both **PNC2** and **PNC3** oligomers, the % conversion of hydroxyl end-groups of **PNC2-OH** chains to vinyl end-groups was observed to be only 40%. The difference in reactivity of the hydroxyl end-groups of **PNC2-OH** and **PNC3-OH** chains during end-capping reactions was likely due to steric differences arising from the different orientations of the methylene-hydroxide end-groups (ie. endo- and exo- relative to the norbornane ring). Since less than 50% of the end-groups of the **PNC2v** solids were vinyl-terminated, only **PNC3v** oligomers were used in hydrosilylation reactions to ensure good yields of nanocomposite molecules. The NMR data for **PNC2v** oligomers are summarized below, complete with peak annotations (refer to Figure 3.10).

^{1}H NMR: 1.38-1.46 ppm (6H, doublet, 4a + 2b), 2.33 ppm (4H, singlet, 2β + 2c), 3.61-3.63 ppm (0.3H, two triplets, e of endgroups), 3.80-4.55 ppm (4H, broad quartet, 4C_{α}), 4.61-4.63 ppm (0.2H, doublet, two #1 protons from allyl group), 5.26-5.38 (.1H, quartet, #3 proton from vinyl end-group), 5.90-5.94 (.2H, quartet, two #2 protons from vinyl end-group)

^{13}C{^{1}H} NMR: 22.1 ppm (singlet, a), 38.9-39.6 ppm (multiple overlapping singlets, β & b & c), 42.8 ppm (singlet, d), 60.6 ppm (singlet, e), 62.6 ppm (singlet, e), 66.1-66.7 ppm (singlet, C_{α}), 68.3 ppm (singlet, #1 from ally group), 118.8 ppm (singlet, #3 from vinyl end-group), 131.5 ppm (singlet, #2 from vinyl end-group), 154.9 ppm (singlet, carbonate)

3.5 Estimation of PNC Chain Sizes

As stated earlier, the structural properties of the synthesized PNC oligomers were characterized by spectroscopic methods, elemental analysis, and GPC. NMR Peak assignments were made using the spectroscopic predictions of ChemDraw Ultra (Cambridge Soft) software. The thermal behavior of the PNC chains were investigated via DSC and TGA, and TGA-MS was used to analyze the mechanisms of their thermolysis. The sections below summarize the properties of the different types of PNC chains that were synthesized and also discuss the impact of these properties on their applicability as sacrificial materials for producing porous thin films with ideal pore morphologies.

3.5.1 End-group Analysis via ^{1}H NMR: Estimation of M_n and $\langle r^2 \rangle^{1/2}$ of Chains

The M_n of the synthesized PNC chains were estimated via end-group analyses of their respective ^{1}H NMR spectra, as done by other researchers.[81, 82, 84, 85, 98, 129, 168, 169, 184] To perform end-group analysis of a hydroxyl-terminated PNC chain, its ^{1}H NMR spectra was analyzed to find the ratio of the integrals of the protons of the α-carbons (C_α) and the methylene-oxide (CH_2O) groups, which are labeled as e in Figure 3.10. Since the C_α atoms and $C\underline{H}_2O$ groups were known to have two protons each, the ratio of the integrals of their respective protons were used to find the degree of polymerization (n), as shown in equation (3.1) and equation (3.2). The M_n value was calculated by finding the total molecular weights of all the repeat units and end –groups, as shown in equation (3.3).

$$\frac{\int C_\alpha}{\int (CH_2O)} = \frac{\int C_\alpha}{\int e} = \frac{(4n+4)}{4} = n+1 \tag{3.1}$$

$$n = \left(\frac{\int (C_\alpha - H)}{\int e} \right) - 1 \tag{3.2}$$

$$M_n = (2*155) + 28 + (n*182) = 338 + (n*182) \equiv [(n+1)*182] + 156 \tag{3.3}$$

Figure 3.16 shows an expansion of a ^{1}H NMR spectrum of a batch of **PNC3-OH** for the spectral region that was used in end-group analysis. To get an accurate ratio of the integral values for the protons at the C_α and e ($C\underline{H}_2O$) positions, the integral of the $C\underline{H}_2O$ protons in Figure 3.16 were set to unity. End-group analysis of the oligomer was then performed by substituting the integrals from Figure 3.16 into equation (3.2) and equation (3.3) to produce the numerical expressions shown in equation (3.4) and equation

(3.5). The n and M_n values for other oligomers were estimated using an identical procedure and the results are summarized in Table 3.1. The reaction conditions used to synthesize the PNC chains are listed in Table 3.2.

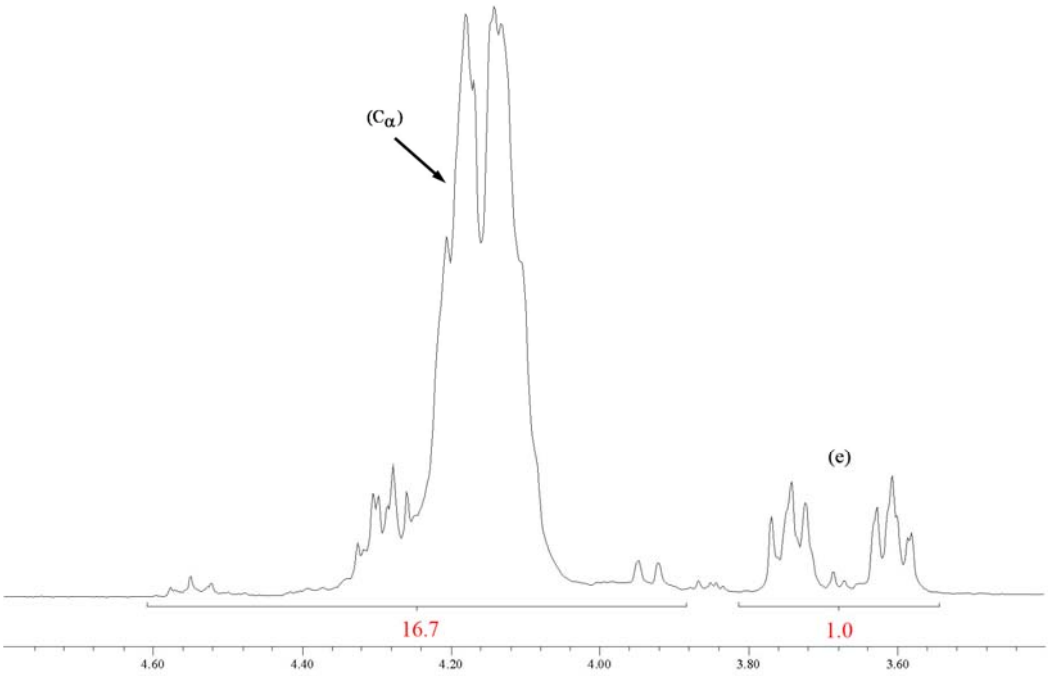

Figure 3.16 – An expansion for the ^{1}H NMR spectrum of **PNC3-OH** chains for the spectral region used in end-group analysis

$$n = \left(\frac{\int (C_\alpha - H)}{\int e} \right) - 1 = \left(\frac{16.7}{1} \right) - 1 = 15.7 \approx 16 \tag{3.4}$$

$$M_n = [(n+1)*182] + 156 = (16.7*182) + 156 = 3{,}189 \tag{3.5}$$

Table 3.1 – Summarized results for the end-group analyses of synthesized oligomers

Type of PNC oligomer	Batch #	Degree of Polymerization (n)	M_n (g/mol)
PNC1-OH	A	7.2	1,648
PNC1-OH	B	7.3	1,667
PNC2-OH	A	6.3	1,489
PNC2-OH	B	8.5	1,889
PNC3-OH	A	9.2	1,976
PNC3-OH	B	15.37	3,135
PNC3-OH	C	15.7	3,190

Table 3.2 – Reaction conditions used to synthesize PNC oligomers. All reactions were performed under reflux in DCM solvent (ie. 40 ^{o}C)

Type of PNC oligomer	Batch #	Dilution (ml of DCM per gram of diol)	Reaction Time (hrs)	Molar ratio of 18-crown-6 ether to diol (mole%)
PNC1-OH	A	5.8	71	4.9
PNC1-OH	B	3.9	71	2.9
PNC2-OH	A	11	42	7.1
PNC2-OH	B	27	48	7.0
PNC3-OH	A	15	45	6.0
PNC3-OH	B	17	45	6.3
PNC3-OH	C	16	44	5.5

Table 3.1 shows that polycondensation produced low-M_w PNC oligomers with degrees of polymerization between 7 and 17. This indicates that in the absence of agglomeration these sacrificial molecules would produce small pore sizes upon decomposition since pore dimensions are known to scale with the size of the porogen used.[3] If we model the PNC chains as random coils and ignore the volume occupied by the chain's skeleton (excluded volume), then we can estimate their root mean square end-to-end distance or $\langle r^2 \rangle^{1/2}$, as shown in equation (3.6); where, "n" is the number of repeat units calculated from end-group analysis, and "L" is the end-to-end length of each repeat unit.[185]

$$\left\langle r^2 \right\rangle^{1/2} = \left(nL^2\right)^{1/2} = L\sqrt{n} \tag{3.6}$$

Hence, the value of $<r^2>^{1/2}$ for an ensemble of polymer chains will be proportional to the square root of their average molecular weight.[185] Thus, the sizes of different batches of polymer chains with the same skeletal repeat units can be compared, as shown in equation (3.7).

$$\left\langle r^2 \right\rangle_B^{1/2} = \left\langle r^2 \right\rangle_A^{1/2} \sqrt{\left(\frac{n_B}{n_A}\right)} = \left\langle r^2 \right\rangle_A^{1/2} \sqrt{\left(\frac{M_{n,B}}{M_{n,A}}\right)} \tag{3.7}$$

For a rigid-rod chain structure, the end-to-end distance is simply the product of the unit length and the number of repeat units.[185] Although all the types of PNC chemical structures (refer to Figure 3.1 or Figure 3.9 and Figure 3.10) have one bicycle[2.2.1]heptane ring and one carbonate linkage per skeletal repeat unit, the positions of the carbonate linkages on the norbornane rings are different, which causes their repeat unit lengths to differ slightly, as shown in Table 3.3.

Table 3.3 – End-to-end lengths of repeat units of PNC oligomers

Type of PNC oligomer	**PNC1-OH**	**PNC2-OH**	**PNC3-OH**
L (angstroms)	4.99	4.02	4.02

The sizes of both random coil and rigid-rod chain structures for all the oligomers were determined by substituting the values of the unit lengths and the values for the number of repeat units (used n + 2 to account for end groups) into equation (3.6) and equation (3.7),. The estimated values of $<r^2>^{1/2}$ and rigid-rod end-to-end distances are

listed in Table 3.4 along with the values of the parameters used to calculate them. Although the small $\langle r^2 \rangle^{1/2}$ values were encouraging results for sacrificial chains, the actual volume occupied by the oligomers in the solution-state would be larger than the unperturbed dimensions of its random coils because of the effects of osmotic swelling.[97, 185-190] Both DLS and GPC analyses were used to estimate the hydrodynamic volume occupied by each of the synthesized PNC oligomers, as outlined in the following section.[97, 185-194]

Table 3.4 – Estimated sizes of PNC oligomers using random-coil and rigid-rod models

PNC type	Batch #	(n + 2)	L (nm)	$\langle r^2 \rangle^{1/2}$ (nm)	End-to-end distance for rigid-rods (nm)
PNC1-OH	A (4)	9.2	0.499	1.51	4.59
PNC1-OH	B (3)	9.3	0.499	1.52	4.64
PNC2-OH	A (19)	8.3	0.402	1.16	3.34
PNC2-OH	B (20)	10.5	0.402	1.30	4.22
PNC3-OH	A (24)	11.2	0.402	1.35	4.50
PNC3-OH	B (25)	17.37	0.402	1.68	6.98
PNC3-OH	C (26v)	18.7	0.402	1.74	7.52

3.5.2 GPC and DLS: Estimation of Hydrodynamic Radii and PDI

The size, morphology, and transport properties of flexible polymer chains in solution-state are affected by both thermodynamics and the hydrating power of the surrounding solvent.[185] The Stokes-Einstein equation, shown in equation (3.8), is frequently used to determine the diffusion-derived hydrodynamic radius, $R_{H,D}$, from DLS data.[97, 186, 187, 189, 192, 193] The symbol D_0 refers to the translational diffusion coefficient of the chains at infinite dilution, η_0 is the viscosity of the solute-free solvent,

T is the absolute temperature, and k_B is Boltzmann's constant (1.381 x 10^{-23} Joules per Kelvin).

$$R_{H,D} = \frac{k_B T}{6\pi\eta_0 D_0} \tag{3.8}$$

Multiple solutions of **PNC3-OH** chains were made in chloroform of concentrations ranging from 10 mg/ml to approximately 70 mg/ml. The solutions were then analyzed by a DLS (DAWN EOS model) to obtain their optical scattering profiles.[97] The DLS software of the DLS then automatically calculated the autocorrelation functions of each of the scattering profiles, and hence determined the particle sizes within the solutions. In order to obtain a distribution of the diffusion-derived hydrodynamic radii, $R_{H,D}$, the regularization analysis option was selected.

The solutions with **PNC3** concentrations equal to or higher than 50 mg/ml were observed to have multi-modal size distributions, as shown in Figure 3.17 and Figure 3.18. Attempts to analyze more dilute solutions (concentrations of 10-30 mg/ml) were unsuccessful - the scattering intensity was too low to produce autocorrelation functions with which to calculate particle sizes. It is clear that the peak labeled 1 in Figure 3.17 was not due to actual sizes of oligomeric chains since it corresponded to $R_{H,D}$ values less than the length of a single repeat unit of **PNC3** (0.4 nm). Thus, peak 1 was a mathematical artifact, which was produced from the noise in the scattering profiles observed by the DLS detector or from artificial noise in the autocorrelation functions. By referring to Table 3.4, we observe that the estimated $R_{H,D}$ values corresponding to the peaks labeled 2 and 3 in Figure 3.17 were larger than the end-to-end distances of rigid-rods, indicating that chain agglomeration had occurred in the solution. To promote

dispersion of agglomerated chains, the concentrated solutions were placed in ultrasonic baths for over 20 minutes and then rescanned using the DLS.

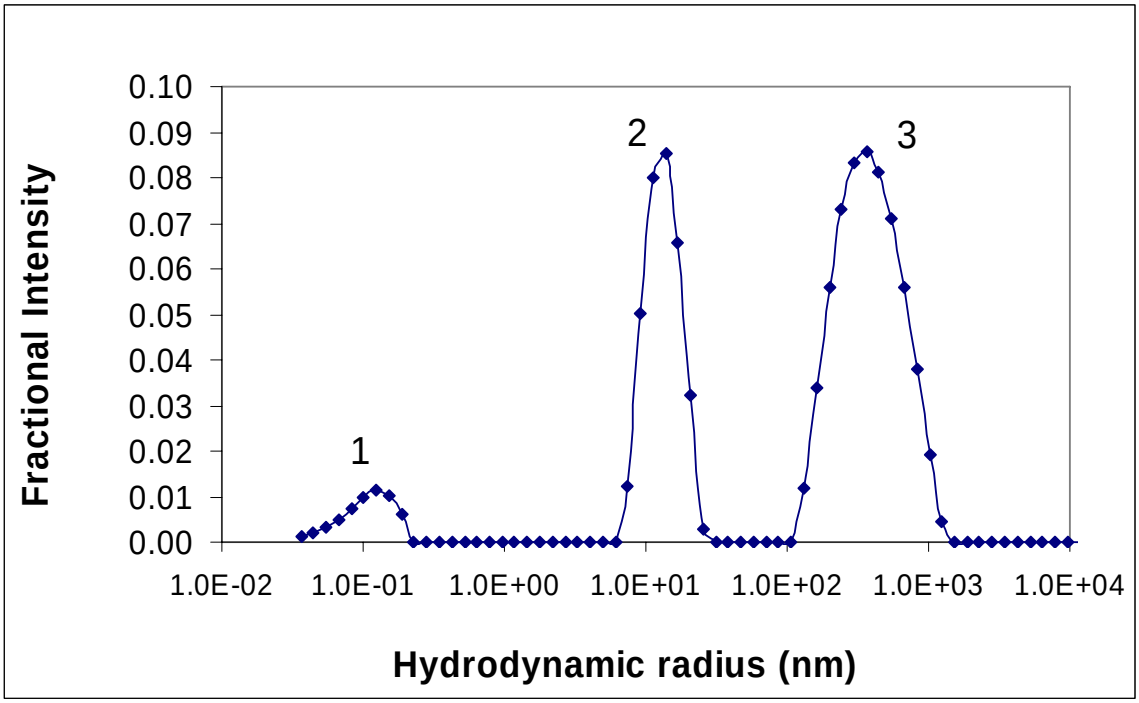

Figure 3.17 – DLS data for a 72 mg/ml solution of batch #C's **PNC3-OH** chains dissolved in chloroform

It was observed that the sonication treatments caused the scattering intensities of the solutions to decrease below the threshold of the DLS detector, and autocorrelation functions could not be reliably calculated. The significant decreases in the optical scattering intensity after the sonication treatment confirmed that the chains had indeed agglomerated in the concentrated solutions, since scattering intensities are proportional to particle size dimensions raised to the exponent 4.[97, 195-199] Qualitative analysis of the DLS results implied that the actual sizes of the freely-dispersed oligomers were below the detection limit for the DLS model that was used; the manufacturer of the DLS model

that was used confirmed that it does not reliably estimates particles below 10 nm in size. Since batch #C's **PNC3** chains were the largest of the synthesized oligomers (see Table 3.4), the other synthesized chains would produce even lower optical scattering intensities and no further DLS experiments were attempted. As an alternative to DLS, GPC experiments were used to estimate the hydrodynamic sizes of the PNC chains, as described below.

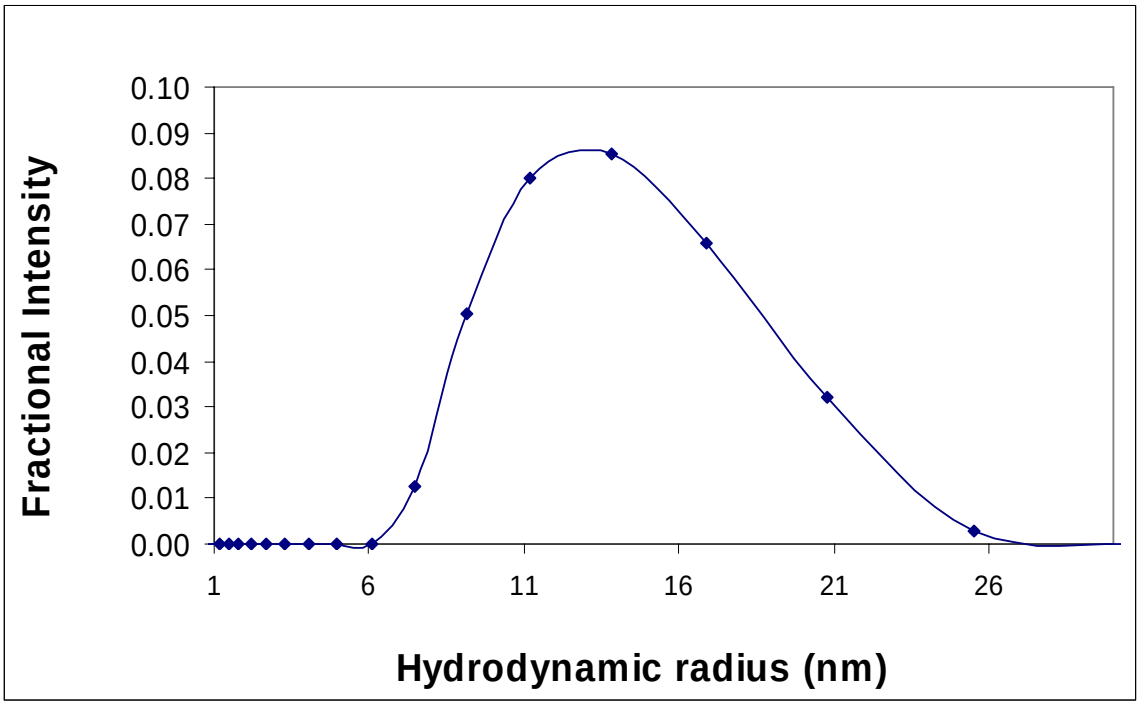

Figure 3.18 –Selected DLS data for batch #C's **PNC3-OH** chains showing only particles with $R_{H,D}$ in the range 1.0 to 30 nm (same as peak 2 in Figure 3.17 on a linear scale)

The Mark-Houwink-Sakurada (MHS) relationship, shown in equation (3.9), relates the intrinsic viscosity, [η], of polymer chains (of sufficiently long chain size) to their molecular weight via a power-law relationship.[185, 189, 193] By assuming that the polymer chains act as hard non-draining spheres, their molar hydrodynamic volume,

$V_{H,m}$, can be found by multiplying the intrinsic viscosity with the molecular weight. Hence, multiplying both sides of equation (3.9) produces the expression shown in equation (3.10). [174, 193]

$$[\eta] = KM^{a} \tag{3.9}$$

$$V_{H,m} = KM^{(1+a)} \tag{3.10}$$

The hydrodynamic volume of a single chain, $V_{h,}$, can be back-calculated from viscosity data by dividing $V_{H,m}$ by Avogadro's number, as shown in equation (3.11). [189] Since the relationship between the volume and radius of a hard sphere is well known, equation (3.12), the hydrodynamic radius of a single hard-spherical coil of the polymer chain (calculated from viscosity data), $R_{H,\eta}$, can be back-calculated from the MHS relationship. By equating the right hand sides of equations (3.11) and (3.12), and rearranging the expression to explicitly solve for $R_{H,\eta}$, equation (3.13) is produced.

$$V_H = \frac{[\eta]M}{2.5N_A} = \frac{KM^{(1+a)}}{2.5N_A} \tag{3.11}$$

$$V_H = (4/3)\pi\left(R_{H,\eta}\right)^3 \tag{3.12}$$

$$R_{H,\eta} = \left[\frac{3KM^{(1+a)}}{10\pi N_A}\right]^{1/3} \tag{3.13}$$

GPC can be used to obtain both V_H and $R_{H,\eta}$, via the use of universal calibration curves.[174, 186, 189, 193] To produce a universal calibration plot, the times taken for a wide M_w range of polystyrene (PS) standards of narrow PDI to elute through a GPC system are first recorded. Equations (3.11) or (3.13) are then used in conjunction with

MHS constants reported in literature (for the type of PS chains and solvent system used) to determine the values of V_H and $R_{H,\eta}$ that correspond to each PS standard.[185, 188, 189, 192, 193] Finally, the logarithm of the V_H values ($Log(V_H)$) or the logarithm of the $R_{H,\eta}$ values ($Log(R_{H,\eta})$) are plotted against the elution times corresponding to their specific PS standards.[174, 189, 193] A third-order polynomial equation is used to fit the data points of the universal calibration plot, so that any elution time can be correlated to V_H and the $R_{H,\eta}$ of non-PS chains in the same solvent-system. The universal calibration is based on the assumption that different chemical species with identical hydrodynamic volumes will be eluted at similar rates. The values of the MHS constants reported in literature for atactic-PS chains in THF solvent are listed in Table 3.4 along with the applicable ranges of M_w that the reported constants are valid.

Although the MHS constants shown in Table 3.5 show good agreement for PS chains in THF for a wide range of M_w (2×10^4 to 4×10^7), these values are not valid for low-M_w oligomers ($M_w < 10{,}000$).[185, 193] The deviation of experimentally measured low-M_w PS properties from the MHS relationship is due to the dependence of long-range solvent-polymer interactions on the sizes of the polymer chains. The hydrodynamic radius, R_H, of a polymer chain is related to the hydrodynamic radius of the unperturbed chain, $R_{H,\theta}$, as shown in equation (3.14).

Table 3.5 – MHS constants of atactic-PS chains in THF obtained from literature sources

K (ml/g)	a	Valid for the following range of M_w (g/mol)	Reference #
0.01363	0.714	2×10^4 to 4×10^6	[185], [191]
0.01363	0.710	2×10^5 to 4×10^7	[189]
0.01314	0.714	2×10^4 to 4×10^7	[194]

$$R_H = \left(R_{H,\theta}\right)\alpha_H \tag{3.14}$$

The hydrodynamic radius expansion factor, α_H, is a measure of the long-range solvent-polymer interactions (eg. osmotic swelling), whereas the parameter $R_{H,\theta}$ is a measure of short-range interactions (eg. steric hindrance).[185, 186, 190, 193] For small M_w, the influence of long-range interactions on the overall morphology of chains decreases and eventually becomes negligible as the chain size decreases below a critical dimension ($M_w = M^*$). Thus, for small chains with $M_w < M^*$, $\alpha \rightarrow 1.0$ and $R_H \rightarrow R_{H,\theta}$ as $M_w \rightarrow 0$.[186, 190] The behavior of polymer chains in solution can be divided into three M_w regimes; the first regime corresponds to very small oligomeric chains ($M_w < 5{,}000$ for PS) in which the chains exist in an unperturbed state, which is independent of the solvent type, and governed by the power law relationship shown in equation (3.15).[185, 186]

$$[\eta]_\theta = K_\theta M^{1/2} \tag{3.15}$$

The second regime ($6{,}000 < M_w < 10{,}000$ for PS) is a transition region in which the solution-state behavior of polymer chains is between the theta and MHS states.[193] In the third regime, the polymer chains are large enough ($M_w >> 10{,}000$ for PS) for the MHS relationship to accurately describe their behavior. The published literature values for K_θ and corresponding theta temperatures for selected theta solvents are shown in Table 3.6. Although the values of the theta-state parameter for atactic-PS are known, intrinsic viscosity is highly dependent on temperature, hence, only the K_θ values that correspond to theta temperatures near 25^{o}C should be used to estimate the dimensions of the polymer chains at ambient temperature.[185] If we substitute $K = K_\theta = 0.08$ ml/g and $a = 0.5$ into equation (3.13), then equation (3.16) is produced. Equation (3.16) is valid for atactic-PS chains with very low-M_w near ambient conditions, and the dimensions of the unperturbed chains would be irrespective of the solvent type.

Table 3.6 – Theta-state parameters for atactic-PS chains for selected theta solvents

Theta solvent	Theta temperature (^{o}C)	K_{θ} (ml/g)	Reference #
Cyclohexane	34.5	0.0846	[185]
Dioctyl phthalate	22.0	0.080	[185]
Decalin (99% trans)	20.4	0.081	[185]

$$R_{H,\theta} = \sqrt{M}\left[\frac{3(0.080\ \text{ml/g})}{10\pi N_A}\right]^{1/3} \tag{3.16}$$

Table 3.7 shows the M_w and corresponding elution times for the atactic-PS standards used to calibrate the GPC unit in THF eluent. By substituting the MHS values listed in Table 3.5 into equation (3.13), three different sets of $R_{H,\eta}$ were calculated for each of the PS standards. Equation (3.16) was used to calculate the theta-state hydrodynamic radii for the PS standards to obtain accurate chain dimension in the low-M_w regime, and all the calculated values for $R_{H,\eta}$ and $R_{H,\theta}$ are listed in Table 3.8.

Table 3.7 –Elution times for the atactic-PS standards used to calibrate the GPC in THF

Elution Time (min)	M_w (g/mol)	Log(M_w)
14.775	620,000	5.792
17.2	65,000	4.813
18.48	30,300	4.481
18.572	28,500	4.455
20.017	13,200	4.121
24.45	1,360	3.134
24.633	1,260	3.100

The three sets of calculated $R_{H,\eta}$ values were in good agreement over the entire range of M_w used to calibrate the GPC unit. Additionally, the $R_{H,\eta}$ were only slightly larger than $R_{H,\theta}$ in the oligomeric regime (highlighted rows of Table 3.8). The close agreement of the results was encouraging given that the $R_{H,\eta}$ and $R_{H,\theta}$ values were calculated using data derived from independent research groups.[185, 189, 191, 194]

Table 3.8 – $R_{H,\eta}$ and $R_{H,\theta}$ values for PS standards calculated from literature data

M_w (g/mol)	$R_{H,\eta}$ in nm (derived from ref. [185], [191])	$R_{H,\eta}$ in nm (derived from ref. [189])	$R_{H,\eta}$ in nm (derived from ref. [194])	$R_{H,\theta}$ in nm (derived from ref. [185])
620,000	26.08	25.62	25.76	18.17
65,000	7.19	7.08	7.10	5.88
30,300	4.65	4.58	4.59	4.02
28,500	4.49	4.43	4.43	3.90
13,200	2.89	2.86	2.86	2.65
1,360	0.79	0.78	0.78	0.85
1,260	0.76	0.75	0.75	0.82

Since the diffusivity of polymer chains is highly dependent on their molecular weight, the experimental $R_{H,D}$ data are typically expressed as empirical power law relationships of M_w such as the expressions shown in equations (3.17). Table 3.9 shows tabulated values for the empirical $R_{H,D}$ relationships derived from experimental literature data of atactic-PS of narrow PDI in THF.

$$R_{H,D} = xM^{y} \tag{3.17}$$

The $R_{H,D}$ empirical constants of PS in THF were substituted into Equation (3.17) to calculate the $R_{H,D}$ values for the PS standards listed in Table 3.7. These values, listed in Table 3.10 were also in close agreement with the viscosity-derived hydrodynamic

radii. Hence, we could be confident of the hydrodynamic data used to plot the universal calibration curve for the GPC experiments in THF. For each of the PS standards with M_w >10,000 shown in Tables 3.6 and 3.7, the average of the $R_{H,\eta}$ and $R_{H,D}$ values was taken to be the actual hydrodynamic radius for that specific chain. For the two oligomeric PS standards (highlighted) in Tables 3.6, the $R_{H,\theta}$ values was taken to be the hydrodynamic radius at each M_w. Table 3.7 was then used to correlate the hydrodynamic radii to the elution time, to generate a universal calibration curve for GPC in THF, as shown in Figure 3.19.

Table 3.9 –Tabulated values for empirical $R_{H,D}$ equation derived from literature sources

x (nm)	y	Valid for the following range of M_w	Reference #
0.0137	0.564	2.0×10^4 to 1.8×10^6	[187]
0.0172	0.551	3.7×10^4 to 7.6×10^6	[189]

Table 3.10 – $R_{H,D}$ values for PS standards calculated from literature data

M_w (g/mol)	$R_{H,D}$ in nm (derived from ref. [187])	$R_{H,D}$ in nm (derived from ref. [189])
620,000	25.33	26.812
65,000	7.10	7.731
30,300	4.62	5.075
28,500	4.46	4.907
13,200	2.89	3.210
1,360	0.80	0.917
1,260	0.77	0.879

The plotted points in Figure 3.19 were fit using a three-order polynomial; the equation of the best-fit line was $\log(R_H \text{ in nm}) = -0.0014*(\text{elution time in min})^3 + 0.0877*(\text{elution time in min})^2 - 1.9701*(\text{elution time in min}) + 15.82$. For any PNC oligomers that had M_n values lower than 1,260 g/mol (ie. longer elution times than

smallest PS standard), the best-fit line of Figure 3.19 was extrapolated to the appropriate elution time to provide a rough estimate of the hydrodynamic radius of the chains. In addition to producing small pores, an ideal sacrificial polymer should have a narrow distribution of chain lengths so that after decomposition, the resultant pores will be of largely uniform dimensions throughout the film. To estimate the PDI of PNC chains, Table 3.7 was used to generate a relative calibration curve for GPC in THF, as shown in Figure 3.20. The data points in Figure 3.20 were also fit to a three-order polynomial; the equation of the best-fit line was $\log(M_w) = -0.0026*(\text{elution time in min})^3 + 0.1613*(\text{elution time in min})^2 - 3.5922*(\text{elution time in min}) + 31.892$. It is important to note that all the M_n, M_w, and PDI values calculated from GPC data were not absolute values, but only relative estimates of chain sizes and polydispersity.

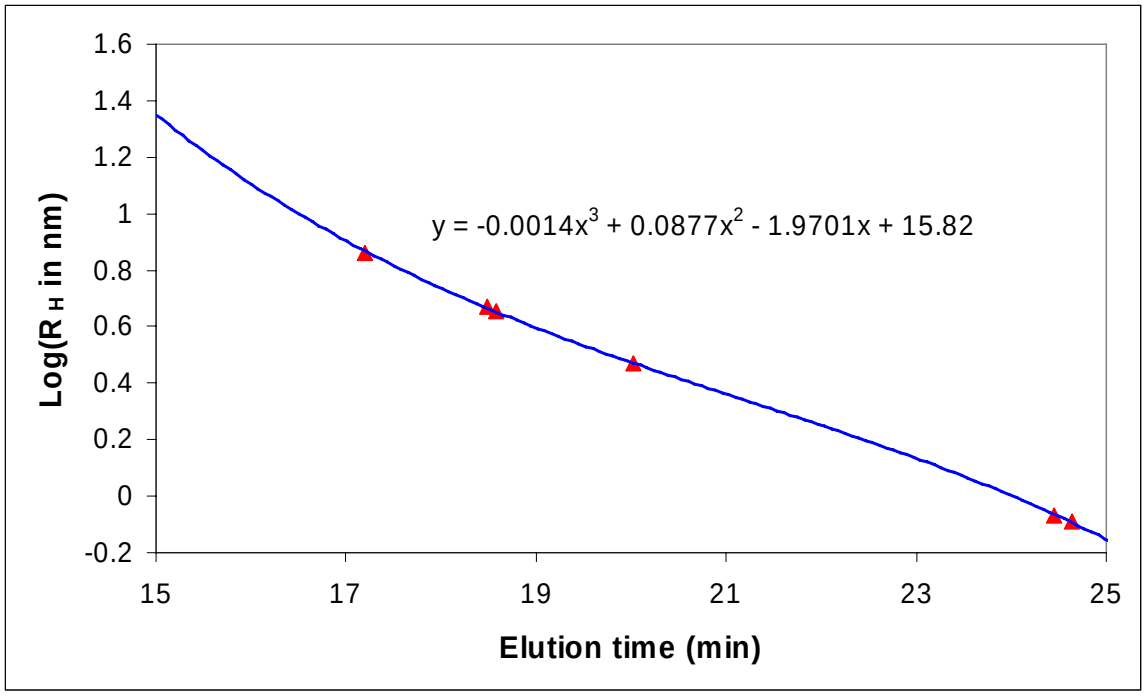

Figure 3.19– Universal calibration plot for GPC in THF

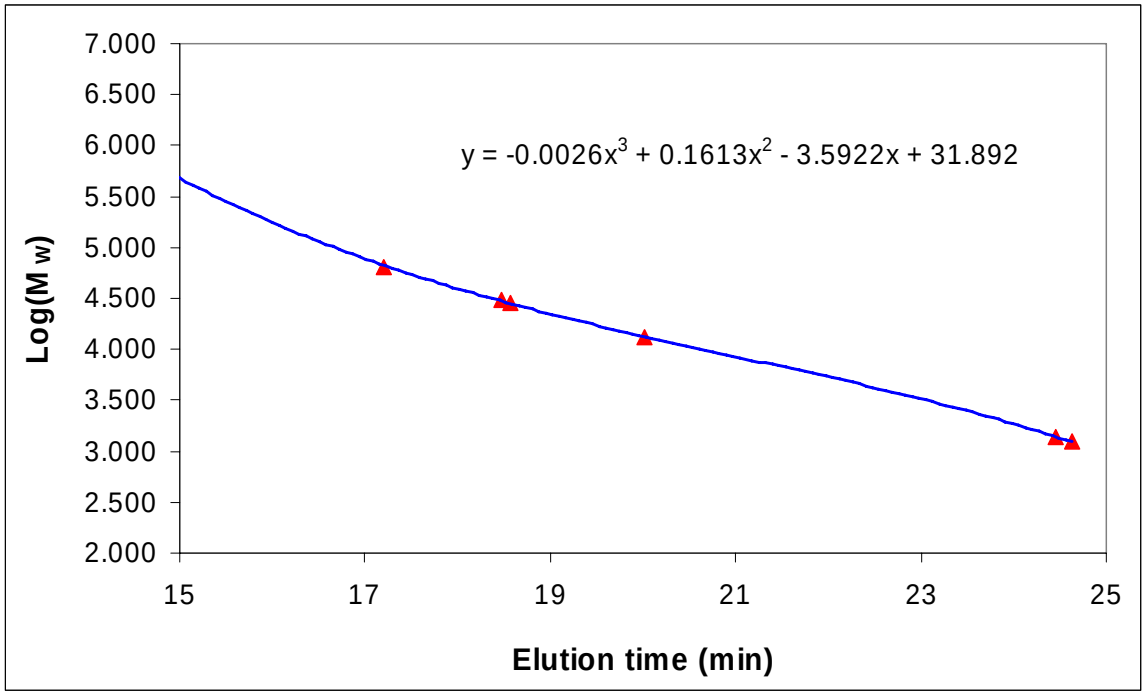

Figure 3.20 – Relative calibration curve for GPC in THF

PNC1-OH chains were analyzed by GPC using THF as the eluent, and found to have bimodal size distributions, as shown in Figure 3.21 and Figure 3.22. The bimodal size distributions of **PNC1-OH** oligomers were due to the formation of two condensation products; namely, cyclic carbonate **13** and very short linear **PNC1-OH** chains (represented by the GPC peaks labeled with the numerals 2 and 1, respectively in both Figure 3.21 and Figure 3.22). As mentioned earlier, the by-product **13** was formed as a result of the cyclization of the diol **6** during the reaction between diol **6** and CDI, and was the cause of the poor yields of recovery for polycondendesed-**PNC1** oligomers. Since all of the peaks in Figure 3.21 and Figure 3.22 corresponded to elution times beyond that of the smallest PS standard (M_w = 1206 g/mol), the best-fit equations shown in the calibration plots (Figure 3.19and Figure 3.20) were extrapolated to provide a rough

estimate of the R_H values for each oligomeric chain. The estimated hydrodynamic radii of **PNC1-OH** chains are shown in Figure 3.23 and Figure 3.24.

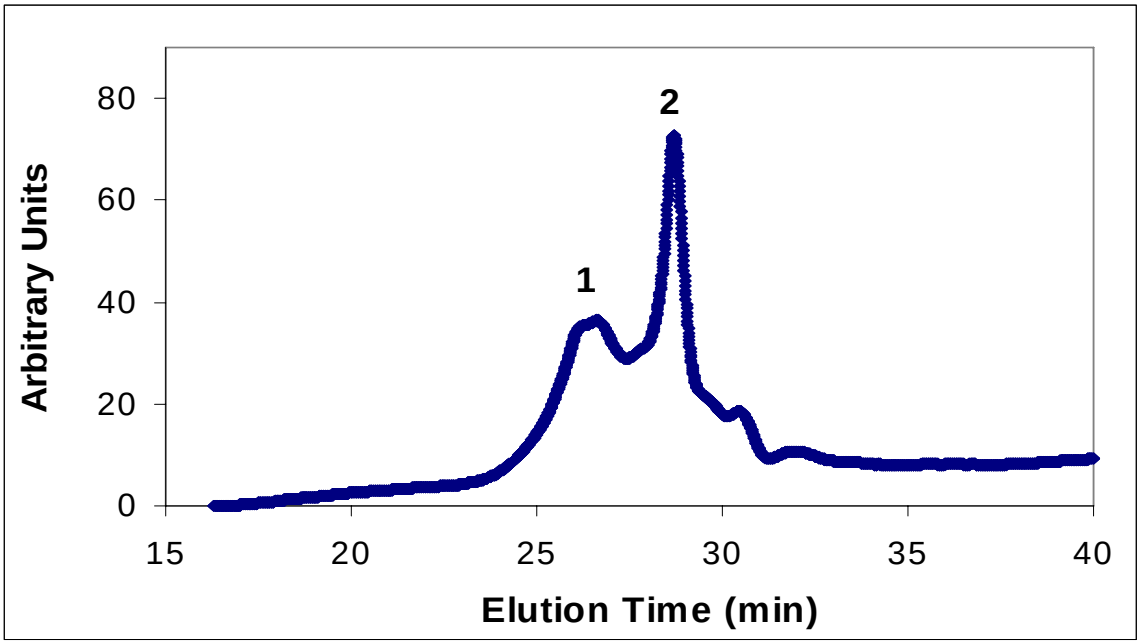

Figure 3.21 – GPC trace (in THF) of batch #A of **PNC1-OH** chains

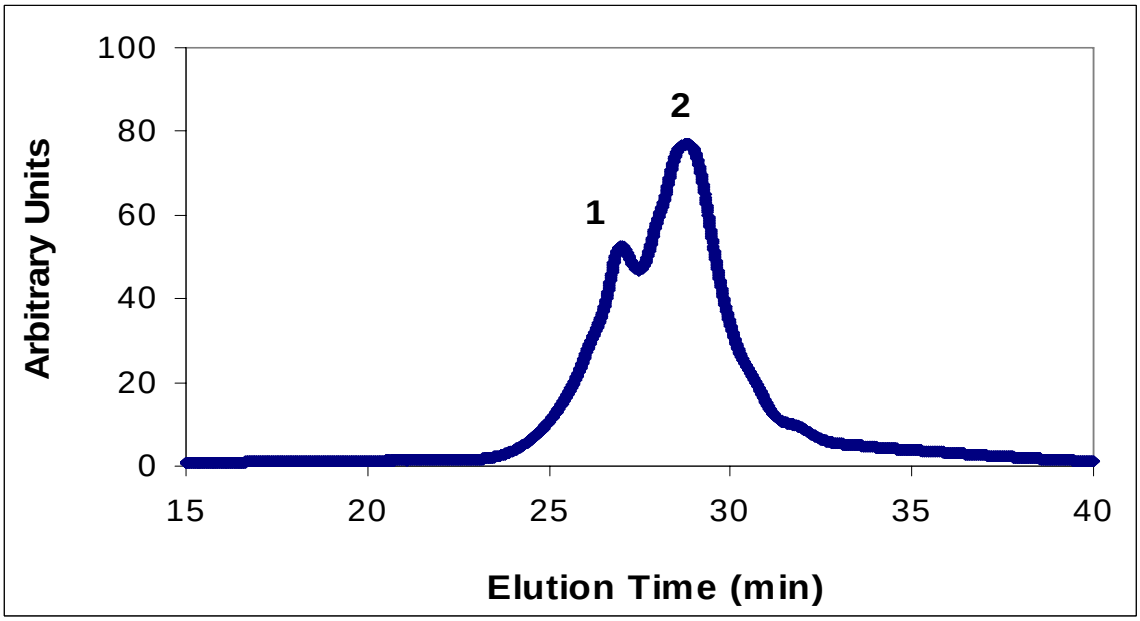

Figure 3.22 – GPC trace (in THF) of batch #B of **PNC1-OH** chains

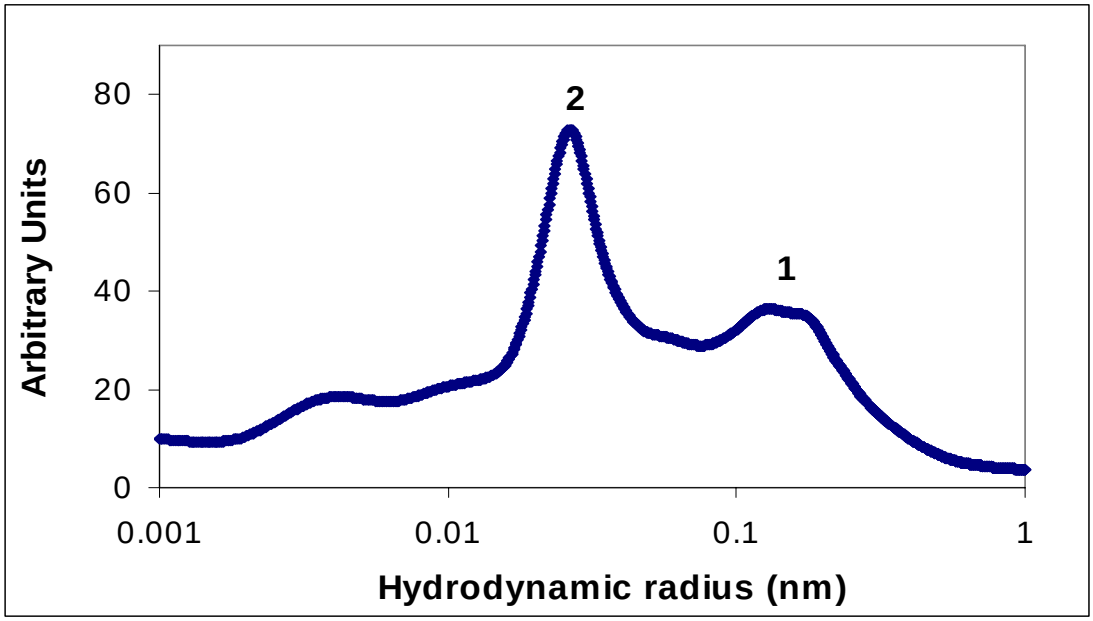

Figure 3.23 – Plot showing the R_H (nm) of batch #A's **PNC1-OH** chains estimated using the universal calibration curve for GPC in THF

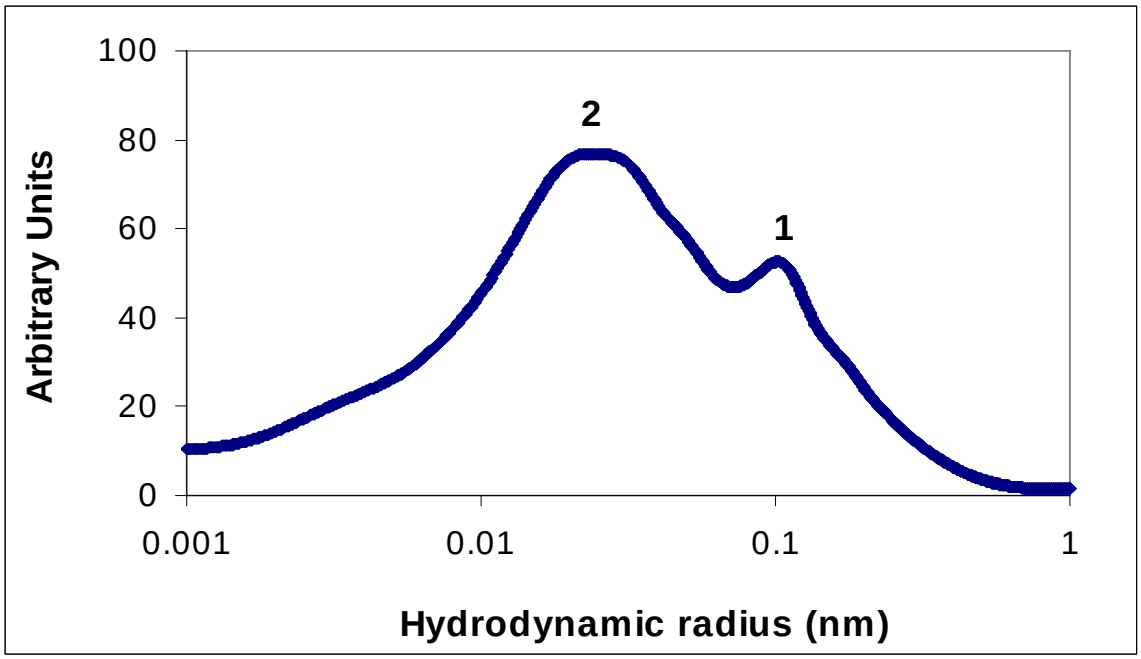

Figure 3.24 – Plot showing the R_H (nm) of batch #B's **PNC1-OH** chains estimated using the universal calibration curve for GPC in THF

From Figure 3.23 and Figure 3.24 it can be seen that the majority of **PNC1-OH** chains had R_H values in THF in the range 0.12-0.17 nm for batch #A, and about 0.10 nm for batch #B, respectively. These R_H values were unreliably low since the length of a single **PNC1** repeat unit is about 0.5 nm (refer to Table 3.4) - the R_H of oligomeric chains in a good solvent should be at least as large as their $\langle r^2 \rangle^{1/2}$ value, if not larger. This discrepancy is due to differences in the rates of elution of PS and PNC chains of similar hydrodynamic radii. It is apparent that in THF solvent, PNC chains are eluted more slowly than PS chains since the PS standard with R_H = 0.85 nm (refer to Table 3.7) took only 24.45 minutes to be eluted through the GPC column, whereas the **PNC1-OH** chains took over 25 minutes to be eluted although their actual R_H was at least 1.5 nm (refer to Table 3.4). Hence, the R_H values for **PNC1-OH** chains were consistently underestimated by the GPC universal calibration curves.

The differences in rates of elution for PS and **PNC1** chains of similar hydrodynamic radii may be partly due to differences in the intrinsic viscosities of PS and **PNC1** chains. Since the MHS parameter values for **PNC1** are not known, the R_H of their chains cannot be accurately determined from GPC data. Since both DLS and GPC could not provide accurate experimental estimations of R_H for **PNC1-OH** chains, the $\langle r^2 \rangle^{1/2}$ values shown in Table 3.4 were assumed to be reasonable estimates of the actual dimensions of **PNC1-OH** chains free of agglomeration. Hence the pores produced from these chains should ideally be about 1.5 nm in size in a templated film when phase-segregation is avoided prior to polymer decomposition.

The best-fit line of the relative GPC calibration plot (Figure 3.20) was used to estimate the relative values of M_n and M_w (and hence the PDI) for the **PNC1-OH**

oligomers. The M_n, M_w, and PDI for batch #A of **PNC1-OH** were estimated to be 1440 g/mol, 1460 g/mol, and 1.01, respectively.[1] The M_n, M_w, and PDI for batch #B of **PNC1-OH** were estimated to be 1500 g/mol, 1540 g/mol, and 1.02, respectively. Although the values obtained from GPC analysis were not absolute, they did provide a reasonable estimate of the M_n calculated from end-group analyses, and the PDI values obtained from GPC data should be fairly accurate since they are only ratios of the relative values of M_w and M_n.

The GPC analyses of **PNC1-ROP** chains were performed by Promerus LLC using PS standards in THF, and found to have unimodal size distributions with M_n, M_w, and PDI values of 13900 g/mol, 21400 g/mol, and 1.55, respectively. Owing to the differences in elution rates of **PNC1** chains and PS standards, no attempt was made to estimate the R_H of **PNC1-ROP** chains using GPC data. Based on the relative molecular weights estimated by GPC data, the M_n of **PNC1-OH** oligomers were about $1/10^{th}$ the weight of **PNC1-ROP** chains. If we ignore the excluded-volume effects and substitute the M_n values from Table 3.4 and the relative M_n ratio of the **PNC1-ROP** and **PNC1-OH** chains into equation (3.7), then the chains received from Promerus LLC had an estimated $\langle r^2 \rangle^{1/2}$ value of 4.74 nm. Hence, both types of **PNC1** chains would produce fairly small pore sizes in templated films (assuming that phase-segregation could be avoided), but the bimodal size distributions of the **PNC1-OH** chains would be undesirable since they would produce pores with a broad size distribution in templated films.

---

[1] Only the GPC peaks that were labeled 1 in Figures 3.16 through Figure 3.24 were included in the calculations of Mn, Mw, and PDI, because the molecules represented by the GPC peaks labeled with numeral 2 were cylclic monomers.

In addition to producing **PNC1-OH** oligomers with a bimodal size distribution, polycondensation produced linear **PNC1** oligomers in very low yields (never higher than 9%). Thus, polycondensation was deemed to be an impractical synthesis route for obtaining graftable **PNC1** oligomers in amounts that were useful in producing nanocomposite molecules. Thus, neither the **PNC1-ROP** chains received from Promerus LLC (unreactive end-groups) nor those synthesized in the laboratory via polycondensation (poor yield) were applicable in the synthesis of nanocomposites for use in templated films. However, the large quantity of **PNC1-ROP** produced by Promerus LLC afforded its use as a photodefinable sacrificial material for performing proof-of-concept experiments for the direct-write processing of templated porous films.[1, 2]

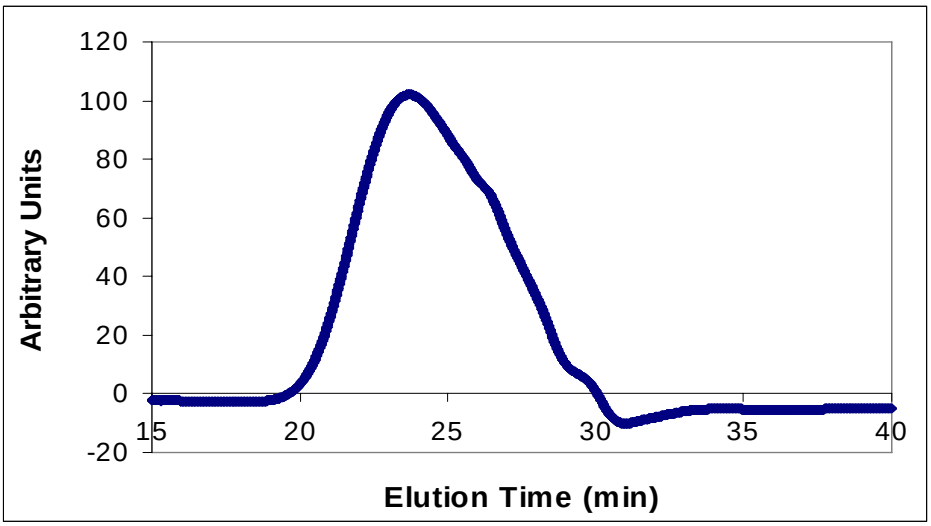

Figure 3.25 – GPC trace (THF as eluent) of batch #A of **PNC2-OH** chains

In contrast to the bimodal distributions of linear, **PNC1-OH** oligomers, **PNC2-OH** chains had unimodal size distributions, as shown in Figure 3.25 and Figure 3.26. Since portions of the peaks in both Figure 3.25 and Figure 3.26 corresponded to

corresponded to elution times beyond that of the smallest PS standard (M_w = 1206 g/mol), the best-fit equations shown in the calibration plots (Figure 3.19 and Figure 3.20) were extrapolated to provide a rough estimate of the R_H values for each oligomeric chain.

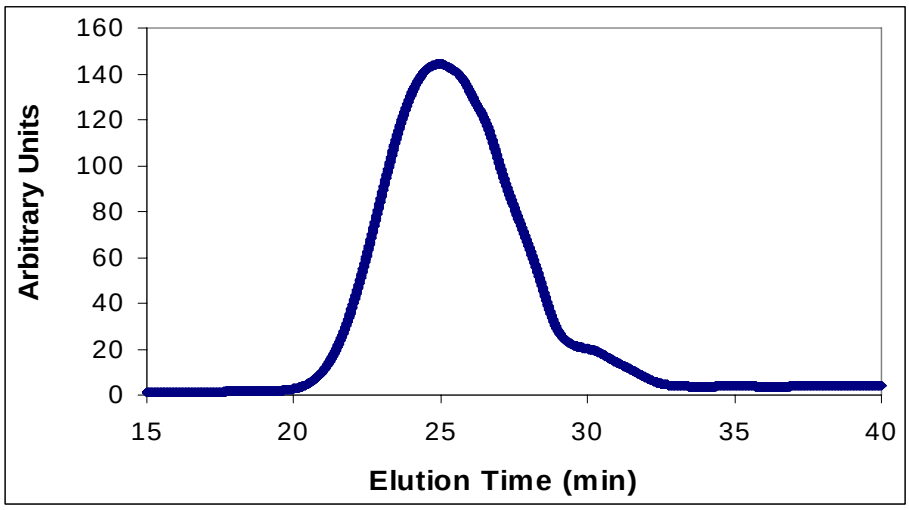

Figure 3.26 – GPC trace (THF as eluent) of batch #B of **PNC2-OH** chains

From Figure 3.27 and Figure 3.28, we observe that the majority of **PNC2-OH** chains had R_H values (in THF solvent) lying within the range 0.10-1.2 nm for batch #A, and 0.05-0.85 nm for batch #B, respectively. These R_H values were unreliably low since the length of a single **PNC2** repeat unit is about 0.4 nm (refer to Table 3.4) - the R_H of oligomeric chains in a good solvent should be at least as large as their $\langle r^2 \rangle^{1/2}$ value, if not larger. As described earlier, this discrepancy was caused by differences in the rates of elution of PS and PNC chains of similar hydrodynamic radii. It is apparent that in THF solvent, **PNC2** chains are eluted more slowly than PS chains since the PS standard with R_H = 0.85 nm (refer to Table 3.7) took only 24.45 minutes to be eluted through the GPC

column, whereas the **PNC2-OH** chains took over 25 minutes to be eluted although their actual R_H was at least 1.16 nm (refer to Table 3.4).

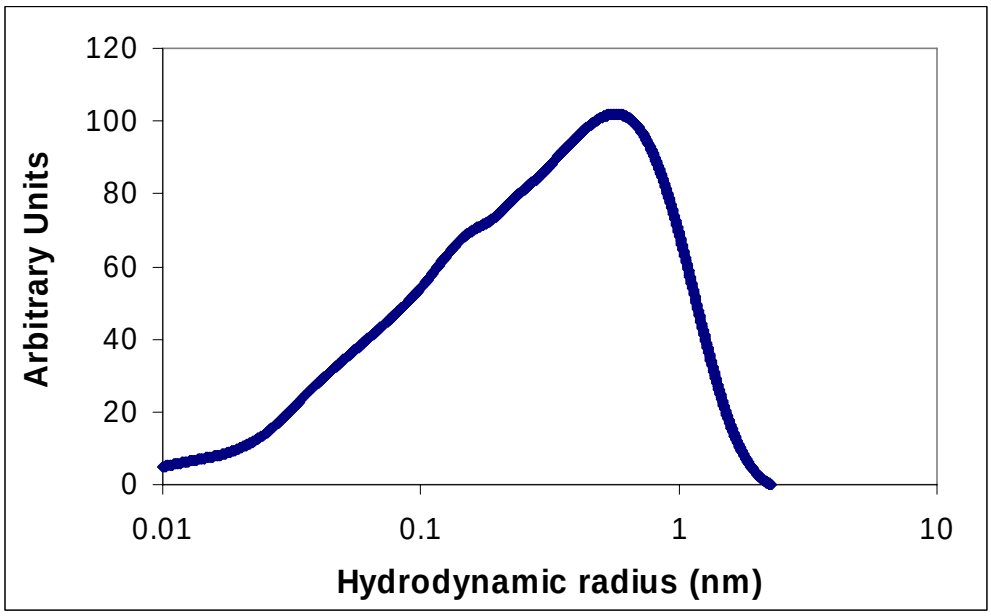

Figure 3.27 – Plot showing the R_H (nm) of batch #A's **PNC2-OH** chains estimated using the universal calibration curve for GPC in THF

Hence, the R_H values for **PNC2** chains were consistently underestimated by the GPC universal calibration curves. The differences in rates of elution for PS and **PNC2** chains of similar hydrodynamic radii may be partly due to differences in the intrinsic viscosities of PS and **PNC2** chains. Since the MHS parameter values for **PNC2** are not known, the R_H of their chains cannot be accurately determined from GPC data. Since both DLS and GPC could not provide accurate experimental estimations of R_H for **PNC2** chains, the $\langle r^2 \rangle^{1/2}$ values shown in Table 3.4 were assumed to be reasonable estimates of the actual dimensions of **PNC2** chains free of agglomeration. Hence the pores produced

from these chains should ideally be about 1.2-1.3 nm in size in a templated film when phase-segregation is avoided prior to polymer decomposition.

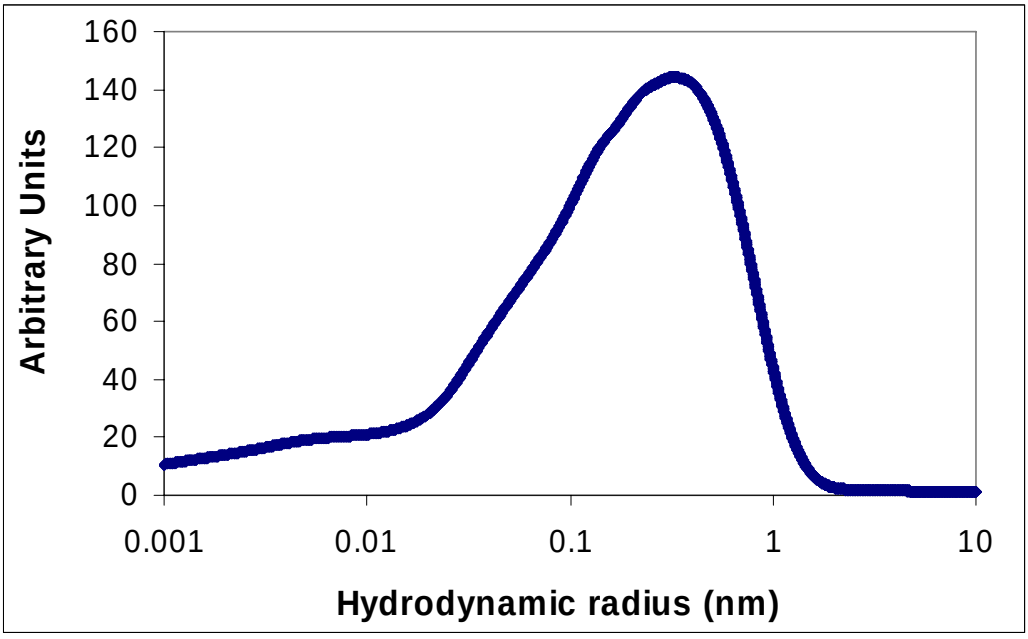

Figure 3.28 – Plot showing the R_H (nm) of batch #B's **PNC2-OH** chains estimated using the universal calibration curve for GPC in THF

The best-fit line for the relative GPC calibration plot shown in Figure 3.20 was used to estimate the relative values of M_n and M_w (and hence PDI) for **PNC2-OH**. The M_n, M_w, and PDI values for batch #A of **PNC2-OH** oligomers were estimated to be 2540 g/mol, 3450 g/mol, and 1.36, respectively. The M_n, M_w, and PDI values of batch #B for **PNC2-OH** oligomers were estimated to be 2130 g/mol, 2620 g/mol, and 1.23, respectively. Hence, the **PNC2** chains were small and of narrow size distribution, which was an encouraging since pores produced from the decomposition of its chains possess ideal properties for porous films if phase-segregation could be avoided.[3]

Due to poor solubility in both THF and toluene solvents, **PNC3** chains were analyzed by GPC using chloroform as the eluent. In comparison to THF and toluene solvent-systems, the literature data for PS in chloroform solvent is sparse - with only two sets of MHS constants reported in chloroform.[185] The values of the MHS parameter for atactic-PS chains in chloroform solvent are listed in Table 3.11 along with the applicable ranges of M_w that the reported constants are valid. Table 3.12 shows the M_w and corresponding elution times for the atactic-PS standards used to calibrate the GPC unit that used chloroform as its eluent.

Table 3.11 – MHS constants of atactic-PS chains in chloroform obtained from literature

K (ml/g)	a	Valid for the following range of M_w (g/mol)	Reference #
7.16	0.76	1.2×10^5 to 2.8×10^6	[185]
11.2	0.73	7.0×10^4 to 1.5×10^6	[185]

Table 3.12 –Elution times for the atactic-PS standards used to calibrate the GPC in THF

Elution Time (min)	M_w (g/mol)	Log(M_w)
25.092	3900000	6.591
26.05	1980000	6.297
26.091	996000	5.998
26.567	629000	5.799
27.86	210000	5.322
29.06	70600	4.849
30.113	28600	4.456
31.761	10900	4.037
34.523	3000	3.477
36.01	1300	3.114

The $R_{H,\eta}$ values for each of the PS standards in chloroform were calculated by substituting MHS values from Table 3.11 into equation (3.13), as described previously.

Since the unperturbed-state (theta-state) of a polymer chain is irrespective of solvent type, equation (3.16) was used to obtain the chain dimensions of the PS standards listed in Table 3.12 in the low-M_w regime (highlighted rows). For comparison purposes, all the calculated values for the $R_{H,\eta}$ and $R_{H,\theta}$ of PS standards in chloroform are listed together in Table 3.13.

Table 3.13 – $R_{H,\eta}$ and $R_{H,\theta}$ values for PS standards in chloroform

M_w (g/mol)	First set of $R_{H,\eta}$ values (nm) (derived from Ref. [185])	Second set of $R_{H,\eta}$ values (nm) (derived from Ref. [185])	Average of $R_{H,\eta}$ (nm)	$R_{H,\theta}$ (nm) (derived from Ref. [185])
3,900,000	75.74	65.24	70.49	45.56
1,980,000	51.23	44.13	47.68	32.47
996,000	34.47	29.70	32.08	23.03
629,000	26.45	22.78	24.61	18.30
210,000	14.05	12.10	13.07	10.57
70,600	7.49	6.45	6.97	6.13
28,600	4.45	3.83	4.14	3.90
10,900	2.55	2.20	2.37	2.41
3,000	1.21	1.04	1.13	1.26
1,300	0.75	0.64	0.70	0.83

Due to the discrepancy in the reported values of the MHS constants for PS in chloroform (refer to Table 3.11), the calculated $R_{H,\eta}$ values shown in Table 3.13 did not agree as well as those for PS in THF.[185] Additionally, a literature review did not yield any experimental data for predicting $R_{H,D}$ values of PS chains in chloroform; hence, there was not enough literature data to conclusively determine which of the two sets of $R_{H,\eta}$ values in Table 3.13 was more accurate. Fortunately, the deviation between the $R_{H,\eta}$ values in Table 3.13 decreased as the M_w of the PS standards decreased, until it was

about 2 nm for M_w = 210,000 g/mol and below 1 nm for M_w < 30,000 g/mol. Thus, only the averages of the $R_{H,\eta}$ values corresponding to M_w equal to or below 210,000 g/mol were used to generate the universal calibration plot for GPC in chloroform. As stated earlier, $R_{H,\theta}$ values provided the most accurate estimate of the true hydrodynamic radii in the oligomeric regime (highlighted); hence, these values were taken to be the actual hydrodynamic dimensions for the PS standards with M_w = 1,300 g/mol and M_w = 3,000 g/mol.

A universal calibration curve for the PS standards in chloroform (Figure 3.29) was generated by the previously described procedure. The plotted points in Figure 3.29 were fit using a three-order polynomial; the equation of the best-fit line was log(R_H in nm) =-0.0005*(elution time in min)^3 + 0.0566*(elution time in min)^2 – 2.2353*(elution time in min) + 30.141. For any PNC oligomers that had longer elution times than smallest PS standard, the best-fit line was extrapolated to the appropriate elution time to provide a rough estimate of the hydrodynamic radius of the chains. To estimate the M_n, M_w, and PDI of **PNC3** chains, Table 3.12 was used to generate a relative calibration curve for GPC in chloroform, as shown in Figure 3.30. The data points in Figure 3.30 were also fit to a three-order polynomial; the equation of the best-fit line was log(M_w) = -0.0011*(elution time in min)^3 + 0.1175*(elution time in min)^2 – 4.4028*(elution time in min) + 60.412. It is important to note that all the M_n, M_w, and PDI values calculated from GPC data were not absolute values, but only relative estimates of chain sizes and polydispersity.

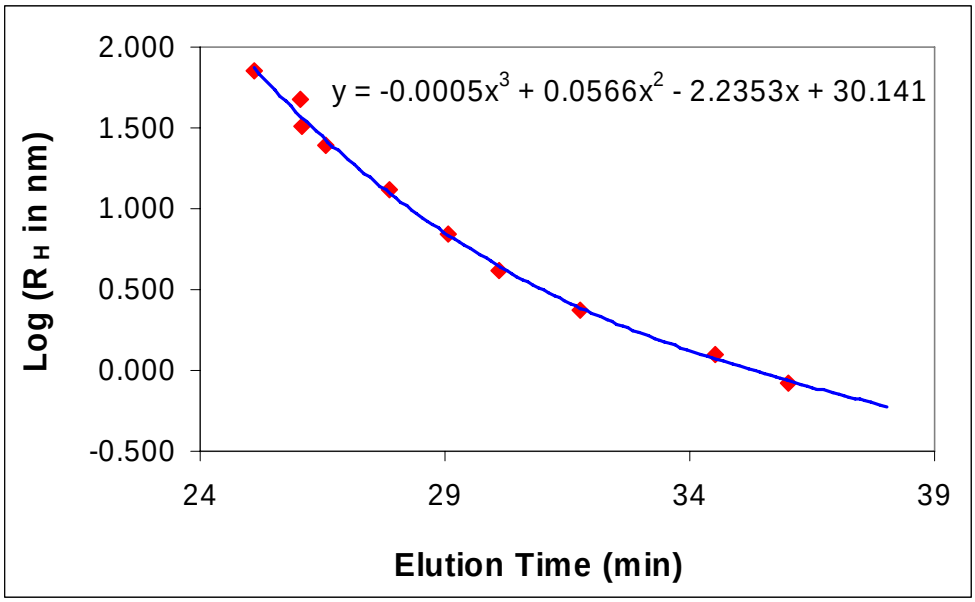

Figure 3.29 – Universal calibration plot for GPC in chloroform

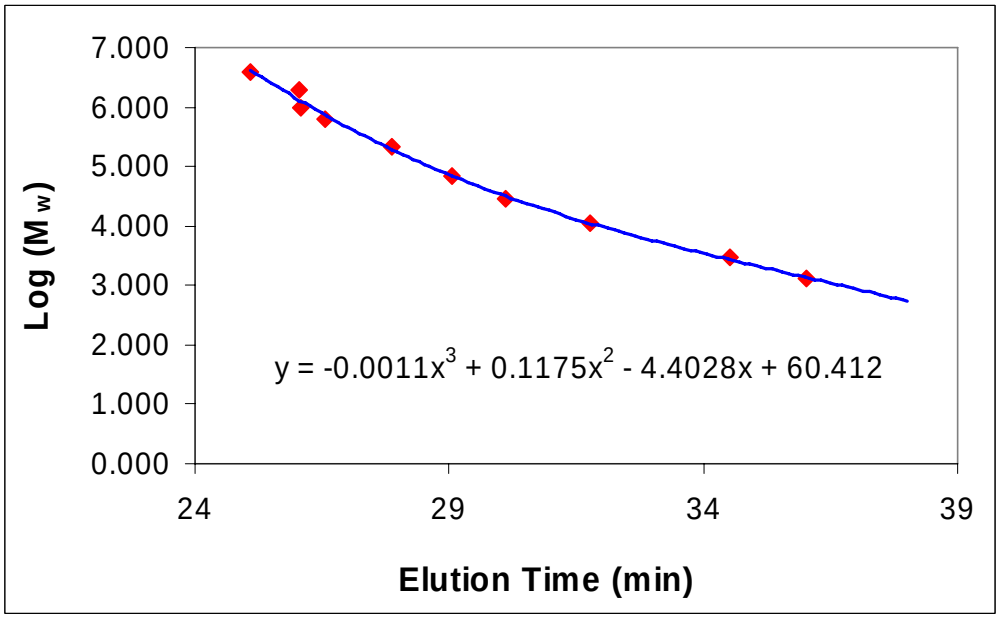

Figure 3.30 - Relative calibration curve for GPC in chloroform

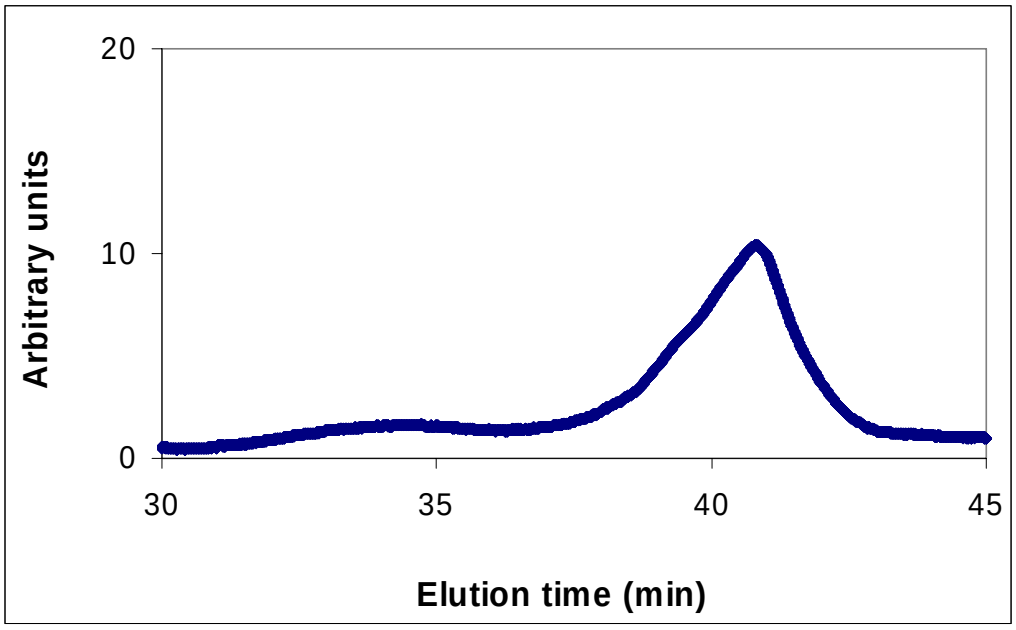

Figure 3.31 – GPC trace (in chloroform) of batch #B's **PNC3-OH** chains

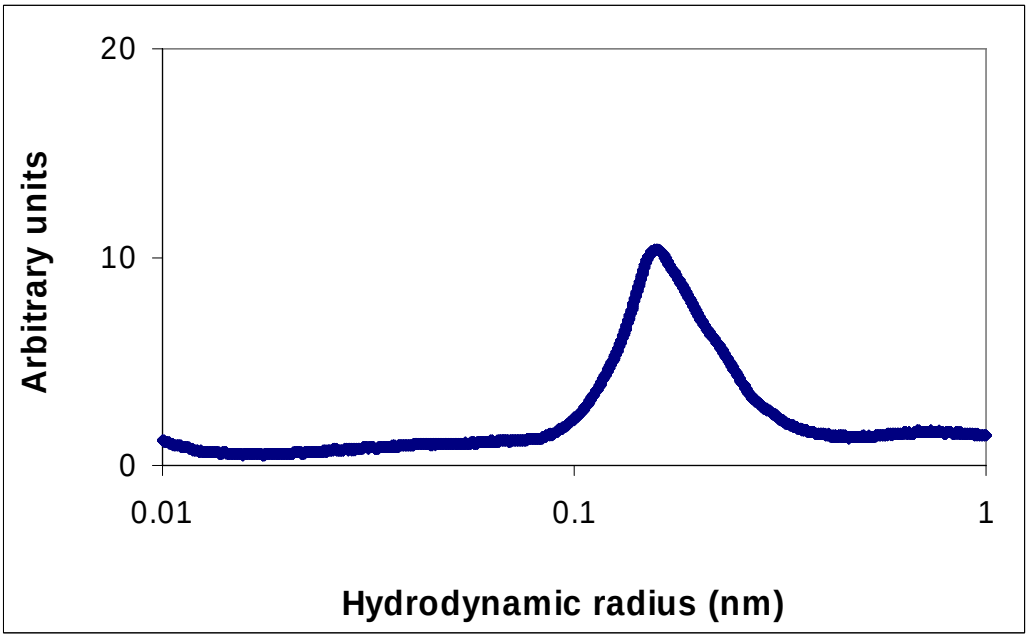

Figure 3.32 - Plot showing the R_H (nm) of batch #B's **PNC3-OH** chains estimated using the universal calibration curve for GPC in chloroform

Batch #A's **PNC3** chains were observed to have multimodal size distributions, and they were not analyzed any further due to their undesirable PDI. The other batches (#B and #C) of **PNC3** had unimodal size distributions, as shown in Figure 3.31. Using the equation of the best-fit line shown in Figure 3.29, the majority of **PNC3** chains were estimated to have R_H values in the range of about 0.11-0.35 nm for batch #B and 0.19-0.31 nm for batch #C, respectively. These R_H values were unreliably low since the length of a single **PNC3** repeat unit is about 0.4 nm (refer to Table 3.4) - the R_H of oligomeric chains in a good solvent should be at least as large as its $\langle r^2 \rangle^{1/2}$ value, if not larger. As described for previous results, this discrepancy was caused by differences in the rates of elution of PS and **PNC3** chains of similar hydrodynamic radii. It is apparent that in chloroform solvent, **PNC3** chains are eluted more slowly than PS chains since the PS standard with R_H = 1.26 nm (refer to Table 3.7) took only 34.52 minutes to be eluted through the GPC column, whereas the **PNC3-OH** chains took over 36 minutes to be eluted although their actual R_H was at least 1.7 nm (refer to Table 3.4). Hence, the R_H values for **PNC3** chains were consistently underestimated by the GPC universal calibration curves.

The differences in rates of elution for similar hydrodynamic radii may be partly due to differences in the intrinsic viscosities of PS and **PNC3** chains. Since the MHS parameter values for **PNC3** are not known, the R_H of their chains cannot be accurately determined from GPC data. Since both DLS and GPC could not provide accurate experimental estimations of R_H for **PNC3** chains, the $\langle r^2 \rangle^{1/2}$ values shown in Table 3.4 were assumed to be reasonable estimates of the actual dimensions of **PNC3** chains free of agglomeration. Hence the pores produced from these chains should ideally be about 1.4-

1.7 nm in size in a templated film when phase-segregation is avoided prior to polymer decomposition. The best-fit line for the relative GPC calibration plot shown in Figure 3.30 was used to estimate the relative values of M_n and M_w (and hence PDI) for **PNC3-OH**. The M_n, M_w, and PDI values for batch #B's of **PNC3-OH** oligomers were estimated to be 732 g/mol, 720 g/mol, and 1.02, respectively. The M_n, M_w, and PDI values of batch #C for **PNC3-OH** oligomers were estimated to be 118, 109, and 1.08, respectively. Hence, the **PNC2** chains were small and of narrow size distribution, which was an encouraging since pores produced from the decomposition of its chains possess ideal properties for porous films if phase-segregation could be avoided.

Based on both the $\langle r^2 \rangle^{1/2}$ values estimated by end-group analysis (refer to Table 3.4) and the PDI values estimated by GPC, the synthesized **PNC2** (both batches) chains and **PNC3** (only batches #B and #C) chains were deemed to have ideal properties for producing small pores of narrow size distributions in templated films. The remaining synthesis objective for these oligomers was to increase their phase-compatibility with HSQ by covalently bonding them to siloxane and silsesquioxane molecules, which would serve as compatibilizers for the PNC segments.

CHAPTER 4

THERMOLYTIC AND ACIDOLYTIC DECOMPOSITION OF PNC OLIGOMERS: MECHANISM AND KINETICS

4.1 Photoacid Generators (PAGs) Used

The term photoacid generator (PAG) refers to a photoinitiator that releases an acid due to radiation-induced cleavage reactions.[95-100, 102, 104, 203-222] The PAGs used in this study were Rhodorsil 2074, tris(tert-butyl phenyl)sulfonium triflate [TTBPS-Tf], and tris(tert-butyl phenyl)sulfonium nonaflate [TTBPS-Nf], with their respective structures (**5, 6,** and **7**), shown in Figure 4.1.

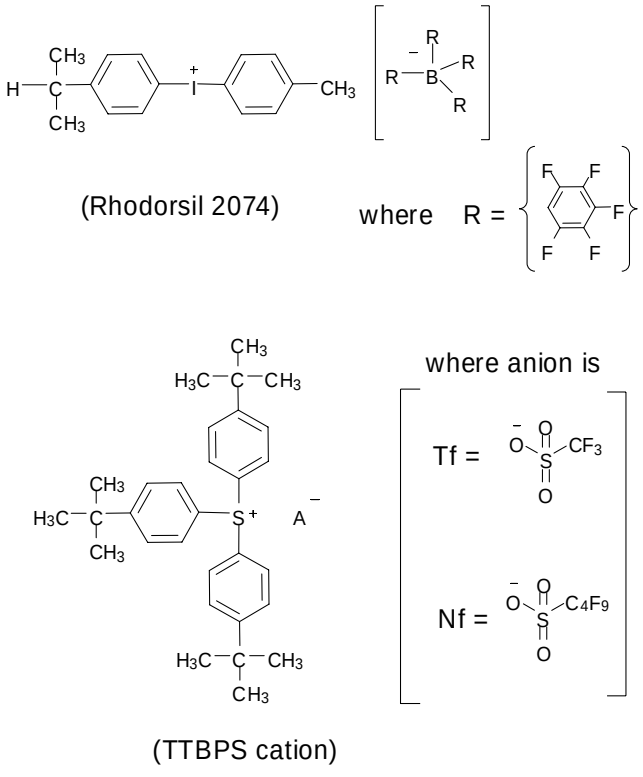

Figure 4.1 – Chemical structures of ionic PAGs

Rhodorsil 2074, TTBPS-Tf, and TTBPS-Nf were obtained from Rhodia, Sigma-Aldrich, and Midori-Kagaku, respectively. HPLC grade MIBK solvent was obtained from Sigma-Aldrich and used without further purification.

4.2 Thermolytic and Acidolytic Decomposition of Polycarbonates

When heated above their degradation temperature, aliphatic and aromatic polycarbonate chains undergo main chain scission reactions that release volatile decomposition products.[56, 79-81, 83-85, 87-89, 99] The presence of acids molecules has also been shown to catalyze the thermolysis of polycarbonate chains, leading to the development of polycarbonate/PAG photoresist systems.[82-85, 88, 89, 167] The wt% of residue after decomposition, the onset temperature for decomposition (T_d), and the values of the kinetic parameters are all dependent on the chemical structures of the polycarbonate chains.[82, 84, 85, 99] Aromatic polycarbonates have high thermally stabilities and tend to leave more post-decomposition residue than aliphatic polycarbonates. Poly(bisphenol-A-carbonate or PBAC does not begin to thermolyzes until at least 350^{o}C, but leaves a final residue of just over 20 wt%.[87] Depending on their specific chemical structure, aliphatic polycarbonates may have T_d values from under 200^{o}C to about 350^{o}C, and produce negligible amounts of residue.[1, 2, 89, 98, 99, 168, 169] This "clean" decomposition behavior makes aliphatic polycarbonate chains attractive materials for sacrificial systems.

Numerous researchers have successfully designed and synthesized aromatic-aliphatic polycarbonate structures with tunable properties, such as high T_g to minimize chain movement during thermal processing, targeted T_d values, high rates of

decomposition, and negligible residue.[56, 79-82, 84, 85, 88, 167] Due to the weight losses that accompany the decomposition of sacrificial polymers, TGA studies are widely used to investigate their thermal stabilities and decomposition kinetics.[98-100, 168, 169] Additionally, the analysis of the gaseous decomposition products using mass-spectrometry has allowed researchers to investigate the mechanisms by which the polycarbonates are decomposed.[81, 88, 89, 167]

4.3 Thermal Stabilities and Thermolytic Decomposition Kinetics

As stated earlier, both the onset of decomposition and the kinetic parameters for the decomposition reaction are dependent on the specific chemical structure of the polycarbonate being analyzed. Within each category of polymeric structure (ie. aromatic or aliphatic), thermal stability tends to decrease in the order: primary carbonate linkage > secondary carbonate linkage > tertiary carbonate linkage (where the structure of each carbonate linkage is defined in Figure 4.2.[81, 82, 84, 85, 88, 99] Since the onset of thermolytic decomposition is governed by the activation energy of the reactions, the rate of decomposition for isothermal conditions increases in the order: primary carbonate linkage < secondary carbonate linkage < tertiary carbonate linkage.[81, 82, 84, 85, 88, 99] As shown in Figure 3.1, each of the polycarbonates studied in this work was an aliphatic homopolymer, with a repeat unit consisting of a norbornane ring and a primary carbonate linkage in one of three combinations of location and orientation on the norbornane ring.

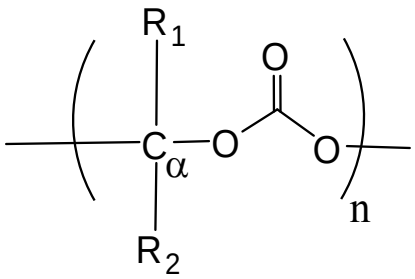

Where,

Primary: R_1 and R_2 = H

Secondary: R_1 = H, R_2 = C_xH_y

Tertiary: R_1 and R_2 = C_xH_y

Figure 4.2 – General structure of primary, secondary, and tertiary carbonate linkages

4.3.1 Relative Thermal Stabilities of PNCs

The decomposition profiles of **PNC1-ROP**, **PNC1-OH**, **PNC2-OH**, **PNC3-OH**, and **PNC3v** oligomers were analyzed by dynamic TGAs. The relative thermal stabilities of all the sacrificial polymers were then compared on the same temperature scale, as shown in Figure 4.3. We observe that the polymers with the least thermal stability were **PNC1-OH** and **PNC2-OH**, followed by **PNC3-OH**, then the vinyl-terminated chains (ie. **PNC2v** and **PNC3v**), and then **PNC1-ROP**. The temperatures at which each polymer reached 10 wt% loss (T_{d10}) and 50wt% loss (T_{d50}) are listed in Table 4.1. By comparing the T_{d10} values of **PNC1-OH**, **PNC2-OH** and **PNC3-OH** chains, it is clear that both the location and the orientation of the carbonate linkages with respect to the norbornane rings (refer to Figure 3.1) influences the relative thermal stability of the polycarbonate structure. It is possible that this may be due to differences in their respective packing densities or relative differences in the bond strains within their repeat units. The T_{d10} value for **PNC1-OH** (203^{o}C) is similar to the one reported by Murayama (207^{o}C) for an unsaturated version of **PNC1-OH** macromolecules.[129] This implies that the impact of unsaturated bonds in the **PNC1** structure is minimal compared to the influence of the location and orientation of the carbonate linkages.

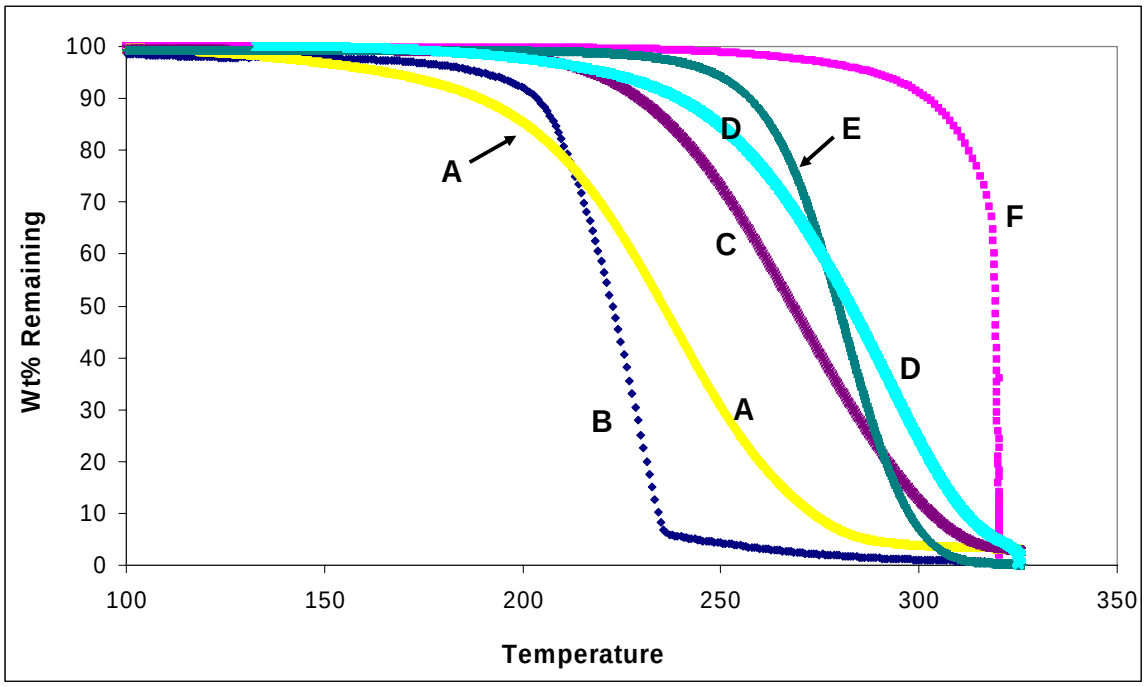

Figure 4.3 – Combined plot showing dynamic TGA curves of the following oligomers: (A) **PNC2-OH**, (B) **PNC1-OH**, (C) **PNC3-OH**, (D) **PNC2v**, (E) **PNC3v**, and (F) **PNC1-ROP**.

Table 4.1 – Tabulated listing comparing the decomposition behavior of multiple PNC oligomers with different chemical structures under constant heating rates (3°C/min)

Oligomeric Structure	T_{d10} (°C)	T_{d50} (°C)
PNC1-ROP	302	320
PNC1-OH	203	223
PNC2-OH	188	235
PNC3-OH	229	268
PNC2v	240	283
PNC3v	257	279

From Table 4.1 we see that vinyl-terminated PNC chains (ie. **PNC2v** and **PNC3v**) had higher thermal stabilities than their respective hydroxyl-terminated analogues (ie. **PNC2-OH** and **PNC3-OH**). Hydroxyl end-groups are known to initiate backbiting reactions in aromatic polycarbonates, via the hydrolysis and cleavage of carbonate linkages, leading to main chain scission.[87] Hence, the conversion of the terminal

hydroxyl groups on PNC chains to vinyl groups eliminated the vulnerability of carbonate linkages to OH-induced degradation, which resulted in an increase in the onset temperature of thermolytic decomposition, as seen in Table 4.1. Although the identities of the **PNC1-ROP**'s end-groups were kept confidential by Promerus LLC, they were known to be unreactive, unlike **PNC1-OH**'s hydroxyl end-groups. Hence, the relatively high thermal stability of **PNC1-ROP**'s chains compared to all the OH-terminated PNC chains was likely due to the unreactive nature of **PNC1-ROP**'s end-groups. Although **PNC1-ROP** chains could not be grafted with siloxane and silsesquioxane compatibilizers, their high thermal stability made them attractive photodefinable porogens for use in the direct-write process. This is because a sacrificial polymer with high thermal stability is less susceptible to premature decomposition prior to the surrounding HSQ matrix, which allows a wider range of processing conditions to be used to produce UV-induced porosity. For this reason, **PNC1-ROP** oligomers were used as sacrificial materials in templated direct-write films in order to perform proof-of-concept experiments of porous films.[1, 2]

4.3.2 Determination of Kinetic Parameters via Dynamic TGAs

Hua's method, outlined below, was used to determine the values of the kinetic parameters of the PNCs via the analysis of dynamic TGA profiles.[98] Similar to other sacrificial polymers, polycarbonates have been shown to decompose via first-order kinetics, as shown in equation (4.1). The symbols w, t, and K stand for the weight either in absolute units of milligrams (mg) or relative units of wt%, time in seconds, and the

overall rate constant in units of reciprocal seconds (sec^{-1}). Equation (4.2) shows the solution to the ordinary differential equation shown in equation (4.1).

$$-\left(\frac{dw}{dt}\right) = Kw \tag{4.1}$$

$$-\left(\frac{d(\ln w)}{dt}\right) = K \tag{4.2}$$

By making use of the Arrhenius relationship, the rate constant term was expanded into the right hand side of equation (4.3); where, k_0 is the pre-exponential rate constant in units of sec^{-1}, E_A is the activation energy in units of joules per mole ($J\ mol^{-1}$), and R is the gas constant (equal to 8.314 joules per mole per Kelvin ($J\ mol^{-1}\ K^{-1}$). Equation (4.4) was then produced by substituting the right hand side of equation (4.2) with the right hand side of equation (4.3).

$$K = k_0 \exp\left(\frac{-E_A}{RT}\right) \tag{4.3}$$

$$-\left(\frac{d(\ln w)}{dt}\right) = k_0 \exp\left(\frac{-E_A}{RT}\right) \tag{4.4}$$

Since the heating rates were constant for all dynamic TGA experiments, the time variable could be expressed in terms of a temperature variable, as shown in equation (4.5). The symbol T is the absolute temperature in units of Kelvin (K), C is the constant heating rate in units of $K\ sec^{-1}$ (equivalent to ^oC/second), and T_0 is the initial absolute temperature in units of K. By making use of the change of variables, the time derivative can be expressed as a temperature derivative, as shown in equation (4.6). The right hand side of equation (4.6) is then substituted into equation (4.4) to produce equation (4.7)

$$t = \frac{\left(T - T_0\right)}{C} \tag{4.5}$$

$$dt = \frac{d\left(T - T_0\right)}{C} = \frac{dT}{C} \tag{4.6}$$

$$-\left(\frac{d\left(\ln w\right)}{dT}\right) = \frac{k_0}{C}\exp\left(\frac{-E_A}{RT}\right) \tag{4.7}$$

To linearized equation (4.7), the natural logarithms of both sides of the expression are taken, as shown in equation (4.8). By plotting the left hand side of equation (4.8) against the variable (1/T), the values of the kinetic parameters k_0 and E_A can then be back-calculated from the y-intercept, $\ln(k_0/C)$, and the slope, E_A/R, respectively. Since all the dynamic TGAs were performed with constant heating rates of 3oC/min, the value of C is always equal to (1/20) K^{-1} or 0.05 K^{-1}.

$$\ln\left[-\left(\frac{d\left(\ln w\right)}{dT}\right)\right] = \ln\left(\frac{k_0}{C}\right) - \frac{E_A}{RT} \tag{4.8}$$

As an example of how the k_0 and E_A are determined, Figure 4.4 shows a plot that was used to calculate the kinetic parameters corresponding to **PNC3-OH**. The plotted points were fitted using least-square residuals analysis and the y-intercept and slope were found to be equal to 22.14 in ln(Kelvin) and -1.409 x 10^4 K, respectively. Thus, the values of k_0 and E_A for **PNC3-OH** decomposition were estimated to be 1.98 x 10^8 s^{-1} and 117 kJ mol-1, respectively. The calculated values of the kinetic parameters of all the PNC oligomers are summarized in Table 4.2.

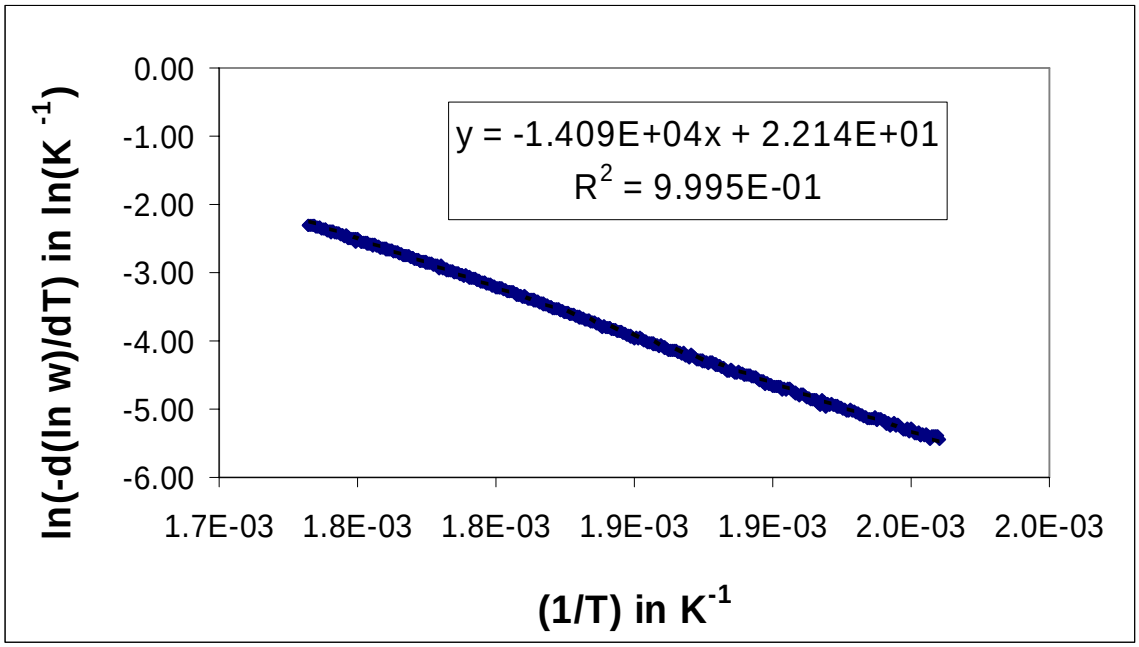

Figure 4.4 – Kinetic plot derived for dynamic TGA data for **PNC3-OH** oligomers. The equation of the best-fit line is shown in the inset.

Table 4.2 –Kinetic parameters for thermolytic decomposition of PNC oligomers derived from dynamic TGA data

Oligomer	Slope (Kelvin)	y-intercept (ln Kelvin)	k_0 (s^{-1})	E_A (kJ/mol)
PNC1-ROP	-4.440×10^4	71.70	6.88×10^{29}	369
PNC1-OH	-2.340×10^4	44.5	1.06×10^{18}	195
PNC2-OH	-8.809×10^3	13.68	4.37×10^4	73.2
PNC3-OH	-1.409×10^4	22.14	2.06×10^8	117
PNC2v	-1.234×10^3	18.67	6.40×10^6	103
PNC3v	2.098×10^4	34.93	7.39×10^{13}	174

4.3.3 Determination of Kinetic Parameters via Isothermal TGAs

To validate the use of dynamic TGA data in calculating the values of the kinetic parameters for PNC decomposition, equations were derived for calculating kinetic parameters using isothermal TGAs, as outlined below. Equations (4.1) through Equation (4.4) are valid for both isothermal and non-isothermal (ie. dynamic heating) conditions,

except that for isothermal kinetics analyses partial derivatives must be used. This is because the time variable cannot be substituted by a temperature variable since isothermal TGAs do not have any dynamic heating rates (ie. equation (4.5) and equation (4.6) are no longer valid). Instead, equation (4.4) is linearized by taking the natural logarithms of both sides of the expression, as shown in equation (4.9).

$$\ln\left[-\left(\frac{\partial(\ln w)}{\partial t}\right)_T\right] = \ln k_0 - \left(\frac{E_A}{RT}\right) \tag{4.9}$$

Multiple isothermal TGAs must be performed to generate enough data to plot the left hand side of equation (4.9) against the variable (1/T). Hence, for each of the temperatures at which isothermal TGAs were performed, the term (ln w) was plotted against time, as shown in Figure 4.5.

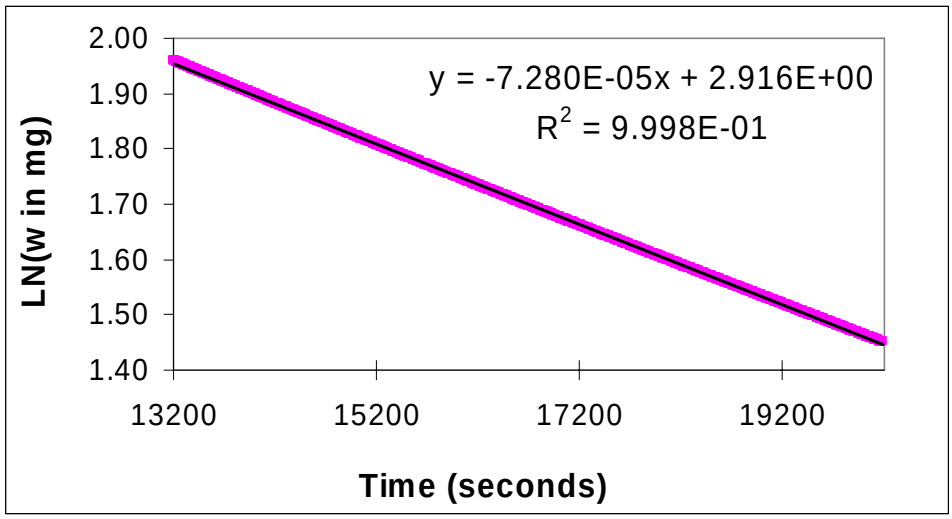

Figure 4.5 – Plot summarizing the isothermal TGA data for **PNC3-OH** at 225°C

The plotted points for each temperature were then fitted using a least-square residuals analysis, in order to find the slope of the plot, $\partial(\ln w)/\partial t$. The term the left hand

side of equation (4.9) was found for each temperature by plotting its TGA data in the same format as Figure 4.5, and then calculating the natural logarithm of its negative slope. Table 4.3 summarizes the mathematical results of analyzing the isothermal TGAs of **PNC3-OH** at the following temperatures: 200°C, 225 °C, 250 °C, 275°C, and 290°C.

Table 4.3 – Summary of isothermal TGA for **PNC3-OH**

Temp (°C)	T (K)	1/T (K^{-1})	$\partial(\ln w)/\partial t$	$\ln(-\partial(\ln w)/\partial t)$
200	473.15	2.113E-03	-1.798E-05	-10.926
225	498.15	2.007E-03	-7.280E-05	-9.528
250	523.15	1.911E-03	-3.004E-04	-8.110
275	548.15	1.824E-03	-1.296E-03	-6.648
290	563.15	1.776E-03	-2.291E-03	-6.079

Finally, the entries in Table 4.3 were used to plot the terms on the left hand side of equation (4.9) against their corresponding reciprocal temperatures (1/T), as shown in Figure 4.6. This composite plot summarized all the isothermal TGA data for **PNC3-OH**, and was used to determine the kinetic parameters of thermolytic-decomposition for **PNC3-OH** using equation (4.9). The data points in Figure 4.6 were then fitted using a least-square residuals analysis, and the values of k_0 and E_A were back-calculated from the values of the y-intercept, $\ln(k_0)$, and the slope (E_A/R), respectively. The results of the best-fit analysis of Figure 4.6 are listed in Table 4.4, along with the corresponding values of the kinetic parameters for the thermolysis of **PNC3-OH** oligomers.

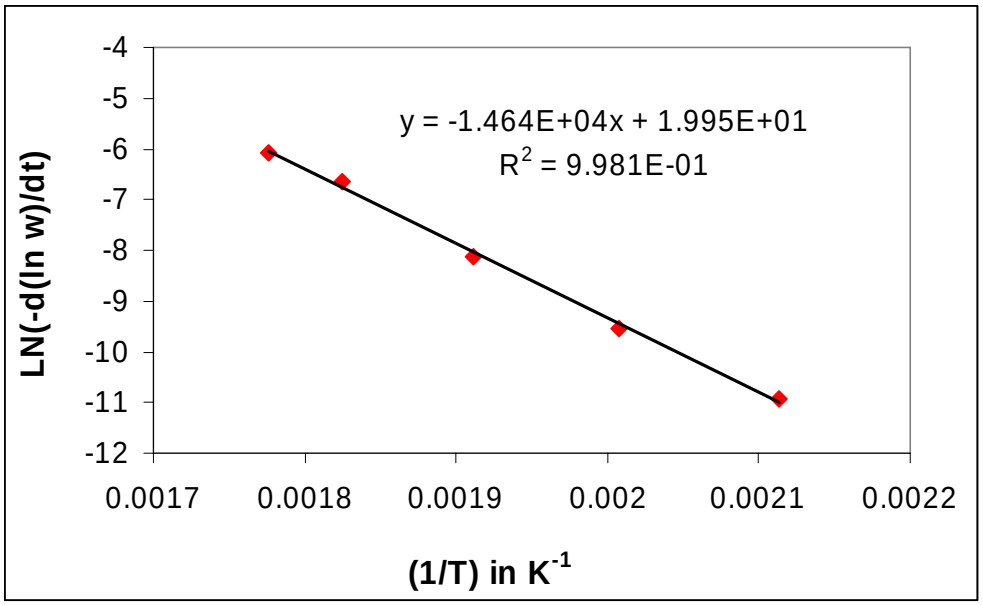

Figure 4.6 – Composite plot summarizing all isothermal TGA data for **PNC3-OH** at the following temperatures: 200 °C, 225 °C, 250 °C, 275°C, and 290 °C.

A comparison of the entries in Table 4.2 and Table 4.4 shows fairly good agreement (both k_0 values are of the same order of magnitude and the deviation in EA values is only 5 kJ/mol) between the values of the kinetic parameters for **PNC3-OH** decomposition derived from dynamic TGA data and isothermal TGA data, respectively. Wedlake also reported good agreement for the results of kinetic parameters derived from isothermal TGA data and dynamic TGA data.[100]

Table 4.4 – Summarized results of isothermal TGA data of **PNC3-OH** at the temperatures 200 °C, 225 °C, 250 °C, 275°C, and 290 °C.

Slope (Kelvin)	y-intercept in ln(sec)	k_0 (s^{-1})	E_A (kJ/mol)
-14,643	20.63	9.14×10^8	122

Kinetic data was generated much faster using dynamic TGA data than isothermal TGA data because a single dynamic TGA curve was sufficient to provide kinetic estimates, whereas several isothermal TGA experiments were needed runs with temperatures spread over a wide temperature window. The number of TGA runs required for kinetic analyses had a direct impact on the amount of sacrificial material available for other characterization methods since at least 5 mg of sample was used per TGA experiment. Additionally, the mathematical manipulations required for analyzing dynamic TGA data was found to be minimal (a single plot was generated to calculate kinetic data from dynamic TGA results). In contrast, isothermal TGA results required a separate plot to be generated for each temperature in order to determine the terms on the left hand side of equation (4.9); finally, an extra composite plot was used to calculate the final kinetic parameter values. Hence, dynamic TGAs were selected as the preferential source of data for performing kinetics studies of PNC decomposition.

4.4 Acidolytic Decomposition in PNC1-ROP/PAG Blends

As shown in Figure 4.3 , the Td_{10} for thermolytic-decomposition of **PNC1-ROP** oligomers is about 302^{o}C, and its final decomposition temperature is 325^{o}C under a constant dynamic heating rate of 3^{o}C/min. However, both thermally-released acids and photogenerated acids are able to catalyze the decomposition of **PNC1-ROP** chains, effectively decreasing the temperature at which they begin to de-polymerize and volatilize. By performing TGA studies on **PNC1**/PAG blends, it was possible to compare the thermal stabilities of each of the PAG shown in Figure 4.1, and determine its applicability in the direct-write process shown in Figure 1.2.[1, 2] The larger the

temperature difference between the TGA curves corresponding to UV-initiated acidolytic decomposition (irradiated PAG) and thermally-generated acidolytic decomposition (no UV) for a polymer/PAG mixture, the wider the processing temperature window is for the direct-write process. This is because wide temperature differences between the two TGA curves allow for the complete decomposition of all the sacrificial chains in the exposed regions during the PEB step without causing any decomposition in the unexposed regions. Thus, PAG molecules that displayed the largest differences between the Td_{10} and T_{d50} values for thermally-released acids and the T_{d10} and T_{d50} values of UV-released TGA curves for **PNC1-ROP**/PAG mixtures were deemed optimal for use in the direct-write formulations. To investigate the relative thermal stability of each of the PAGs shown in Figure 4.1, **PNC1-ROP**/PAG blends were made with the same PAG loading (3 wt%) with respect to dry **PNC1-ROP** polymer. After drying each of these mixtures in a vacuum oven to remove any volatile solvents, they were analyzed using TGA under dynamic heating (constant heating rates of 3^{o}C/min).

4.4.1 Thermal Stability of Diphenyl Iodonium PAG

It has been known for several years that PAGs with diphenyl iodonium cations tend to have low thermal stability as can be seen in Figure 4.2.[200-202] The PAG used in the blends shown in Figure 4.7 was Rhodorsil 2074, and the acid that it released upon both thermal excitation and UV-excitation was hydrogen tetrakis(perfluorophenyl)borate or HTPFPB. The T_{d10} and the T_{d50} values for thermally releasing HTPFPB was not significantly higher than the T_{d10} and T_{d50} values for the UV-irradiated TGA curve, as shown in Table 4.5. As stated previously, a PAG must have a high thermal stability to be

compatible with selective decomposition of PNC otherwise any UV-defined patterns of porosity (and corresponding refractive index profiles) in a film will be destroyed upon heating the film during the PEB step due to the thermal-release of HTPFPB. This is because sacrificial polymer chains both in exposed and unexposed regions would be decomposed by the acid molecules, hence, selective decomposition would not be achieved. Thus the thermal properties of Rhodorsil 2074 PAG were incompatible with selective UV-patterning of porosity, although it could be used for producing blanket porosity in templated direct-write films.

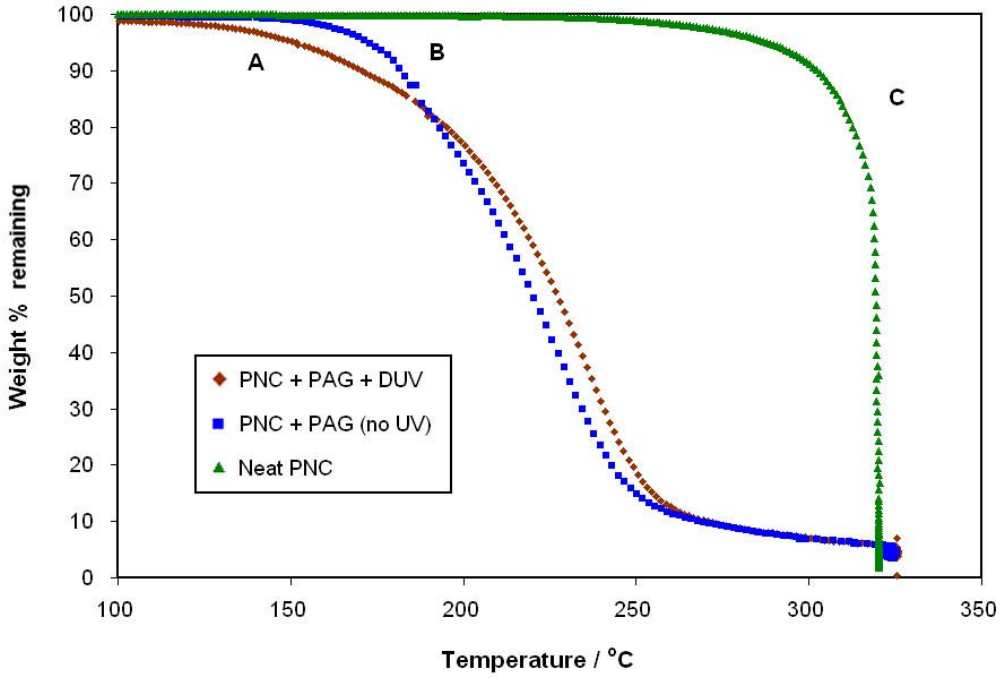

Figure 4.7 – Dynamic TGAs of (A) a **PNC1-ROP**/Rhodorsil 2074 PAG blend exposed to 1 J cm^{-2} DUV radiation, (B) unexposed **PNC1-ROP**/Rhodorsil 2074 PAG blend, and (C) pure **PNC1-ROP**.

Table 4.5 – Properties of **PNC1-ROP**/Rhodosril 2074 PAG blends

Type of acid release	T_{d10} (°C)	T_{d50} (°C)
Thermal release	182	220
UV-release	169	227

4.4.2 Relative Thermal Stability of Triphenyl Sulfonium PAGs

Ionic PAGs with cations derived from the photosensitive triphenyl sulfonium moiety are attractive due to their high thermal stability relative to diphenyl iodonium PAGs.[200, 201] As seen in Figure 4.8 and Table 4.6, TTBPS-Tf had the following desirable properties: relatively high thermal stability with respect to the PEB temperatures required to decompose **PNC1-ROP** after UV-exposure as well as the ability to decompose **PNC1-ROP** rapidly due to the high strength of the photoacid released, which was triflic acid.[200, 201]

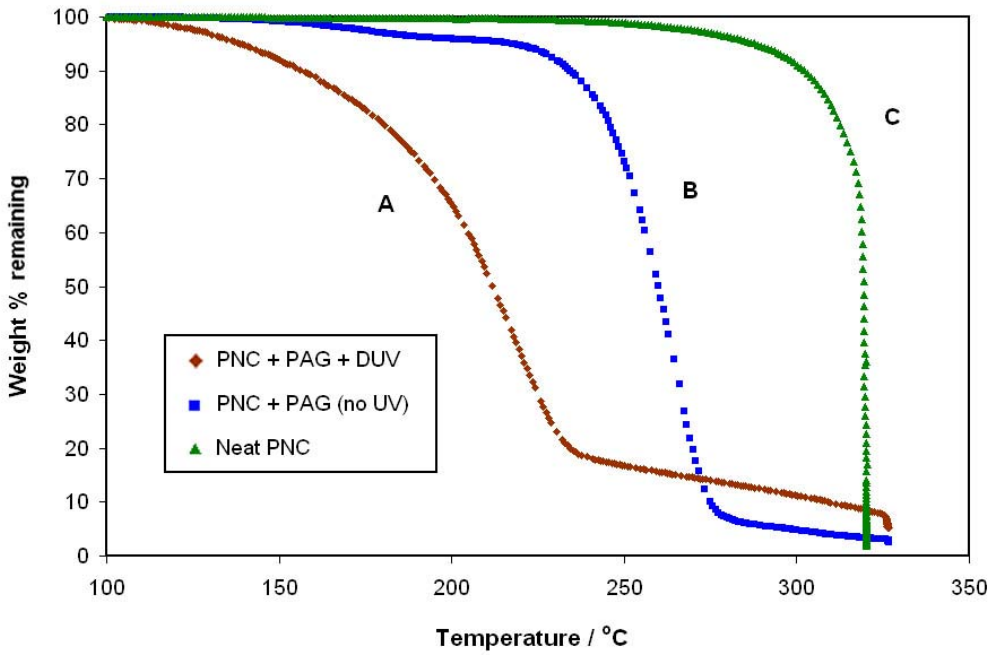

Figure 4.8 – Dynamic TGAs of (A) **PNC1-ROP**/TTBPS-Tf PAG blend exposed to 1 J cm^{-2} DUV, (B) unexposed **PNC1-ROP**/TTBPS-Tf PAG blend, and (C) pure **PNC1-ROP**

Table 4.6 – Properties of **PNC1-ROP**/ TTBPS-Tf PAG blends

Type of acid release	T_{d10} (°C)	T_{d50} (°C)
Thermal release	236	273
UV-release	152	212

Further dynamic TGA studies showed that TTBPS-Nf had desirable properties similar to TTBPS-Tf, as shown in Figure 4.9 and Table 4.7. Hence, it was determined that both TTBPS-Tf and TTBPS-Nf were suitable PAGs for use in the direct-write system, since they would allow selective decomposition of polycarbonate chains solely in UV-irradiated regions if the PEB temperature was well below the onset temperatures for thermal release of their respective acids.

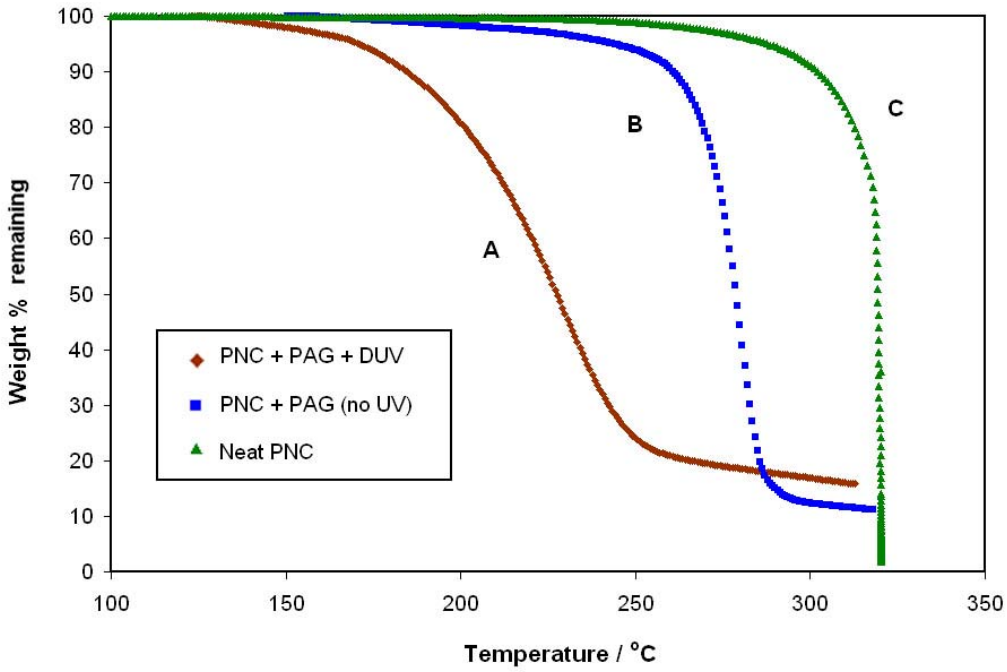

Figure 4.9 - Dynamic TGAs of (A) **PNC1-ROP**/TTBPS-Nf PAG blend exposed to 1J cm^{-2} DUV, (B) unexposed **PNC1-ROP**/TTBPS-Nf PAG blend, and (C) pure **PNC1-ROP**.

Table 4.7 – Properties of **PNC1-ROP**/ TTBPS-Nf PAG blends

Type of acid release	T_{d10} (^{o}C)	T_{d50} (^{o}C)
Thermal release	261	278
UV-release	185	227

4.4.3 Isothermal Decomposition Profiles of PNC1/TTBPS-Tf Mixtures

In order for the SOG matrix to mechanically support porosity, it must be rigid enough to avoid pore collapse during decomposition of the sacrificial polymer. In conventional SOG processing, the resins are spin-coated onto silicon wafers to form planar dielectric films that become rigid when heated above their glass transition temperature.[13-17, 21] Although HSQ is typically thermally cured above 350^{o}C, researchers reported evidence for HSQ cure reactions below 350^{o}C, [17] and we have successfully hardened HSQ by baking them at 200^{o}C for 2 hours.[1] To determine the compatibility of thermal curing with the direct-write process shown in Figure 1.2, isothermal TGA studies of **PNC1-ROP/**TTBPS-Tf mixtures were performed for several temperatures above and below the glass transition temperature of the HSQ matrix, which is 194-195^{o}C as determined by DSC. The results of the isothermal TGA experiments, shown in Figure 4.10, indicated that above the glass transition temperature, the **PNC1-ROP**/PAG mixtures experienced significant loss, and the rate of the weight loss increased with increasing temperature.

This is because at temperatures above 195^{o}C, TTBPS-Tf was thermally activated to produce triflic acid, leading to acid-catalyzed decomposition and volatilization of **PNC1-ROP**. However, at temperatures below 195^{o}C, the **PNC1-ROP**/PAG mixture experienced a total weight loss of less than 5 wt% even after being heated isothermally for up to 2 hours, showing that at temperatures below the glass transition temperature of

the HSQ matrix, either the PAG was thermally stable or the rate of acidolytic decomposition of **PNC1-ROP** was very low.

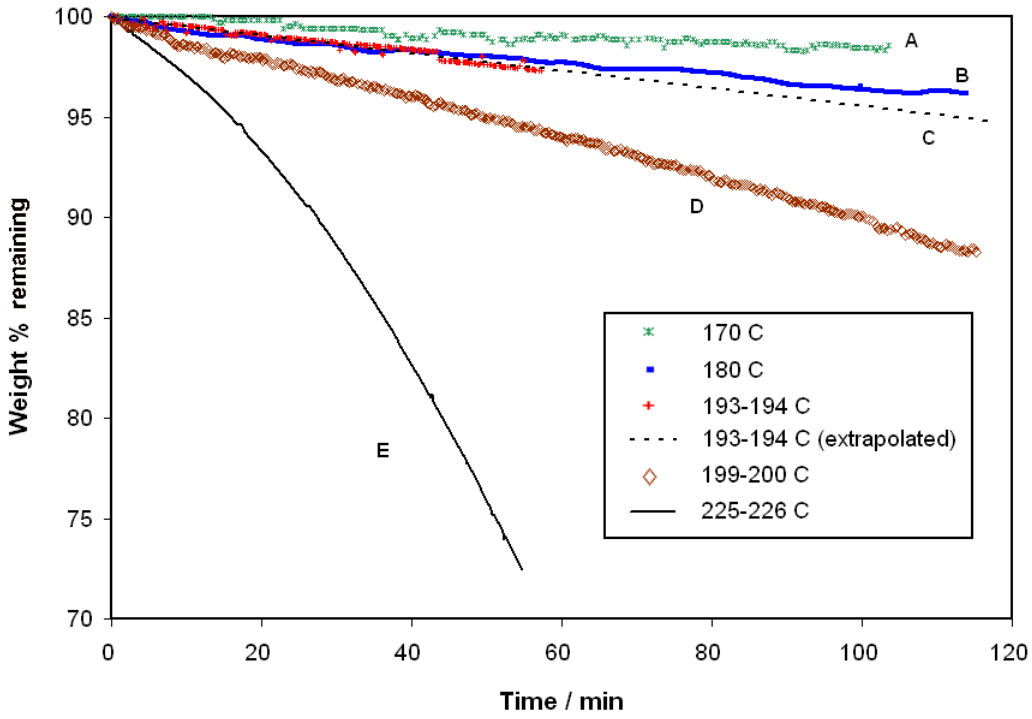

Figure 4.10 – Isothermal TGAs of unexposed **PNC1-ROP**/TTBPS-Tf PAG mixtures held at (A) 170°C, (B) 180°C, (C) 193-194°C [with experimental data extrapolated past 60 min], (D) 199-200°C, and (E) 225-226°C.

Ellipsometry provided further evidence for the thermal activation of triphenyl sulfonium PAGs above the glass transition temperature of HSQ in that the refractive index of HSQ/TTBPS-Tf/**PNC1-ROP** films with a **PNC1-ROP** loading of 10% dropped from 1.413 to 1.365 when heated at 200°C for 2 hours without any prior irradiation whereas the refractive index of pure HSQ control films remained stable at about 1.38 under the same physical conditions. Hence, the curing of HSQ above its glass transition temperature was deemed incompatible with the direct-write process because it would lead

to the thermal activation of the PAG and hence the decomposition of **PNC1-ROP** throughout the film. However, due to low chain mobility, the thermal curing of HSQ below its glass transition temperature occurs on too large a timescale for feasible mass fabrication of direct-write films. To successfully crosslink the matrix below the Tg of HSQ, base-catalyzed gelation reactions were employed, as described in a later chapter. [1, 2, 35, 183, 203-206]

4.5 PNC Decomposition Mechanism via TGA-MS studies

As stated earlier, the analysis of the gaseous decomposition products using mass-spectrometry (MS) provided a means of determining the mechanism of decomposition of the sacrificial polymers.[81, 88, 89, 167, 207] Figure 4.11 shows the influence of the TGA's furnace temperature on the intensities of the MS peaks related to CO_2 (m/e = 44, 45, 46) and C^+ carbocations (m/e=12) during the decomposition of **PNC3-OH** chains. The MS peaks related to CO_2 were produced by hydrolysis of carbonate linkages and internal elimination at the beta-carbon (C_β), which resulted in main chain scission of polymer chains into smaller oligomeric units, diol monomers, and unsaturated molecules, as shown in Figure 4.12.[79-81, 86, 89, 91, 92, 99, 167, 180] By comparing the MS results shown in Figure 4.11 with the **PNC3-OH** TGA results shown in Figure 4.3 and Table 4.1, we see that the relative amount of CO_2 detected by MS correlated very well with the rate of decomposition of the **PNC3-OH** sample (the maximum signal for the CO_2 peak and the steepest slope of the dynamic TGA both occurred with the TGA furnace temperature was about 270^{o}C). As carbonate linkages were hydrolyzed, CO_2 molecules were produced, which were quickly swept into the MS chamber and

detected.[79, 80, 88] Hence, the CO_2 MS peak intensity provided a convenient marker for the relative rate of decomposition of the polymeric chains.

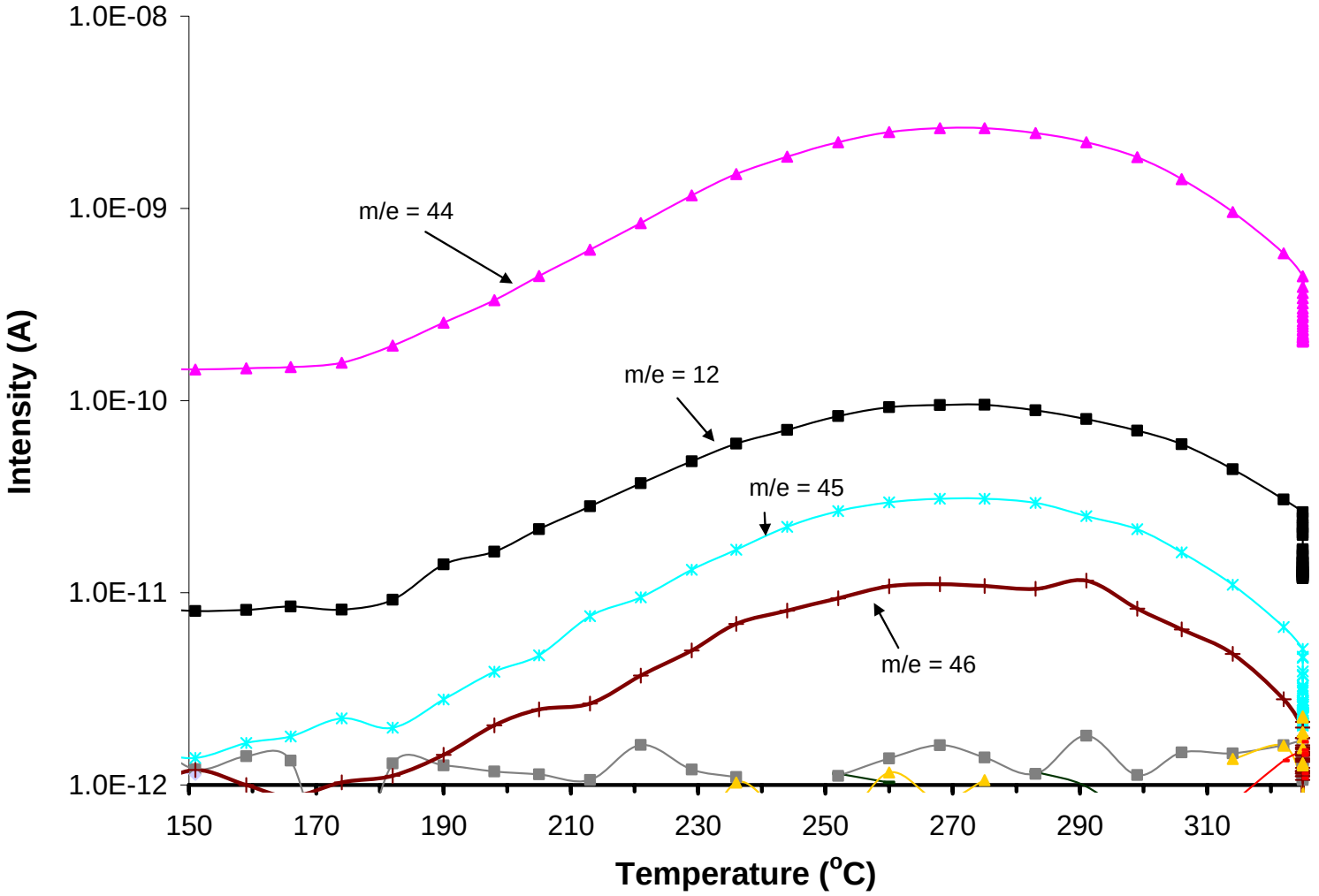

Figure 4.11 – Plot showing the temperature dependence of the CO_2 MS peak intensity during **PNC3-OH** decomposition

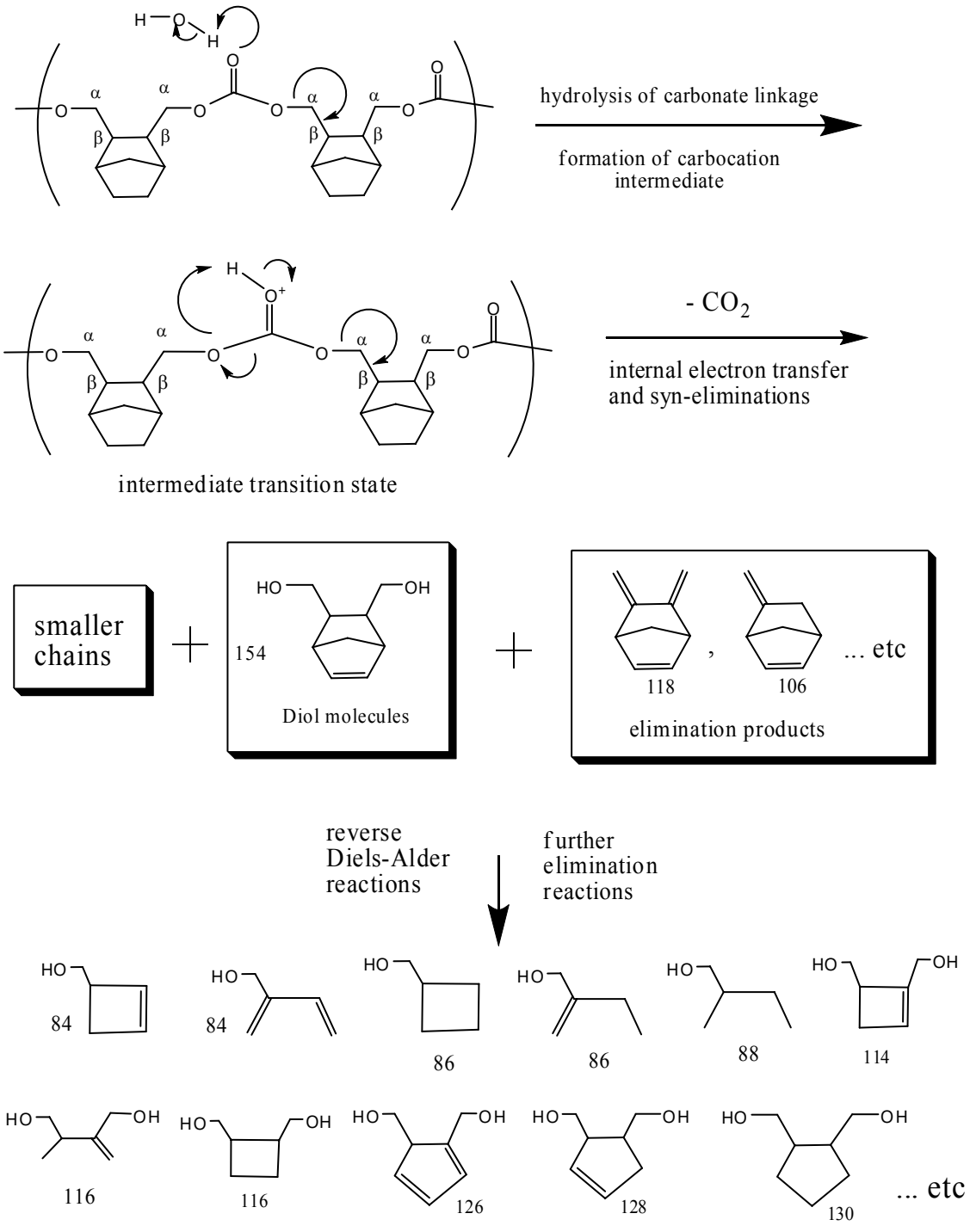

Figure 4.12 – Mechanism for the hydrolysis of carbonate linkages and production of carbon dioxide during the decomposition of **PNC2** and **PNC3** oligomers

The hydrolysis of carbonate linkages and other oxy-carbonyl groups is catalyzed by acid molecules; resulting in the lowering of the onset for thermolysis of polycarbonates.[79, 80, 88, 89, 180] By comparing the results in Table 4.1 with those in Table 4.5 through Table 4.7, we can clearly see that the release of superacids by the PAGs shown in Figure 4.1 resulted in the reduction in the decomposition temperatures of **PNC1-ROP** from 229^{o}C to as low as 152 ^{o}C for T_{d10} and from 268^{o}C to as low as 220^{o}C for T_{d50}. Although the rate law for acid-catalyzed decomposition of polycarbonates is a complex function of temperature, amount of remaining sample, concentration of acid in the remaining sample, acid strength, and acid volatility, we can qualitatively say that acidolytic decomposition has a lower effective E_A than the corresponding E_A values for thermolytic decomposition of neat oligomers, which are shown in Table 4.2.

Figure 4.13 shows the overall relative abundance of the major MS peaks detected during the dynamic heating of a **PNC3-OH** sample in the TGA furnace (refer to Figure 4.3); similar results were observed during the decomposition of **PNC1** and **PNC2** oligomers (see Appendix A). From MS peak assignments (see Appendix A), we observe that the major volatile products detected during the decomposition were water (m/e = 18), ethylene gas (m/e=28), carbon dioxide (m/e=44), cyclopentadiene or CPD (m/e=66), and numerous other fragmentation products (eg. m/e=79, 91, 264, etc). Researchers have shown that when norbornene and norbornane rings are subjected to high temperatures, they fragment via a retro Diels-Alder reaction producing cyclopentadiene and ethylene gas as major products.[207-209] Thus the MS results implied that reverse Diels-Alder reactions played a significant role in the decomposition of all three types of PNC chains, as shown in Figure 4.14.

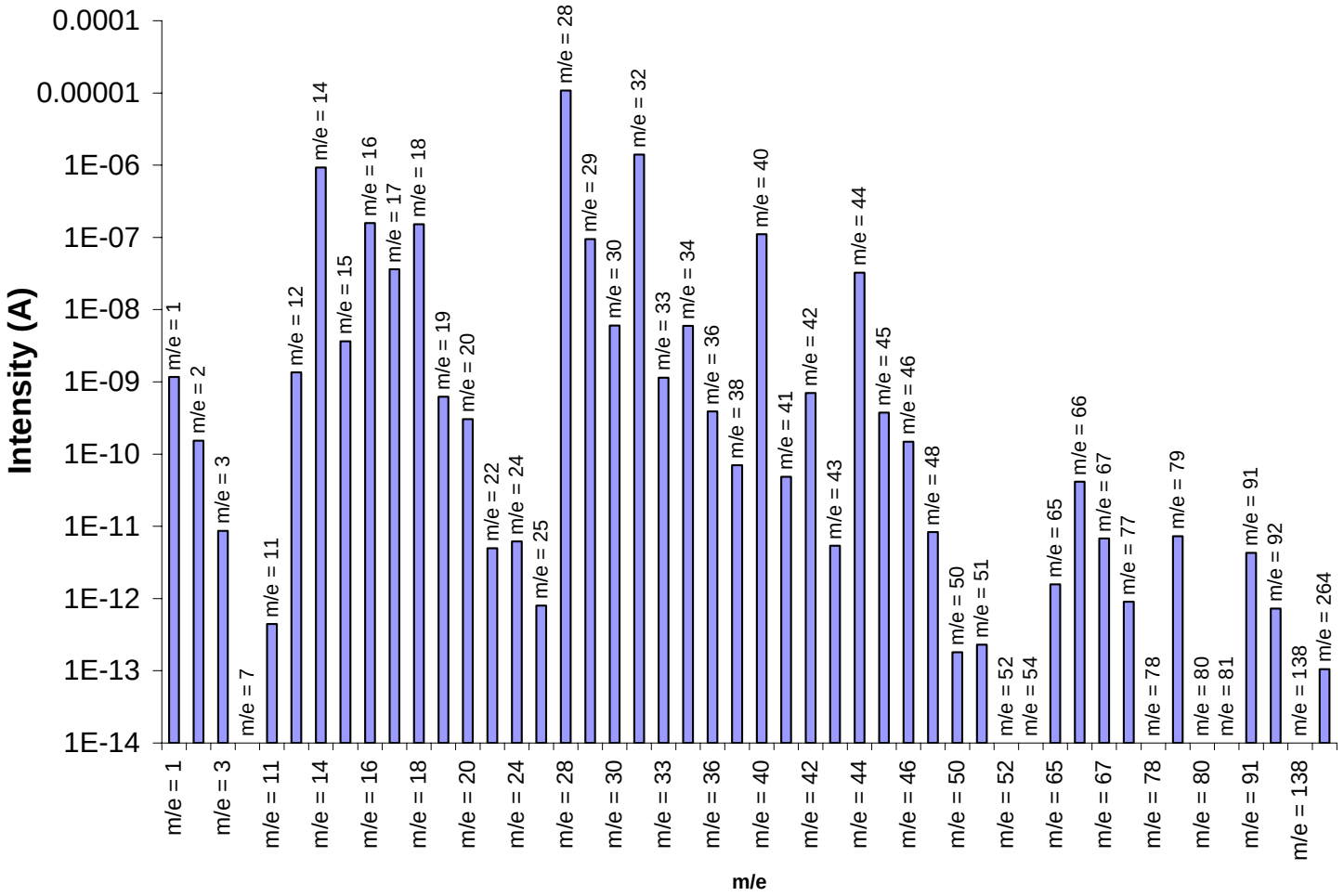

Figure 4.13 – Overall relative abundance of MS peaks detected during **PNC3-OH** decomposition. The plot shows MS peaks for all masses with amu <300 and total intensities $>10^{-14}$ A)

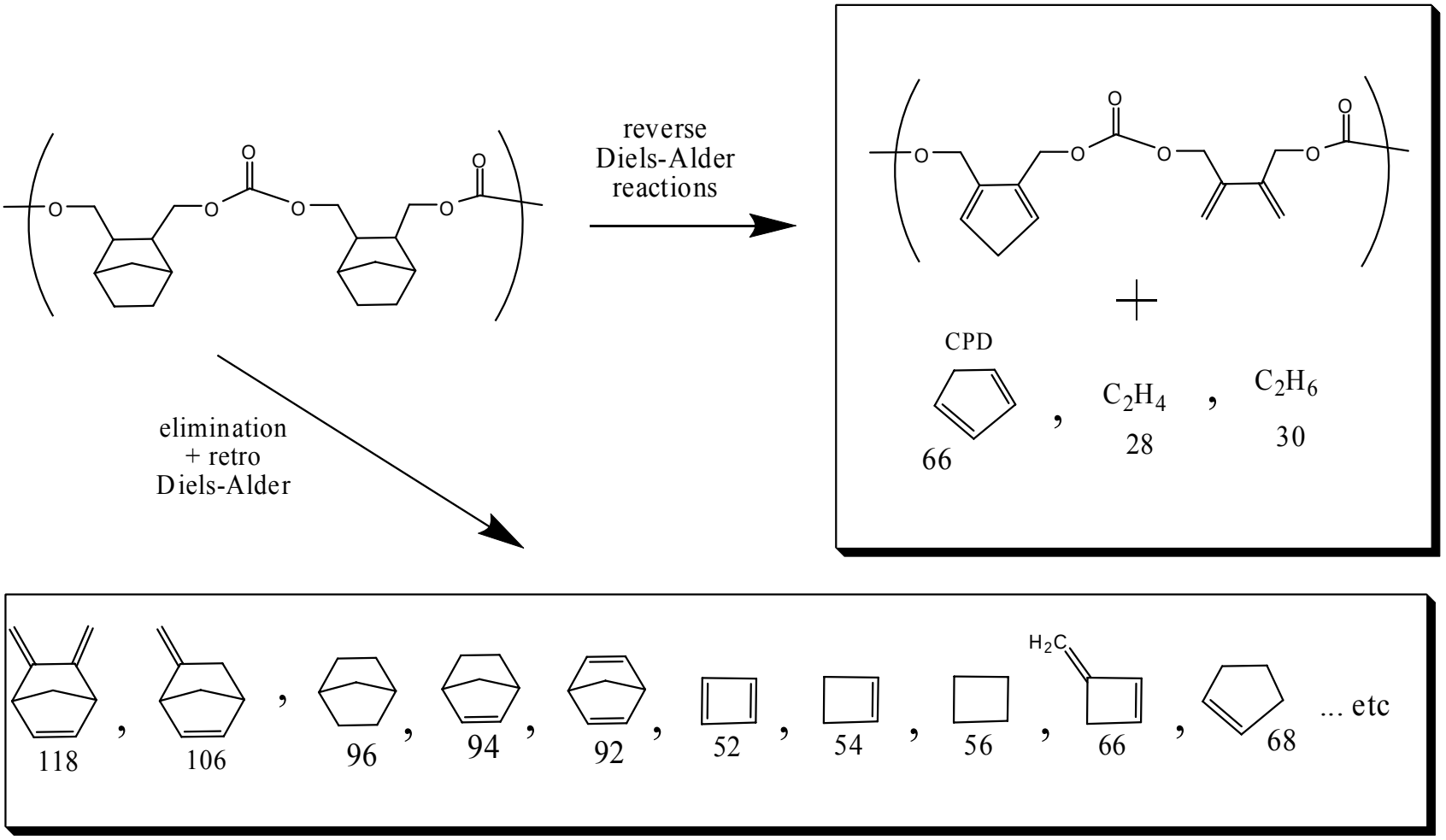

Figure 4.14 – Mechanism showing the reverse Diels-Alder fragmentation of **PNC2** and **PNC3** chains. Smaller decomposition products containing norbornene or norbornane rings also fragment in a similar fashion

One of the main degradation mechanisms for aromatic polycarbonates produces ether linkages and cyclic oligomers via backbiting reactions within reaction intermediates.[87] The high thermal stability and acidolytic stability of polyethers accounts for the significant decomposition residue observed for aromatic polycarbonates and other types of polycarbonates that contain ether linkages. Aliphatic polycarbonates, such as PNCs, typically display clean decomposition behavior due to the absence of ether link formation during thermolysis. From the TGA results shown earlier (see Figure 4.3), we observe that all the types of PNC chain structures studied in this work left negligible residue once the decomposition had been completed. This implied that backbiting reactions, shown in Figure 4.15, are either thermodynamically unfavorable for PNCs at the temperatures used in our TGA studies, or their reaction rates were very low (the E_A values for these reactions may have been much higher than the E_A values for the major PNC decomposition mechanisms).

Although some of the MS peaks (see Figure 4.13 and Appendix A) were identified as containing ether links, the low intensities of these peaks (signals were all below 10^{-12} A) indicated that the rates of this reactions were several orders of magnitude lower than the decomposition reactions shown in Figure 4.12 and Figure 4.14. Hence, there was no evidence of ether link formation being a major mechanism for the decomposition of PNCs for the conditions used in our decomposition studies. Thus the major mechanisms for PNC decomposition were: hydrolysis of carbonate linkages accompanied by elimination reactions, and reverse Diels-Alder reactions of norbornene-containing and norbornane-containing molecules and chains. [79-81, 86, 89, 91, 92, 99, 167, 180, 207-209]

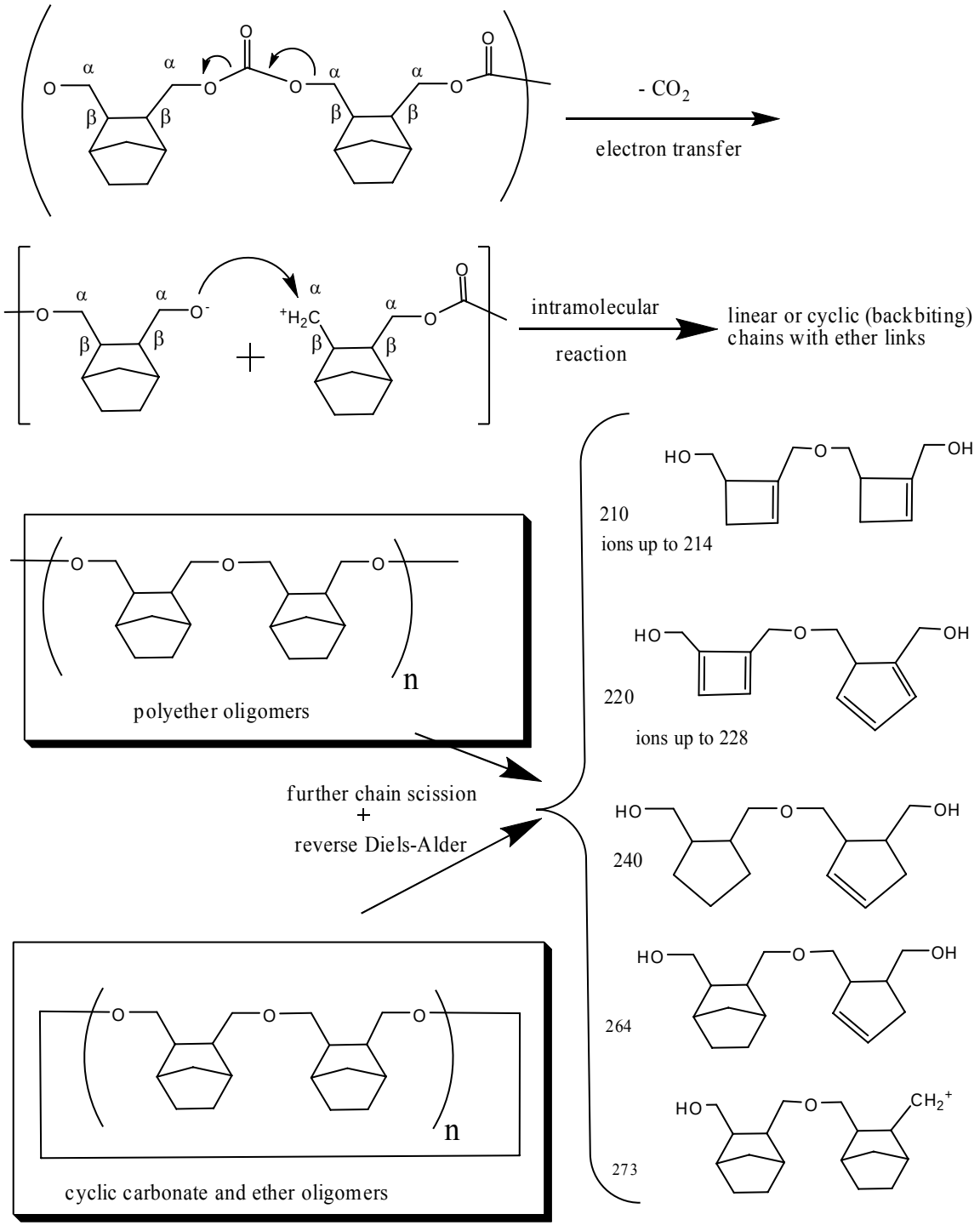

Figure 4.15 – Mechanism for the formation of ether linkages in PNCs

CHAPTER 5

CHARACTERIZATION OF SILOXANE AND SILSESQUIOXANE PRECURSORS

5.1 Materials Used

Anhydrous dichloromethane (DCM), anhydrous trimethylchlorosilane (TMCS), $CDCl_3$, and type-3A (4-8 mesh) molecular sieves were purchased from Fisher Scientific. $CDCl_3$ was stored in a refrigerator over the molecular sieves to avoid moisture uptake. Tetramethylsilane (TMS) and $Cr(acac)_3$ were obtained from Sigma Aldrich and NMR samples were prepared via methods outlined in chapter 2. Anhydrous TMCS was stored in a freezer to maintain its stability. All glassware was purchased from Chemglass and silanized with TMCS, then vacuum-dried at 80^{o}C or higher, then cooled under a dry nitrogen atmosphere prior to use. Disposable polypropylene-casing Luer-lock type syringes, stainless steel Luer-lock type syringe tips, PTFE membrane syringe filters with 0.2 μm pores, and PTFE-coated stirrer bars were all purchased from VWR.

The term photobase generators (PBGs) refers to photoinitiators that release bases when activated by either high temperatures or UV radiation.[55-57, 197, 200, 201, 207-218] The photobase generators (PBGs) used were N-cyclohexl-*para*-toluene sulfonamide (CTS), *ortho*-nitrobenzyl cyclohexylcarbamate (NBC), and N-methylnifedipine, as shown in Figure 5.1. CTS and NBC were commercially obtained from Lancaster Synthesis and Midori Kagaku respectively. Since N-methylnifedipine

was not commercially available, it was synthesized and purified according to the method reported in literature and its structure was verified by ^{1}H-NMR analysis.[203, 204]

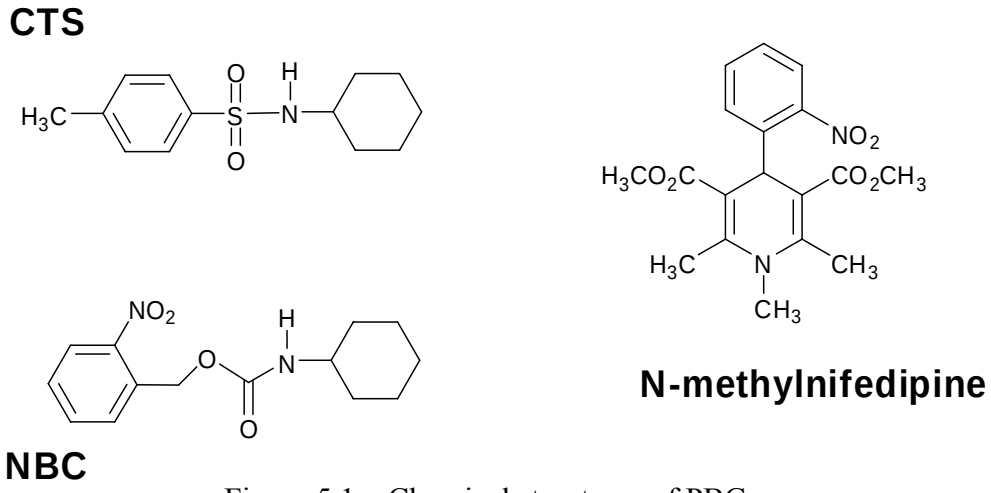

Figure 5.1 – Chemical structures of PBGs.

Silane terminated polydimethylsiloxane (PDMSH) was obtained from Gelest and used without further purification. Octa(dimethylsiloxy)silsesquioxane or $Q_8M_8^H$ POSS was also obtained from Gelest. The spin-on glass (SOG) POSS matrix material used in this study was hydrogen silsesquioxane (HSQ) resin. This HSQ resin was obtained as a solution in methyl isobutyl ketone (MIBK) solvent that is sold under the tradename FOx® by Dow Corning. The chemical structures of PDMSH chains and $Q_8M_8^H$ cages are shown in Figure 5.2 and HSQ resin is shown in Figure 5.3. By convention, the chemical structures of monofunctional-, difunctional-, and trifunctional-methylsiloxane groups are abbreviated by the symbols M, D, and T, respectively; while quartenary-siloxanes are abbreviated by the symbol Q, as shown in Figure 5.4.[3, 18, 179, 181, 182, 210]

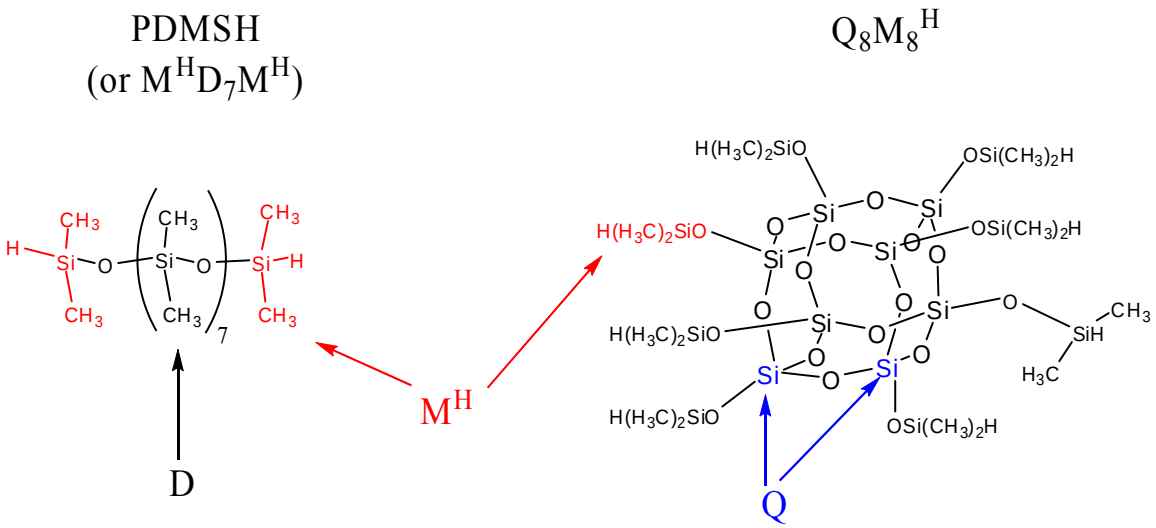

Figure 5.2 – Chemical Structure of the PDMSH oligomeric chains and Q8M8^H cages used in the grafting reaction

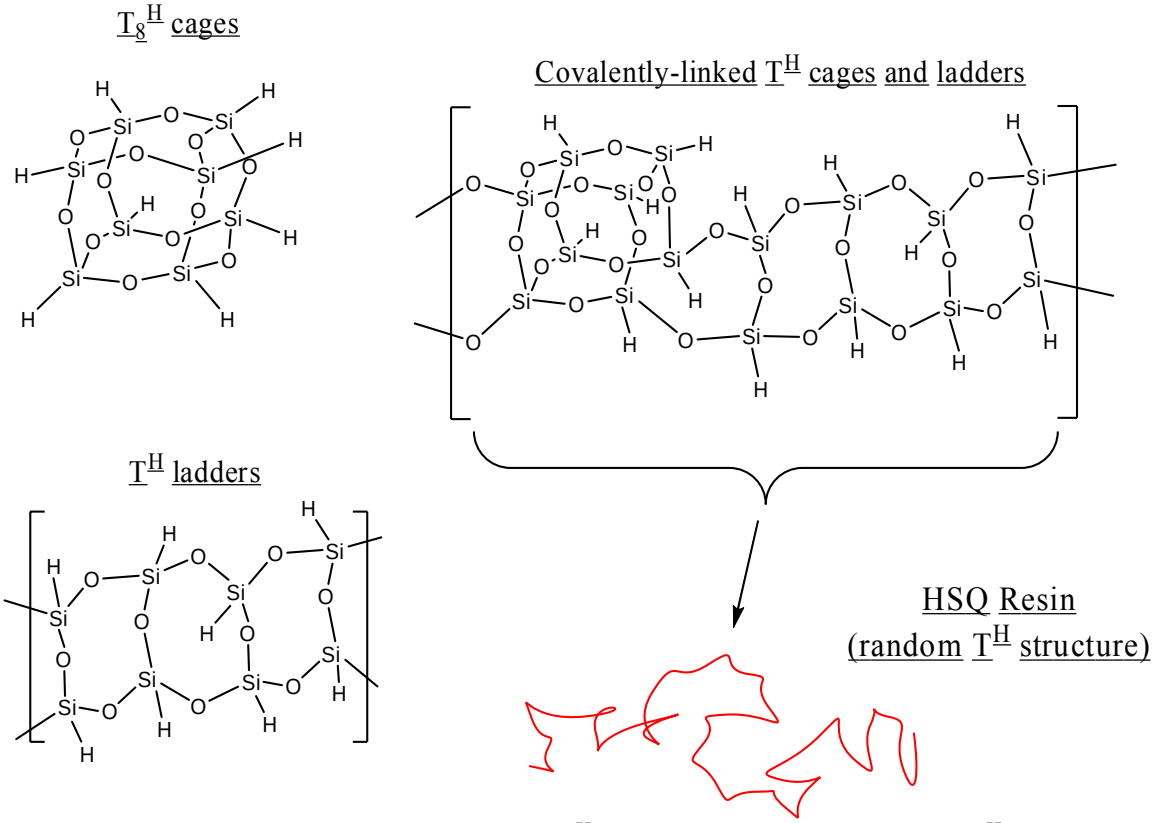

Figure 5.3 –Idealized chemical structure a T^H resin chain with alternating $T_4{}^H$ ladder and $T_8{}^H$ cages repeat units

M group (Trimethylsiloxy-)

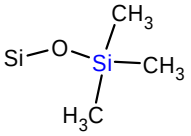

D group (dimethylsiloxy-)

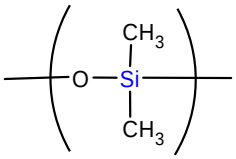

T group (trisiloxymethyl-)

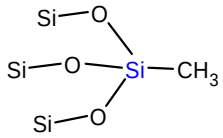

Q group (quarternary-siloxane)

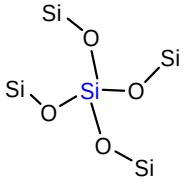

Figure 5.4 – General chemical structures of common organosilicon groups

Superscripts on the M, D, and T symbols refer to substitutions other than methyl groups on the silicon atom, while subscripts on all four symbols refer to the number of similar-type siloxanes which are covalently linked (eg. HSQ is a T^H POSS structure with a general formula of $H_xSi_xO_{1.5x}$). Below is a list of frequently used abbreviations for organosilicon groups along with their meanings.[3, 18, 95, 178, 179, 181, 182, 210-231]

- M : The trimethylsilyl end-group or its silicon atom ($\underline{Si}Me_3$)
- M^H : The dimethylsilane end-group or its silicon atom ($\underline{Si}Me_2H$)
- M^{OH} : The dimethylsilanol end-group or its silicon atom ($\underline{Si}Me_2OH$)
- M^{CH2} : The dimethylsiloxy-methylene group or its silicon atom ($O\underline{Si}Me_2CH_2$). This group is formed when M^H groups undergo hydrosilylation reactions with vinyl-containing organic groups
- D : The dimethylsiloxy group or its silicon atom ($O\underline{Si}Me_2$)
- D^H : The methyl-hydrosiloxy group or its silicon atom ($O\underline{Si}HMe$)
- D^{OH} : The methyl-hydroxysiloxy group or its silicon atom ($O\underline{Si}(OH)Me$)
- T : The methyl-trisiloxy end-group or its central silicon atom ($Me\underline{Si}(OSi)_3$)
- T^H : The hydro-trisiloxy end-group or its central silicon atom $H\underline{Si}(OSi)_3$)

- T^{OH} : The silanol-trisiloxy end-group or its central silicon atom ($HO\underline{Si}(OSi)_3$). In organosilicon literature, the terms Q_3 and T^{OH} are synonymous.

- T^{CH2} : The trisiloxysilyl-methylene group or its silicon atom ($(SiO)_3\underline{Si}Me_2CH_2$). This group is formed when T^H groups undergo hydrosilylation reactions with vinyl-containing organic groups

- Q : The quartenary siloxane group or its silicon center ($\underline{Si}(OSi)_4$). In organosilicon literature, the Q abbreviation is also referred to as Q_4.

- Q_3 : The silanol-trisiloxy end-group or its central silicon atom ($HO\underline{Si}(OSi)_3$). The abbreviations Q_3 and T^{OH} have equivalent meanings.

5.2 Purification of Silsesquioxanes

Unlike the POSS structures, which were found to be hydrophilic, PDMSH chains did not need to be dried of moisture since polydimethylsiloxane groups are inherently hydrophobic. To desorb all traces of moisture from the $Q_8M_8^H$ solids, they were placed in Nalgene plastic vials and vacuum dried overnight at 80°C, and then allowed to cool to ambient under an inert N_2 atmosphere. Dry, clear-colored $Q_8M_8^H$ crystals were recovered. The dried $Q_8M_8^H$ solids were added to reaction flasks within 30 minutes of being exposed to air again. HSQ or T^H resin was purchased from Dow Corning as a 22 wt% solution in MIBK solvent (sold as FOx-16). Like $Q_8M_8^H$, T^H resin was also found to be hydrophilic due to the presence of silanol groups in its chemical structure. To recover dry T^H resin solids without causing the co-reaction of silanol bonds (gelation), the resin was silanized prior to removal of the MIBK solvent, as described below. 22g of Fox-16 solution (contained 22 wt% or 4.84g of dry HSQ resin) was added to a pre-

silanized flask. The Fox-16 solution was diluted by mixing it with 45 ml of dry DCM solvent prior to transferring the co-solvent mixture to a pre-silanized addition funnel. A separate solution was made of 7.826g (72.1 mmoles) of TMCS in 40 ml of anhydrous DCM, and this solution was transferred to a pre-silanized, 3-neck flask. The 3-neck flask was attached to the addition funnel, a Schlenk line, and a silicone-oil bubbler. The entire apparatus was continuously purged with dry N_2 gas while the dilute HSQ solution was added dropwise to reaction flask containing the excess TMCS. The dropwise addition took 135 minutes to be completed, and the reaction mixture was stirred overnight with a continuous N_2-purge stream to prevent the buildup of HCl gas, which was produced as a by-product of the silanol capping reactions.

The reaction mixture was then transferred to a pre-weighed boiling flask and concentrated to about 7g (approximately 3 ml of solution) before being pipetted dropwise into 75 ml of dry acetonitrile. During dropwise addition of the concentrated solution to acetonitrile, a white precipitate (HSQ resin) was observed. The suspension was vacuum filtered through a pre-weighed and pre-silanized, fine-porosity fritted-glass filter to recover wet T^H resin solids. The solids were dried overnight at 70^{o}C under high vacuum and weighed. 4.57g of dry T^H resin solids were recovered (94% yield) and the solids were transferred to a dry Nalgene vial containing a clean Teflon-coated magnetic stirrer bar. The vial was sealed and the stirrer bar was used to grind the recovered solids into a fine powder to facilitate dissolution in common solvents. The Nalgene vial holding the dry HSQ solids was stored in a refrigerator to avoid any further formation of silanol groups.

5.3 Characterization of HSQ (T^H) Resin

5.3.1 ^{1}H NMR and 29Si{^{1}H} NMR Analyses of Recovered HSQ Resin Solids

HSQ resin has a distribution of structures ranging from the simple cage and ladder structures to highly complex networks.[5, 6, 8, 107, 197-220] Figure 5.5 and Figure 5.6 respectively show the ^{1}H NMR and 29Si{^{1}H} NMR spectra of the purified T_n^H resin solids. Literature sources show that broad ^{1}H NMR peak in Figure 5.5 between δ = 4.2 ppm and δ = 4.6 ppm was produced from the overlapping of separate T_n^H protons singlet peaks (ie. $(SiO)_3SiH$), which confirmed that the HSQ resin was composed of multiple chemical structures.[95, 210, 212, 214, 218, 232]

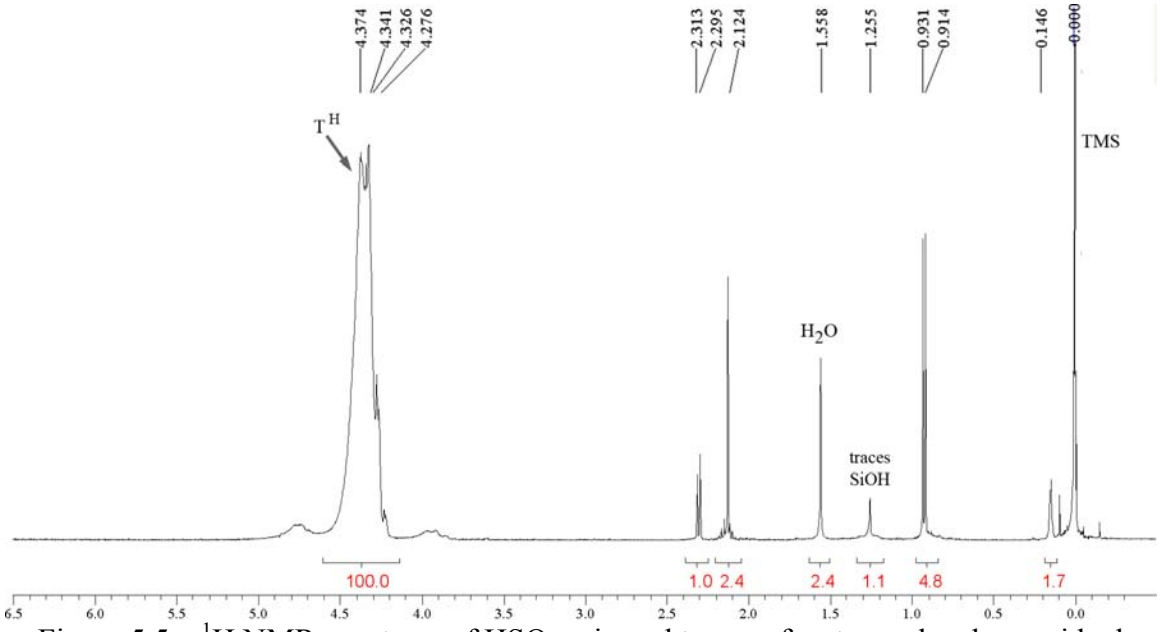

Figure 5.5 – ^{1}H NMR spectrum of HSQ resin and traces of water molecules, residual silanol bonds, and Dow Corning's proprietary surfactant

Owing to the sensitivity of ^{29}Si chemical shifts to slight differences in the chemical environment of silicon groups, ^{29}Si NMR analysis was used to distinguish between different silicon groups present in the T^H resin.[3, 18, 179, 181, 182, 210] By referring to literature sources, the overlapping $^{29}Si\{^1H\}$ peaks in Figure 5.6 between δ = -83.6 ppm and δ = -88.4 ppm were identified with the following T^H groups (arranged in the order left to right) in the resin: T_8^H, T_{10}^H, T_{12}^H, T_{14}^H, and T_{16}^H. [95, 182, 210-212, 214, 218, 224] The broad peak between δ = -100 ppm and δ = -125 ppm was an artifact that was produced by the Q silicon groups in the glass probe of the NMR equipment. [3, 18, 179, 181, 182, 210]

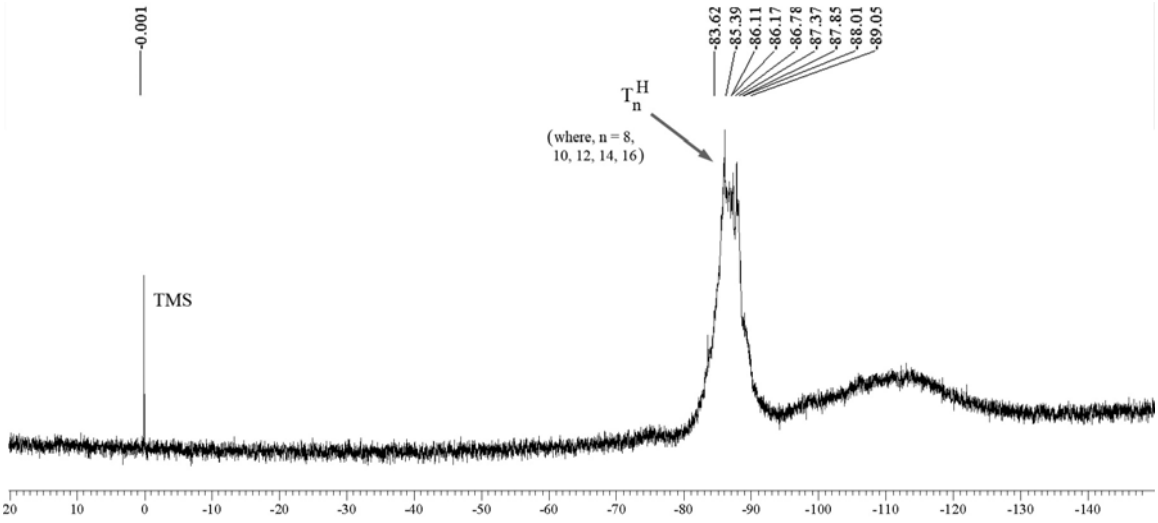

Figure 5.6 – $^{29}Si\{^1H\}$ NMR spectrum of HSQ resin, where n is equal to the following integers from left to right: 8, 10, 12, 14, and 16

The determination of a distribution of T^H structures in HSQ resin was in good agreement with the results of other researchers.[95, 181, 211, 212, 218, 233] As stated earlier, the actual chemical structure of HSQ resin is highly complex; with a randomly

ordered sequence of T^H ladders and T^H cages and a distribution of $T_n{}^H$ cage structures (ie. n varies between 8 and 16). [5, 6, 8, 107, 197-220] Additionally, the chemical structures of the end-groups do not have any distinguishable features that are different from the T^H units in the main chain, which excludes the use of end-group analysis in estimating the average size of HSQ chains. However, Dow Corning provided a certificate of analysis for the HSQ resin, which showed that the T^H chains had an average molecular weight of 11,700 (determined by GPC analysis). Su and co-workers experimentally measured a radius of gyration of 3.65 nm for HSQ chains having a number-average molecular weight of 26,500.[95] Since the batch of HSQ resin received from Dow Corning had a molecular weight less than 26500, its radius of gyration was smaller than 3.65 nm.

5.3.2 Reactions During Thermal Crosslinking and Base-Catalyzed Gelation

The reactions that occur during the thermal curing of HSQ films have been extensively studied by numerous researchers, and been found to occur in one of four main mechanisms depending on the physical and chemical conditions used during the curing: cage-to-network bond rearrangement, redistribution of both silane and siloxane bonds, thermal dissociation of silane bonds, and oxidation of silane bonds.[13, 15-17, 210, 234, 235] Although none of these thermal curing reactions are thermodynamically favorable below 200^{o}C, cage-to-network bond rearrangements occur from 200-350^{o}C, redistribution reactions occur from 250-450^{o}C, thermal dissociation of silane bonds occur from 350-450^{o}C, and oxidation reactions occur above 400^{o}C.[15-17] Cage-to-network rearrangements are caused by the inherent instability of $T_{12}{}^H$, $T_{14}{}^H$, and $T_{16}{}^H$ cage structures, which are a result of the internal strains produced by their non-tetrahedral

siloxane bond angles, but do not result in any change in stoichiometry.[210-212, 218, 233, 236] During rearrangements, T^H cage-type siloxane bonds reorient themselves into open, three dimensional network-type siloxanes, resulting in the crosslinking of adjacent HSQ chains and the formation of a rigid, silica-like solid.[5, 6, 8, 107, 197-220] The redistribution reactions involve the cleavage of both silane and siloxane bonds, which facilitates both the formation of covalent links between adjacent HSQ chains and the conversion of T^H structures to silica-like Q structures. Several redistribution reactions occur simultaneously, and the major types are shown in equation (5.1) through equation (5.3).[15-17] From 250-350^{o}C, equation (5.1) is the dominant redistribution reaction step but as the amount of -$OSiH_2O$- linkages (appears as. $H_2SiO_{4/2}$ term in the equations) between HSQ chains increases or the temperature rises, the reactions shown in equation (5.2) and equation (5.3) become dominant. [15-17] Since all the redistribution reactions occur at the same time, the a crosslinked HSQ matrix has a highly complex chemical structure composed of multiple types of silicon groups. From 350-450^{o}C, the network redistribution reactions and thermal dissociations of silane bonds occur simultaneously to produce silica-like Q, as shown in equation (5.4). [15-17]

$$2\ HSiO_{3/2} \rightarrow H_2SiO_{2/2} + SiO_{4/2} \quad (5.1)$$

$$HSiO_{3/2} + H_2SiO_{2/2} \rightarrow H_3SiO_{1/2} + SiO_{4/2} \quad (5.2)$$

$$HSiO_{3/2} + H_3SiO_{1/2} \rightarrow SiO_{4/2} + SiH_4 \quad (5.3)$$

$$4\ HSiO_{3/2} \rightarrow 3\ SiO_{4/2}\ \ SiH_4 \quad (5.4)$$

Above 450^{o}C, oxidation reactions convert silane bonds to siloxane bonds, eventually producing a silicon dioxide structure.[11, 13, 14] Although the formation of Q

structures increases the mechanical strength of HSQ films, it also degrades the low-k properties of HSQ since the chemical structure of the matrix approaches that of SiO_2.[11, 13, 14, 16, 19, 234, 237] Hence, the physical conditions during the thermal curing of HSQ films must be tightly controlled to produce rigid films with optimal low-k properties (the optimal temperature has been shown to be between 350-400^oC in a low-oxygen environment).[11, 13, 16, 234] As shown in the previous chapter, the physical conditions required for thermal curing of HSQ films is incompatible with the direct-write process since PAGs are unstable above 200^oC (refer to Figure 4.10). On the other hand, if the matrix is not rigid enough to support porosity then the decomposition of templated sacrificial polymers would lead to the collapse of any resultant pores.

Silane bonds, which are present in the HSQ chemical structure, are hydrolytically unstable and can be easily hydrolyzed to form silanol groups. [179, 183, 205, 236] These silanol sites can then undergo subsequent sol-gel condensation reactions with adjacent silanol and silane groups to produce siloxane bonds, as shown in equation (5.5) and equation (5.6).[1, 2, 183, 203-206, 219] As the sol-gel reactions proceed, a rigid silica-like network is formed, similar in principle to the effect of thermally curing HSQ.[1, 2, 11, 13, 14, 19, 36, 210, 237]

$$\text{—Si-OH} + \text{HO-Si—} \rightarrow \text{—Si-O-Si—} + H_2O \quad (5.5)$$

$$\text{—Si-OH} + \text{H-Si—} \rightarrow \text{—Si-O-Si—} + H_2 \quad (5.6)$$

A frequently cited mechanism for the hydrolysis of silanes, proposed by Sommer, involves the induced polarization of the silicon center by a nucleophile followed by the attack of the electropositive silicon center by a water molecule with retention of bond orientation, as shown in Figure 5.7.[183] The d-orbitals present in silicon atoms allow

silicon centers to form pentacoordinate and hexacoordinate transition states during reactions.[179, 183] Then there is an internal rearrangement of the temporary bonds in the transition state that leads to the formation of a silanol group. According to West, the hydrolysis of cyclic silanes such as HSQ cages is thermodynamically favorable because the pentacoordinate transition state relieves the bond strains present in the original cyclic structures.[236]

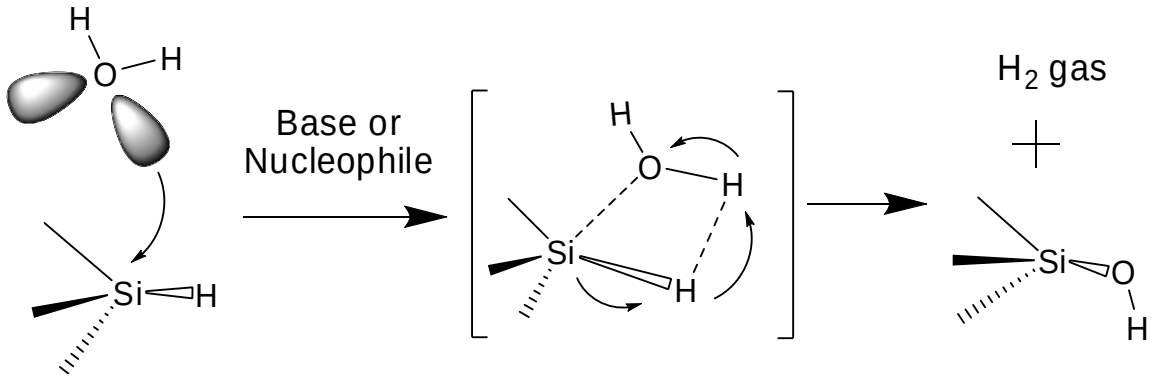

Figure 5.7 – The S_ni-Si mechanism for the hydrolysis of silane bonds.[14, 16, 19]

Since sol-gel reactions can be catalyzed at relatively low temperatures by either bases or nucleophiles, gelation reactions can be used to crosslink HSQ films below the thermal activation temperature of PAGs during direct-write processing.[1, 2, 25, 35, 179, 183, 203-206] The extent and rate of gelation is highly dependent on several factors including: the amount of catalyst present, the strength of the base, the reaction temperature, the reaction time, and the amount of moisture.[1-3, 25, 35, 42, 205, 210, 219, 230, 236]

5.3.3 Gelation Studies: Cage-to-Network Rearrangements and Rigidity

Gelation experiments were performed on spun-coated HSQ films with the goal of investigating whether the HSQ framework could be crosslinked via base-catalysis, and if so, how the gelation reactions were affected by the factors listed above. The bases used in the gelation experiments were ammonia vapor, cyclohexylamine and N-methylnifedipine hydroxide (the latter two bases were released by the PBGs shown in Figure 5.1). For the ammonia treatments, a shallow aluminum tin was filled with 26 mol% aqueous ammonia solution before being placed underneath an overturned crystallizing dish. The closed vapor-liquid system was allowed to equilibrate for 20 minutes before spun-coated HSQ films thickness were placed under the overturned dish to expose them to ammonia vapor. The ammonia treatments were performed at ambient temperature for various times ranging from 1-45 minutes. To determine the overall influence of temperature gelation via the ammonia treatment, the ammonia treatments were repeated in preheated ovens held at either 50^{o}C or 100^{o}C and equilibrated before inserting HSQ films for similar amounts of time to the ambient gelation experiments. For gelation experiments involving the use of PBGs, solutions of each of the PBGs shown in Figure 5.1 were made in MIBK solvent and then mixed with HSQ resin to form PBG-HSQ blends with PBG loadings between 1% and 13 wt% (with respect to dry HSQ resin). The PBG-HSQ solutions were then spin-coated onto silicon wafers and then exposed to ultraviolet radiation followed by a PEB for 30 minutes at temperatures above 120^{o}C in order to release bases and catalyze the crosslinking of the HSQ films.

In addition to FTIR analyses, the mechanical properties of all gelled HSQ films were characterized by nanoindentation using Oliver and Pharr's method, which is now

well established in literature.[3, 14, 16, 101, 237] According to literature, the FTIR spectrum of HSQ has stretch peaks centered at wavenumber values of 2250 cm^{-1}, 1130 cm^{-1} and 1070 cm^{-1}, which respectively corresponding to silane bonds, cage-type siloxane bonds, and network-type siloxane bonds.[11, 13-17, 19, 36, 234] When spin-coated HSQ films were exposed to ammonia gas, the FTIR stretch peak due to the silane bonds decreased, and a small peak centered at 3740 cm^{-1} appeared, as shown in Figure 5.8. The new peak in Figure 5.8 was due to the formation of silanol groups, confirming that silane bonds in the T^H resin were gradually being converted to silanol bonds during gelation. [179, 183, 205, 236] As the highly reactive silanol bonds condensed with adjacent silanol bonds, the amount of network-type siloxane bonds increased, as shown in Figure 5.9.

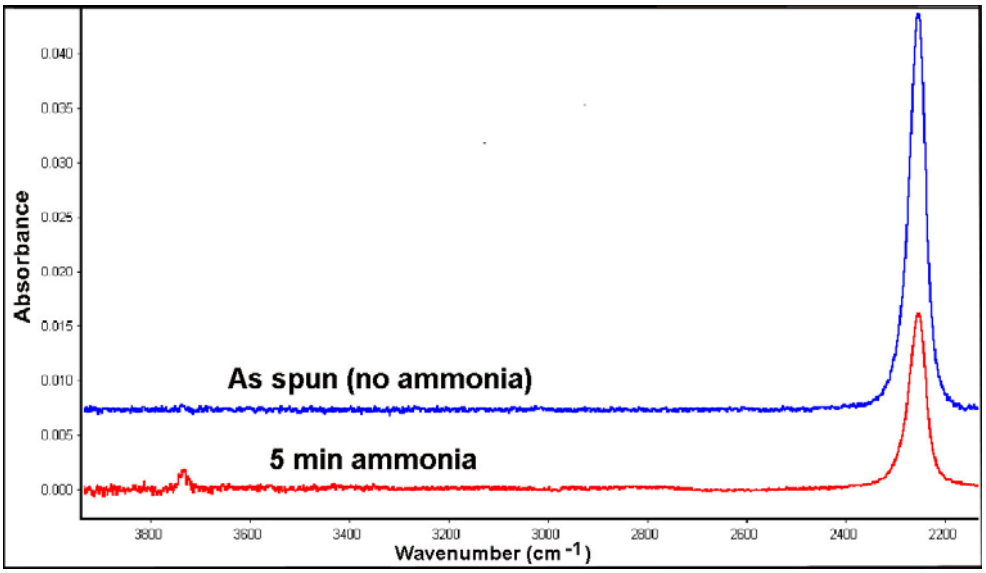

Figure 5.8 – Comparison of the silane and silanol content between an untreated (as spun) HSQ film and a film gelled for 5 minutes using saturated ammonia vapor at 25°C. The baseline of the untreated HSQ spectrum was offset for clarity.

The decrease in cage-type siloxane peaks in Figure 5.9 was due to the scission of these bonds via base-catalyzed hydrolysis, resulting in opening up the cage structure to form pentacoordinate transition states as reaction intermediates.[179, 183] The chemical structure of the unstable intermediates then preferentially rearranged to form an open network structure, which had less bond strain than the closed cage structures as described by West.[236] Hence, during gelation the ratio of the areas of cage-type siloxane peaks to network-type siloxane peaks decreased, and this ratio served as a measure of extent of HSQ crosslinking reaction.[11, 13, 14, 16, 17, 19]

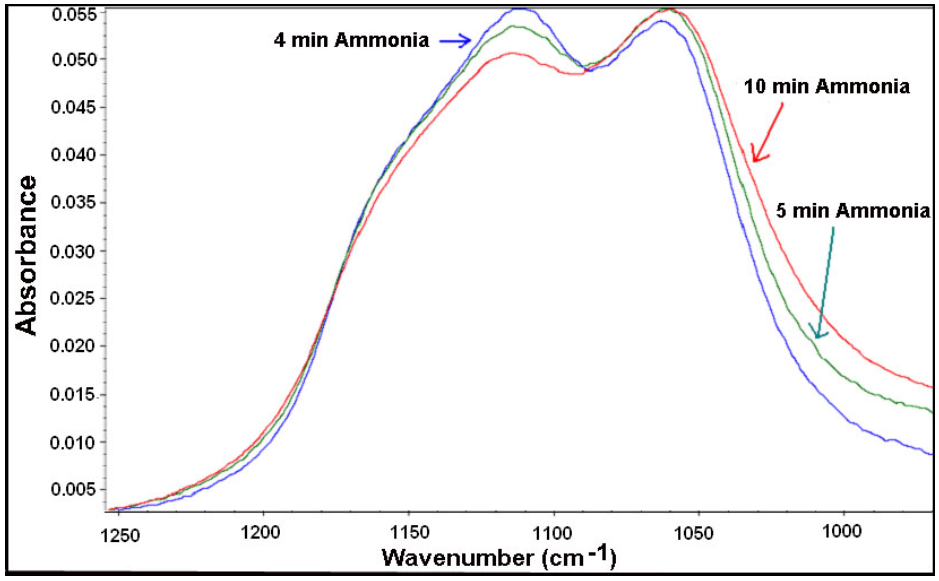

Figure 5.9 – Comparison of cage and network-type siloxane peak in HSQ films gelled for 4 (blue), 5 (green), and 10 minutes (red) using saturated ammonia vapor at 25°C.

Similar to methods cited in literature, photobase generators (PBGs) were mixed in formulations with HSQ in order to harden the matrix upon activation of the PBG via blanket UV-exposure or by thermal activation.[1, 2, 203, 204] Once activated, the PBGs released bases that catalyzed the cross-linking of HSQ units via the sol-gel condensation

of silanol bonds formed from the hydrolysis of silane bonds and rearrangement of hydrolyzed cage-type siloxane bonds to network-type bonds. [56, 57, 203, 204, 238-241] The average reduced moduli (E_r) of films gelled using either a basic vapor (ammonia gas) or a photobase are shown in Figure 5.10 along with their respective FTIR cage/network peak area ratios. It can be seen from Figure 5.10 that the reduced modulus of gelled films increased as the cage/network peak area ratio decreased.[14, 16, 19] This confirmed that as the relative amount of networked siloxane bonds to cage bonds increased, the HSQ matrix became more rigid.[14, 16, 19]

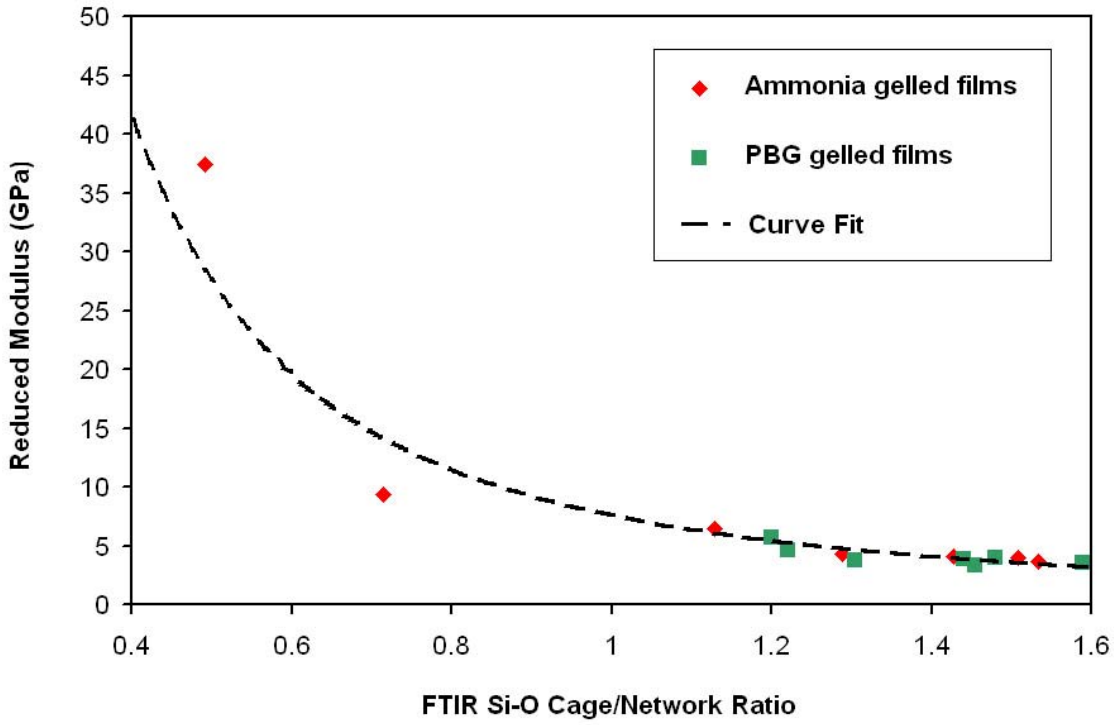

Figure 5.10 – Correlation between reduced moduli and cage/network ratios for HSQ films gelled using (♦) ammonia vapor at ambient temperature and (□) UV-released bases from PBGs after PEBs. For clarity, a curve fit (----) is used to show the trend in the data.

HSQ films that were exposed to saturated ammonia vapor for 3 minutes at ambient conditions had a final E_r of 3.65 GPa. This was observed to be about the same rigidity of gelled HSQ/PBG films with initial CTS or NBC loadings of about 3 wt% with respect to dry HSQ. The loading of N-methylnifedipine required to give an equivalent reduced modulus after activation of the PBG was only 1 wt% with respect to HSQ. When compared using a mass basis, the base released by N-methylnifedipine was the most efficient at crosslinking HSQ films, as shown in Figure 5.11. Even a molar basis confirms that N-methylnifedipine hydroxide base was much more efficient at hardening HSQ than the cyclohexylamine base released by the other two PBGs since the molecular weight of N-methylnifedipine is the largest of the three PBGs studied, then.[56, 57, 203, 204, 238-241]

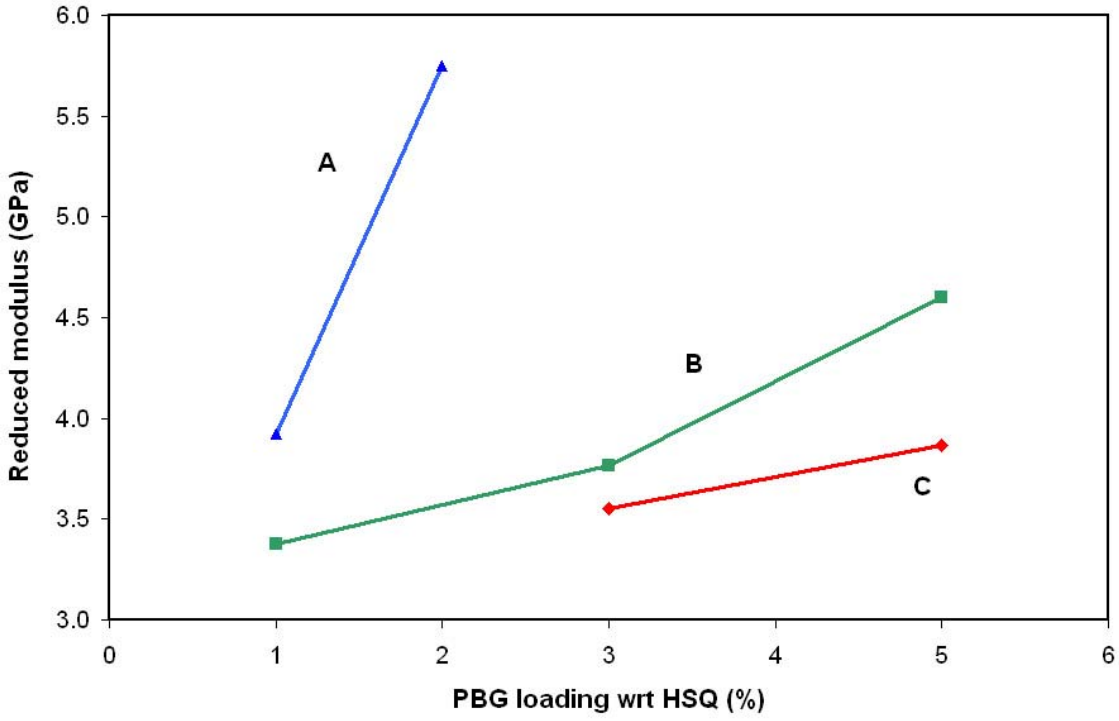

Figure 5.11 – Relative comparison of mechanical rigidity induced by bases released by (A) N-methyl nifedipine, (B) NBC, and (C) CTS at different PBG loading levels.

The presence of direct-written porosity in UV-exposed areas was indicated by refractive index values dropping below that of pure HSQ control films (1.389) that underwent similar heating cycles. By using the Lorentz-Lorenz refractive index mixing rule to estimate induced porosity, it was observed that the level of rigidity needed for direct-written films to be able to support 10 vol% porosity corresponded to E_r values of at least 3.5 GPa while 20 vol% porosity required E_r values of over 4 GPa. Films with E_r less than 3.1 GPa after gelation had refractive indices equal to that of the HSQ control samples after the decomposition of **PNC1-ROP**. This result implied that the matrix was not rigid enough to support porosity because pores that were formed ultimately collapsed resulting in non-porous HSQ films.

5.3.4 Gelation: Influence of Water Content on Extent of Bond Transformations

According to the hydrolysis mechanism shown in Figure 5.7, water is necessary for the hydrolysis of the silane bonds in HSQ to occur, and thus it predicts that the water content in the gelled films and/or the vapor above the films is a key factor affecting the extent of gelation of HSQ. In order to validate this, multiple experiments were conducted to test the ability of ammonia gas to catalyze the gelation of HSQ films that were pre-dried on hotplates at about 100^{o}C to drive off the trace amounts of water in the films. Even though the physical conditions were kept constant with those of non-dried films (referred to as 'standard conditions'), which were described in the previous sections, Table 5.1 and Figure 5.12 show that ammonia was not able to gel these films to any significant degree since their c/n ratios remained as high as original values of as-spun films. Although the gelation-catalysts were present in the pre-dried films, the amount of

water molecules that were available to take part in the hydrolysis of silane bonds was negligible and thus very few silanol bonds were formed, leading to poor gelation results. As a confirmation of the overwhelming importance of water content in the HSQ gelation system, ammonia treatments were repeated as before but using non-dried HSQ films and performed in chambers that were pre-humidified with steam. These humidified conditions resulted in much lower c/n ratios, as shown in Table 5.1, indicating that higher levels of humidity favored gelation.

Table 5.1 – Comparison of ranges of c/n ratios of multiple HSQ films treated with ammonia gas for 10 minutes under varying physiochemical conditions

Temperature of ammonia treatments	c/n ratio of pre-dried films	c/n ratios of films treated under standard conditions	c/n ratios in humidified chambers
25°C	1.61	1.39-1.41	1.0-1.11

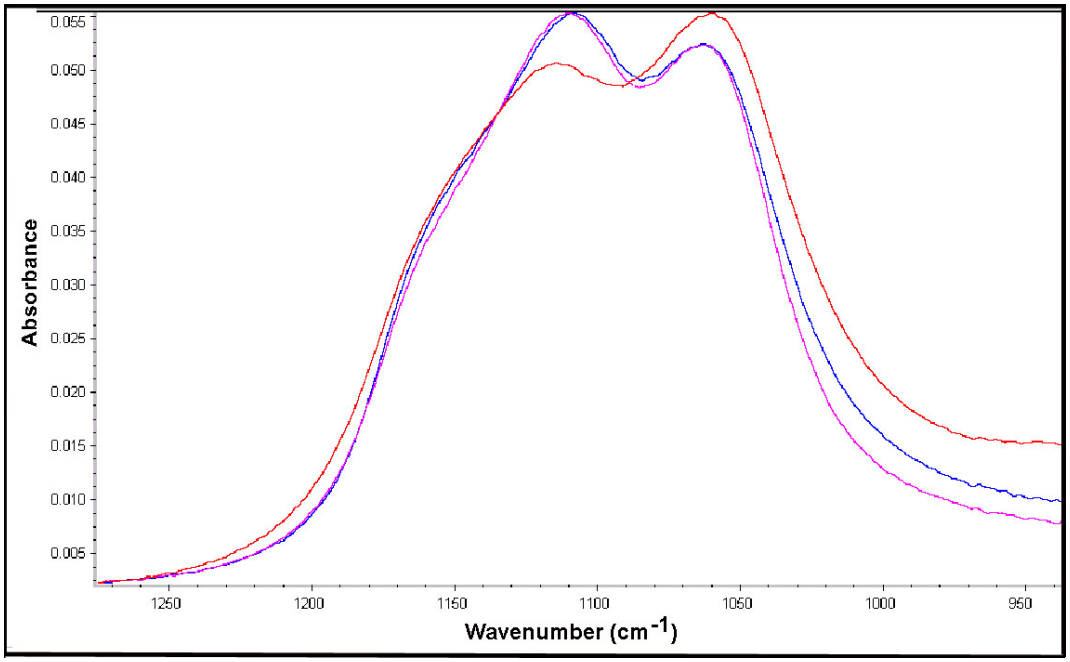

Figure 5.12 – FTIR spectra of HSQ films that were as-spun (pink), gelled for 10 minutes using standard ammonia treatments (red), and pre-dried ammonia treated films (blue)

To further test the influence of water content on the gelation of HSQ films, standard ammonia treatments were performed at elevated temperatures, and FTIR was used to compare the gelation results with those of ambient runs. As shown in Figure 5.13, the degree of crosslinking of HSQ *decreased* dramatically as the oven temperature was increased from ambient to 50^{o}C and again when increased further to 100^{o}C; the FTIR curves of films treated with ammonia at both 50^{o}C and 100^{o}C were barely distinguishable from as-spun films, indicating that a negligible amount of gelation reactions had occurred at these temperatures. These results were unexpected because according to the Arrhenius effect, the pre-exponential rate constants for the gelation reaction should have increased as temperature was raised. Additionally, increases in temperature drove more ammonia gas from the aqueous ammonia solutions into the vapor phase, leading to increases in the amount of ammonia catalyst in the system.

To understand the results, we must take into account that as the oven temperatures were increased, more water was driven from the HSQ films into the vapor phase. Since the HSQ films had only trace amounts initially, the above-ambient temperatures effectively hindered the base-catalyzed crosslinking of the films by removing the water molecules necessary for hydrolysis of the silane bonds within the films. The effective decrease in water content as the temperature was raised played a more crucial role in dictating the extent of gelation of the HSQ films than the increases in both the pre-exponential rate constants and the amount of ammonia catalyst. By combining the results shown in Figure 5.13 with those shown in Figure 5.12 and Table 5.1 it is clear that the amounts of water molecules present in the system used for gelation films, either within the films or within the air above the films, was the most dominant factor affecting the

degree of crosslinking of HSQ films. This is because, unlike FOx-1x® resin, HSQ films contain only trace amounts of water. Thus, water content was the limiting component for the solid-phase gelation reactions, in the absence of which bases were ineffective at promoting gelation.

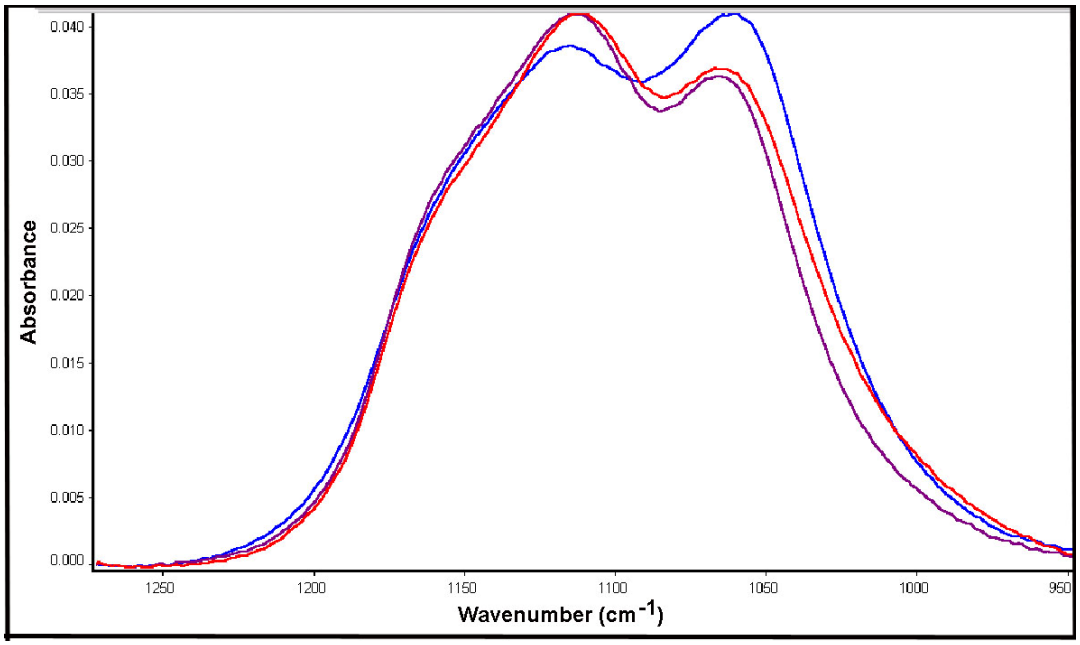

Figure 5.13 - Comparison of crosslinking in HSQ films that were exposed to ammonia for 10 minutes at 25°C (blue), 50°C (red), and 100°C (purple).

5.3.5 Gelation: Sol-Gel Induced Film Shrinkage of HSQ Matrix

As stated earlier, water molecules are active participants of both the hydrolysis and condensation reactions.[28, 60, 179, 205, 242] As siloxane bonds were formed and water molecules were displaced from the sol-gel skeletons, the film density increased along with the film rigidity. [14, 15] Although sol-gel reactions are reversible, the water molecules produced during the gelation step of the direct-write process were permanently lost during bake steps as a result of volatilization. Researchers have shown that in

addition to hardening films, the sol-gel chemical interactions result in film shrinkage, which can be very significant since a water molecule is generated for every pair of silanol bonds that react directly with each other. To determine the degree of film shrinkage induced by gelation, the thicknesses of all gelled HSQ films were tracked using ellipsometry and recorded. It was observed that both ammonia-treatments and photobase treatments caused HSQ films to shrink by about 5-6% with respect to the thicknesses of as-spun films.

In comparison to the gelation, crosslinking of HSQ via thermal curing (baking for an hour at 350-400^{o}C in inert atmosphere) only caused the thicknesses of HSQ films to decrease by less than 1%.[15] The reason that thermal curing did not result in significant film shrinkage was because only the structural transformations corresponding to rearrangement and redistribution reactions took place; hence, the densification that is associated with the loss of silane bonds did not occur.[243, 244] As discussed in a later section, the differences in film shrinkage effects caused by gelation and thermal cure reactions result in morphological differences in the internal pore structures of direct-written and thermally-induced porous films.

5.4 Characterization of $Q_8M_8^H$ Cages

5.4.1 ^{1}H NMR and ^{29}Si{^{1}H} NMR Analyses of $Q_8M_8^H$

The ^{1}H NMR spectrum of $Q_8M_8^H$ is shown in Figure 5.6, complete with annotations for the silane protons (septet peaks from δ = 4.72-4.76 ppm) and methyl protons (doublet peaks at δ = 0.25-0.26 ppm) that are present in the M^H (ie. $OSiMe_2H$) groups.[210, 229, 231] We clearly observe from Figure 5.6 that the ratio of the ^{1}H NMR

integrals of the peaks corresponding to the silane protons and the methyl protons was 1:6, which agrees with the stoichiometry of the M^H groups. Figure 5.7 shows the $^{29}Si\{^1H\}$ NMR spectrum of $Q_8M_8^H$, with annotations for the Q silicon peak (ie. $\underline{Si}(OSi)_4$) and M^H silicon peak.[18, 210, 229, 231]

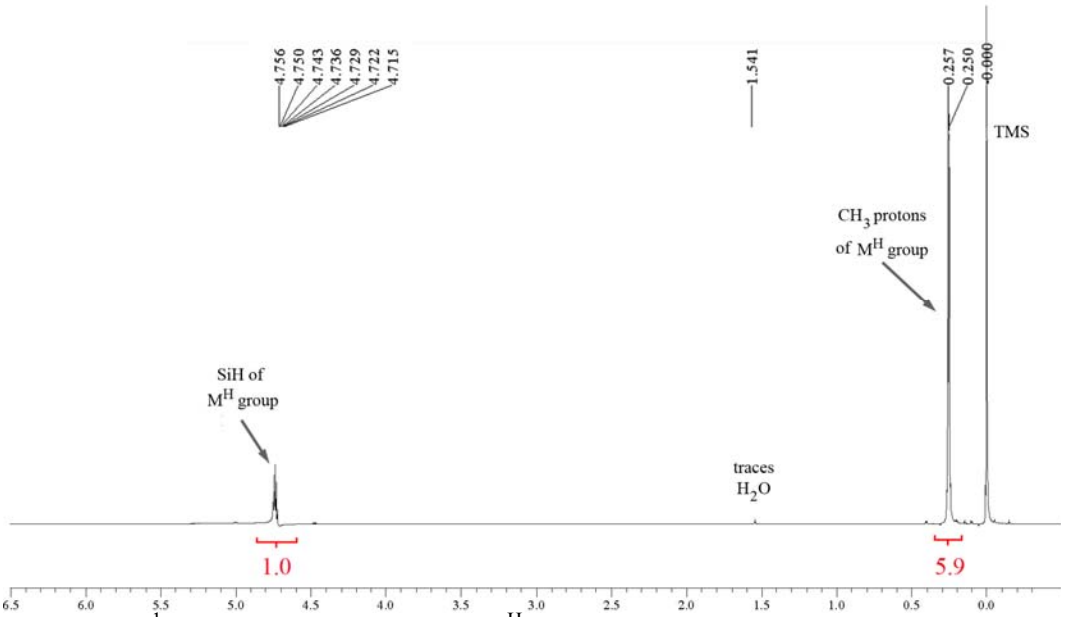

Figure 5.14 – ^1H NMR spectrum of $Q_8M_8^H$ showing the silane and methyl proton peaks

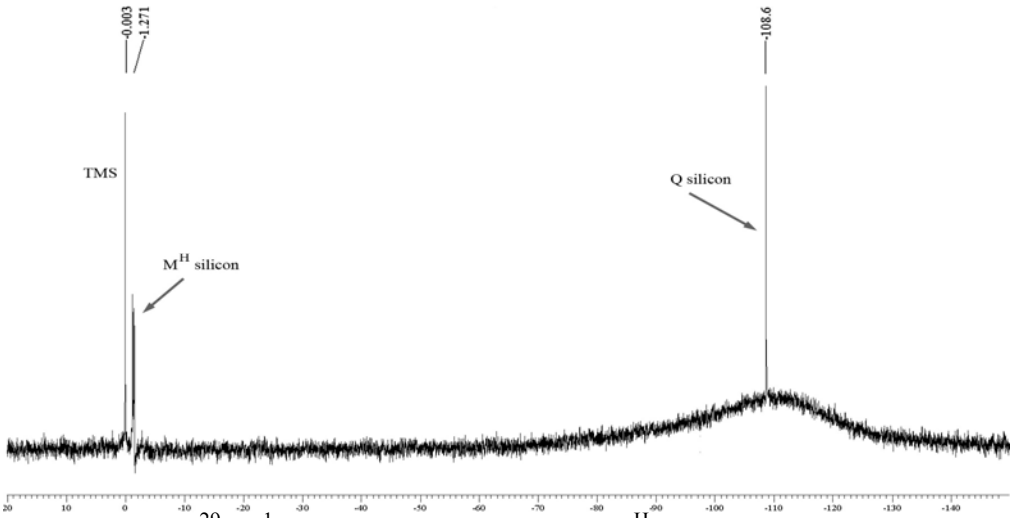

Figure 5.15 - $^{29}Si\{^1H\}$ NMR spectrum of $Q_8M_8^H$ showing the silicon peaks corresponding to the M^H and Q groups

The broad peak between δ = -100 ppm and δ = -125 ppm was an artifact that was produced by the Q silicon groups in the glass probe of the NMR equipment).[3, 18, 179, 181, 182, 210] Both NMR spectra of $Q_8M_8^H$ had narrow well-resolved (free of overlapping) NMR peaks and only two types of silicon groups were present (M^H and Q). This indicated that $Q_8M_8^H$ crystals were not composed of a distribution of chemical structures, unlike the HSQ resin (refer to Figure 5.5 and Figure 5.6). Although end-group analysis of $Q_8M_8^H$ silicate cages could not be performed since they are not linear chains, published crystallographic data for $Q_8M_8^H$ and other POSS cages (eg. T_8^H) shows that their POSS cores have end-to-end distances less than 1 nm across.[210, 222, 224, 232, 233, 245, 246]

5.4.2 Bond Fragmentations and Sol-Gel Reactions in $Q_8M_8^H$ Cages: Solid-State DP-MAS ^{29}Si NMR Studies and TGA-MS Analyses

Since the pendant M^H groups in $Q_8M_8^H$ cages have silane group functionality, the Q-POSS structure is susceptible to the sol-gel reactions, which were discussed earlier in gelation studies of HSQ films.[1, 2, 183, 203-206, 219] This phenomenon was confirmed when PNC-Q8M8H nanocomposites (whose synthesis and purification procedures are discussed in chapter 6) were observed to contain silanol groups on their POSS cages, which led to the gelation of the nanocomposites into insoluble solids if the silanols were not quickly silanized with TMCS. The similarity of the $Q_8M_8^H$ and HSQ chemical structures, and the general tendency of cyclic siloxanes to rearrange themselves into tetrahedral siloxane networks to relieve internal bond strains strongly suggests that the bond rearrangement and redistribution reactions that occur during the thermal curing

of HSQ films may also take place when $Q_8M_8^H$ is heated.[15-17, 236] If this scenario is accurate, then the fragmentation and gelation reactions of $Q_8M_8^H$ and HSQ resin chains would facilitate their covalent bonding due to crosslinking co-reactions. The co-hydrolysis cross-condensation of different sol-gel precursors via gas-phase or liquid-phase chemistry is a well-established method of producing silica-like hybrid films; thus, the co-reactions between $Q_8M_8^H$ and HSQ resin structures is practical.[3, 18, 179, 181, 182, 205, 210, 219] Hence, the POSS segments of PNC-$Q_8M_8^H$ nanocomposite molecules were intended to offer dual functionality of: (a) compatibilizing the polycarbonate chains with the surrounding HSQ matrix, and (b) providing a means of physically preventing phase-segregation via the crosslinking of $Q_8M_8^H$ with HSQ.

Solid-state DP-MAS ^{29}Si NMR studies and TGA-MS analyses were both performed on $Q_8M_8^H$ samples to determine the influence of high temperatures on the chemical structure of $Q_8M_8^H$ and also to determine what bond transformations were taking place during heating. The detailed procedures by which DP-MAS ^{29}Si NMR studies and TGA-MS analyses were performed were outlined earlier in chapter 2. Figure 5.16 shows the TGA profiles of two $Q_8M_8^H$ samples that were dynamically heated in a TGA furnace in N_2 atmosphere; $Q_8M_8^H$ sample A had traces of moisture present prior to heating and sample B was vacuum dried overnight at 80^{o}C to make it moisture-free prior to heating. From Figure 5.16 we see that in the absence of moisture (sample B), the POSS fragmented into volatile products that were swept out of the TGA furnace by the N_2 purge stream. When the POSS was heated in the presence of water molecules, both hydrolysis reactions as well as sol-gel condensation of fragmentation products took place that produced a thermally-stable residue, as observed for sample A in Figure 5.16.

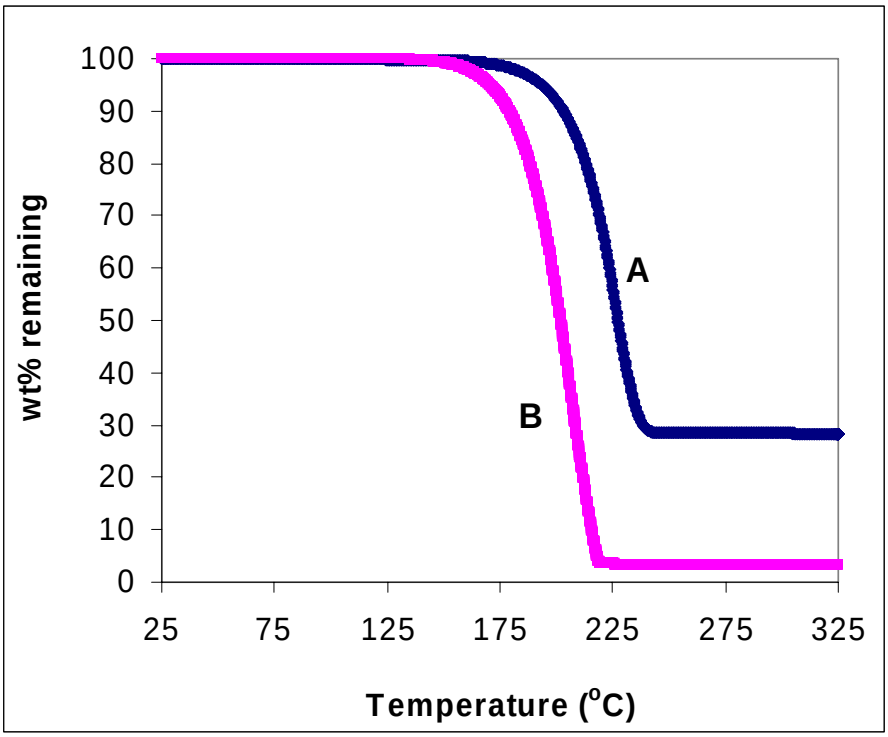

Figure 5.16 – Dynamic TGA profiles of two $Q_8M_8^H$ samples. Sample (A) not vacuum dried prior to heating and sample (B) vacuum dried prior to heating

The overall relative abundance of the major MS peaks detected during the dynamic heating of $Q_8M_8^H$ sample A is shown in Figure 5.17. MS data for the fragmentation of moisture-free $Q_8M_8^H$ (ie. sample B) is shown in Appendix B. From the assignments of the MS peaks in Figure 5.17 to chemical species (see Appendix B), we observe that numerous silicon-containing gases were evolved during the heating of $Q_8M_8^H$, including: Si^+ (m/e = 28), SiC^+ (m/e = 40), $HSiMe_2OH$ (m/e = 77), $HOSiMe_2O^+$ (m/e = 91), $Si(OH)_4$ (m/e = 96), etc. Sol-gel literature references confirmed that the evolution of these volatile products was consistent with all of the following types of reactions: the formation of multiple types of silanol groups via the hydrolysis of both

siloxane and silane bonds and the condensation of silanol intermediates to form both linear and cyclic siloxanes.[18, 21, 45, 60, 179, 181-183, 205, 210, 219, 236, 242]

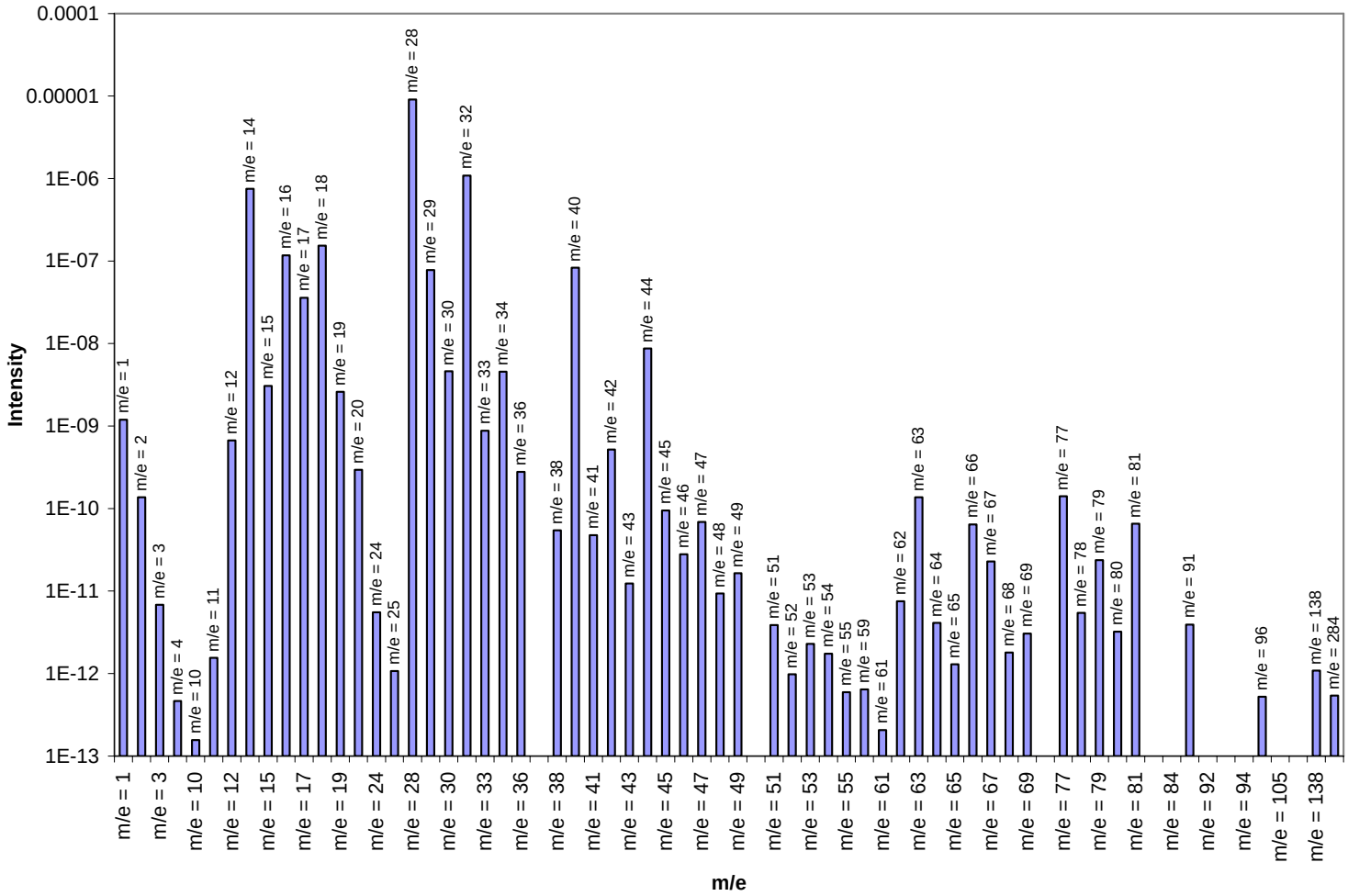

Figure 5.17 - Overall relative abundance of MS peaks detected during heating of $Q_8M_8^H$ sample A, which contained traces of moisture. The plot shows MS peaks for all masses with amu <300 and total peak intensities > 10^{-13} A

The TGA-MS results of $Q_8M_8^H$ were very encouraging since they suggested that nanocomposite molecules containing POSS segments could be covalently bonded to the HSQ matrix in a templated film. This would prevent movement of PNC chains prior to their decomposition, leading to the production of uniformly distributed small pores. As a means of validating the MS results for $Q_8M_8^H$, the residue of sample A was analyzed by solid-state DP-MAS ^{29}Si NMR, as shown in Figure 5.18.

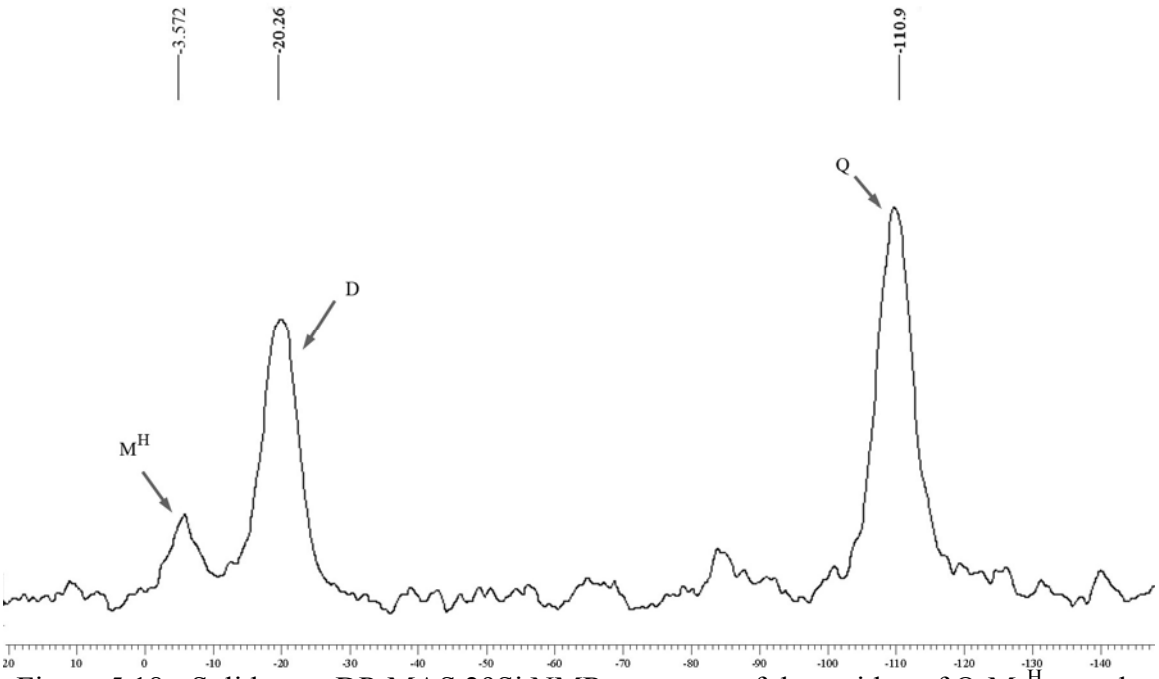

Figure 5.18 - Solid-state DP-MAS 29Si NMR spectrum of the residue of $Q_8M_8^H$ sample A (dynamically heated to 325^{o}C in the presence of traces of moisture)

^{29}Si Literature sources showed that residue was composed of M^H, D, and Q silicon groups (refer to Figure 5.4) within its chemical structure.[18, 179, 181, 182, 210, 215, 217, 219, 247] Since the initial chemical structure of $Q_8M_8^H$ did not dimethylsiloxy-linkages, the formation of D groups proved that silane bonds of the initial M^H groups

were hydrolyzed prior to the condensation of the resultant silanol groups (M^{OH}) with other terminal groups to form D linkages, as shown in equation (5.7) through equation (5.9).

$$-OSiMe_2H + H_2O \rightarrow -OSiMe_2OH + H_2 \quad (5.7)$$

$$-OSiMe_2OH + HOSiMe_2O- \rightarrow -OSiMe_2- + H_2O \quad (5.8)$$

$$-OSiMe_2H + HOSiMe_2O- \rightarrow -OSiMe_2- + H_2 \quad (5.9)$$

5.5 Spectroscopic Characterization of PDMSH Chains

5.5.1 ^{1}H NMR and ^{29}Si{^{1}H} NMR Analyses of PDMSH Chains

The ^{1}H NMR spectrum of PDMSH is shown in Figure 5.19, complete with annotations for the silane protons (septet peaks from δ = 4.67-4.73 ppm) of the M^H groups, the methyl protons of the M^H groups (doublet peaks at δ = 0.18-0.19 ppm), and the methyl protons (broad peak at δ = 0.07-0.09 ppm) of the D groups. [178, 215-217, 223, 225, 248] We clearly observe from Figure 5.19 that the ratio of the integral of the silane proton peak to those of the peaks corresponding to the methyl protons of the M^H and D groups, was 1:6:22. Based on end-group analysis, the average PDMSH oligomer must have had 7 D units per chain (Since each PDMSH chain had two M^H groups and each D repeat unit had a total of six protons). By calculating the formula weights of an $M^HD_7M^H$ chain structure, we observe that the M_n of the PDMSH oligomers was 652. This result is in close agreement with the expected range of molecular weights (400< M_n <600) that Gelest listed for their PDMSH product, which was based on their GPC data. By using equation (3.6) and siloxane and silane bond lengths and bond angles obtained

from literature [179], the $\langle r^2 \rangle^{1/2}$ values of the oligomeric PDMSH chains were calculated to be 1.57 nm long.

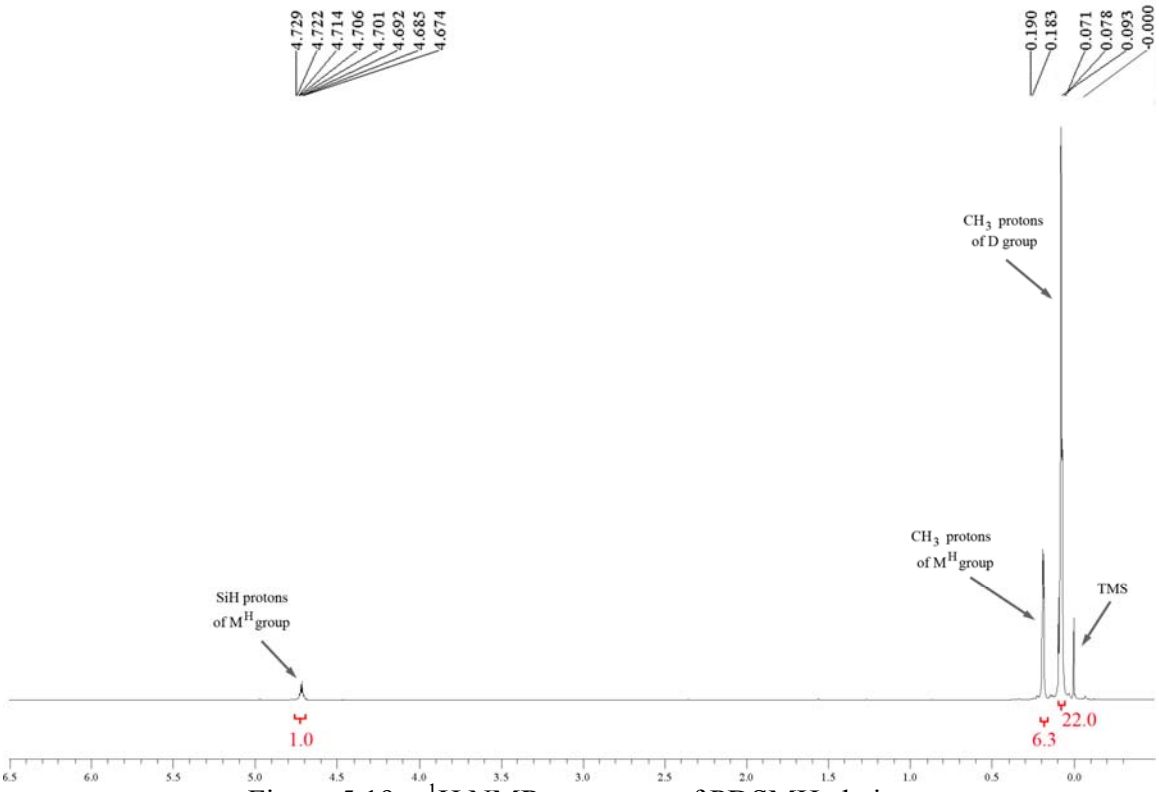

Figure 5.19 – ^{1}H NMR spectrum of PDSMH chains

Figure 5.20 shows the $^{29}Si\{^{1}H\}$ NMR spectrum for PDMSH, with the silicon-29 peaks between -4.50 ppm and -6.90 ppm corresponding to the M^H groups and the silicon-29 peaks between -17.74 ppm and -21.91 ppm corresponding to the D groups.[18, 174, 179, 181, 182, 215-217, 247]

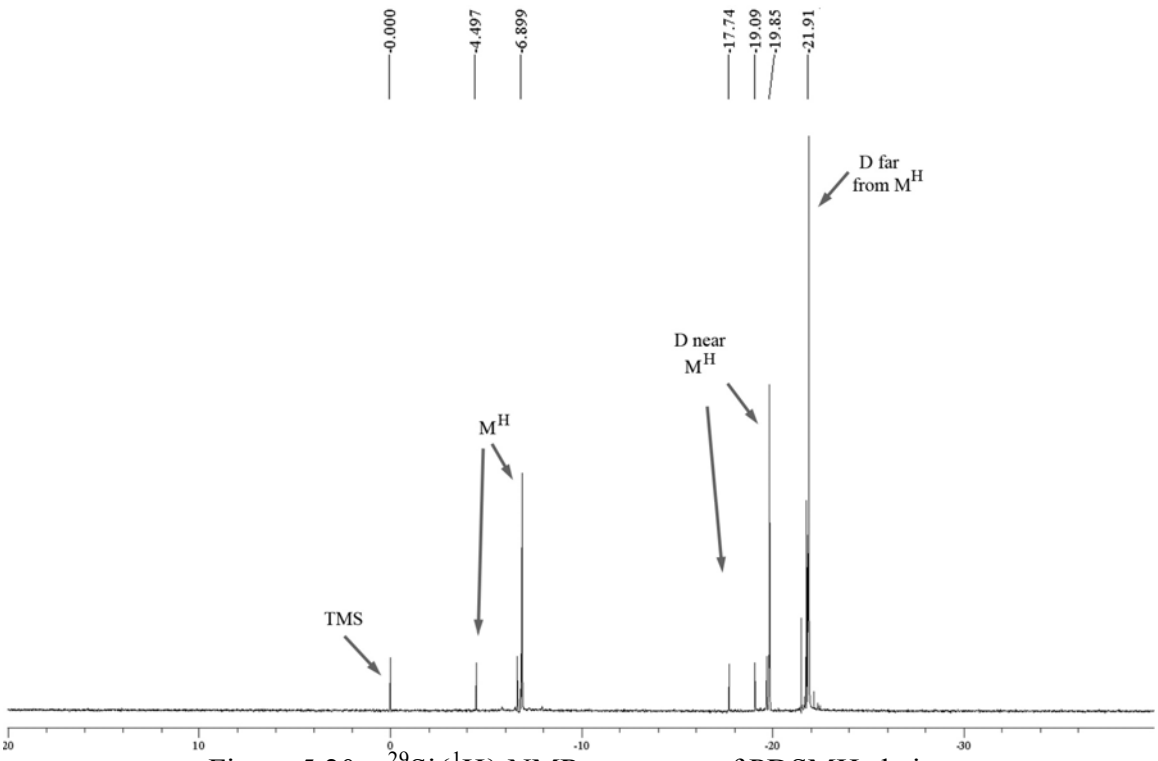

Figure 5.20 – $^{29}Si\{^{1}H\}$ NMR spectrum of PDSMH chains

5.4.2 TGA-MS Analysis of PDMSH Chains

TGA-MS analyses were performed on PDMSH samples to determine the influence of high temperatures on the chemical structure of the siloxane chains and also to determine what bond transformations were taking place during heating. Since PDMSH existed in the liquid state, the oligomeric chains evaporated when heated in the TGA furnace, as shown in Figure 5.21. The overall relative abundance of the major MS peaks detected (for the gases evolved with amu <129) during the dynamic heating of PDMSH is shown in Figure 5.22. The number of chemical species detected by the MS during the heating of the silicone was too many (every mass from amu =1-300 was detected) to be attributed simply to evaporation of the silicone's chains.

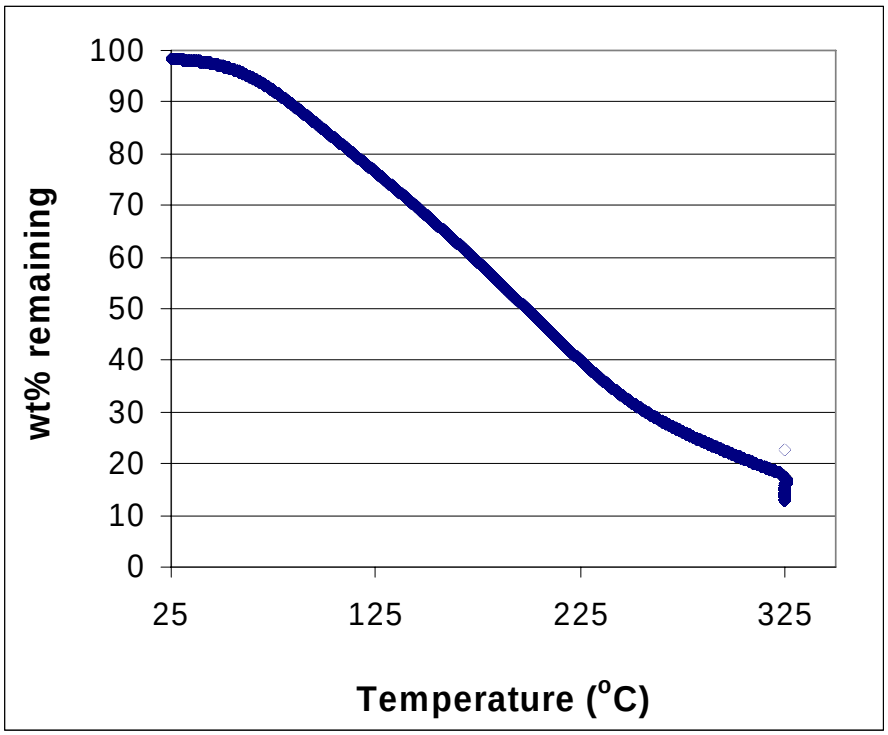

Figure 5.21 – TGA profile of PDMSH during dynamic heating

From the identification of the chemical species (refer to Appendix B) showed that several decomposition products were given off by PDMSH during the thermal analyses including: SiC^+ (m/e = 40), $SiMe_2^+$ (m/e = 58), $^+SiMe_2O$ or D (m/e = 74), $HOSiMe_2O^+$ or M^{OH} (m/e = 91), $SiMe_2OSiMe_2O^+$ (m/e = 148), and numerous small cyclic siloxanes and linear siloxanes such as D_3 (m/e = 192) and D_4 (m/e = 296).[18, 174, 179, 181, 182, 215-217, 247, 249] As shown in Figure 5.23, linear siloxanes are known to depolymerize at high temperatures reversibly into cyclic siloxanes (D_3, D_4, etc) and smaller linear siloxane chains especially when the silicone chains are terminated by reactive end-groups such as silanes.[179, 249] Additionally, silicones degrade hydrolytically in the presence of water at temperatures as low as 150°C, producing pairs of silanol-terminated chains per siloxane bond cleaved, as shown in Figure 5.24.[60, 179]

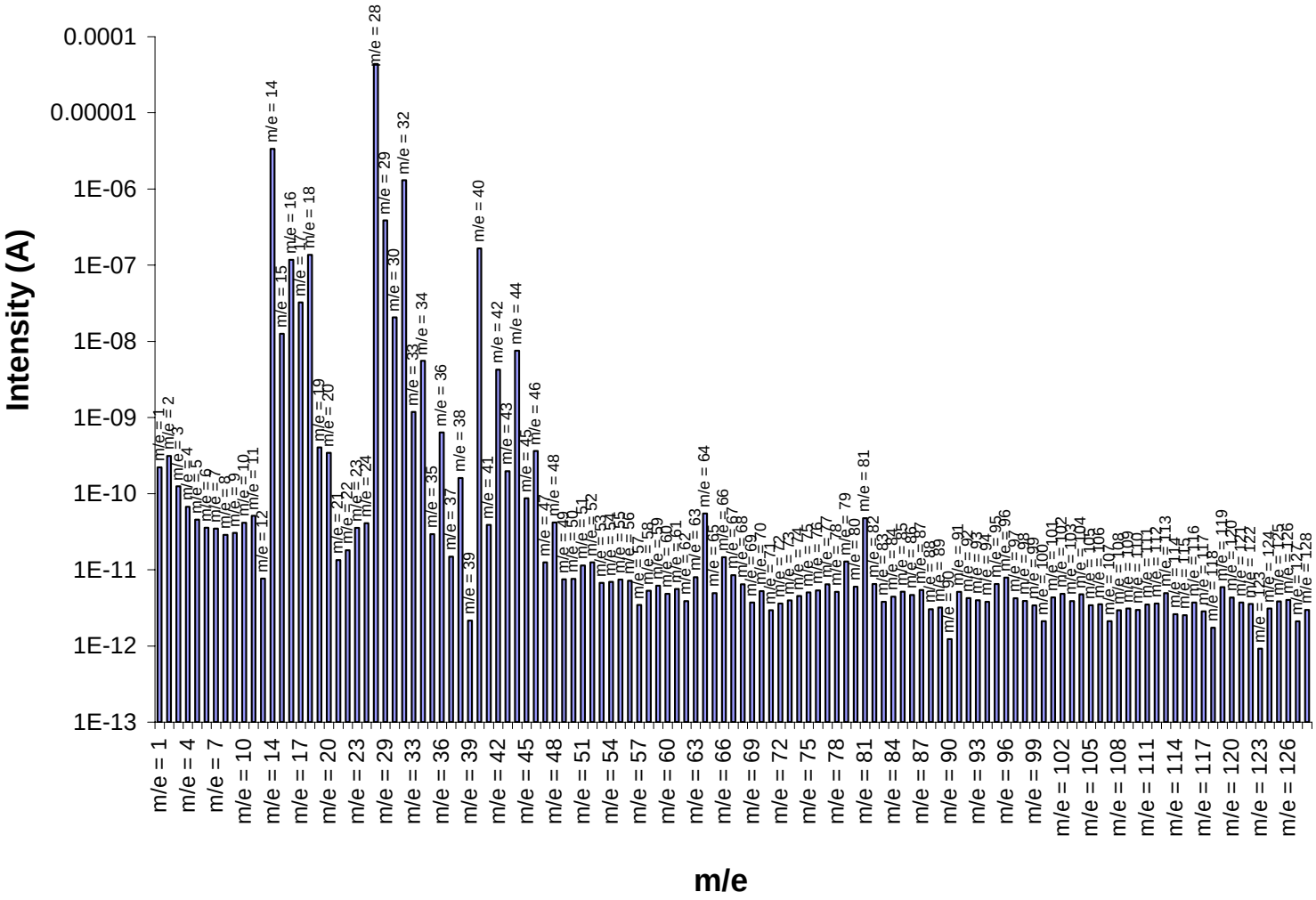

Figure 5.22 – Overall relative abundance of MS peaks detected during heating of PDMSH. The plot shows MS peaks for all masses with amu <129 and total peak intensities > 10^{-13} A

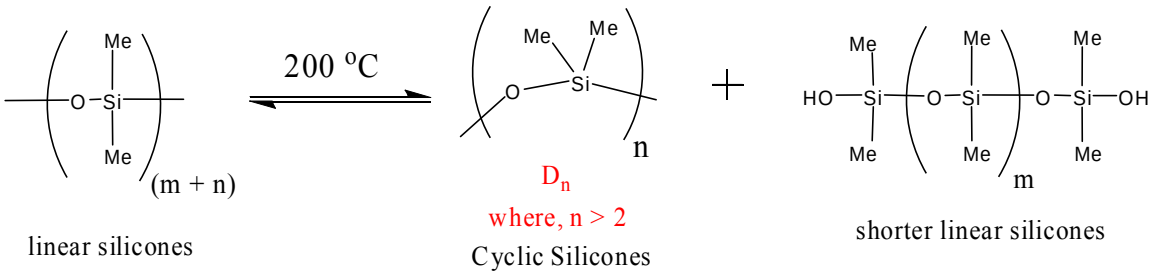

Figure 5.23 – Thermolytic de-polymerization of silicone chains

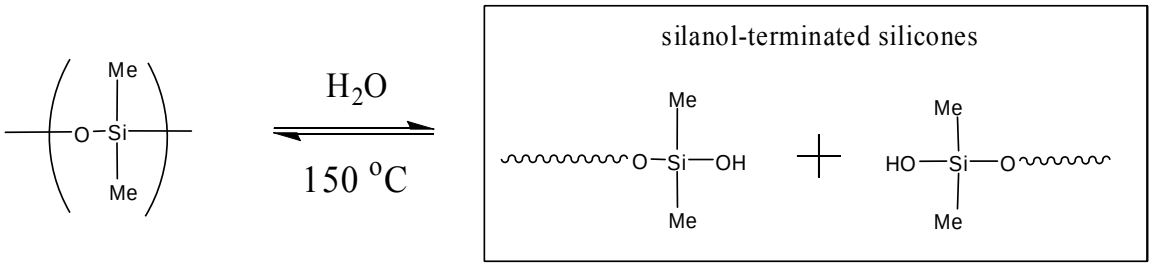

Figure 5.24 – Hydrolytic cleavage of silicone chains

Hence, at temperatures below 150°C only evaporation of PDMSH oligomers occurred in the TGA furnace, whereas at higher temperatures the chemical structure of the oligomers began to degrade via a combination of hydrolytic cleavage and thermally-induced de-polymerization to produce numerous linear and cyclic siloxane decomposition products.[179] The fragmentation of the decomposition products via de-protonation, de-methylation, de-hydroxylation, etc accounted for the detection of chemical species weighing amu = 1-300, which was the entire detection range of the MS tool. We may deduce from the TGA-MS results that PNC-PDMSH nanocomposites would contain two sacrificial segments (both PNC and PDMSH) owing to both of these types of chains being unstable at high temperatures. This assumption is later confirmed in chapter 6 where the PNC-PDMSH nanocomposites are shown to fully decompose into volatile products with minimal residue after being heated dynamically to 325°C.

CHAPTER 6

SYNTHESIS AND CHARACTERIZATION OF PNC-SILOXANE AND PNC-SILSESQUIOXANE NANOCOMPOSITE MOLECULES

6.1 Materials Used

Anhydrous dichloromethane (DCM), anhydrous trimethylchlorosilane (TMCS), $CDCl_3$, and type-3A (4-8 mesh) molecular sieves were purchased from Fisher Scientific. $CDCl_3$ was stored in a refrigerator over the molecular sieves to avoid moisture uptake. Tetramethylsilane (TMS) and $Cr(acac)_3$ were obtained from Sigma Aldrich and NMR samples were prepared via methods outlined in chapter 2. TMS and anhydrous TMCS were stored in a freezer to maintain their stability. Reagent grade hexane, toluene, acetone, and chloroform were purchased from VWR and stored over type-3A molecular sieves to prevent moisture uptake. Activated carbon was obtained from Sigma Aldrich in powder form, poured onto a watch glass, and dried overnight at 80^{o}C under high vacuum conditions prior to use. Reagent-grade xylene solvent (mixture of isomers) was also purchased from Sigma Aldrich, and used without further purification.

All glassware was purchased from Chemglass and silanized with TMCS, then vacuum-dried at 80^{o}C or higher, then cooled under a dry nitrogen atmosphere prior to use. PDMSH and $Q_8M_8^H$ were obtained from Gelest and HSQ resin was obtained from Dow Corning as a solution in MIBK solvent (FOx-16). PDMSH was used as received, and $Q_8M_8^H$ was dried of moisture, as detailed in chapter 5. The dry $Q_8M_8^H$ solids were added to reaction flasks within 30 minutes of being exposed to air again. The procedure

used to recover dry HSQ resin solids free of silanol groups from the FOx-16 solution was discussed in chapter 5. The dry T^H resin was refrigerated in a Nalgene storage vial prior to use in hydrosilylation reactions to prevent the formation of silanol groups in its structure. The procedures for synthesizing and purifying vinyl terminated **PNC3v** oligomers were outlined in an earlier chapter. Platinum divinyl-tetramethylsiloxane complex or Pt(dvtms) was purchased from Gelest as a solution in dry xylene solvent (2.25 wt% platinum metal). Prior to use, the stock catalyst solution was diluted to a concentration of approximately 0.0153 wt% (0.68 mM) platinum metal and stored in a refrigerator in an opaque vial. All reactions were carried out under filtered yellow lighting to avoid photo-oxidation of the catalyst during the hydrosilylation reactions. Disposable polypropylene-casing Luer-lock type syringes, stainless steel Luer-lock type syringe tips, PTFE membrane syringe filters with 0.2 μm pores, and PTFE-coated stirrer bars were also purchased from VWR.

6.2 Grafting via Hydrosilylation

All the grafting reactions used to covalently link the **PNC3v** oligomers and the siloxane and silsesquioxane precursors operated via hydrosilylation mechanisms. Hydrosilylation refers to the addition of silane bonds (Si-H) to unsaturated organic bonds (eg. C=C, C≡C, C≡N, C=O, etc). [179, 181, 182, 250, 251] The overall reactions for the grafting of **PNC3v** oligomers to the siloxane and silsesquioxane precursors used in this study are summarized by equation (6.1).

$$R_1SiH \quad + \quad CH_2{=}CHR_2 \rightarrow \quad R_1SiCH_2CH_2R_2 \qquad (6.1)$$

Hydrosilylation reactions are catalyzed by both homogenous and heterogenous transition metal catalysts, the majority of which are derived from one of the following metals: platinum, cobalt, rhodium, ruthenium, and iridium.[179, 181, 182, 250-252] Platinum catalysts are highly efficient (required loadings are on the order of 1-100 ppm with respect to the limiting reactants), they have been shown to be highly selective towards alkene and alkyne bonds in the presence of other unsaturated groups such as carbonyls (carbonate linkages are not hydrosilylated so long as the molecules contain unsaturated carbon-carbon bonds), and their reaction mechanism and reaction rate laws are better understood than the other catalysts.[179, 181, 182, 251] Hence, Pt(dvtms) was chosen as the catalyst for the hydrosilylation reactions between vinyl-terminated polycarbonates and the siloxane and silsesquioxane precursors listed above. Although hydrosilylation reactions are commonly used by researchers to introduce organic functionality into silicon-based frameworks, care must be taken to ensure that no moisture is present otherwise the catalysts will facilitate the insertion of hydroxyl groups at the silicon center to form silanol groups (silanols produce hydrolytic instability and eventually promote gelation).[95, 181, 213, 214, 221, 229, 231, 251, 253-255] For this reason, the reactants, solvents, glassware, and other components used in the reaction system (including the syringes used to remove aliquots from the reaction mixtures and their tips) were all thoroughly dried prior to each use.

Researchers have also shown that silane terminated linear siloxanes (eg. PDMSH) and cylic siloxanes (eg. tetramethyl-tetrasiloxane or D_4^H) efficiently undergo hydrosilylation with the following groups: vinyl, alkyne, methacrylate, and nitrile groups.[178, 215-217, 223, 225, 248] Although there have been no reports of aliphatic

polycarbonate chains being grafted via hydrosilylation, Kim and co-workers successfully hydrosilylated vinyl-terminated PBAC chains using both small silanes (eg. tripropylsilane) and small silane-terminated siloxanes (eg. tetramethyldisiloxane or D_2^H).[256] Since the carbonate linkages in their PBAC chains remained stable throughout their hydrosilylation reactions, Kim and co-workers's results provided evidence that **PNC3v** chains could be hydrosilylated without degrading their main chain structures.

$Q_8M_8^H$, and HSQ *cages* (octahydridosilsesquioxane or T_8^H) have both been shown to be highly reactive towards hydrosilylation with various unsaturated functional groups except if they were sterically hindered.[95, 182, 213, 214, 221, 229, 246, 250, 253, 255, 257] Although there have not been any reports of the synthesis of silsesquioxane-polycarbonate compounds, there have been a multitude of successful grafting reactions between silsesquioxane cages and other macromolecules, which implied that the grafting of **PNC3v** oligomers to $Q_8M_8^H$ was feasible.[213, 255, 257] A literature review yielded only one report of the successful hydrosilylation of HSQ resin's *chains*, which implied that HSQ *chains* may have much lower than their T_8^H *cage* counterparts due to steric hindrance.[95] However, successfully grafting of sacrificial chains directly to the HSQ resin structure would solve all phase-compatibility issues between the organic and inorganic phases, leading to monodisperse porous films with small pore sizes. Hence, PDMSH, Q8M8H, and HSQ *chains* were all used as co-reactants with **PNC3v** oligomeric chains in hydrosilylation reactions. The synthesis and purification procedures for each grafted nanocomposite are summarized in the following sections.

6.3 Hydrosilylation of PNC3v with PDMSH: Type-1 Nanocomposites (NC1)

6.3.1 Synthesis and Purification of NC1 Molecules

Hydrosilylation reactions were used to graft **PNC3v** chains to **PDMSH** chains to form type-1 nanocomposite molecules (**NC1**), as shown in Figure 6.1. The procedures for synthesizing and purifying a typical batch of **NC1** solids are summarized below. Prior to adding reactants, a pre-silanized, 100 ml 3-neck flask was heated above 100°C, while under high vacuum conditions to desorb any moisture from its sidewalls. Then the flask was backfilled with dry N_2 gas and allowed to cool to ambient under the inert atmosphere. 0.412g (approximately 0.22 mmoles) of **PNC3v** solids, 1.246g (1.96 mmoles) of PDMSH, and 0.358g of a 0.0153 wt% solution of Pt(dvtms) in xylene (platinum loading of 900 ppm with respect to **PNC3v** chains) were added to the flask.

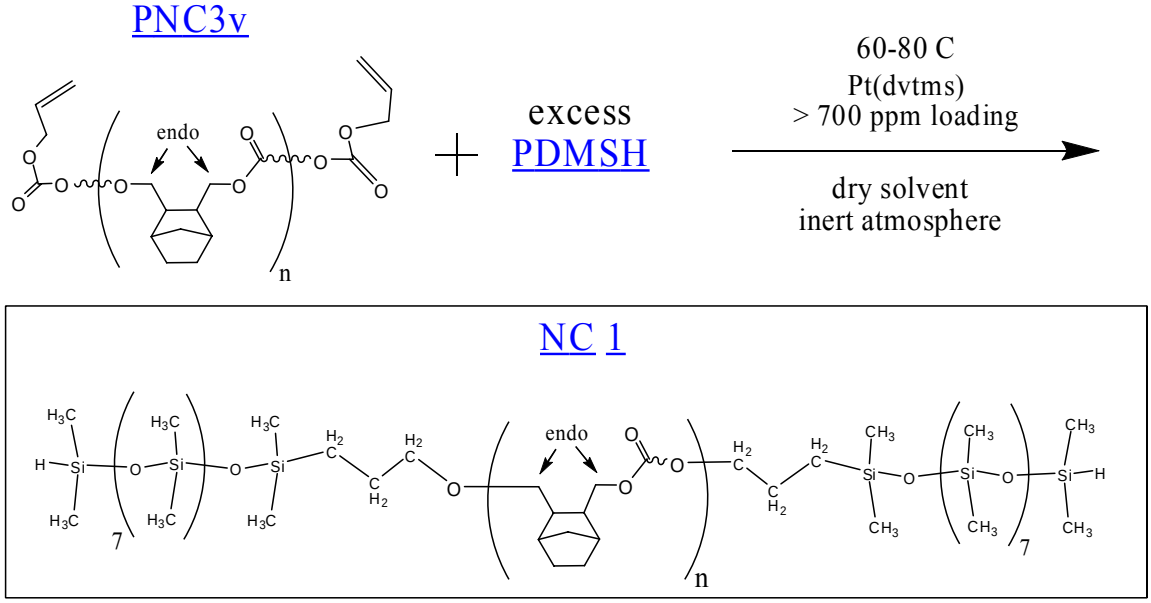

Figure 6.1 – Reaction scheme for the synthesis of **NC1** hybrid molecules

Then 40 ml of dry toluene was added to dissolve the reactants, and the flask was sealed using two 2-way valves and one air-tight plug that held an immersion thermometer in place. One of the valves was connected to a vacuum pump, and the other was connected to a cylinder of high-purity dry Nitrogen gas. The flask was then evacuated until the bubble point of toluene was reached before being backfilled with N_2 gas. The cycle of evacuation and N_2-backfilling was repeated at least 5 times to remove all traces of moisture from the system. I then removed the vacuum line connection from one of the valves and replaced it with a connection to a silicone-oil bubbler. I then lowered the reaction flask into a preheated oil bath while venting the gases through the oil bubbler to prevent the buildup of pressure. The solvent temperature (tracked by the immersion thermometer) steadily rose and stabilized at 81^{o}C within 15 minutes of initial heating under vigorous stirring.

The reaction mixture was stirred for a total of 16.5 hours under the inert atmosphere, during which 4 ml aliquots of the reaction mixture were periodically removed, purified, and analyzed by ^{1}H NMR to determine the reaction completion (tracked the disappearance of the vinyl proton peaks). Since the chemical shifts of the ^{1}H NMR peaks corresponding to M^{H} groups and M^{CH2} groups (ie. -$OSiMe_2CH_2$-) are well characterized in literature, the hydrosilylation reactions were tracked via the appearance of a new proton peak at δ = 0.5-0.6 ppm and the disappearance of vinyl protons.[179, 181, 182, 215-217, 231, 248] The new ^{1}H NMR peak confirmed that silicon-methylene bonds were being formed due to the conversion of M^{H} groups to M^{CH2} groups (ie. hydrosilylation reaction was successful). After the hydrosilylation reaction was confirmed to have reach 100% completion (ie. when no vinyl protons could be detected

in the ^{1}H NMR spectrum of the last aliquot), the reaction mixture was cooled to ambient temperature, and then stirred with about 0.5 g of activated charcoal to deactivate the Pt(dvtms) catalyst.[248, 255]

The mixture was then filtered into a pre-silanized addition funnel and attached to a pre-silanized 3-neck flask containing 4.25g (39.1 mmoles) of TMCS diluted in 35ml of anhydrous DCM solvent. The 3-neck flask was also connected to a cylinder of high-purity N_2 gas and a silicone-oil bubbler. The filtrate was then added dropwise to the excess silanization agent under vigorous stirring and a constant flow of dry N_2-gas to sweep away all HCl gas that was produced during the addition. The dropwise addition took about 2 hours to be completed, and the reaction mixture was stirred overnight under a continuous N_2-purge stream to cap all silanol end-groups that had formed on the PDMSH chains due to traces of moisture being present during the hydrosilylation reaction.

The silanization reaction mixture was transferred from the 3-neck flask to a pre-weighed and pre-silanized boiling flask and concentrated to less than 5 ml using a rotary evaporator. The concentrated solution was then added dropwise to excess dry acetone to selectively precipitate the **NC1** hybrid molecules. The resulting suspension was vacuum filtered through a fine-porosity fritted-glass filter and the filtration residue was washed with copious acetone to remove any PDMSH oligomers that had been entrained in the precipitate. To increase the yield of recovered **NC1**, the traces of solids on the sidewalls of the boiling flask were dissolved in 5 ml of DCM, and the solution was added dropwise to excess fresh acetone, to produce another suspension. The second suspension was filtered and the residue washed with fresh acetone. The solids recovered from both

suspensions were combined and dried overnight in an 80°C oven under high vacuum conditions. A total of 0.394g of product was recovered (corresponded to a yield of 53% based on the theoretical mass of **NC1** when all **PNC3v** chains are grafted to two PDMSH chains). As an alternative to using hot toluene as the reaction solvent, hydrosilylation reactions were successfully carried out in dry chloroform solvent under reflux conditions. Due to the lower temperature of these reflux reactions (chloroform boils at 62°C), 21.5 hours were needed to completely hydrosilylate all the vinyl groups of **PNC3v** chains.

6.3.2 ^{1}H NMR and ^{29}Si{^{1}H} NMR Analyses of NC1 Samples

Figure 6.2 shows the chemical structure of hybrid **NC1** molecules, complete with annotations that correspond its ^{1}H NMR and ^{29}Si{^{1}H} NMR peaks. During the hydrosilylation reaction, some of the M^{H} groups were observed to be hydrolyzed due to traces of moisture being present in the reaction mixture. During the silanization step the M^{OH} silanol groups were reacted with TMCS to cap them with unreactive trimethylsilyl groups (ie. -$SiMe_3$ or M). The siloxane chain on the right hand side of Figure 6.2 has 8 D groups and one M group, which is the chemical structure of a PDMS chain that has been end-capped with $SiMe_3$ groups. The protons of these $SiMe_3$ end-groups are labeled #9 in Figure 6.2, and appear in the ^{1}H NMR spectrum with the same annotation. The annotated ^{1}H NMR spectrum of **NC1** is shown in Figure 6.3 and the ^{1}H NMR spectra of the ungrafted precursors (ie. **PNC3v** and PDMSH oligomers) are shown in chapter 3 and chapter 5, respectively. The ^{1}H NMR peak in Figure 6.3 at δ = 0.53-0.57 ppm (ie. peak #4) was due to the Si-CH_2 bond that was formed as a result of the hydrosilylation reaction between the silane protons of the M^{H} groups in PDMSH and the vinyl groups of **PNC3v** oligomers.[178, 215-217, 223, 225, 248]

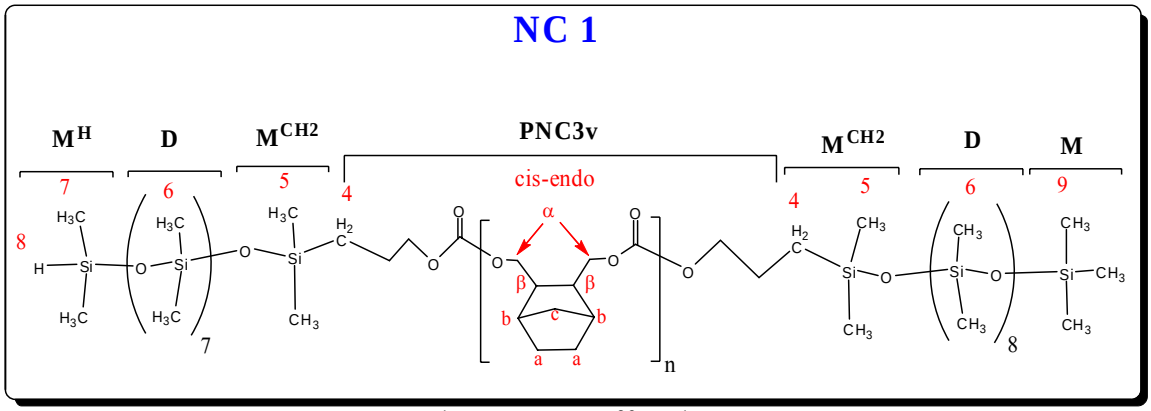

Figure 6.2 – Annotations for the ^{1}H NMR and $^{29}Si\{^{1}H\}$ NMR peaks of **NC1** molecules

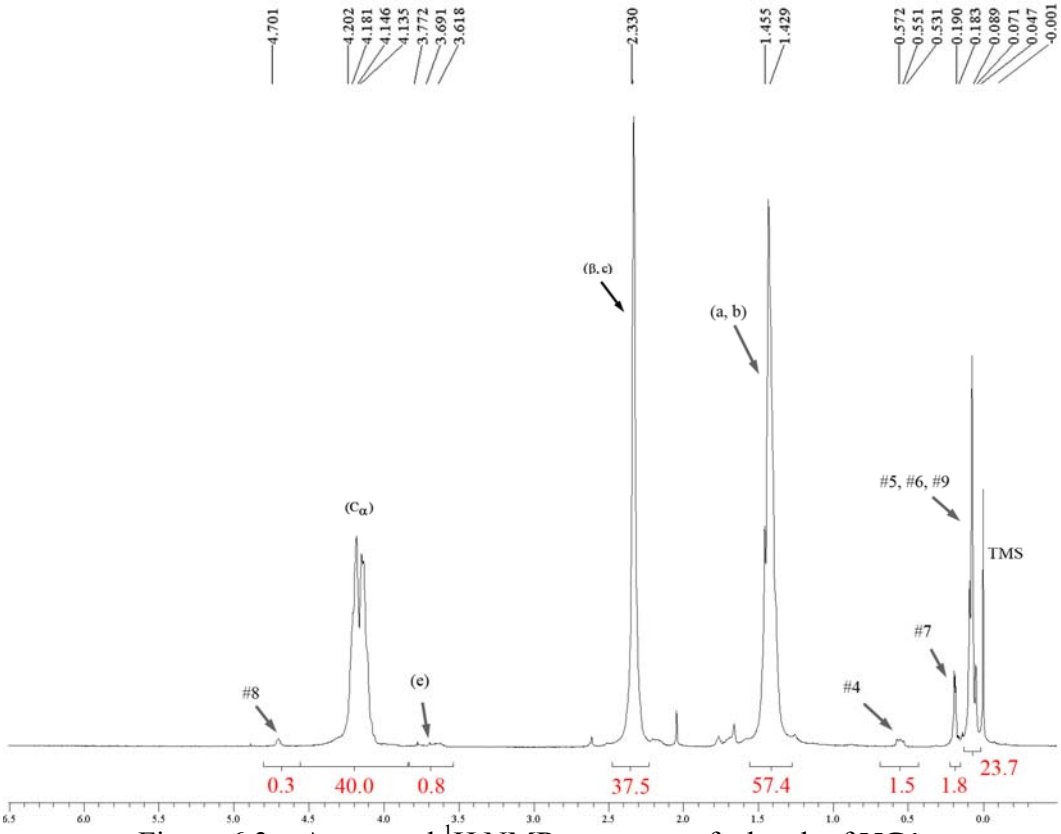

Figure 6.3 – Annotated ^{1}H NMR spectrum of a batch of **NC1**

Figure 6.3 shows that all the vinyl groups had been hydrosilylated, and as discussed in chapter 3, the presence of hydroxyl end-groups (peak e) on some of the PNC

chains was due to the incomplete conversion of OH groups during the end-capping of **PNC3-OH**. The ratio of grafted to ungrafted end-groups was 2:1 (ratio of peak #4 to peak e), which agreed with the original ratio of vinyl end-groups to OH end-groups in **PNC3-OH**. Thus, two-thirds of all the **PNC3** end-groups solids were grafted to PDMSH chains in **NC1**, which does not necessarily mean that only two-thirds of all PNC oligomers were grafted (since a PNC chain could have one OH end-group and one grafted end). Attempts to separate the two different types of PNC chains (either grafted & ungrafted or double-grafted & mono-grafted) proved unsuccessful.

From the integrals in Figure 6.3 we also observe that the ratio of peak #8 to peak #4 is 1:6, which agrees with the stoichiometry of silane and methyl protons in the M^H groups. At δ = 0.05-0.09 ppm the methyl protons peaks of the M^{CH2}, M, and D groups (peaks #5, #6, and #9, respectively) overlap with each other, producing a large combined integral (the ratio of the combined integral to that of peak #7 is equal to 23.7/1.8 = 13.17). We know from earlier ^{1}H NMR analysis of the PDMSH chains (see chapter 5) that there were originally 14 methyl groups attached to D silicons (peak #6) and 4 methyl groups attached to M^H silicons (peak #7) so the ratio of each group's respective methyl protons (peak #6 to peak #7) is equal to 3.50 if we ignore the extra D groups that were formed during $SiMe_3$ capping of traces of M^{OH} silanol groups. Hence, the ratio of the combined integrals of peaks #5 and #9 to the integral of peak #7 is 13.17-3.5 = 9.67. From stoichiometry, we also know that the M^{CH2} groups have six methyl protons (peak #5) for every two Si-CH_2 protons (peak #4); hence, the ratio of peak #5 to peak #4 is 3.0. The ratio of the integrals of peak #5 to peak #7 is 2.5, as calculated by the expression shown in equation (6.2). The ratio of the integrals of peak #9 to peak #7 was then back-

calculated as 9.67-2.5 = 7.17. Since each M group had 3 methyl groups while each MH group had only two methyl groups, there were approximately 2.5/1.5=1.67 M end-groups per M^H end-group, which corresponds to 62.5% M of all ungrafted end-groups in the PDMS chains of the **NC1** molecules.

$$\frac{\int \text{peak \#5}}{\int \text{peak \#7}} = \left(\frac{\int \text{peak \#5}}{\int \text{peak \#4}}\right) \times \left(\frac{\int \text{peak \#4}}{\int \text{peak \#7}}\right) = 3.0 \times \frac{1.5}{1.8} = 2.5 \qquad (6.2)$$

The annotated $^{29}Si\{^1H\}$ NMR spectrum of **NC1** is shown in Figure 6.4 and the annotated $^{29}Si\{^1H\}$ NMR spectra of the ungrafted PDMSH oligomers are shown in chapters 5.[18, 174, 179, 181, 182, 215-217, 247] The $^{29}Si\{^1H\}$ NMR peak at δ = 7.4 ppm corresponded to the M^{CH2} silicon (ie. $\underline{Si}Me_2CH_2$) that was formed as a result of the hydrosilylation reaction between the silane protons of the M^H groups in PDMSH and the vinyl groups of **PNC3v** oligomers.[18, 179, 181, 182, 217, 247]

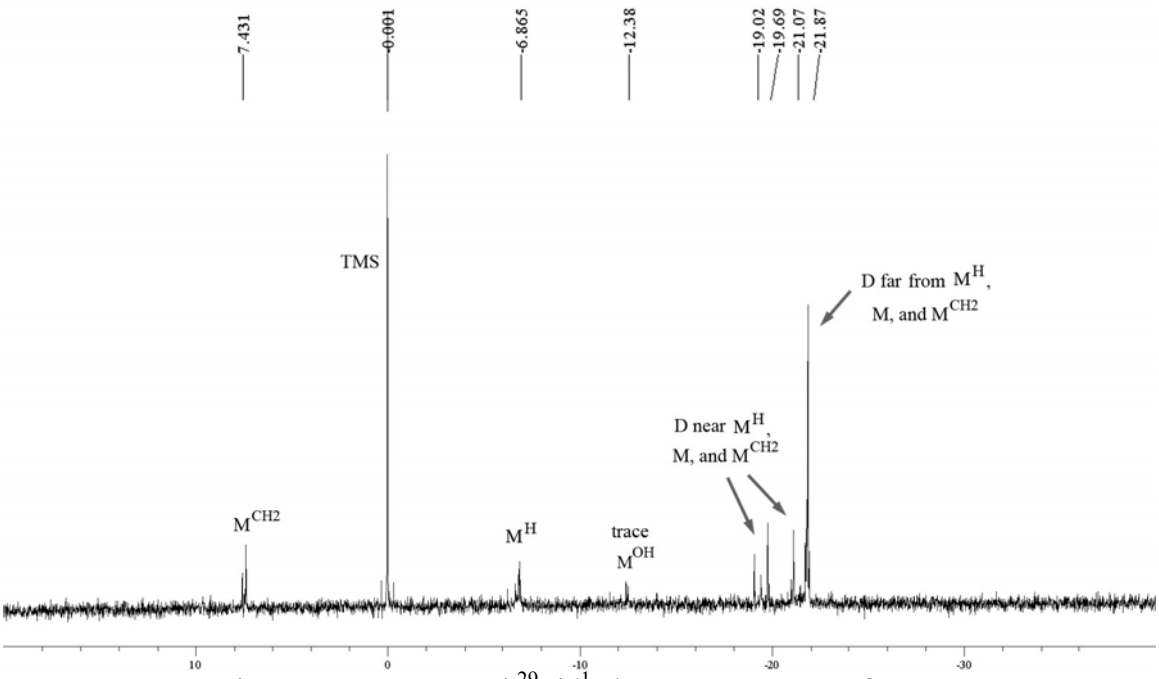

Figure 6.4 - Annotated $^{29}Si\{^1H\}$ NMR spectrum of **NC1**

6.3.3 GPC Analysis of NC1

Based on the spectroscopic results, the solids recovered from the synthesis of **NC1** hybrid molecules were a mixture of double-grafted **PNC3** chains (ie. the **NC1** molecule shown in Figure 6.1 and Figure 6.2) and either mono-grafted **PNC3** chains or ungrafted **PNC3-OH** chains, or a blend of all three types of molecules. Since all attempts at isolating the **NC1** solids from the ungrafted or mono-grafted **PNC3** chains failed, these blends were later templated in HSQ films and decomposed to produce porous films. As shown in a later chapter, TEMS results showed that porous films obtained from **NC1** blends had bimodal pore size distributions, which suggested that the mixtures were composed of only two components. GPC experiments confirmed that **NC1** blends had bimodal size distributions, as shown in Figure 6.5.

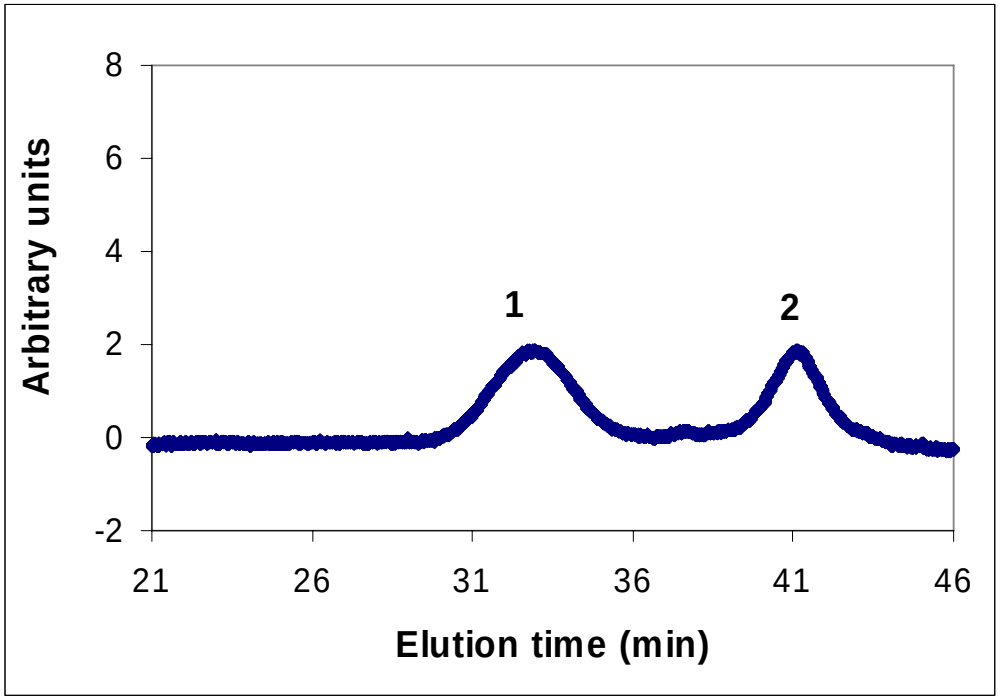

Figure 6.5 – GPC trace of solids recovered from synthesis of **NC1** nanocomposites

By comparing the GPC trace of **NC1** with the GPC trace of the batch of **PNC3** chains that were used to synthesize **NC1** (Figure 3.31) we see that GPC peak 2 in Figure 6.5 corresponds to ungrafted **PNC3** chains, while peak 1 corresponds to the larger hybrid molecule. Recall from **NC1**'s ^{1}H NMR results that after all the vinyl end-groups had been hydrosilylated the ratio of grafted Si-CH_2 linkages to ungrafted OH end-groups was 2:1. Thus, the GPC and NMR results are consistent with **NC1** blends being two-component mixtures with 67 mole% being actual hybrid **NC1** molecules (**PNC3v** chains double-grafted to PDMSH chains) and 33 mole% being ungrafted **PNC3-OH** chains. The inability to isolate **NC1** molecules from the ungrafted **PNC3-OH** oligomers provided an unforeseen benefit; namely, the mixture provided a means of directly comparing the miscibility of **NC1** molecules and ungrafted **PNC3** chains with the surrounding HSQ matrix since both types of molecules were dispensed from the same solutions and processed in the same HSQ layers. Hence, the effectiveness of short PDMSH chains as compatibilizers for **PNC3** chains could be determined directly from TEM results of the films templated with the **NC1** blends.

As shown in equation (6.3), the number-average molecular weight of NC1 molecules was calculated using the molecular weights of its precursors which were estimated in earlier chapters (M_n of batch #B of **PNC3-OH** was equal to 3135 g/mol and M_n of PDMSH was equal to 652 g/mol).

$$M_n \text{ of NC1} = 3135 + 2*652 = 4439 \text{ g/mol} \qquad (6.3)$$

Since the molar composition of the **NC1** blends were already determined from NMR data, it was straightforward to calculate both the wt% of free oligomers and the

total wt% of all **PNC3** chains in the **NC1** blends, as shown in equation (6.4) and equation (6.5), respectively.

$$wt\%\ \text{free PNC} = \left[\frac{\left(3135 * 1/3\right)}{\left(4439 * 2/3\right) + \left(3135 * 1/3\right)}\right] \times 100 = 26.1\% \qquad (6.4)$$

$$wt\%\ \text{total PNC} = \left[\frac{3135}{\left(4439 * 2/3\right) + \left(3135 * 1/3\right)}\right] \times 100 = 78.3\% \qquad (6.5)$$

The weight fraction of total polycarbonate chains was compared to TGA results to determine the weight loss due to the fragmentation of the silicone segments. Additionally, the weight fraction of free PNC chains in the **NC1** blends proved useful in later discussion of the TEM results of HSQ films templated with **NC2** solids.

6.4 Hydrosilylation of PNC3v with $Q_8M_8^H$: Type-2 Nanocomposites (NC2)

6.4.1 Synthesis and Purification of NC2 Molecules

Hydrosilylation reactions were used to graft **PNC3v** chains to $Q_8M_8^H$ cages to form type-2 nanocomposite molecules (**NC2**), as shown in Figure 6.6. The procedures for synthesizing and purifying a typical batch of **NC2** solids are described below. Prior to adding reactants, a pre-silanized, 100 ml 3-neck flask was heated above 100°C, while under high vacuum conditions to desorb any moisture from its sidewalls. Then the flask was backfilled with dry N_2 gas and allowed to cool to ambient under the inert atmosphere. 0.464g (approximately 0.25 mmoles) of **PNC3v** solids, 2.246g (2.21 mmoles) of $Q_8M_8^H$, and 0.170g of a 0.0153 wt% solution of Pt(dvtms) in xylene

(platinum loading of 380 ppm with respect to **PNC3v** chains) were added to the flask. Then 40 ml of dry toluene was added to dissolve the reactants, and the flask was sealed using two 2-way valves and one air-tight plug that held an immersion thermometer in place. One of the valves was connected to a vacuum pump, and the other was connected to a cylinder of high-purity dry Nitrogen gas. The flask was then evacuated until the bubble point of toluene was reached before being backfilled with N_2 gas. The cycle of evacuation and N_2-backfilling was repeated at least 5 times to remove all traces of moisture from the system. After the last N_2-backfill, the connection to the vacuum line was removed and the apparatus was connected to a silicone-oil bubbler.

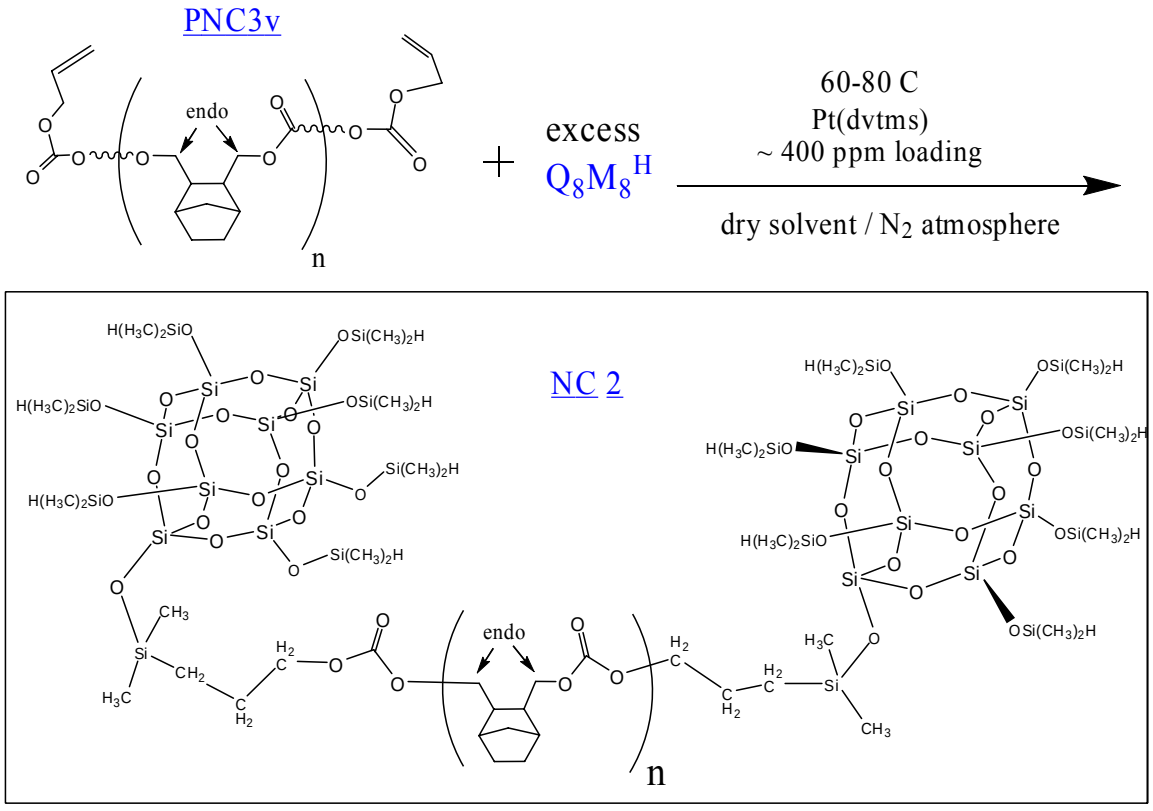

Figure 6.6 – Reaction scheme for the synthesis of **NC2** hybrid molecules

The reaction flask was lowered into a preheated oil bath while venting the gases through the oil bubbler to prevent the buildup of pressure. The solvent temperature (tracked by the immersion thermometer) steadily rose and stabilized at 86^{o}C within 15 minutes of initial heating under vigorous stirring. The reaction mixture was stirred for a total of 10.5 hours under the inert atmosphere, during which 4 ml aliquots of the reaction mixture were periodically removed, purified, and analyzed by ^{1}H NMR to determine the reaction completion (tracked the disappearance of the vinyl proton peaks). After the hydrosilylation reaction was complete, the reaction mixture was cooled to ambient temperature, and then stirred with about 0.5 g of activated charcoal to deactivate the Pt(dvtms) catalyst.[248, 255]

The mixture was then filtered into a pre-silanized addition funnel and attached to a pre-silanized 3-neck flask containing 5.10g (47.0 mmoles) of TMCS diluted in 35ml of anhydrous DCM solvent. The 3-neck flask was also connected to a cylinder of high-purity N_2 gas and a silicone-oil bubbler. The filtrate was then added dropwise to the excess silanization agent under vigorous stirring and a constant flow of dry N_2-gas to sweep away all HCl gas that was produced during the addition. The dropwise addition took about 2 hours to be completed, and the reaction mixture was stirred overnight under a continuous N_2-purge stream. This silanization step was essential to the recovery of **NC2** product because silanol bonds were always observed to be produced even though the reaction system was carefully dried prior to hydrosilylation. Multiple attempts at purifying and recovering the **NC2** solids without performing this silanization step invariably resulted in the loss of the reaction products to gelation.

The solution was transferred from the 3-neck flask to a pre-weighed and pre-silanized boiling flask and concentrated to less than 5 ml using a rotary evaporator. The concentrated toluene solution was then added dropwise to excess dry hexane to selectively precipitate the **NC2** hybrid molecules. The milky-white suspension was vacuum filtered through a fine-porosity fritted-glass filter and the filtration residue was washed with copious hexane to remove any ungrafted $Q_8M_8^H$ cages that had been entrained in the precipitate. To increase the yield of recovered reaction product, the traces of solids on the sidewalls of the boiling flask were redissolved in 5 ml of DCM, and the solution was then concentrated and dropwise added to fresh hexane as before. The second suspension was filtered and the residue washed with fresh hexane, and recovered solids were combined. The product was dried overnight in an 80^{o}C oven under high vacuum conditions. A total of 1.082g of product was recovered (corresponded to a quantitative yield based on the theoretical mass of **NC2** when all **PNC3v** chains are grafted to two $Q_8M_8^H$ cages). Attempts at performing the hydrosilylation reaction in chloroform and DCM solvents under reflux conditions (62^{o}C and 40^{o}C, respectively) were abandoned due to the sluggishness of the reaction (100% completion took more than 72 hours in chloroform and more than a week in DCM).

6.4.2 ^{1}H NMR and ^{29}Si{^{1}H} NMR Analyses of NC2 Samples

Figure 6.7 shows the chemical structure of hybrid **NC2** molecules, complete with annotations that correspond its ^{1}H NMR and ^{29}Si{^{1}H} NMR peaks.[18, 95, 179, 181, 182, 210, 229, 231] During the hydrosilylation reaction, some of the M^H groups were observed to be hydrolyzed due to traces of moisture being present in the reaction mixture.

During the silanization step the M^{OH} silanol groups were reacted with TMCS to cap them with unreactive trimethylsilyl groups (ie. -$SiMe_3$ or M). The siloxane chain on the right hand side of Figure 6.7 has a D group and an M group, which are both produced when an M^{OH} silanol is end-capped with $SiMe_3$ groups. The protons of the $SiMe_3$ end-groups are labeled #15 in Figure 6.7, and appear in the ^1H NMR spectrum with the same annotation. The annotated ^1H NMR spectrum of **NC2** is shown in Figure 6.8 and the ^1H NMR spectra of the ungrafted precursors (ie. **PNC3v** and $Q_8M_8^H$) are shown in chapter 3 and chapter 5, respectively.

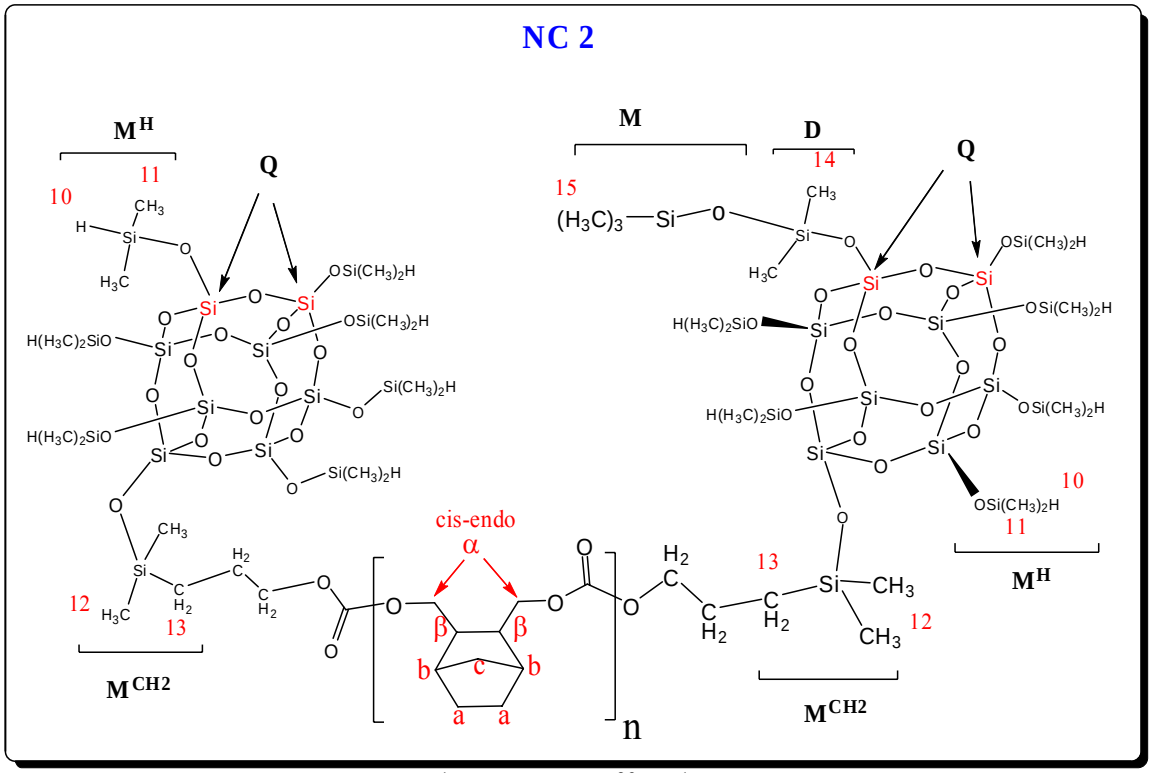

Figure 6.7 – Annotations for the ^1H NMR and $^{29}Si\{^1H\}$ NMR peaks of **NC2** molecules

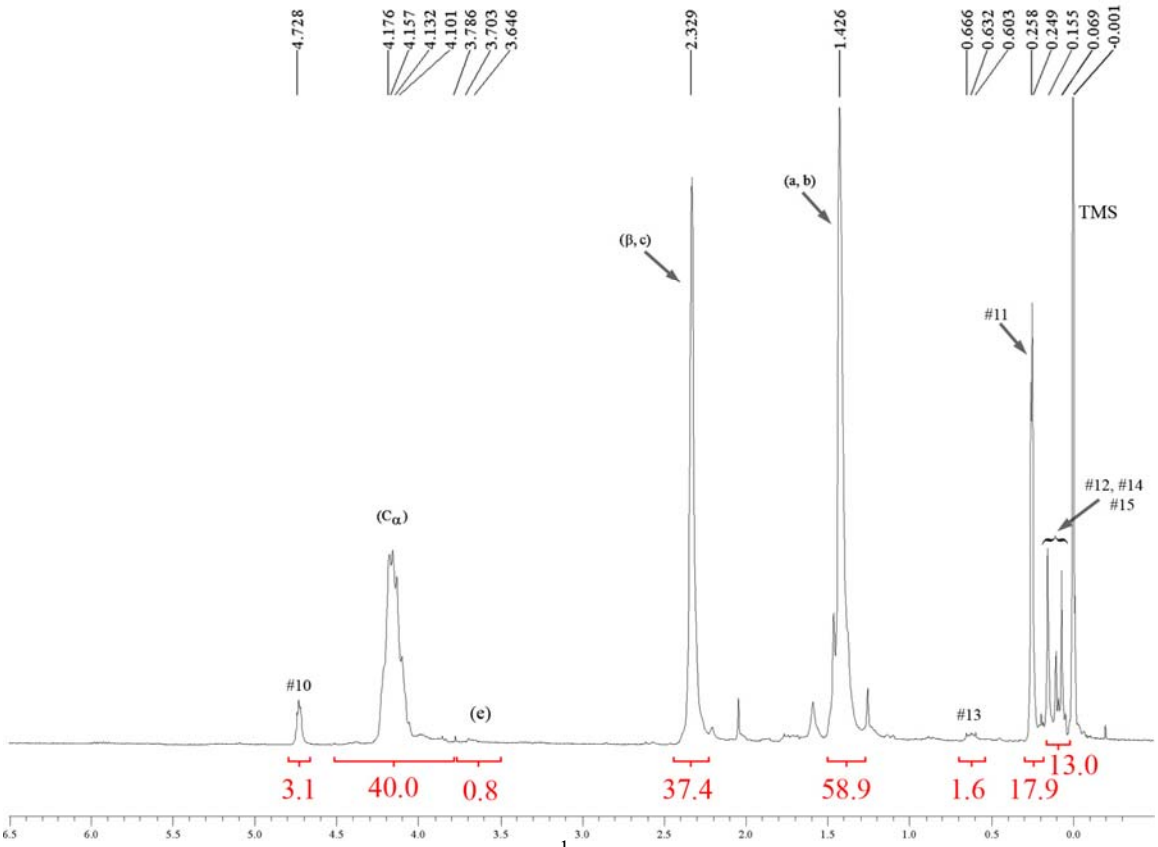

Figure 6.8 – Annotated ^{1}H NMR spectrum of **NC2**

We can see from Figure 6.8 that the ratio of protons from Si-C<u>H</u>$_2$ groups (ie. integral of peak #13) to protons from residual C<u>H</u>$_2$OH end-groups on the PNC chains (ie. integral of peak <u>e</u>) is equal to 2:1. This ratio agrees with the ^{1}H NMR results for **PNC3v** blends (refer to Figure 3.15), which showed that there were twice as many vinyl end-groups as OH end-groups on the oligomeric **PNC3** chains. The integral of peak #11 is about six times as large as peak #10, which agrees with the stoichiometric ratio of silane protons to methyl protons in the M^{H} groups of the POSS segment. From stoichiometry we know that there are six methyl protons in the M^{CH2} group for every Si-C<u>H</u>$_2$ linkage produced; hence the ratio of peak #12 to peak #13 is equal to 3. Thus, the integral of peak #12, which overlaps with peaks #14 and peak #15, is equal to 3*1.6 = 4.8. The

complementary part of the integral to the far right of Figure 6.8 is due to the methyl protons of the M and D groups that were formed when M^{OH} silanol groups were silanized by TMCS molecules. Figure 6.9 shows the annotated $^{29}Si\{^{1}H\}$ NMR spectrum for **NC2** and the ^{1}H NMR spectra of $Q_8M_8^{H}$ is shown in chapter 5. The silicon-29 peak at -13.1 ppm corresponds to the M^{CH2} groups (refer to Figure 6.7) that were produced as a result of the hydrosilylation reaction between the silane bonds of the M^{H} group and the vinyl end-groups of **PNC3v**.[18, 210, 229, 231]

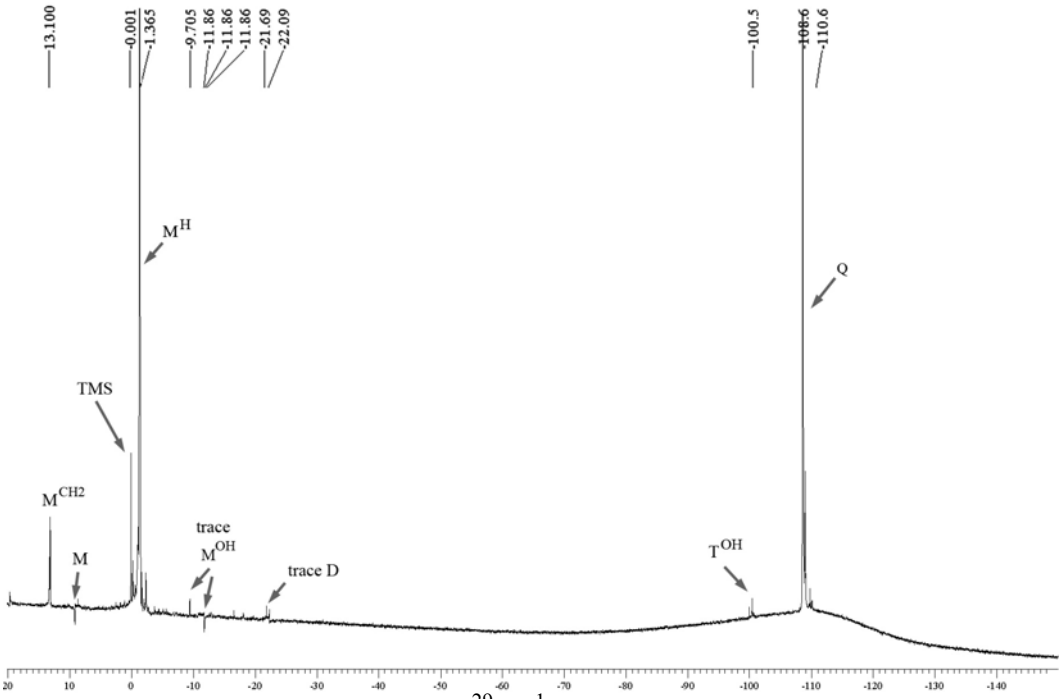

Figure 6.9 – Annotated $^{29}Si\{^{1}H\}$ NMR spectrum of **NC2**

The broad shallow peak between δ = -100 ppm and δ = -125 ppm was an artifact that was produced by the Q silicon groups in the glass probe of the NMR equipment).[3, 18, 179, 181, 182, 210] Figure 6.9 also shows traces of M^{OH} silanols and T^{OH} silanols (ie. $HOSi(OSi)_3$), which were respectively formed by the hydrolysis of silanes bonds and

siloxane bonds.[18] The D groups were produced by each of the following sol-gel condensation reactions: (a) condensation between two silanol bonds, (b) condensation between silanol bonds and silane bonds, (c) condensation between silanol groups and TMCS during the silanization step (refer to chapter 5 for sol-gel reactions). [3, 18, 60, 179, 181-183, 205, 210] Although the ability of both $Q_8M_8^H$ and HSQ to undergo sol-gel reactions made them vulnerable to avoid gelation, these sol-gel reactions were ultimately advantageous since they afforded a means for covalently linking the nanocomposite molecules to the HSQ resin in templated films.

6.4.3 GPC Analysis of NC2

Based on the spectroscopic results, the solids recovered from the synthesis of **NC2** hybrid molecules were a mixture of double-grafted **PNC3** chains (ie. the **NC2** molecule shown in Figure 6.6 and Figure 6.7) and either mono-grafted **PNC3** chains or ungrafted **PNC3-OH** chains, or a blend of all three types of molecules. Since all attempts at isolating the **NC2** solids from the ungrafted or mono-grafted **PNC3** chains failed, these blends were later templated in HSQ films and decomposed to produce porous films. As shown in a later chapter, TEM results showed that porous films obtained from **NC2** blends had bimodal pore size distributions, which suggested that the mixtures were of only two components. Similar to the GPC results of **NC1** blends, GPC traces of **NC2** blends had bimodal size distributions, and one of the GPC peaks corresponded to ungrafted **PNC3-OH** oligomers. In the previous section we saw that ^{1}H NMR results of the ratio of grafted Si-CH_2 linkages to ungrafted OH end-groups in the overall **NC2** mixture was 2:1. Thus, the GPC and NMR results were consistent with

NC2 blends being two-component mixtures with 67 mole% being hybrid **NC2** molecules (**PNC3v** chains double-grafted to PDMSH chains) and 33 mole% being ungrafted **PNC3-OH** chains. The similarity of the composition and makeup of the **NC1** and **NC2** blends was not unexpected since both of these blends were synthesized from **PNC3v** precursors with similar ratios (ie. 2:1) of vinyl end-groups to OH end-groups.

As discussed earlier for **NC1** blends, the difficulty encountered in separating **NC2** molecules from the ungrafted **PNC3-OH** components provided the unforeseen benefit of allowing the relative compatibility of **NC2** molecules and ungrafted **PNC3** chains with the surrounding HSQ matrix to be compared in the same chemical environment. Hence, the effectiveness of the POSS segments at (1) compatibilizing **PNC3** chains with the HSQ matrix during spincoating, and (2) preventing movement of templated nanocomposites via crosslinking reactions between the POSS segments and the T^H matrix during thermal treatments could both be determined directly from TEM results of the films templated with the **NC2** blends.

As shown in equation (6.6), the number-average molecular weight of **NC2** molecules was calculated using the molecular weights of its precursors which were estimated in earlier chapters (M_n of batch #C of **PNC3-OH** was equal to 3195 g/mol and the M_n of $Q_8M_8^H$ was equal to 1018 g/mol). Similar to **NC1** blends, the wt% of free oligomers and the total wt% of all **PNC3** chains in the **NC2** blends were calculated using molar compositions determined from ^{1}H NMR results, as shown in equation (6.7) and equation (6.8), respectively.

$$M_n \text{ of NC2} = 3195 + 2*1018 = 5231 \text{ g/mol} \quad (6.6)$$

$$wt\%\ \text{free PNC} = \left[\frac{\left(3195 * \frac{1}{3}\right)}{\left(5231 * \frac{2}{3}\right) + \left(3195 * \frac{1}{3}\right)} \right] \times 100 = 23.4\% \qquad (6.7)$$

$$wt\%\ \text{total PNC} = \left[\frac{3195}{\left(5231 * \frac{2}{3}\right) + \left(3195 * \frac{1}{3}\right)} \right] \times 100 = 70.2\% \qquad (6.8)$$

As done by other researchers, the weight fraction of total sacrificial polymer chains was later compared to TGA results to determine the fraction of the total weight loss that was due to the fragmentation of the POSS segments. Additionally, the weight fraction of free PNC chains in the **NC2** blends proved useful in later discussion of the TEM results of HSQ films templated with **NC2** solids.

6.5 Attempted Hydrosilylation Reactions Between PNC3v and HSQ Resin

Hydrosilylation reactions were used in attempts to graft **PNC3v** chains directly to HSQ resin chains, as shown in Figure 6.10. Typical procedures for the reaction and purification were as follows. The procedures for drying the apparatus and preparing the reaction mixtures were similar to those used in the syntheses of **NC1** and **NC2** molecules. Although multiple attempts were made at grafting **PNC3v** directly to HSQ resin chains, ^{1}H NMR analysis showed no evidence of hydrosilylation occurring (no change in peaks, and no Si-C$\underline{H_2}$ peak seen at $\delta \sim 0.5$-0.6 ppm). To promote the forward reactions, more aggressive conditions were employed (toluene was refluxed to raised the reaction temperature to 110^{o}C, the catalyst loading was increased to 1340 ppm with respect to the limiting **PNC3v** chains, and reaction time was even increased to 30 hours) all to no avail.

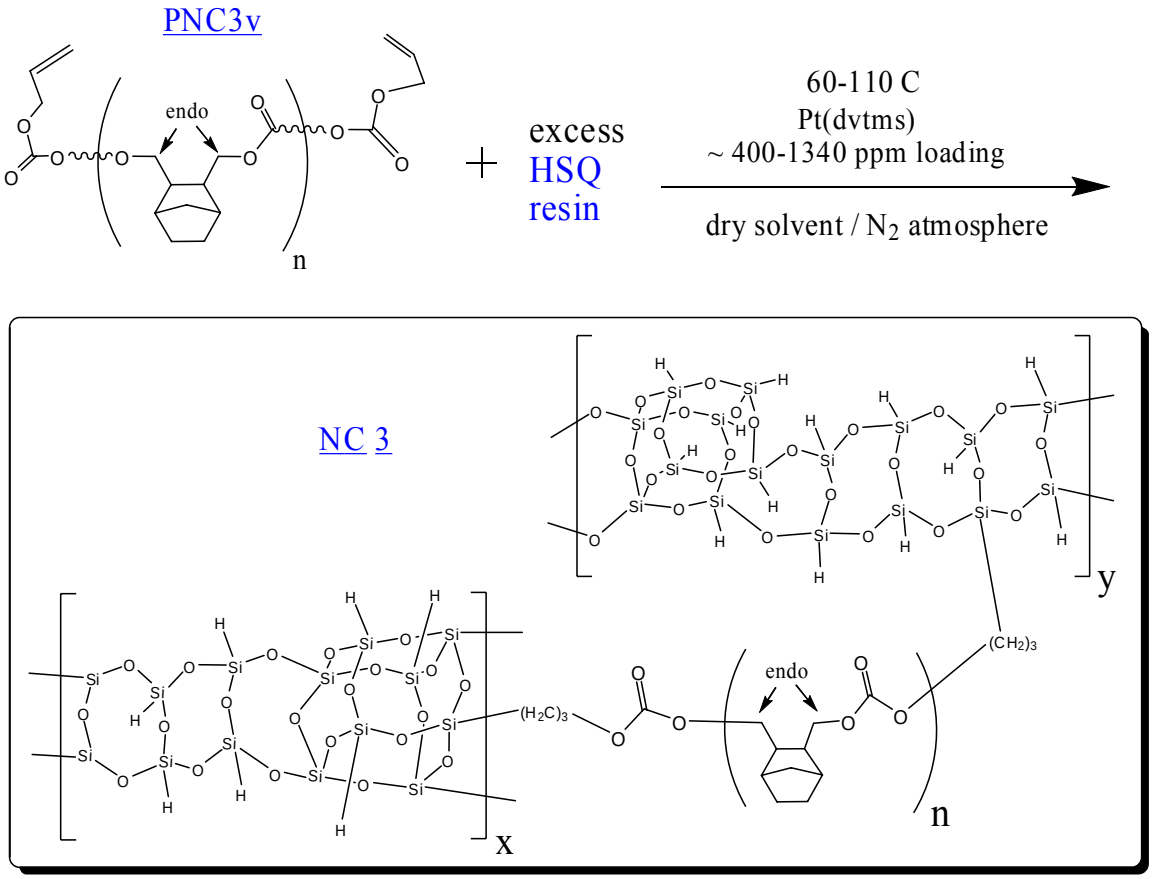

Figure 6.10 – Reaction scheme for the hydrosilylation of **PNC3v** with HSQ resin

It was apparent that the hydrosilylation reactions between **PNC3v** chains and HSQ resin chains were thermodynamically unfavorable at the physical and chemical conditions used in the experiments. This may be due to the large enthalpies required to the overcome steric effects of the co-reactants. One method to overcome this would be to use another non-polar solvent with a higher boiling point than toluene to increase the reaction temperature. The drawback from using high boiling point solvents is that subsequent removal of the solvent during purification becomes extremely difficult, as was witnessed when toluene was used. Additionally, HSQ easily crosslinks when heated; hence, even if hydrosilylation could be achieved by conducting the reaction at higher

temperatures it is likely that the final product would be an insoluble solids rather than a soluble nanocomposite. Although it may still be possible to graft a polycarbonate with a less bulky main chain than the PNC structure (eg. ethylene-carbonate repeat units) to the HSQ resin chains, the properties of polycarbonates are known to vary widely and using more flexible main chains may lead to poor mechanical and thermal properties.[79-82, 84, 89, 98, 167-169] Thus the determination of a polycarbonate chemical structure which would result in oligomers that satisfy all the requirements for being a good sacrificial (eg. thermal properties) while also being conducive to direct hydrosilylation with the HSQ resin would be non-trivial. Nevertheless, this exercise would be useful as a future project since the successful grafting of a porogen directly to a crosslinkable low-k resin has been shown to produce porous films with excellent morphologies such as uniform-dispersion, small pore sizes (as low as 2 nm), and narrow pore size distributions.

Since all the attempts at grafting **PNC3v** chains directly to the T^H resin were unsuccessful, a homogeneous polycarbonate-HSQ phase could not be produced. Fortunately, PNC chains were successfully grafted to both PDMSH and $Q_8M_8^H$ segments to form **NC1** and **NC2** hybrid molecules. Since the backbones of PDMSH, $Q_8M_8^H$, and HSQ resin frameworks all were composed of siloxane bonds, **NC1** and **NC2** hybrid molecules were expected to have greater phase compatibility with HSQ than ungrafted PNC chains. Additionally, the susceptibility of $Q_8M_8^H$ cages to both thermally-induced and hydrolytically-induced crosslinking reactions afforded a convenient route for covalently linking the **NC2** molecules directly to the HSQ resin after spincoating films templated with them. As shown in chapter 8, TEM results of all the templated films were

used to determine the effectiveness of PDMSH and $Q_8M_8^H$ segments at combating phase segregation of grafted PNC chains.

6.6 TGA-MS Analyses of Nanocomposites

TGA analyses were performed on **NC1** and **NC2** blends to determine the total weight loss of the mixtures and also to quantify the weight loss due to the non-polycarbonate segments.[95, 217, 227, 246] As done with the ungrafted precursors of the nanocomposites (refer to chapters 4 and 5), MS was used to determine the degradation mechanism of the decomposition each nanocomposite.[80, 87, 90, 100, 167, 207-209]

6.6.1 TGA-MS Analysis of NC1 blends

Figure 6.11 shows the TGA profile of an **NC1** blends during dynamic heating in a TGA furnace in N_2 atmosphere. From Figure 6.11 we see that almost all the solids in the mixture decomposed into volatile products, leaving a residue of about 2.4wt%. Although the silicone segments of **NC1** molecules were unable to freely evaporate due to being covalently linked to polycarbonate units, we observe that the TGA in Figure 6.11 was about an order of magnitude lower than their weight fraction within the blends, which was back-calculated as 22wt% using equation (6.8). Thus, the PDMSH chains must have undergone fragmentation reactions, as described earlier in chapter 5. The degradation of silicone chains produced volatile decomposition products that were swept away from the TGA furnace by the purging gas, resulting in minimal residue. The gases evolved during decomposition of **NC1** were analyzed MS and compared to those given off during the

decomposition of.ungrafted **PNC3** and PDMSH oligomers (refer to chapter 4 and chapter 5, respectively for their TGA-MS data).

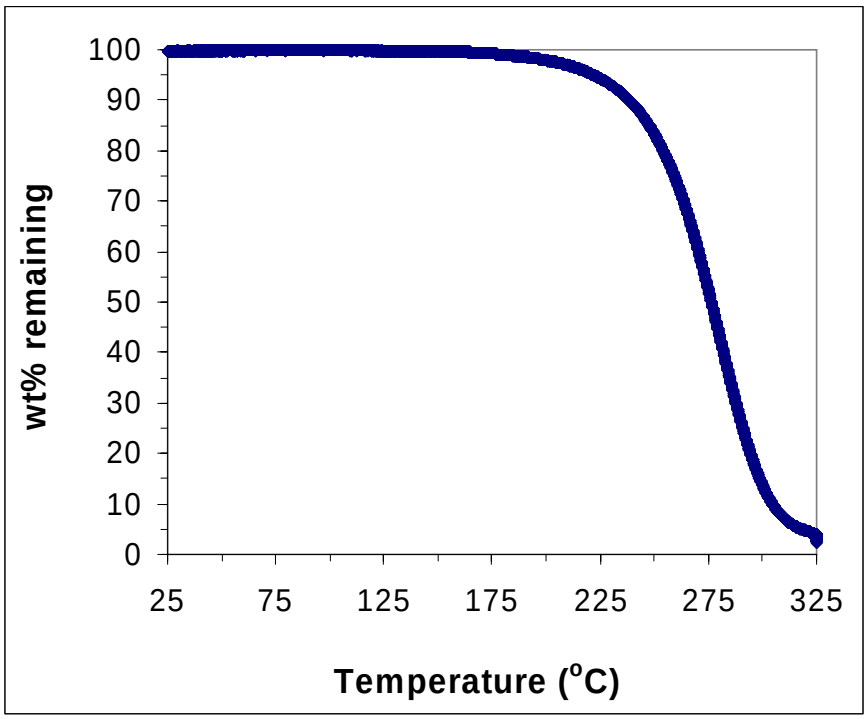

Figure 6.11 – TGA profile of **NC1** during dynamic heating

The overall relative abundances of the MS peaks detected during the dynamic heating of **NC1** in a TGA furnace are shown in Figure 6.12 and appendix C. By referring to the MS data for PNC and PDMSH oligomers (see chapter 4, chapter 5, appendix A, appendix B) we see that the gases given off during decomposition of **NC1** are identical to those detected during the decomposition of its ungrafted precursors. The chemical structures corresponding to the MS peaks are shown in appendix A and appendix B. [18, 174, 179, 181, 182, 207-209, 215-217, 247, 249] Thus, we can infer that the **NC1** hybrid molecules degraded by similar mechanisms to those that took place during the

decomposition of ungrafted PNC (see chapter 4) and ungrafted PDMSH chains (see chapter 5). As discussed in chapter 4, the PNC segments degraded via the following mechanisms: reverse Diels-Alder reactions, internal elimination reactions, and hydrolytic-cleavage of carbonate linkages.[81, 87, 89, 90, 99, 167, 207-209] As shown in chapter 5, silicone segments degraded via thermolytic cleavage of siloxane bonds, and hydrolytic cleavage of siloxane bonds, hydrolysis of silane bonds, and thermal dissociation of silicon-methyl bonds.[18, 174, 179, 181, 182, 215-217, 247, 249]

Additionally, the silanol-terminated decomposition products condensed via sol-gel mechanisms to produce numerous cyclic siloxanes and linear siloxanes such as D_3 (m/e = 192) and D_4 (m/e = 296). [18, 174, 179, 181, 182, 215-217, 247, 249] To track the decomposition of the polycarbonate segments, the intensity of the MS peak for carbon dioxide was plotted against temperature, as shown in Figure 6.13. We observe that the level of carbon dioxide (m/e = 44) detected did not begin increasing above the ambient level until about 190^{o}C, and that the maximum intensity of the carbon dioxide peak occurred at about 281^{o}C. The carbon dioxide levels shown in Figure 6.13 correlate well with the rate of weight loss of **NC1** shown in Figure 6.11; the onset temperature for weight loss occurs just below 200^{o}C and the steepest slope (maximum rate of weight loss) occurs just above 275^{o}C. The close agreement between the TGA results for **NC1** and the amount of CO_2 detected by MS during its decomposition indicates that the carbon dioxide signal was a good marker for tracking the thermal stability of the PNC segments, as was the case with ungrafted **PNC3** oligomers (compare Figure 4.3 with Figure 4.11). The close agreement between the plot shown in Figure 6.13 with that shown in Figure 4.11 indicates the grafting of **PNC3** oligomers to PDMSH segments did not have any

significant effect on the decomposition rate of the polycarbonate chains (ie. kinetic parameter values for decomposition of grafted **PNC3** chains are similar to the values for ungrafted oligomers).

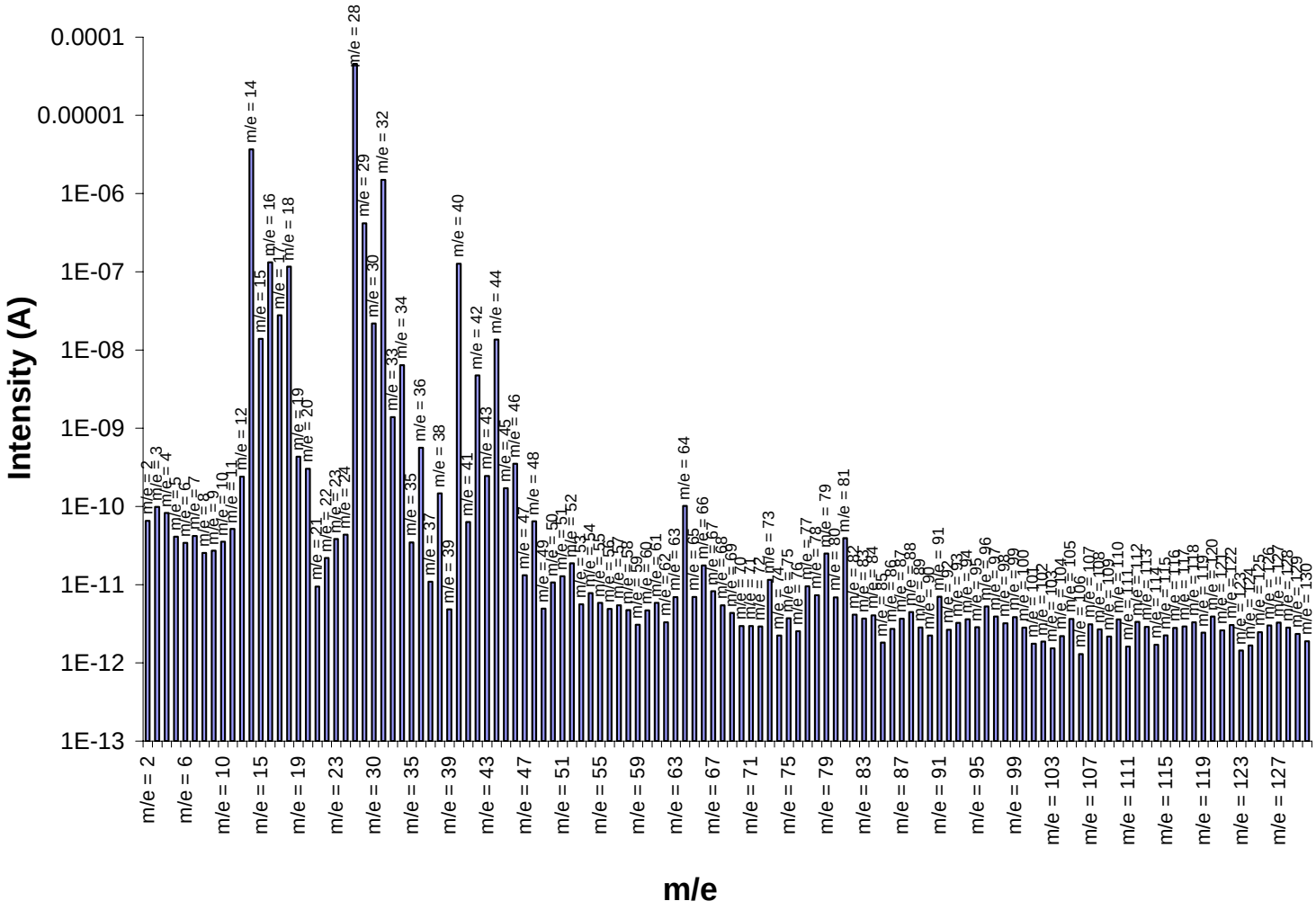

Figure 6.12 – Overall relative abundance of MS peaks detected during decomposition of **NC1**. The plot shows MS peaks for all masses with amu <129 and total intensities $>10^{-13}$ A)

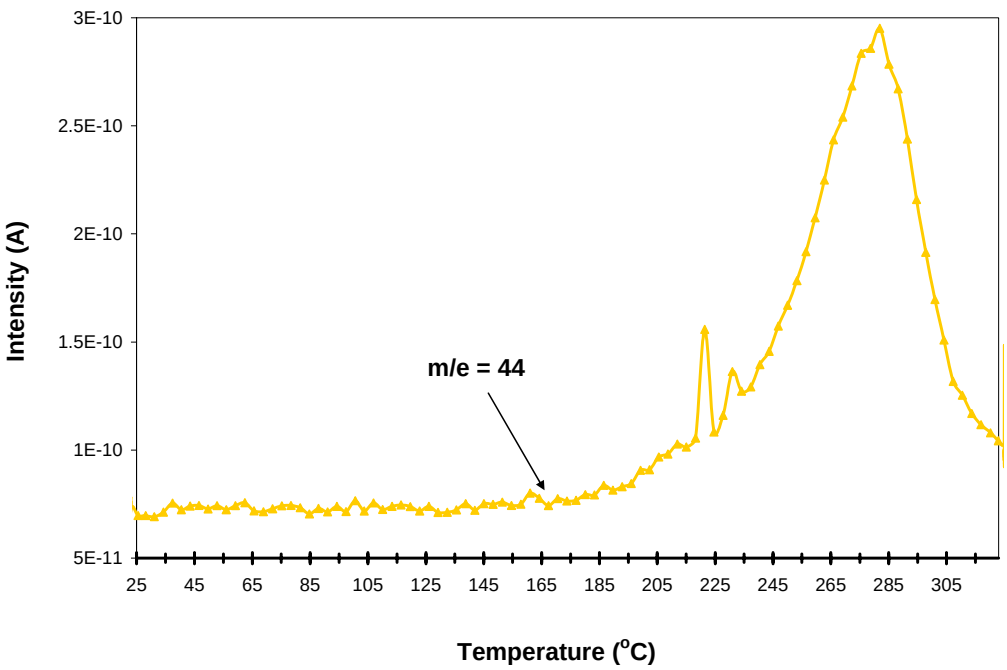

Figure 6.13 – Plot showing temperature dependence of the CO_2 (m/e = 44) MS peak signal level detected by MS during decomposition of **NC1**

6.6.2 TGA-MS Analysis of NC2 blends

Figure 6.14 shows the TGA profile of a sample of **NC2** during dynamic heating in a TGA furnace in N_2 atmosphere. From Figure 6.14 we see that 77% of the solids in the **NC2** blend decomposed into volatile products, leaving 23% of an organosilicate residue (refer to Figure 5.18 for its solid-state ^{29}Si NMR spectrum). From equation (6.8) we know that the total PNC weight fraction in **NC2** blends was 70%, which means that experimentally observed residue was 7% lower than the weight fraction of the POSS segments (30wt%). The 8% deviation between the weight fraction of $Q_8M_8^H$ in the **NC2** blend and the actual ceramic yield was due to the partial decomposition of the POSS segments into volatile components, as discussed in chapter 5.[18, 21, 45, 60, 179, 181-

183, 205, 210, 219, 236, 242] Hence the POSS segments lost 7/30*100 = 23wt% of their formula weight to degradation reactions (refer to chapter 5 for the decomposition of $Q_8M_8^H$).

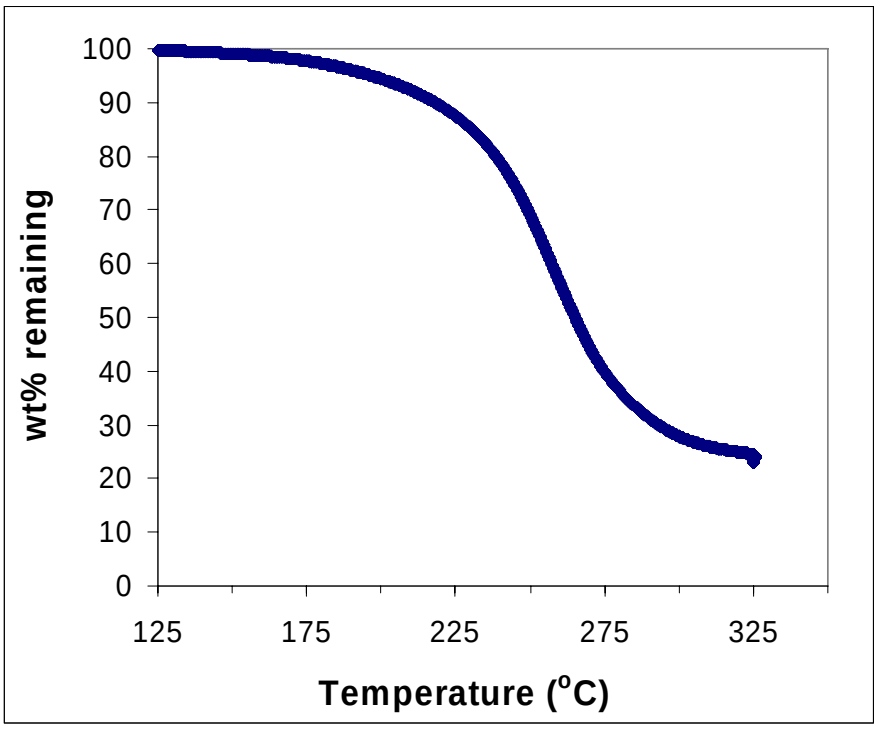

Figure 6.14 – TGA profile of **NC2** during dynamic heating

The overall relative abundances of the MS peaks detected during the dynamic heating of **NC2** in a TGA furnace are shown in Figure 6.15 and appendix C. By referring to the MS data for PNC oligomers and $Q_8M_8^H$ cages (see chapter 4, chapter 5, appendix A, appendix B) we see that the gases given off during decomposition of **NC2** were identical to those detected during the decomposition of its ungrafted precursors. The chemical structures corresponding to the MS peaks are shown in appendix A and appendix B [18, 21, 45, 60, 80, 87, 90, 100, 167, 179, 181-183, 205, 207-210, 219, 236,

242] Thus, we can infer that the **NC2** hybrid molecules degraded by similar mechanisms to those that took place during the decomposition of ungrafted PNC chains (see chapter 4) and ungrafted POSS cages (see chapter 5). As discussed in chapter 4, the PNC segments degraded via the following mechanisms: reverse Diels-Alder reactions, internal elimination reactions, and hydrolytic-cleavage of carbonate linkages.[81, 87, 89, 90, 99, 167, 207-209]

The POSS segments degraded via the following sol-gel mechanisms: the hydrolysis of siloxane bonds, the hydrolysis of silane bonds, and the condensation of silanol-terminated and silane-terminated intermediates to form both linear and cyclic siloxanes.[18, 21, 45, 60, 179, 181-183, 205, 210, 219, 236, 242] As discussed in chapter 5, the susceptibility of both HSQ and Q POSS structures to sol-gel induced crosslinking affords the opportunity to covalently link **NC2** molecules to the HSQ matrix to avoid phase-segregation during thermal treatments. As done with **NC1** blends, the MS peak corresponding to CO_2 was plotted as a function of temperature during the decomposition of **NC2**, as shown in Figure 6.16. As expected, the CO_2 signal correlated well with TGA data shown in Figure 6.14; the onset temperature for weight loss occurs just below 200^{o}C and the steepest slope (maximum rate of weight loss) occurs just above 275^{o}C. The close agreement between the TGA results for **NC2** and the amount of CO_2 detected by MS during its decomposition was expected because since the overwhelming majority of the total weight loss was due to the decomposition of the PNC segments, which accounted for 70wt% of the **NC2** blends.

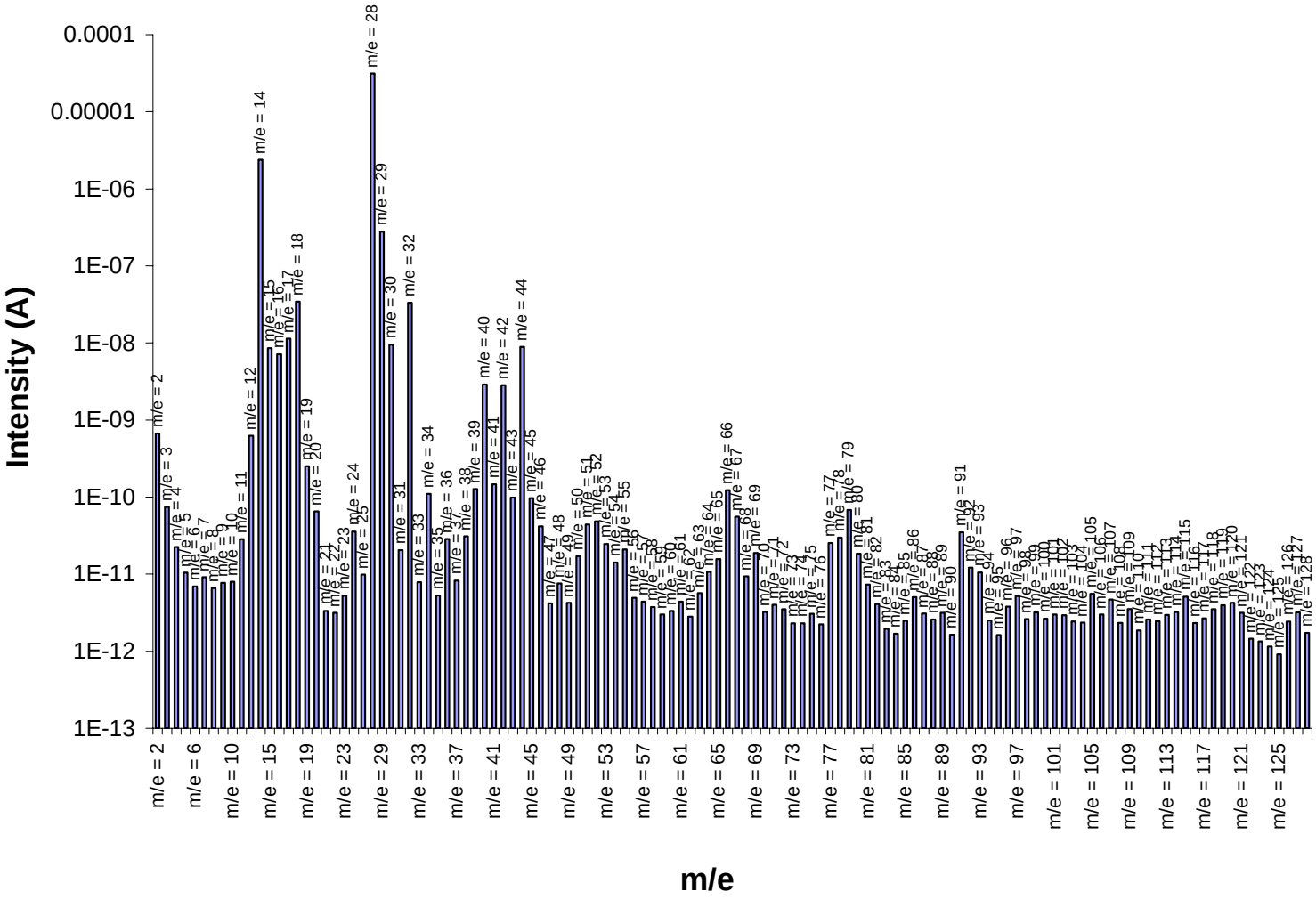

Figure 6.15 – Overall relative abundance of MS peaks detected during decomposition of **NC2**. The plot shows MS peaks for all masses with amu <129 and total intensities $>10^{-13}$ A)

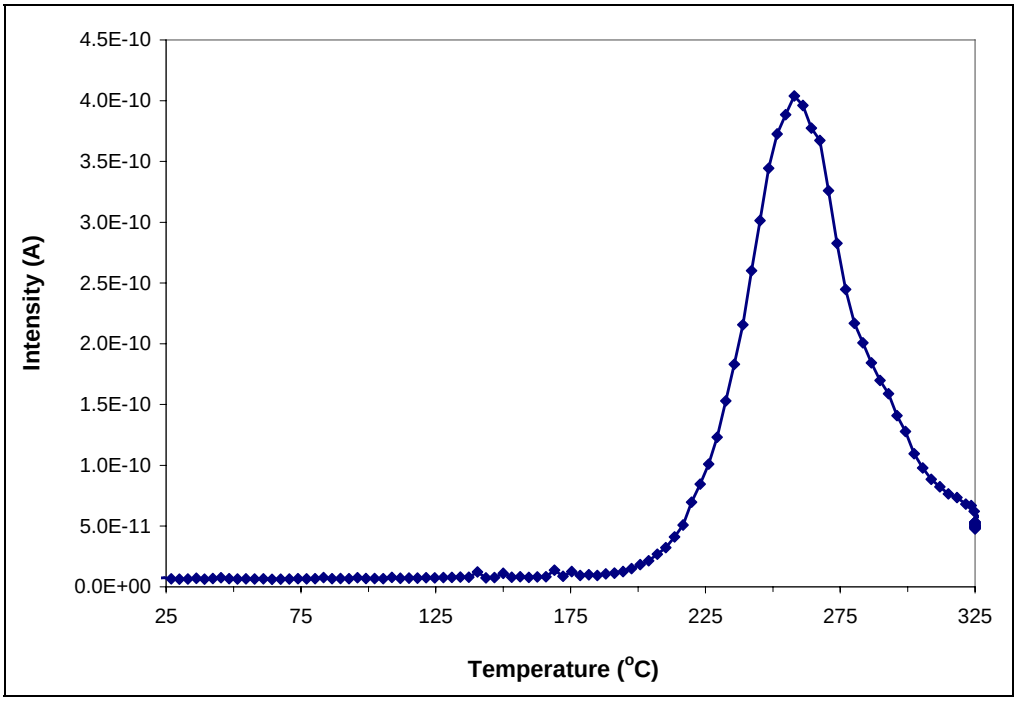

Figure 6.16 – Plot showing temperature dependence of the CO_2 (m/e = 44) MS peak signal level detected by MS during decomposition of **NC2**

The close agreement between the results shown in Figure 6.16 with those shown in Figure 4.3 and Figure 4.11 indicates that the grafting of **PNC3** oligomers to POSS segments did not have any significant effect on the decomposition rate of the polycarbonate chains (ie. kinetic parameters for decomposition of grafted **PNC3** chains are similar to the values for ungrafted oligomers).

CHAPTER 7

PROCESSING AND CHARACTERIZATION OF POROUS FILMS USING UNGRAFTED PNC OLIGOMERS

7.1 Materials Used

HSQ resin was obtained from Dow Corning as a solution in MIBK solvent that is sold under the tradename FOx® by Dow Corning. When it was necessary to recover HSQ resin in dry form in order to change its solvent, it was stabilized via silanization and then purified as described in chapter 5. The porous films whose properties are discussed in this chapter were all templated using either **PNC1-ROP** or **PNC3** as the ungrafted sacrificial polymers. **PNC1-ROP** oligomers were obtained from Promerus LLC and they were synthesized by their polymer chemists via proprietary synthesis and purification procedures. The synthesis and purification procedures for obtaining **PNC3** oligomers were outlined in chapter 3, and the thermal properties of both **PNC1-ROP** and **PNC3** were shown in chapter 4. For films templated with **PNC1-ROP** as the sacrificial polymer, no attempt was made to change the solvent of the FOx-1x® resin since this polymer had adequate solubility in MIBK solvent. Due to poor solubility in MIBK, the films templated with **PNC3** were all spun from chloroform solutions. CTS was obtained from Lancaster Synthesis and TTBPS-Tf, which was obtained from Sigma-Aldrich. N-methylnifedipine was synthesized and its chemical structure validated according to detailed procedures reported in literature.[203, 204] Luer-lock type syringes,

polytetrafluoroethylene (PTFE) membrane syringe filters with 0.2 μm pores, and PTFE-coated stirrer bars were purchased from VWR.

7.2 UV-induced Porosity: Direct-Write layer

For all direct-write films, only **PNC1-ROP** was used as the sacrificial polymer since it had the highest thermal stability of all the types of PNCs studied, as shown in Figure 4.3. The prerequisite for using a polymer with a high thermal stability was due to the need to avoid blanket thermolysis throughout the spun film since this would destroy the photodefinability of porous regions via UV-initiated acidolytic decomposition, as discussed earlier in chapter 4.[1, 2] Blanket DUV exposures were performed using an Oriel 92521 floodlit lamp and blanket i-line (365 nm) UV exposures were performed using an OAI mask aligner. UV-patterning was performed via exposure through a patterned photomask using a Karl-Suss MJB-3 contact aligner. DUV intensities were measured at 240-250 nm and i-line intensities were measured at 365 nm using calibrated UV photometers.

7.2.1 Type-A and Type-B Direct-Write Formulations

CTS was used as the PBG for Type-A direct-write films and N-methylnifedipine was used as the PBG for Type-B direct-write films. The templated PAG used in the both Type-A and Type-B direct-write films was TTBPS-Tf. This PAG was selected due to its high thermal stability, strong photoacid, and its wide range of processing temperatures for the selective UV-decomposition of **PNC1-ROP**, as illustrated in Figure 4.8.[1, 2] Prior to mixing direct-write formulations, separate dilute solutions were made for the following

substances in MIBK solvent: CTS PBG, N-methylnifedipine PBG, TTBPS-Tf PAG, and **PNC1-ROP** sacrificial polymer. FOx-1x® resin was used as supplied from Dow Corning. Although both CTS and N-methylnifedipine PBGs were thermally unstable, their absorbance spectra were very different (CTS was highly absorptive at wavelengths <300 nm and N-methylnifedipine was highly absorptive up to 400 nm). Owing to the different absorption properties of these PBGs, two separate types of direct-write formulations were made, named type-A and type-B.

For Type-A formulations, the separate solutions of CTS, TTBPS-Tf, **PNC1-ROP**, and FOx-1x® resin were mixed to produce the following mass ratios with respect to dry solids: wt PBG to wt PAG to wt **PNC1-ROP** to wt HSQ = 1:2:2:20. For Type-B formulations, the separate solutions of N-methylnifedipine, TTBPS-Tf, **PNC1-ROP**, and FOx-1x® resin were mixed to produce the following mass ratios with respect to dry solids: wt PBG to wt PAG to wt **PNC1-ROP** to wt HSQ = 1:5:10:50 and 1:10:20:100. Both types of direct-write solutions were passed through 0.2 μm PTFE membrane filters prior to spin-coating onto silicon wafers to avoid film non-uniformities arising from the presence of particulates.

7.2.2 Direct-Write Processing

The basic sequence for the direct-write process is shown in Figure 1.2.[1, 2] The first step involved the dispensing of a direct-write formulation onto silicon wafer. The spin-coated film was then cured (hardened) below the thermal activation temperature of the PAG to avoid decomposing the sacrificial polymer throughout the film. The low-temperature curing occurred via base-catalyzed gelation of the SOG matrix where the

bases used were released from the templated PBG molecules.[1, 2, 203-205, 242] To crosslink type-A direct-write films, the samples were placed in a horizontal tube furnace already at 160-170^{o}C and baked for 30 minutes in stagnant air. The baking activated the CTS PBG molecules resulting in the release of cyclohexylamine, which catalyzed the gelation of HSQ.[1, 2, 203-205, 242] Since N-methylnifedipine could be activated either thermally or by UV-exposure >300 nm, type-B direct-write films were crosslinked either by a similar bake procedure to Type-A films (30 minute bake in air at 160-170^{o}C) or exposed to 1 J cm^{-2} of 365 nm UV underneath a filter that prevented DUV from penetrating the films (since it would have prematurely activated the PAG) followed by a PEB at 120^{o}C for 30 minutes in a horizontal tube furnace.[1, 2, 203, 204] After the crosslinking step shown in Figure 1.2, the films were exposed to DUV radiation and post-exposure baked (PEB) to activate the PAG and catalyze acidolytic decomposition of the templated PNC chains in the irradiated regions.[1, 2] The minimum dose of DUV radiation used to fully activate the PAG was 3.8 J cm^{-2}, and the PEB was performed in a preheated horizontal tube furnace at 160-170^{o}C (stagnant air atmosphere) for at least 20 minutes. UV-patterned films were processed in a similar manner to blanket irradiated films except a quartz photomask containing opaque line patterns was used during the DUV exposure to define features on the films.

To prevent **PNC1-ROP** decomposition in unexposed regions and thus maintain the refractive index profile, films were blanket exposed with DUV radiation to activate remaining PAG, followed by either immediate volatilization of acid molecules under high vacuum conditions or immediate neutralization of photogenerated acids using ammonia gas. The films were then heated to about 250^{o}C for 30 minutes while purging the tube

furnace with nitrogen gas at flowrate of 2 L/min to volatilize residual polar species and also to condense residual silanol groups within the SOG matrix. As shown later, this step was necessary because residual polar species degrade the dielectric properties of the porous films. Direct-write control films (HSQPBGPAG), which had the same HSQ, PBG, and PAG loadings as direct-write formulations without any sacrificial polymer were processed in a similar manner to direct-written films to determine the effect of porosity on the average properties of the direct-written matrix.

7.2.3 Dielectric Properties of UV-Written Porous Films

As described in chapter 2, IDEs (comb capacitors) were used to determine the changes in the dielectric constant values of direct-write films and their non-porous control films during each of the processing conditions shown in Figure 1.2. Figure 7.1 compares the dielectric constant results for a type-B direct-written film and its control sample during their processing; the mass ratios of PBG:PAG:**PNC1-ROP**:HSQ in the type-B direct-written film were 2:10:20:100 and the corresponding ratios in the control sample were 2:10:0:100. After gelation, the average polarizability of both the direct-write film and control film increased above that of pure HSQ (k = 2.80) due to the release of bases from their templated PBGs.[3, 5] We see from Figure 7.1 that the direct-write film had a lower dielectric constant (k = 3.10) than its control film (k = 3.55); this effect was because the extra space occupied by the templated polymer chains resulted in the direct-write films having a larger free volume than their control samples. After the UV-exposure step, the dielectric constant of the control sample increased dramatically due to the release of highly polar acids by the activated PAG molecules.[3, 5]

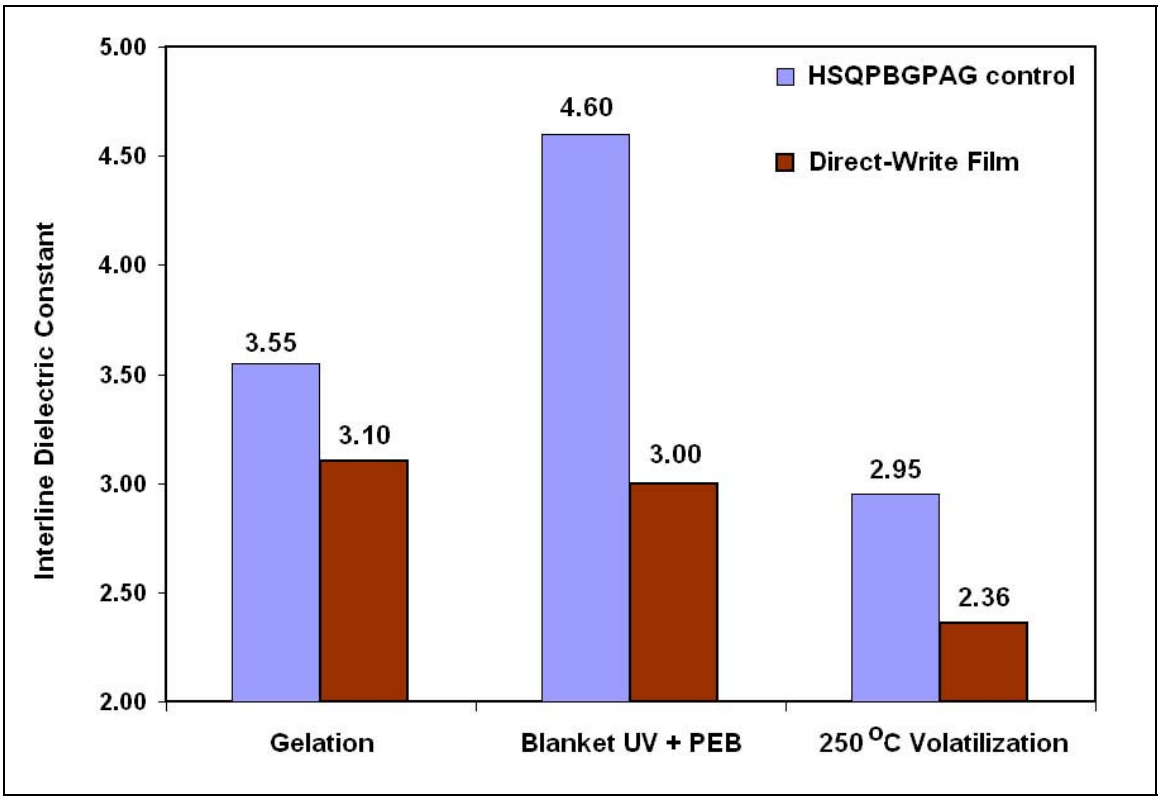

Figure 7.1 – The dielectric constants values for blanket irradiated direct-write films (20% **PNC1-ROP** loading) and control films (0% PNC) for different processing conditions.

The *decrease* in the dielectric constant of the direct-write films after UV-exposure was due to the formation of porosity within their matrix, which was a result of the acidolytic-decomposition of the PNC molecules that was discussed in chapter 4.[1-3, 29, 54, 64, 106] Although photoacids are highly polar, the porosity incorporated in the direct-write film partially counteracted the polarity of the acids and bases, resulting in a *decrease* in the overall polarizability of the templated matrix. The presence of residual polar species in the direct-write films prevented them from achieving their lowest polarizability after decomposition of all the porogen.[3] To achieve the lowest possible dielectric constant values a high temperature volatilization step was used to remove all

acids, bases, and any residual PNC degradation products from the films. As shown in Figure 7.1, the final dielectric constant of the direct-written film was 2.36, which was comparable to published dielectric values of sacrificial polymer systems at similar loading levels.[3, 29, 53, 54, 62, 63, 96] As described earlier in chapter 2, the Maxwell-Garnett mixing rule, equation (2.3), was used to solve for the porosity within porous films.[103] Equation (2.4) is obtained when the dielectric constant of air (k = 1) is substituted into Maxwell-Garnett mixing rule, followed by the rearrangement of the expression to explicitly solve for the vol% occupied by air pockets (ie. the porosity) within a porous film.[3, 29, 53, 54, 62, 64] When the final dielectric constant of the direct-write film and the final dielectric constant of the non-porous control film were substituted into equation (2.4), the level of UV-induced porosity was estimated to be 21 vol%. As discussed in a later section, ungrafted PNC chains could not be used to induce porosities higher than 21 vol% due to their large-scale agglomeration during spincoating.

7.2.4 Refractive Indices UV-Written Porous Films

Figure 7.2 shows values of refractive index of the exposed and unexposed halves of an Type-A film having PBG, PAG and **PNC1-ROP** loadings of 5 wt%, 10 wt%, and 10 wt%, respectively. The refractive index of the direct-write film shown in Figure 7.2 decreased on the irradiated side from 1.406 to 1.344 due to the incorporation of porosity within the matrix. In comparison, the refractive index of its control sample (abbreviated as HSQPBGPAG and having no PNC) remained at 1.379 after undergoing the same bake conditions.

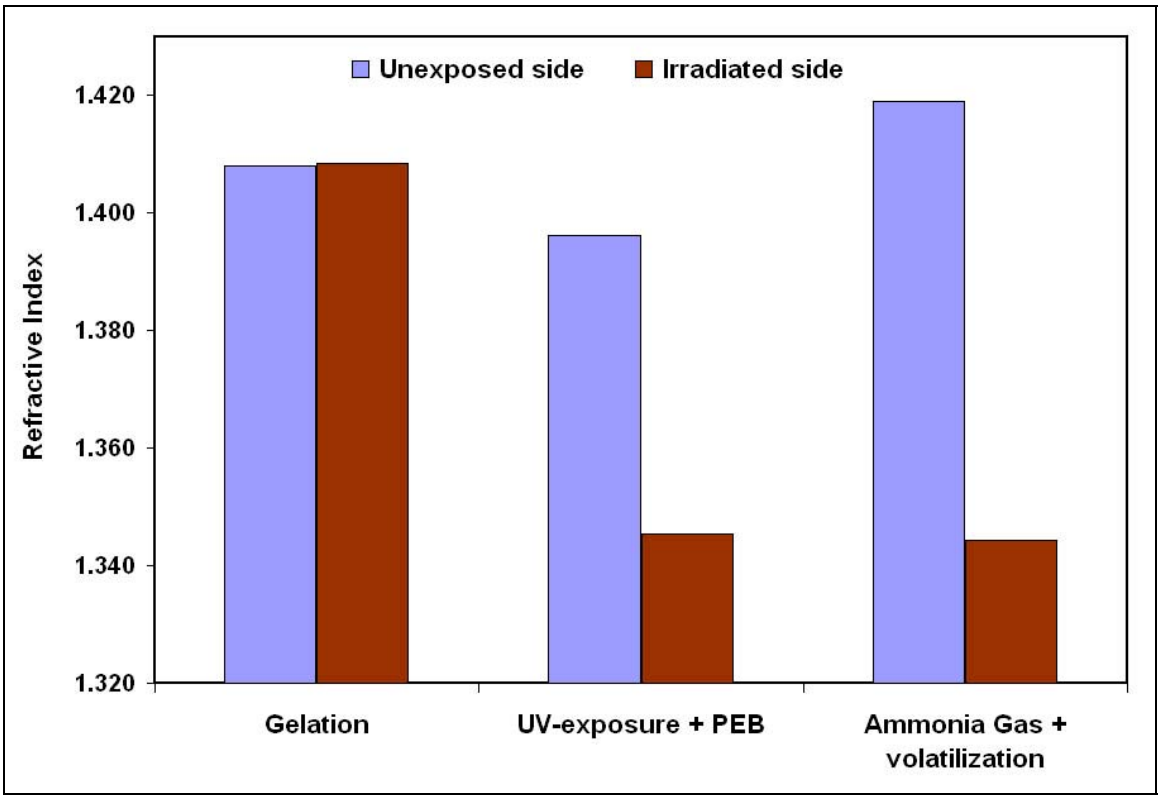

Figure 7.2 – Refractive index values on irradiated and unexposed halves of a type-A direct-write film after sequential processing steps. The **PNC1-ROP** loading was 10 wt%.

Unlike the dielectric constant values, the refractive index values were observed to remain low even directly after the release of photoacids because optical frequencies (~ 10^{14} Hz) are above the maximum frequencies for orientation and distortion polarization.[3] Hence, residual acid and base had a much lower influence on refractive index measurements than on dielectric constant measurements. As further evidence of this, the refractive indices of HSQPBGPAG control films were found to be similar to those of pure HSQ films both after the second and third steps of the direct-write process. The refractive index in the unexposed half of the wafer was fairly constant during the PEB because the unexposed PAG was thermally stable during the 170^{o}C bake; hence, there was the absence of acidolytic decomposition of the **PNC1-ROP**. As shown in

Figure 7.2, the refractive index of both sides of the type-A film increased slightly during the deactivation step. The cause for this increase was likely the increased film density that was produced by the condensation of dangling silanol bonds during the high temperature treatment.

As described in chapter 2, the Lorentz-Lorenz mixing rule was rearranged, as shown in equation (2.2), to solve for the vol% of air within a porous film.[3, 29, 53, 54, 62, 64, 93] At PNC loadings of 10%, type-A direct-write films were estimated to have 8 vol% of UV-induced porosity while type-B direct-films with the same porogen loading were capable of supporting 10 vol% of porosity. It was also observed that the porosity in type-A direct-write films could not be increased higher than 8 vol% even when their PNC loadings were increased above 10 wt%. The limited porosity of type-A direct-write films was due to the inability of CTS PBGs to sufficiently crosslink HSQ so as to support porosity levels higher than 8%. As shown in Figure 5.11, the N-methylnifedipine PBG was much more efficient than the CTS PBG at crosslinking HSQ.[1, 2] This led to type-B direct-write films being more rigid than type-A direct-write films and as a result capable of supporting higher porosity levels, as shown in Table 7.1. At a **PNC1-ROP** loadings of 20 wt% type-B direct-write films had final refractive index values as low as 1.313 while their control samples had refractive index value of 1.398. Thus, type-B films were capable of supporting up to 19 vol% of porosity. The numerical values of porosity calculated using refractive index and dielectric constant mixing rules for this film are in close agreement (Lorentz-Lorenz estimated 19 vol% porosity and Maxwell-Garnett estimated the porosity to be 21 vol%). For similar loading levels of porogen, the differences in the refractive indices of the direct-write films used in this study and their

controls samples were comparable to published data for photobleaching direct-write systems that used polysilanes as the templated porogen.[69-71, 73, 74, 258] The differences between the final optical properties of PAG/polycarbonate direct-write systems and polysilane direct-write systems was due to the differences in the material properties of the sol-gel matrix materials used (HSQ, titania, and silica) and also the differences in the loading levels of the templated porogens.[78]

Table 7.1 – Summarized comparison of the final refractive indices of direct porous films templated with **PNC1-ROP** and their non-porous control films

Type of Porous Film	**PNC1-ROP** loading (wt%)	Final Refractive Index	Estimated Porosity (vol %)
Type-A control film	0	1.379	N/A
Type-B control film	0	1.398	N/A
Direct-written (Type-A)	10	1.344	8%
Direct-written (Type-B)	20	1.313	19%

7.3 Thermally-Induced Porosity

To produce thermally-induced porous films from ungrafted sacrificial polymers, both **PNC1-ROP** and **PNC3** were used as the porogens. Since neither acids nor bases were needed for thermal processing of porous films (HSQ was crosslinked via thermal reaction, as described in chapter 5 and the PNCs were decomposed via thermolytic decomposition, as described in chapter 4), their formulations consisted of only two solutes: PNC and HSQ. Due to differences in the inherent solubility of each the two types of templated polymers, formulations containing **PNC1-ROP** were made using MIBK as their solvent and those containing **PNC3** chains were made using chloroform as their solvent. As stated earlier in chapter 1, the traditional template technique involved

only two processing steps after spincoating; namely, a crosslinking step and a decomposition step.[54] The section below describes the detailed procedure for producing porous HSQ films using only high temperatures to induce reactions.

7.3.1 Thermal Processing

PNC/HSQ solutions were passed through 0.2 μm PTFE membrane filters prior to spin-coating onto silicon wafers to avoid film non-uniformities arising from the presence of particulates. The filtered solutions were then dynamically dispensed onto spinning silicon wafers to form templated spun films. The spin-coated films were then isothermally cured in a horizontal tube furnace in ambient air for 2 hours at 200^{o}C. During the thermal curing step, the internal chemical structure of HSQ rearranged to produce a rigid, silica-like network, as described in chapter 5.[11, 13-17, 19] HSQ films cured under these conditions were observed to be sufficiently rigid to support at least 20 vol% of porosity without pore collapse, and their reduced moduli was measured to be about 4 GPa.[1, 14, 101] After the cure step was completed, the films were inserted into a preheated tube furnace that was purged with nitrogen and held at a temperature of 200^{o}C. Once the films were inserted, a programmable heater was used to increase the temperature of the tube furnace from 200^{o}C to 325 ^{o}C at a controlled rate of 3 ^{o}C/min. The tube furnace was then held at 325 ^{o}C for up to 90 minutes to ensure complete decomposition of the templated porogen (see chapter 4 for TGA curves of PNCs). The tube furnace was then allowed to cool gradually to 200^{o}C before the porous films were withdrawn and characterized.

7.3.2 Dielectric Properties of Thermally-Processed Porous Films

As described in chapter 2, area capacitors were used to determine the dielectric constant values of thermally-processed porous films. Table 7.2 shows the values of the dielectric constants of the porous films and a pure HSQ control sample.

Table 7.2 – Comparison of the final intralevel dielectric constants of non-porous control films and porous films templated with **PNC1-ROP** at a frequency of 100 kHz.

Sample ID of porous films	Type of Film	Polymer loading (wt%)	Dielectric constant of porous film	Estimated Porosity (vol %)
N/A	Control film (pure HSQ)	0	2.80	N/A
K1	Thermally-processed **PNC1-ROP**	20	2.29	20%
K2	Thermally-processed **PNC3**	24	2.31	19%

As described in chapter 2, the Maxwell-Garnett mixing rule was used to calculate the porosity within each of the porous films.[103] According to equation (2.4), the level of thermally-induced porosity in sample K1 and K2 were estimated to be 20 vol% and 19 vol%, respectively. The measured dielectric constants and porosity values for the films shown in Table 7.2 are comparable to literature values (k = 2.0-2.3) for thermally-processed films with similar loading levels of porogen.[3, 29, 53, 54, 62, 63, 96] We observe from Table 7.2 that PNC loadings higher than 20% did not result in higher levels of porosity nor lower dielectric constants. As shown later, this was due to the partial collapse of macro-sized pores that were formed as a result of agglomeration of ungrafted porogen chains during spincoating.[1, 2]

7.3.3 Refractive Indices of Thermally-Processed Porous Films

Table 7.3 shows the final refractive index values for thermally-processed films that were templated with different loadings of ungrafted **PNC1-ROP** and **PNC3** oligomers as well as the optical data for their control films (pure HSQ), which underwent the same processing conditions.

Table 7.3 – Final refractive indices of non-porous control films and thermally-induced porous films templated with **PNC1-ROP**, **PNC3**, and **PNC2** oligomers

Sample ID of porous film	Type of Film	Polymer loading (wt%)	Refractive Index of porous film	Estimated Porosity (vol %)
N/A	Control Film	0	1.394	N/A
R1	Thermally-processed **PNC1-ROP**	10	1.34	12%
R2	Thermally-processed **PNC1-ROP**	20	1.302	21%
R3	Thermally-processed **PNC3**	24	1.313	19%

Thermally processed porous films with initial PNC loadings of 20 wt% had a final refractive index of 1.302 after decomposition and the control films had a final refractive index value of 1.394. As done with the direct-write films, porosity was estimated using the Lorentz-Lorenz mixing rule.[3, 29, 53, 54, 62, 63, 93, 96] The amount of thermally-induced porosity for sample R1, R2, and R3 was estimated to be 12 vol%, 21 vol%, and 19 vol%, respectively. It was observed that loadings higher than 20% of ungrafted PNC chains did not result in higher levels of porosity. As stated in the previous section, this was because the ungrafted chains agglomerated during spincoating and the matrix was unable to fully support the macro-sized pores that were eventually produced.

7.6 TEM Analyses of Porous Films Templated using Ungrafted Oligomers

As described in chapter 2, FIB was used to mill ultrathin cross-sections of porous films for in-plane TEM imaging of the pore structure. Figure 7.3 shows the internal pore structure of a cross-section of a type-B direct-write porous film that was templated with 20% of ungrafted **PNC1-ROP** chains.

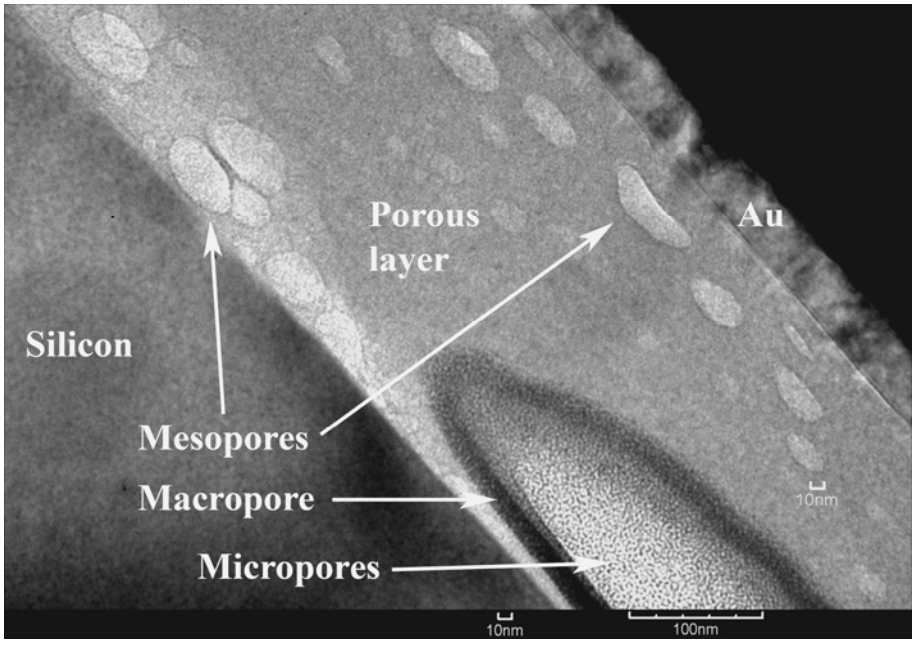

Figure 7.3 – In-plane TEM image of a type-B direct-write porous film templated with 20% **PNC1-ROP**.

The internal structures of thermally-processed porous films initially templated with 20% **PNC1-ROP** chains are shown in Figure 7.4 and Figure 7.5. From Figure 7.3 we see that in addition to medium-sized ellipsoidal pores measuring 20-30nm by 30-50 nm there were also maco-sized pores with lengths ranging from about 100 nm to over 200 nm. The 1 nm wide micropores that are visible in the lower right corner of Figure 7.4 were not due to decomposition of the porogen; rather, they are due to the intrinsic

void space within the HSQ matrix, as reported by other researchers.[3, 11, 16-18, 23, 234]

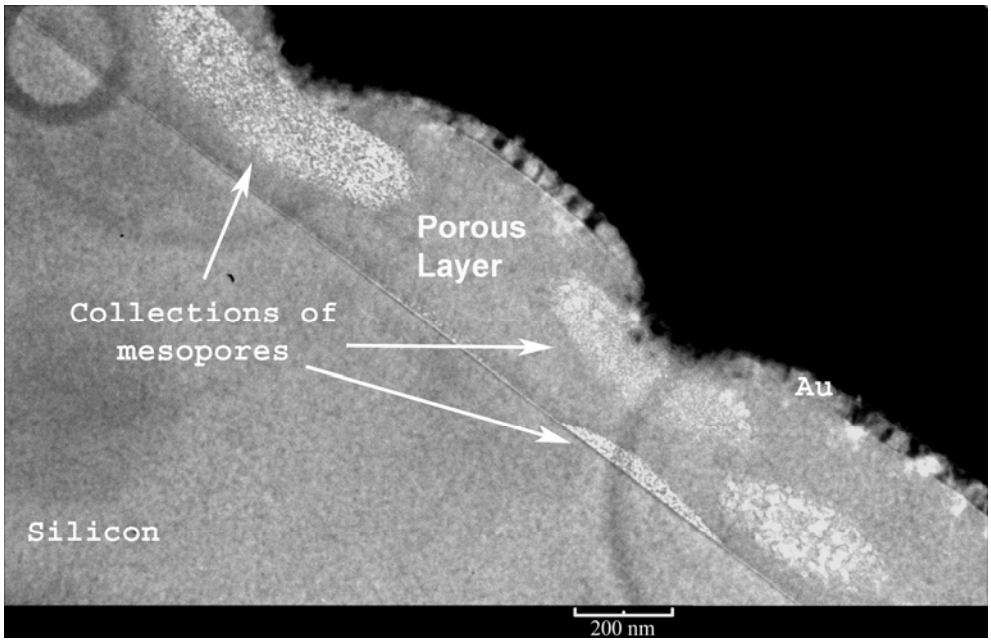

Figure 7.4 – In-plane TEM image of a thermally-processed porous film templated with 20% **PNC1-ROP**.

We know from the size estimates of individual PNC chains with random coil and rigid-rod configurations (refer to Table 3.4) that the average length of individual chains was less than 7 nm. The detection of pores with sizes larger than 7 nm was consistent with the agglomeration of individual sacrificial chains prior to their decomposition. Figure 7.4 and Figure 7.5 provide further evidence for the phase-segregation of the porogen; the macro-sized clusters of mesopores observed in the TEM images were produced due to the agglomeration of the sacrificial chains prior to decomposition. Hence, TEM analysis showed that ungrafted PNC oligomers were phase-incompatible with the HSQ matrix.

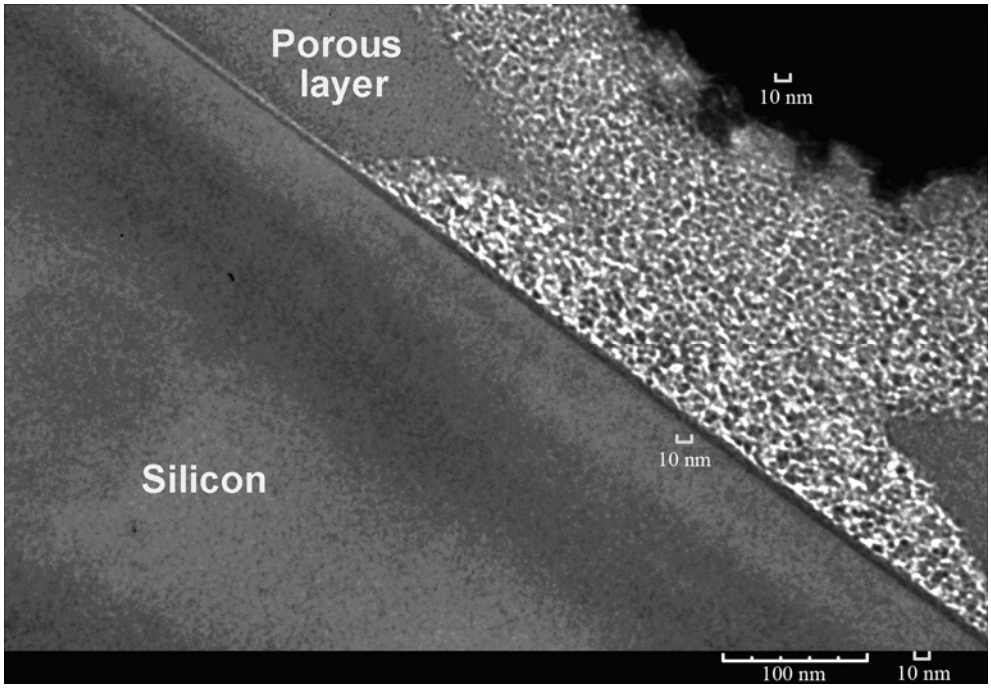

Figure 7.5 – A highly magnified in-plane TEM image of a porous cluster in a thermally-processed porous film templated with 20% **PNC1-ROP**.

To determine if the large-scale movement of the porogen was taking place predominantly during the spincoating step or during subsequent processing steps, the multiple templated films were separately imaged via through-plane TEM imaging after different processing steps. As described in chapter 2, the substrates for the through-plane TEM imaging were ultrathin free-standing silicon nitride membranes, which were fabricated according to the method reported by Lee and co-workers.[107, 108] Formulations of templated films were then spin-coated onto chip-pieces containing multiple free-standing membranes and each film was then processed and later cleaved into individual free-standing membranes. Free-standing membranes were then mounted on to TEM grids and analyzed to view the though-plane distribution of the templated domains after each of the processing steps. To enhance image contrast, all non-porous

films were selectively stained with osmium vapor prior to TEM imaging, as described in chapter 2. ImageJ software was used to analyze the sizes and size distributions of the templated domains before the results were exported as spreadsheet data for further analysis.[259, 260] EXCEL software used to perform statistical analysis so as to quantify any changes in both the size of domains and their overall size distributions during processing.

Figure 7.6 shows a typical through-plane TEM image of an "as spun" film (ie. imaged after spincoating step) that was templated with a 24% loading of ungrafted **PNC3** oligomers. When multiple "as spun" samples were analyzed, the sample-to-sample deviation in the average lengths of the major and minor axes of the elliptical domains was about 1 nm, which was within the standard deviation of the size distributions within each sample. Statistical analysis of multiple "as spun" samples showed that the average length of the major axes of "as spun" domains was 37.6 nm with a standard deviation of 8.6 nm, while the minor axes had an average size of 26.7 nm with a standard deviation of 7.6 nm. The overall size distribution of the major axes of all the domains of multiple "as spun" samples is shown in Figure 7.7. If we compare the dimensions of the "as spun" domains to the estimated sizes of individual PNC chains (refer to Table 3.4), we clearly see that the templated domains are actually clusters of several individual oligomers; thus, phase-segregation was taking place during the spincoating step.

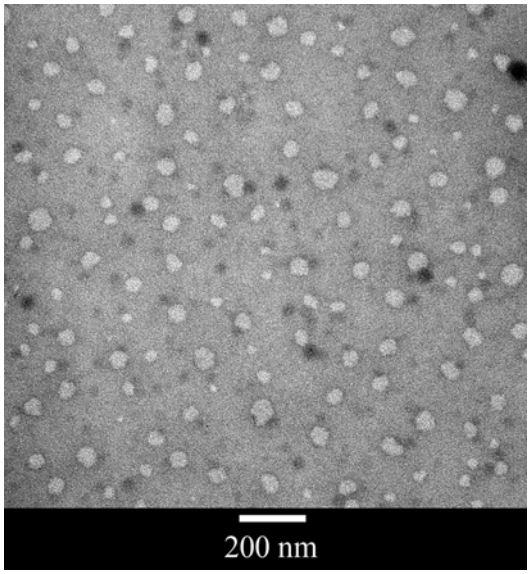

Figure 7.6 – through-plane TEM image of an osmium stained "as spun" film templated with ungrafted **PNC3** chains at a loading of 24%

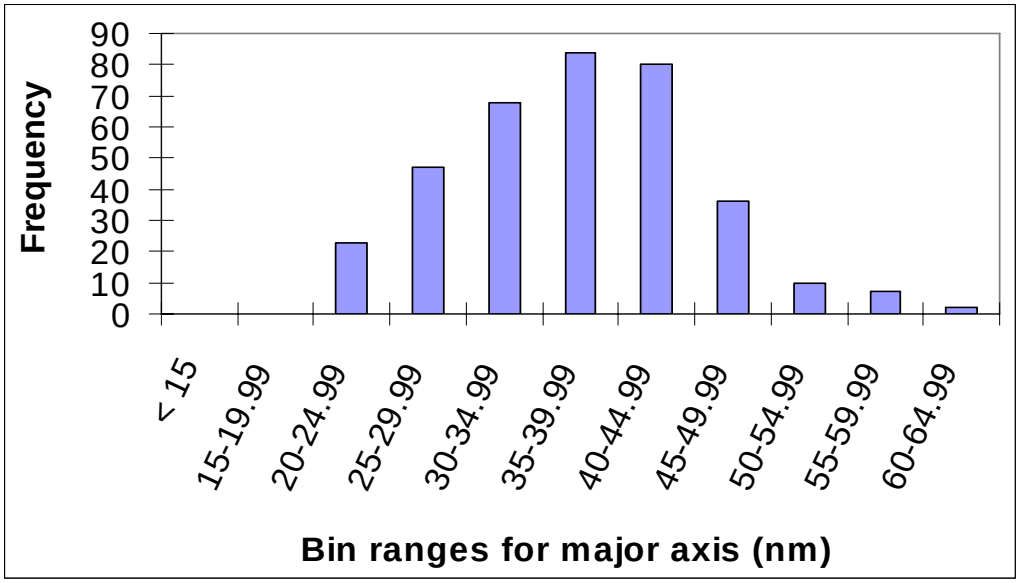

Figure 7.7 – Histogram showing the overall size distribution of the major axes of "as spun" domains in multiple films that were templated with ungrafted **PNC3** oligomers at a loading of 24%

As shown in Figure 7.8, when the agglomerated porogen chains were eventually decomposed, pores were produced with sizes comparable to the "as spun" domains. The

statistical results for multiple templated films of identical loadings of ungrafted **PNC3** chains are summarized in Table 7.4 for each of the processing steps. Since the morphologies of the templated films were largely influenced by the phase behavior during the spincoating steps, a uniform distribution of small pores cannot be achieved in fully-processed films without the compatibilization of the porogen prior to spincoating.

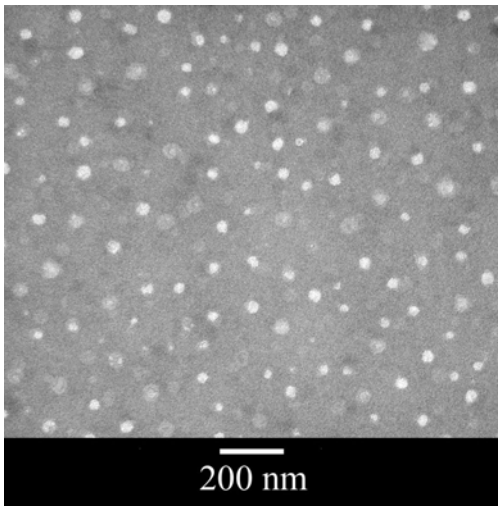

Figure 7.8 – A through-plane TEM of a porous film initially templated with ungrafted **PNC3** chains at a loading of 24%

Table 7.4 – Summary of statistical data for thermally-processed films templated with 24% of ungrafted **PNC3** chains

Last processing step prior to Imaging	Dimensions of major axes		Dimensions of minor axes	
	Average length (nm)	Standard deviation (nm)	Average length (nm)	Standard deviation (nm)
After spincoating	37.4	8.4	26.7	7.6
After curing	35.8	9.1	28.2	6.3
After decomposition	33.6	6.6	27.8	6.1

Researchers have shown that porogen agglomeration can be prevented by covalently bonding the templated porogen molecules directly to the spinnable low-k matrix material.[28, 53, 54, 62-64, 96] Using this technique, pore sizes as low as 10 nm have been formed in polymeric films,[53, 54, 64] and pore sizes as low as 2-3 nm have been reported in silsesquioxane films.[28, 62, 63, 96] As discussed in chapter 6, all attempts at grafting **PNC3** chains directly to the HSQ resin were unsuccessful; however, **PNC3** chains were successfully grafted to matrix-like compatibilizers. It is expected that the matrix-like segments in the hybrid molecules would prevent or at least mitigate large-scale agglomeration of the porogen during spincoating. To determine the phase-compatibility of the nanocomposite molecules with HSQ, they were templated in HSQ films, processed, and analyzed using TEM imaging, as discussed in the following chapter.

CHAPTER 8

PROCESSING AND CHARACTERIZATION OF POROUS FILMS TEMPLATED WITH PNC-SILOXANE AND PNC-SILSESQUIOXANE NANOCOMPOSITE MOLECULES

8.1 Materials Used

HSQ resin was stabilized via silanization and then purified as described in chapter 5. The recovered HSQ solids were then redissolved in chloroform and these solutions were used to make formulations for templated films, as described in chapter 7. The polycarbonate-siloxane hybrid molecules (ie. **NC1**) and polycarbonate-silsesquioxane hybrid molecules (ie. **NC2**) were synthesized and purified according to the procedures detailed in chapter 6. Due to solubility constraints imposed by the **PNC3** segments, all the **NC1** and **NC2** formulations were made in chloroform.

8.2 Thermal Processing of Templated Nanocomposite Films

To ensure a fair comparison between the properties of porous films templated with nanocomposite blends and those templated with their ungrafted **PNC3** precursors, the loadings of **NC1** and **NC2** in their respective formulations films were adjusted to maintain the total amount of sacrificial components at the same loading level as that use for ungrafted **PNC3** films (ie. 24 wt%). The calculated compositions of each nanocomposite blend are shown in chapter 6. The nanocomposite films were thermally-

processed using identical procedures to that used for films templated with ungrafted **PNC3** oligomers, which were described in chapter 7.

8.3 Dielectric Properties of Thermally-Processed Porous Films

As done with the ungrafted **PNC3** films, area capacitors were used to determine the dielectric constant values of thermally-processed porous films produced from the decomposition of **NC1** and **NC2**. The dielectric constants of the porous films initially templated with **NC1** and **NC2** are listed in Table 8.1.

Table 8.1 – Comparison of the final intralevel dielectric constants of non-porous control films and porous films templated with **PNC1-ROP** at a frequency of 100 kHz.

Sample ID of porous films	Type of Film	Total loading of NC blends (wt%)	Equivalent loading of sacrificial segments (wt%)	Dielectric constant of porous film	Estimated Porosity (vol %)
N/A	Control film (pure HSQ)	0	0	2.80	N/A
K3	Porous film templated with **NC1**	24	24	2.21	23
K4	Porous film templated with **NC2**	31	24	2.17	25

As done with previous porous films, the Maxwell-Garnett mixing rule was used to estimate the porosity within each of the porous films.[3, 29, 53, 54, 62, 64, 103] According to equation (2.4), the level of porosity in sample K3 and K4 were estimated to be 23 vol% and 25 vol%, respectively. The measured dielectric constants for the films shown in Table 7.2 are similar to those reported in literature (k = 2.0-2.3) for thermally-processed films with similar loading levels of porogen.[29, 53, 54, 62, 64] By comparing

the results shown in Table 8.1 with those shown in Table 7.2 (sample K2) we observe that, unlike the films templated with only ungrafted PNC, nanocomposite films are able to be produced with porosity levels higher than 20% even though the loading level of sacrificial material in the nanocomposite films was equivalent to that used in the **PNC3** films (ie. 24%). As shown later, the ability for nanocomposite films to support more porosity was due to the hybrid molecules producing smaller pores that were easily supported by the crosslinked matrix. The small pore sizes were a result of the improvement in the phase-compatibility of **PNC3** chains that were grafted to compatibilizer segments. However, as shown in chapter 6, the **NC1** and **NC2** blends could not be completely purified from the residual unreacted **PNC3-OH** chains, which led to a few large domains due to the phase segregation of the residual ungrafted chains during spincoating. Hence, the successful isolation of hybrid molecules from the residual **PNC3** chains would allow higher loading levels to be used, which would result in higher porosity levels and even lower dielectric constants than those shown in Table 8.1.

8.4 Refractive Indices of Thermally-Processed Porous Films

After the decomposition of all sacrificial components, the porous **NC1** and **NC2** films were analyzed by ellipsometry and their refractive indices are shown in Table 8.2. Using the Lorentz-Lorenz mixing rule, the amount of porosity in R4 and R5 were estimated to be 24 vol% and 26 vol%, respectively.[3, 29, 53, 54, 62, 64, 93] These values are higher than the porosity of films templated with ungrafted **PNC3** with equivalent sacrificial content (refer to sample R3 in Table 7.3).

Table 8.2 – Final refractive indices of non-porous control films and thermally-induced porous films templated with **PNC1-ROP**, **PNC3**, and **PNC2** oligomers

Sample ID of porous film	Type of Film	Total loading of NC blends (wt%)	Equivalent loading of sacrificial segments (wt%)	Refractive Index of porous film	Estimated Porosity (vol %)
N/A	Control film (pure HSQ)		0	1.394	N/A
R4	Porous film templated with **NC1**	24	24	1.291	24%
R5	Porous film templated with **NC2**	31	24	1.285	25%

As mentioned in the previous section, it is believed that the reason for the matrix in nanocomposite films to be able to support higher levels of porosity than those templated with ungrafted oligomers was indirectly due to the better phase-compatibility of the hybrid molecules. Unlike the ungrafted chains, the **NC1** and **NC2** molecules did not agglomerate into large domains that eventually produced macro-sized pores. The smaller pores produced by the hybrid molecules were easily supported by the matrix and they did not collapse, whereas the larger pores produced by the ungrafted chains could not be fully supported and partially collapsed. However, as shown in chapter 6, the **NC1** and **NC2** blends could not be completely purified from the residual unreacted **PNC3-OH** chains, which led to a few large domains due to the phase segregation of the residual ungrafted chains during spincoating. As discussed earlier, the successful isolation of hybrid molecules would allow porosity levels to be increased and hence, refractive indices to be decreased below the values shown in Table 8.2.

8.5 TEM Analyses of Porous Films Templated with Nanocomposite blends

As done with the templated **PNC3** films, multiple nanocomposite films were spin-coated onto chip-pieces containing ultrathin free-standing membranes and then separately analyzed by TEM after different processing step. Figure 8.1 and Figure 8.2 show typical "as spun" samples of films templated with **NC1** and **NC2**, respectively. Each of the films shown in Figure 8.1 and Figure 8.2 had nanocomposite loadings such that the total **PNC3** content was identical to those of ungrafted **PNC3** films (ie. 24% polycarbonate loading).

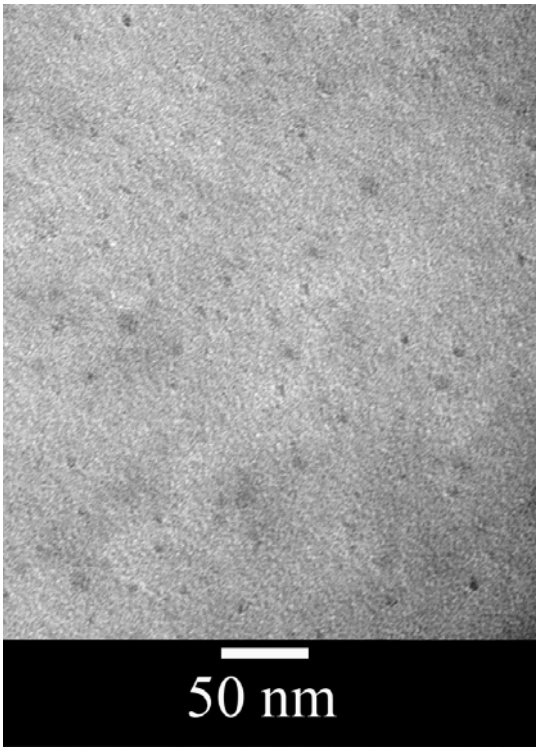

Figure 8.1 – through-plane TEM image of an "as spun" film templated with **NC1** blends at a loading of 32% (the total **PNC3** content was 24%)

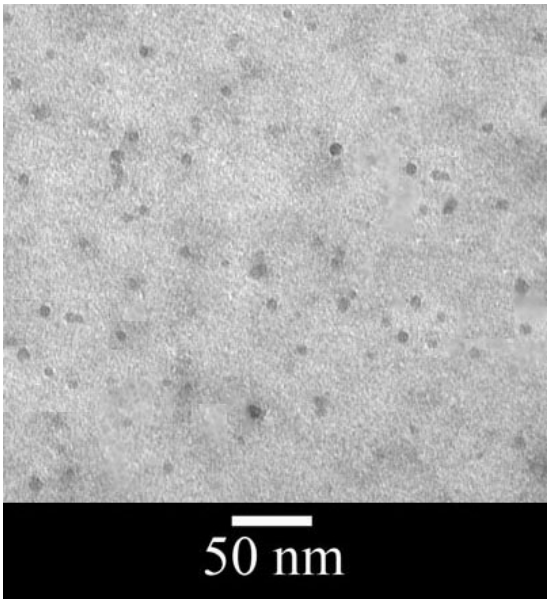

Figure 8.2 - through-plane TEM image of an "as spun" film templated with **NC2** blends at a loading of 31% (the total **PNC3** content was 24%)

As shown in Figure 8.3, films templated with either of the nanocomposite blends were observed to have bimodal size distributions with the vast majority of the domains measured 6-13 nm in length, and a small number of the domains were 24-39 nm in length. The statistical data for "as spun" nanocomposite films is summarized in Table 8.3. We previously observed in chapter 6 (eg. Figure 6.5) that **NC1** and **NC2** solids were both mixtures of hybrid molecules and ungrafted **PNC3** chains and that in both blends about two-thirds of the **PNC3** chains were grafted to compatibilizers and about one-third of the **PNC3** chains remained ungrafted. Additionally, the TEM results of films templated with 24% of ungrafted **PNC3** chains (refer to Figure and Table 7.4) showed that ungrafted PNC chains were phase-incompatible with HSQ and agglomerated during spincoating into domains with an average sizes larger than 30 nm. Thus, it is reasonable to assume that the larger domains observed in the TEM images of nanocomposite films

were due to the agglomeration of residual ungrafted **PNC3** chains that were present in the blends.

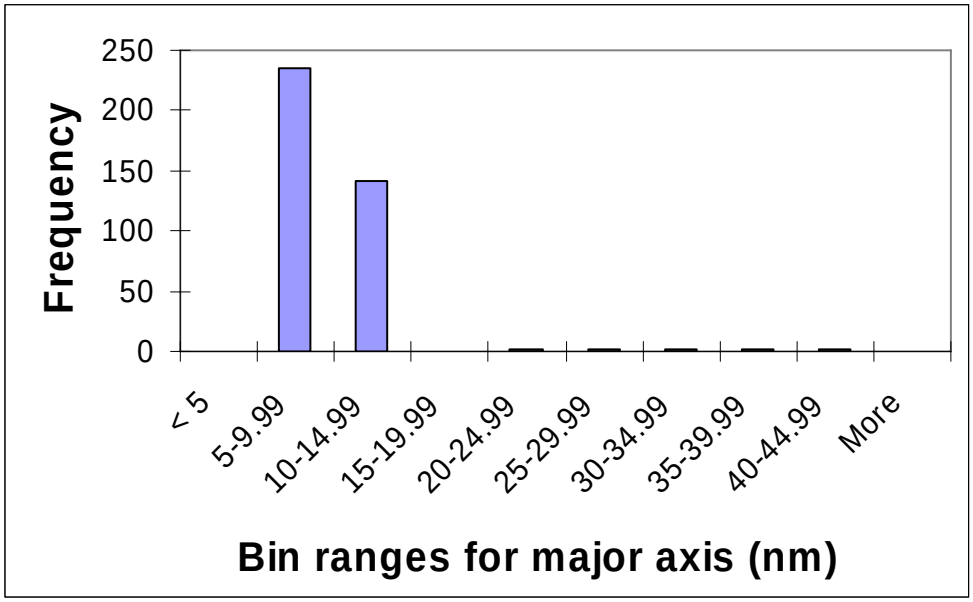

Figure 8.3 - Histogram showing the bimodal size distribution of "as spun" domains in multiple films templated with 32% of **NC1** blends

Table 8.3 – Summary of statistical data for "as spun" films templated with **NC1** and **NC2**

Type of film	Total loading for all solids (wt%)	Loading of PNC chains (wt%)	Type of size distribution	Average length of each category of domain size	
				Smaller domains	Larger domains
NC1	32	24	Bimodal	9.0	32.9
NC1	24	17	Bimodal	8.8	30.3
NC2	31	24	Bimodal	9.1	33.0

If the assumption that each of the two categories of domain sizes (ie. small and large) was composed of only one type of component (hybrid molecules and ungrafted PNC chains, respectively), then the principle of conservation of mass could be used to test this assumption. From the conservation of mass, we know that the fractional

contribution of each blend component towards the total mass of the templated domains should be equal to its weight fraction in the blend. For a binary component system, this is expressed mathematically by equation (8.1) and equation (8.2), which are equivalent expressions.

$$\left(\sum_i m_i\right) + \left(\sum_j m_j\right) = M_i + M_j \tag{8.1}$$

$$\frac{\sum_i m_i}{\left(M_i + M_j\right)} + \frac{\sum_j m_j}{\left(M_i + M_j\right)} = \omega_i + \omega_j = 1 \tag{8.2}$$

The subscripts in the above expressions refer to the specific component of the binary mixture, the symbol m stand for the mass of an individual domain, the symbol M stands for the total mass of a specific component, and the symbol ω refers to the overall weight fraction of each component. Since the masses of individual domains are unknown variables, the terms on the left hand side of equation (8.2) are converted to their volumetric form, as shown in equation (8.3).

$$\frac{\rho_i\left(\sum_i v_i\right)}{\rho_i\left(\sum_i v_i\right) + \rho_j\left(\sum_j v_j\right)} + \frac{\rho_j\left(\sum_j v_j\right)}{\rho_i\left(\sum_i v_i\right) + \rho_j\left(\sum_j v_j\right)} = \omega_i + \omega_j \tag{8.3}$$

Since the mass densities of the hybrid molecules and ungrafted PNC chains should be similar, we can make the assumption that the volume fraction of each component is approximately equal to its weight fraction, as shown in equation (8.4). The symbol v stands for the volume of an individual domain and the symbol V stands for the total volume of all the templated domains.

$$\frac{\left(\sum_i v_i\right)}{V} \approx \omega_i \tag{8.4}$$

The standard equations for calculating the area and volume of an ellipse are shown in equation (8.5) and equation (8.6), respectively. The length and width, which stand for the major and minor axes of the elliptical domains, were obtained from TEM data; thus, allowing areas to be calculated without any further assumptions.

$$\text{area} = \pi\left(\frac{length}{2}\right)\left(\frac{width}{2}\right) \tag{8.5}$$

$$\text{volume} = \frac{4}{3}\pi\left(\frac{length}{2}\right)\left(\frac{width}{2}\right)\left(\frac{height}{2}\right) = \frac{2}{3}(area)(height) \tag{8.5}$$

Since the vertical dimensions of the domains could not be determined directly from TEM data, the total volume was estimated by assuming that the average height of each type of domain was approximately equal to the average size of their minor axes. Using this assumption and the measured value of the areas, the total volume of each type of domain was estimated, as shown in equation (8.6).

$$\sum_i v_i \approx \frac{2}{3}\left(\sum_i (area)_i\right)(\overline{height}) \approx \frac{2}{3}\left(\sum_i (area)_i\right)(\overline{\text{m inor axis}}) \tag{8.6}$$

The fractional volumes of the small and large domains were found for each type of nanocomposite film, and the results are summarized in Table 8.4. From equation (6.4) and equation (6.7) we know that the weight fraction of ungrafted **PNC3** oligomers in **NC1** and **NC2** blends are about 26% and 23%, respectively.

Table 8.4 – Fractional areas and fractional volumes of the larger domains in "as spun" films templated with nanocomposite blends

Loading and type of Film	Total area of large domains (nm^2)	Area fraction of large domains	Average length of minor axis for large domains (nm)	Estimated total volume of large domains (nm^3)	Volume fraction of large domains
32% **NC1**	1.5×10^4	0.14	24.0	2.4×10^5	0.31
24% **NC1**	1.3×10^4	0.13	22.7	2.0×10^5	0.28
31% **NC2**	1.3×10^4	0.13	23.7	2.0×10^5	0.28

Given that the total volumes of the domains were based on an assumed values for the average height, and that in reality there was likely a significant distribution in the volumes of individual domains, the deviations between the actual weight fractions of the ungrafted PNC chains and their estimated fractional volumes are within reasonable limits. Additionally we observe that although the loading of templated **NC1** solids was varied from 24% to 32% (refer to Table 8.4), the fractional areas of the large domains remained almost constant; which is consistent with the bimodal size distribution being caused by the fixed ratios of the ungrafted and grafted PNC chains in each blend. Had the actual cause for the bimodal size distributions been a gradual phase split of all the templated molecules, there should have been a 33% increase in both the fractional area and the fractional volume as the loading of all **NC1** solids was increased from 24% to 32%. As stated earlier, it has been reported by numerous researchers that covalently bonding a porogen to a low-k matrix or matrix-like material is a proven means of combating phase-segregation.[28, 53, 54, 62-64, 96] Thus, the smaller domains that were produced by the **NC1** and **NC2** hybrid molecules are consistent with improvements in the phase-compatibility of the PNC chains.

When the templated films were fully processed so as to decompose all the sacrificial materials, the pore structure characteristics were observed to be similar to those of "as spun" templated films, as shown in Table 8.5. If the experimentally observed pores sizes shown in Table 8.5 are compared with literature values (refer to Table 8.6), we see that the sizes of the smaller pores are within the range of pore sizes reported in literature for low-k materials.[3, 28, 29, 53, 54, 62, 64]

Table 8.5 – Summary of statistical data for porous films originally templated with **NC1** and **NC2** blends

Type of film	Total loading for all solids (wt%)	Loading of sacrificial components (wt%)	Type of size distribution	Average length of each category of pore size	
				Smaller pores	Larger pores
NC1	32	32	Bimodal	9.0	33.4
NC1	24	24	Bimodal	8.8	31.6
NC2	31	24	Bimodal	9.0	32.8

Table 8.6 – Pore sizes reported in literature for templated films

Sizes of pores (nm)	Literature Reference
10	[53, 54, 64]
2-9	[3]
3-30	[28, 29, 62]
2-3	[63, 96]

It should be noted that published data shows that templated systems in which the porogen is not covalently bonded until after spincoating tend to produce larger pores and also wider pore size distributions.[28, 29, 62] This is because these templated systems have no means of preventing the agglomeration of porogen prior to spincoating, as was

observed with the films templated with ungrafted **PNC3** oligomers (refer to chapter 7). The low-k films with the best pore morphology (narrow pore size distribution, pores sizes less than 5 nm, etc) correspond to template systems in which the porogen is directly bonded to a silsesquioxane matrix prior to spincoating.[63, 96] This is the only means of ensuring that no phase-segregation can take place during spincoating; hence, the pores all have sizes equal to those of individual porogen molecules. Although the hybrid **NC1** and **NC2** molecules showed improved phase compatibility when compared to ungrafted PNC domains, the sizes of the pores appear to be larger than the estimated sizes of individual oligomers (refer to Table 3.4). Hence, it is anticipated that if the polycarbonate molecules had been successfully grafted directly to HSQ resin, then the final pore sizes would have been similar to the sizes shown in Table 3.4. Although all attempts at grafting **PNC3** chains directly to the HSQ resin were unsuccessful, it may be possible to graft a polycarbonate with a less sterically hindered chemical structure directly to the HSQ resin.

CHAPTER 9

CONCLUSIONS AND RECOMMENDATIONS FOR FUTURE WORK

PNC oligomers were synthesized and characterized via NMR, elemental analyses, GPC, DSC, and TGA-MS to determine their chemical structures and decomposition behavior. TGA data showed that PNCs were both thermally-labile and acidolytically-labile, allowing them to be used as sacrificial materials in both direct-write and thermally-processed template systems. TGA data was also used to determine the kinetic parameters for the thermolytic decomposition reactions and evolved-gas analysis via mass spectrometry was used to validate the polycarbonate degradation mechanisms have been previously proposed in literature. Ungrafted PNC oligomers were used as sacrificial materials in templated films, and these films were characterized via ellipsometry, dielectric measurements, and TEM imaging. Although porosity values as high as 20% were successfully incorporated into HSQ by the oligomers, TEM data showed that the free-mixing of PNC with HSQ led to phase-segregation during spincoating. The agglomeration of sacrificial chains resulted in unacceptable morphological characteristics in the porous films. To improve the phase-compatibility of the sacrificial chains, PNC oligomers were grafted to small siloxane and silsesquioxane molecules via hydrosilylation reactions. These matrix-like materials served as compatibilizers in order to improve the phase-compatibility of the sacrificial polymers in HSQ films. NMR and GPC analyses showed that the solids recovered from the hydrosilylation reactions were

binary mixtures of hybrid molecules (grafted PNC chains) and residual ungrafted PNC chains. All attempts at isolating the hybrid molecules proved to be unsuccessful and the solids were templated as blends in HSQ films.

TEM imaging showed that the domains in these nanocomposite films had bimodal size distributions due to the presence of two components in the mixtures. The hybrid molecules produced domains ranging in size from about 6-13 nm as a result of improvements in the phase-compatibility of the grafted oligomers. However, the residual ungrafted oligomers in the blends produced larger domains measuring 30-40 nm. Although the siloxane and silsesquioxane molecules were shown to fulfill the stated goal of compatibilizing the PNC chains with HSQ and the domain sizes of hybrid molecules were comparable to those of templated films reported in literature, the difficulty in purifying the hybrid molecules from the ungrafted oligomers limited the benefits of using these blends as porogen materials.

It is believed that separation difficulties can be avoided if the vinyl termination reaction conditions be adjusted to convert all the terminal hydroxyl groups of the PNC chains to vinyl groups. It was noted during preliminary vinyl-termination reactions that the % conversion of hydroxyl groups was promoted by low temperatures. As stated in an earlier chapter, if ice-water was replaced by ethylene glycol or an alternative solvent with a freezing point below $0^{o}C$, then dry ice could be used to cool the reaction mixture to very low temperatures. These cryogenic conditions may result in achieving 100% conversion of the hydroxyl groups. As an alternative to using allyl chloroformate to react with hydroxyl-terminated PNCs, other vinyl-containing molecules may be investigated, which may be more conducive to achieving fully conversion of all the hydroxyl groups.

Grignard reactions are frequently used to convert hydroxyl groups into other groups, and these types of reactions may prove to be more thermodynamically favorable than the previously used reaction system.[179] Hence, the physical and chemical conditions used in the vinyl termination reactions needs to be investigated further in order to attain full conversion of all hydroxyl groups. If all the PNC chains could be successfully terminated with vinyl groups this would allow all PNC chains to be grafted during hydrosilylation reactions; thus, pure hydrosilylation products could be recovered instead of binary mixtures. Pure hybrid molecules would produce monodisperse domains if templated in templated films, and from TEM data we can expect them to have good pore morphologies. It is believed that the morphology exhibited by the **NC1** and **NC2** hybrid molecules could be improved upon by successfully grafting polycarbonate chains directly to HSQ prior to spincoating thin films. Although all attempts at performing this reaction using PNC chains were unsuccessful, it is expected that another type of polycarbonate with a less sterically-hindered chemical structure may be successfully bonded to HSQ. Based on literature data, such a template system can be expected to produce pores as small as the individual polycarbonate chains, which is an ideal morphology for low-k applications.

A literature survey did not yield any reports of PDMS oligomers being used as sacrificial materials in templated low-k films. However, TGA studies (refer to chapter 5 and chapter 6) showed that small PDMSH chains completely decompose when they are dynamically heated from 200-350 ^{o}C, leaving negligible amounts of residue. PDMS oligomers are attractive sacrificial materials because their chemical structure (siloxane backbone) is similar to those of silica-like low matrix materials (eg. silsesquioxanes).

Hence, PDMS oligomers should have high phase-compatibility with HSQ, which may lead to good morphology for templated domains of PDMSH freely-mixed in HSQ. Additionally, the commercial availability of vinyl-terminated PDMS chains also affords the covalent linking of PDMS oligomers directly to HSQ resin via hydrosilylation reactions. Unlike the PNC oligomers, PDMS chains are free of bulky groups that tend to hinder this grafting reaction; thus, we can anticipate the forward reaction to be facile and produce a hybrid PDMS-HSQ spinnable matrix. If these grafting reactions are successful, then the recovered hybrid matrix would produce templated films with excellent porogen morphology: porogen domains would be uniformly dispersed and have the same dimensions as the individual PDMS oligomers (ie. < 2 nm,). As shown earlier in Table 8.6, these characteristics would be among the best published for porous spun low-k films. [63, 96]

APPENDIX A

MASS SPECTROMETRY DATA FOR PNC DECOMPOSITION: IDENTIFICATION OF VOLATILE CHEMICAL SPECIES

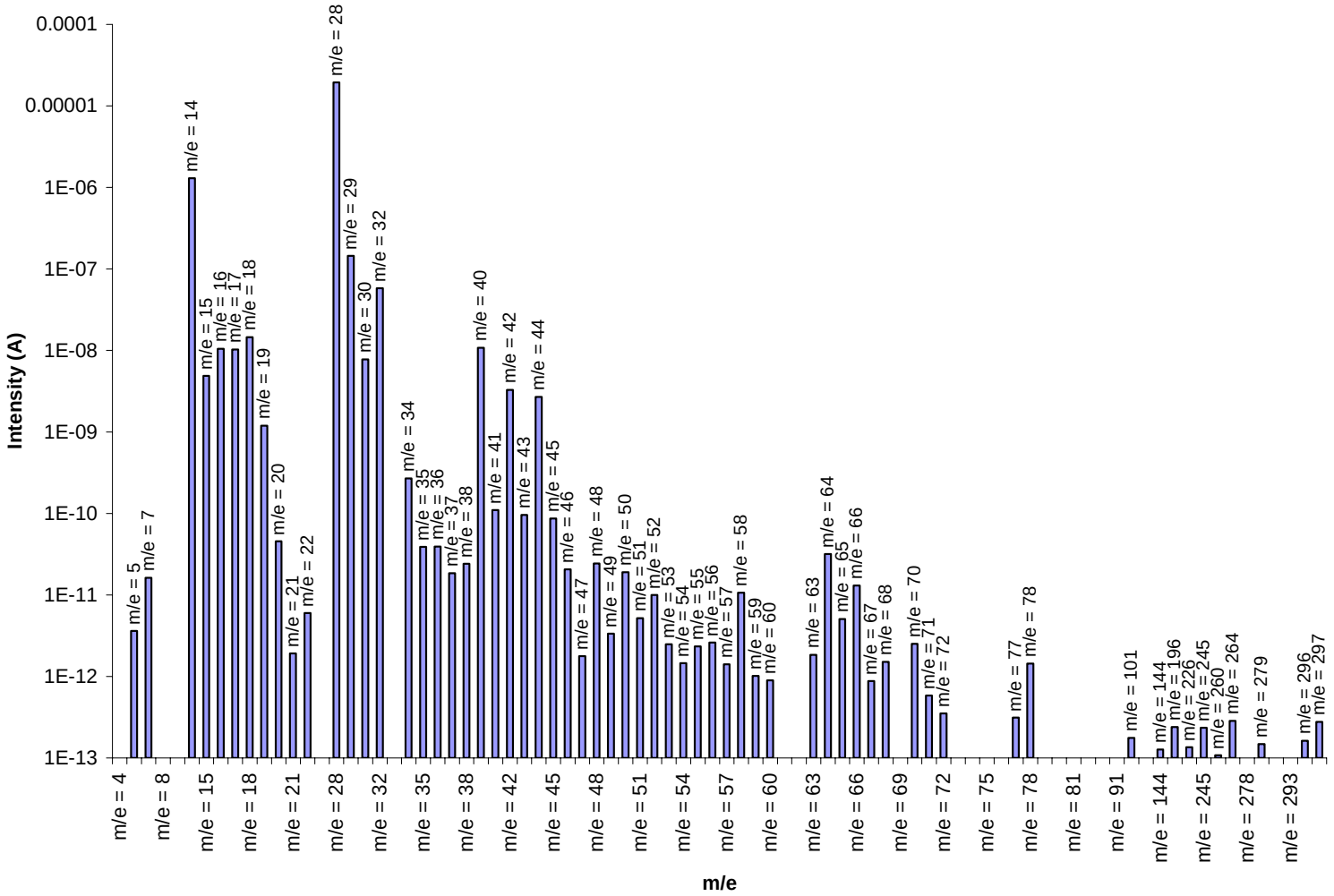

Figure A.1 – Overall relative abundance of MS peaks detected during **PNC1-OH** decomposition. The plot shows MS peaks for all masses with amu <300 and total peak intensities > 10^{-13} A)

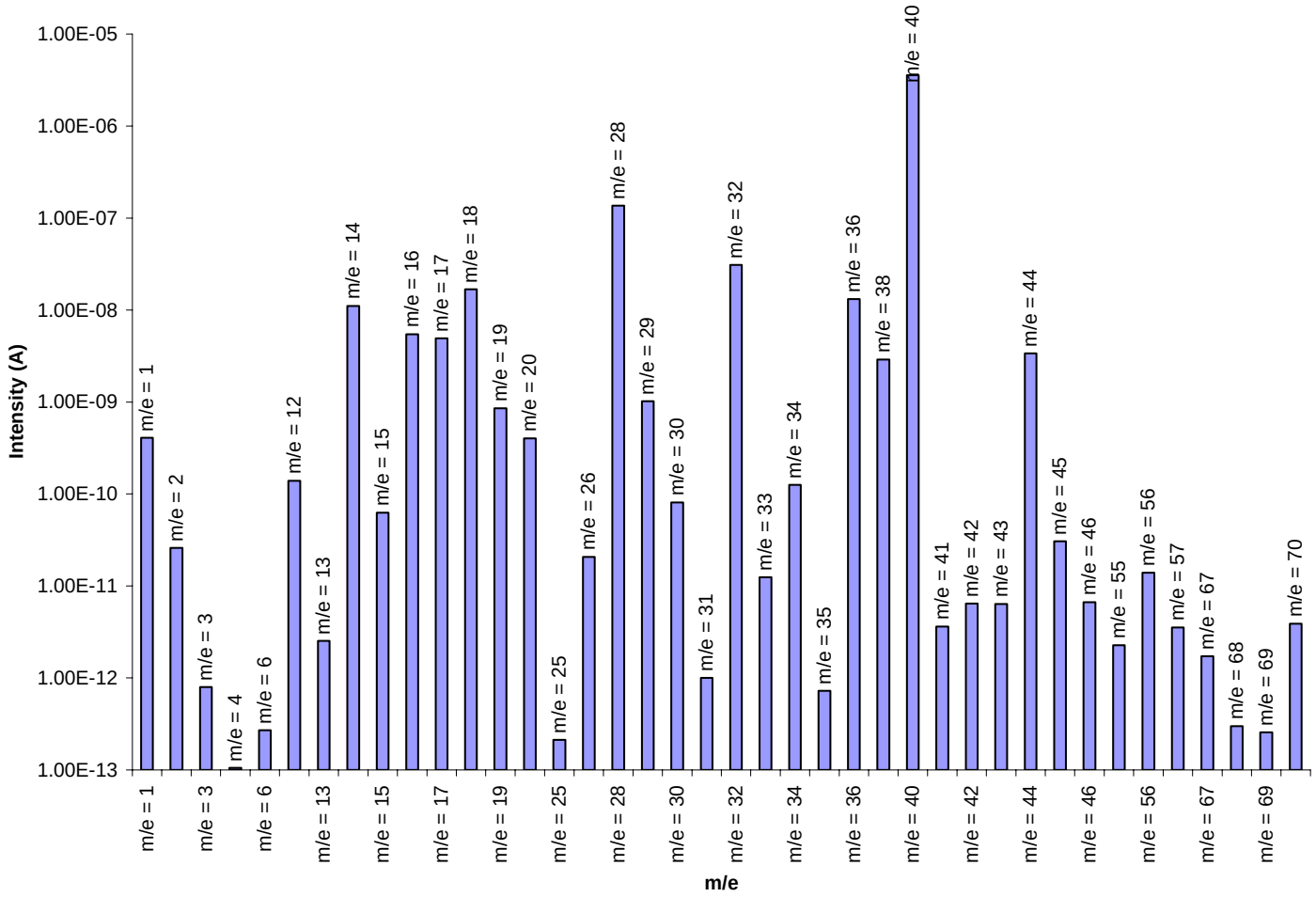

Figure A.2 – Overall relative abundance of MS peaks detected during **PNC2-OH** decomposition. The plot shows MS peaks for all masses with amu <300 and total peak intensities > 10^{-13} A

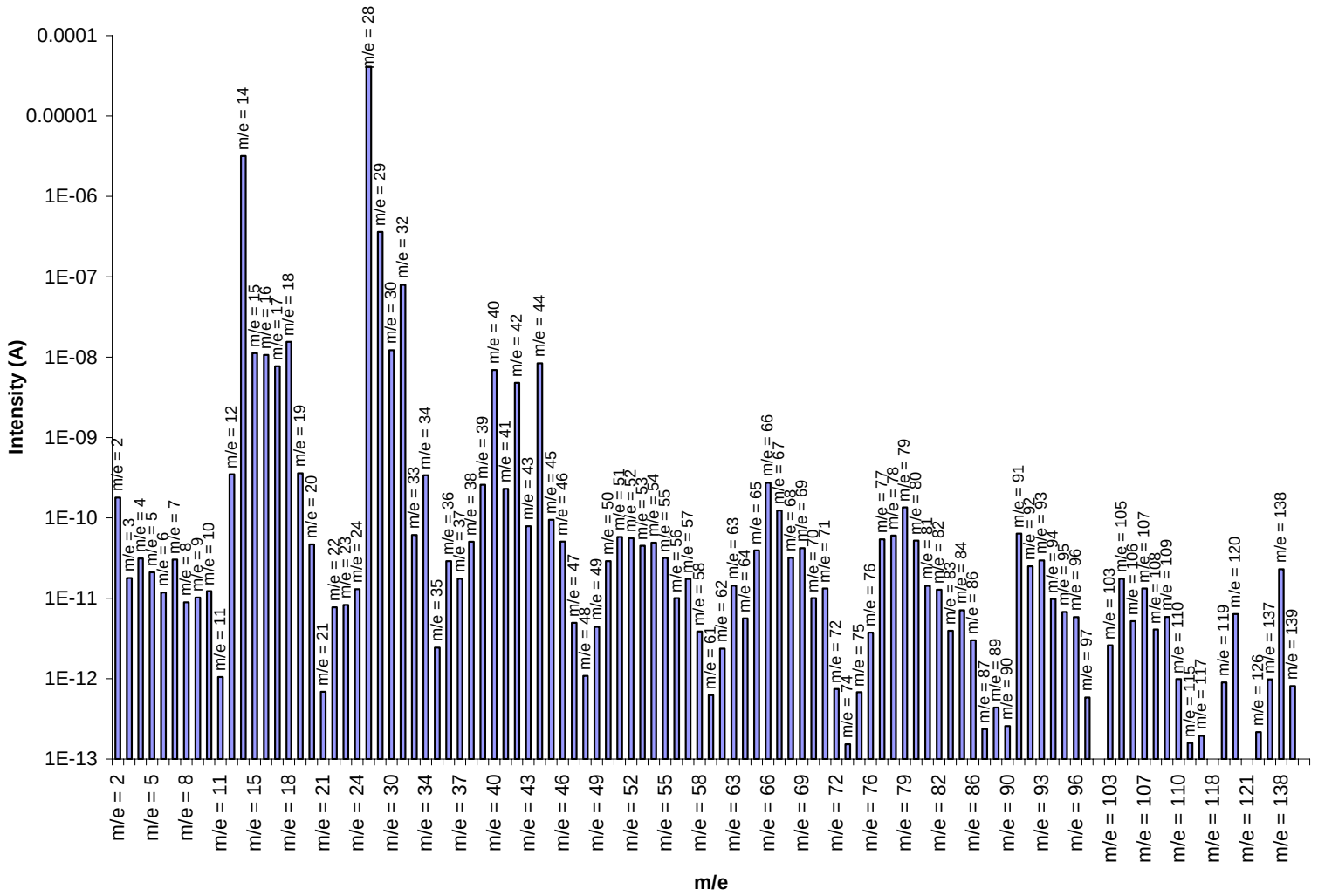

Figure A.3 - Overall relative abundance of MS peaks detected during **PNC3v** decomposition. The plot shows only MS peaks corresponding to masses with amu <170 and total peak intensities > 10^{-13} A.

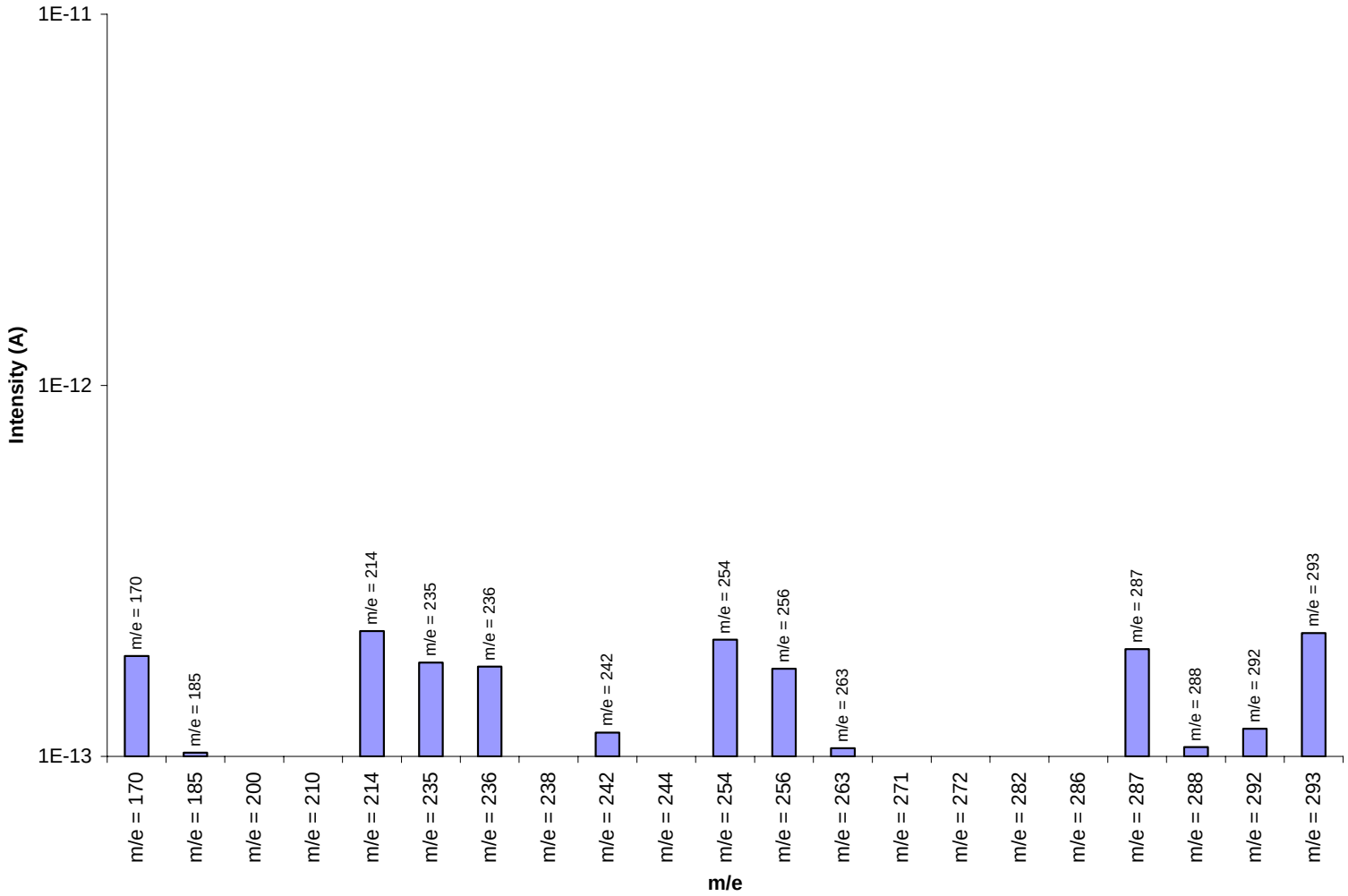

Figure A.4 - Overall relative abundance of trace MS peaks detected during **PNC3v** decomposition. The plot shows only MS peaks corresponding to masses with amu = 160-300 and total peak intensities > 10^{-13} A

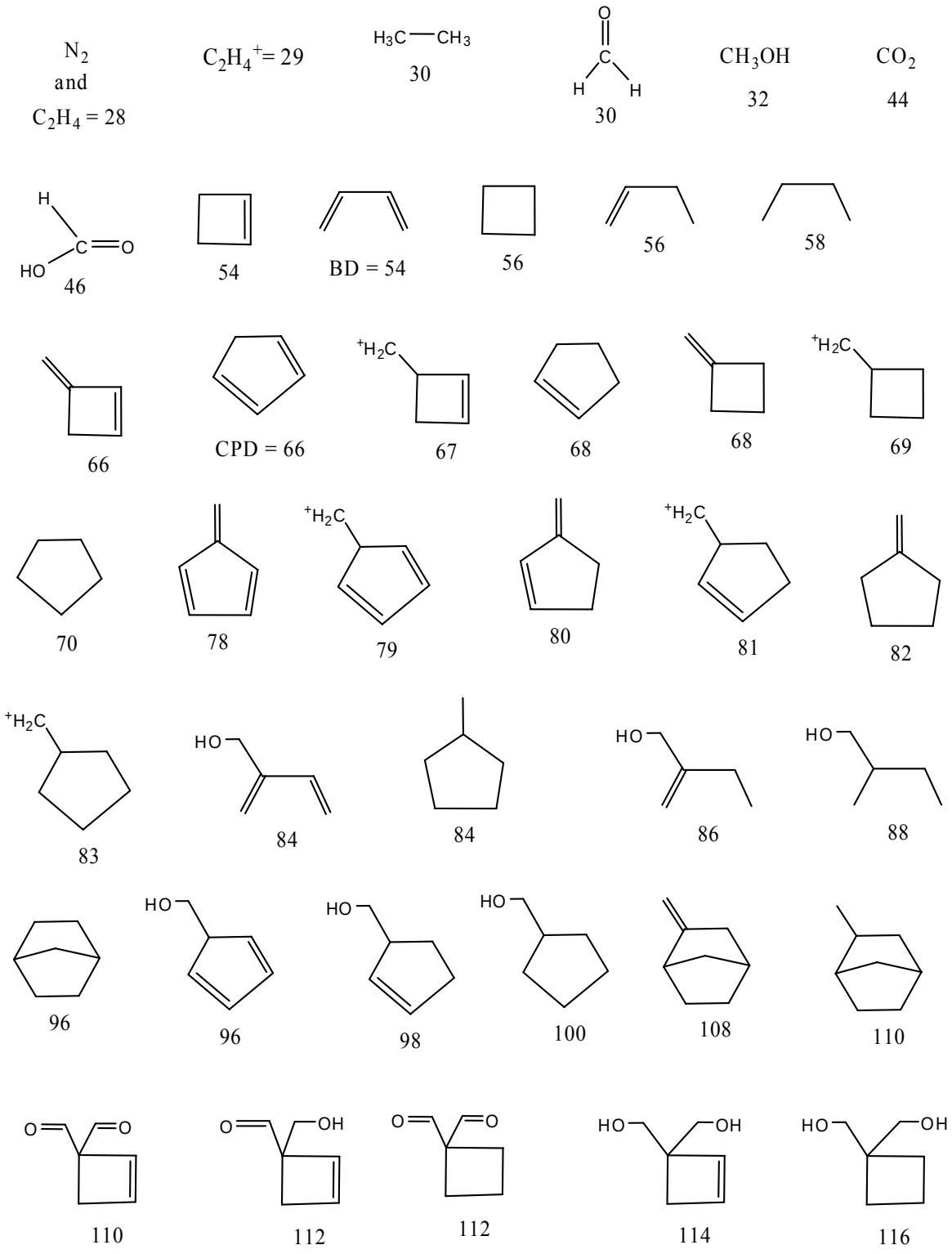

Figure A.5 – **PNC1** decomposition products detected by MS for masses with amu = 28-116

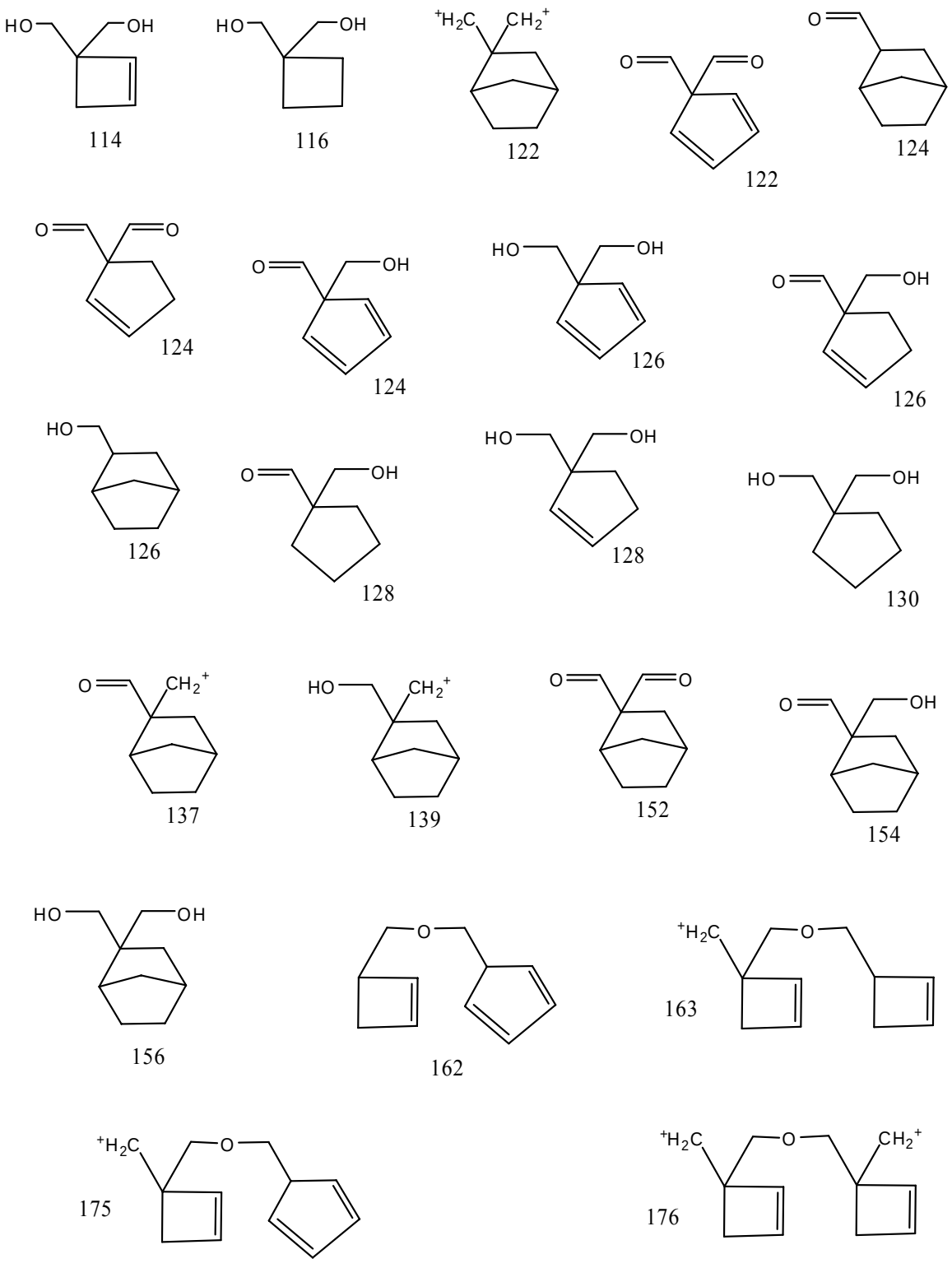

Figure A.6 – **PNC1** decomposition products detected by MS for masses with amu = 114-176

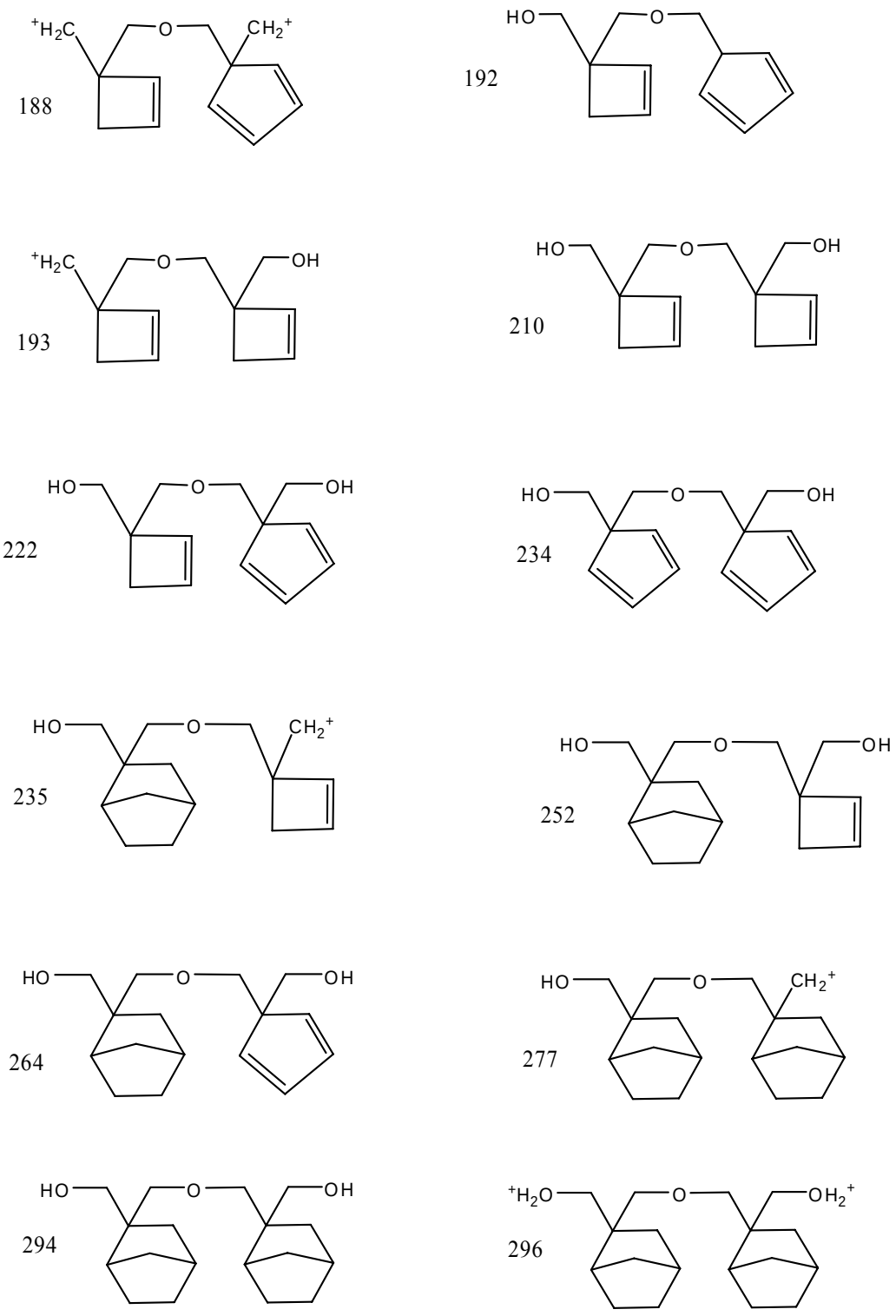

Figure A.7 – **PNC1** decomposition products detected by MS for masses with amu = 188-296

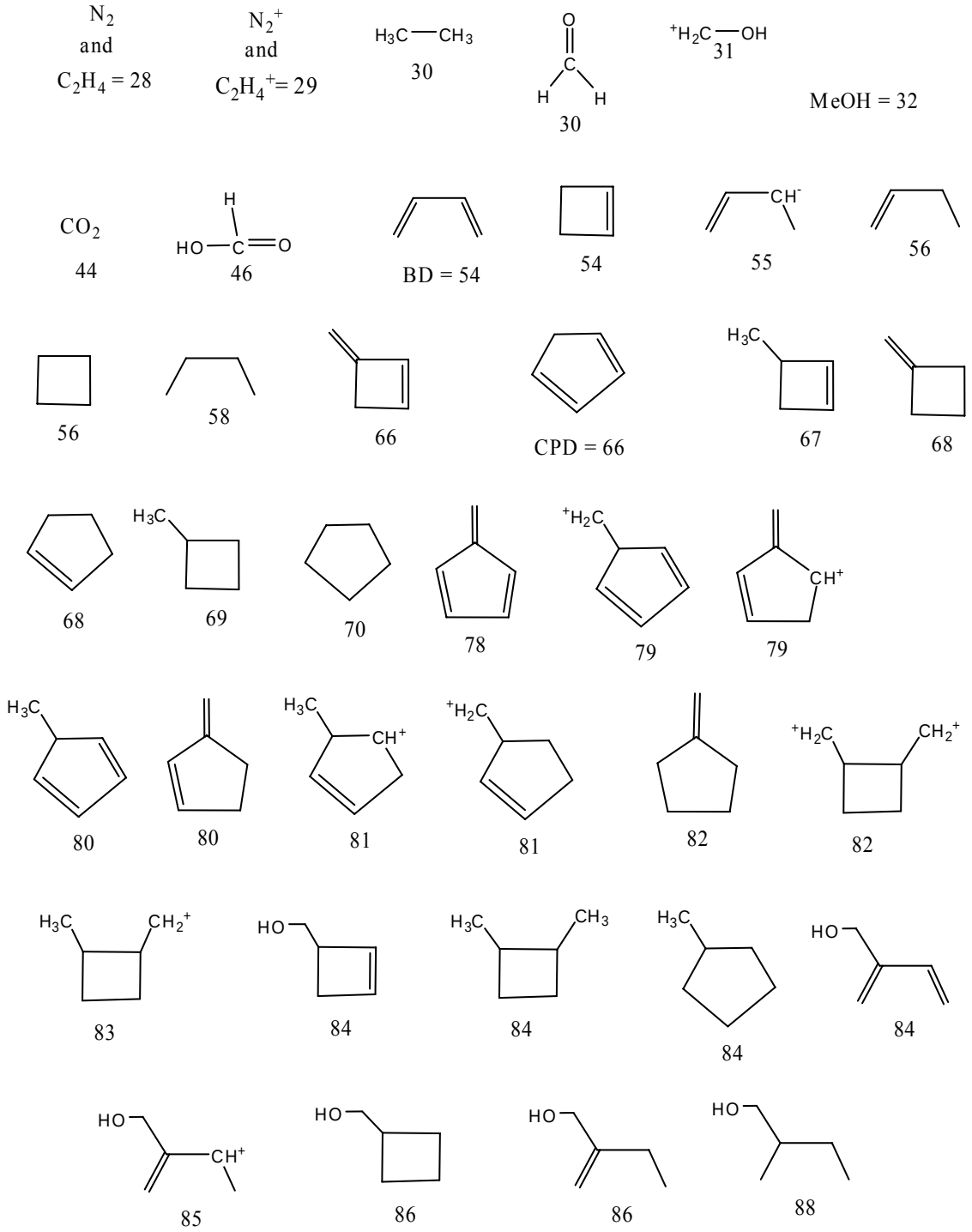

Figure A.8 – **PNC2** and **PNC3** decomposition products detected by MS for masses with amu = 28-88

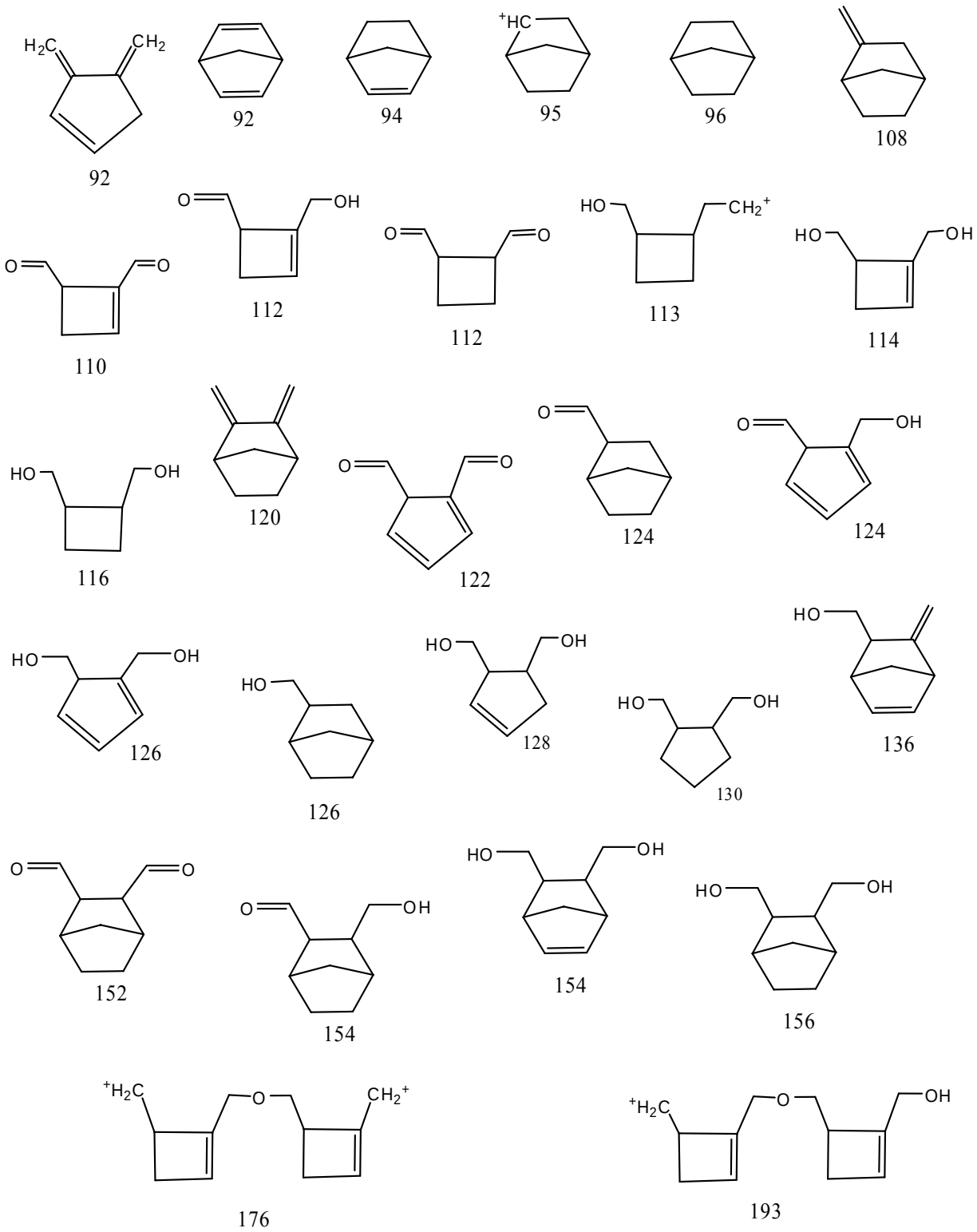

Figure A.9 – **PNC2** and **PNC3** decomposition products detected by MS for masses with amu = 92-193

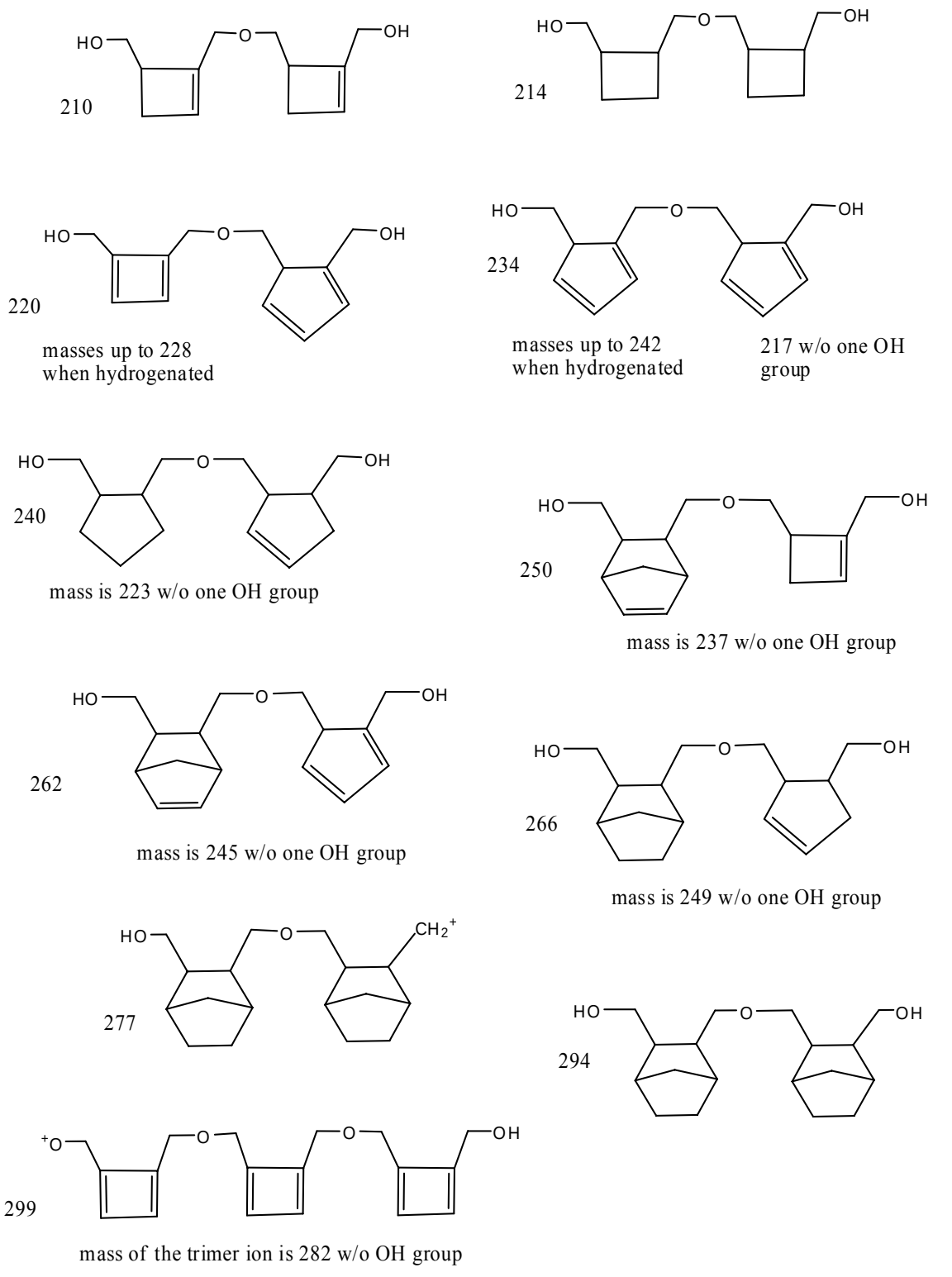

Figure A.10 – **PNC2** and **PNC3** decomposition products detected by MS for masses with amu = 210-299

APPENDIX B

MASS SPECTROMETRY DATA FOR HEATING OF $Q_8M_8^H$ AND PDMSH: IDENTIFICATION OF VOLATILE CHEMICAL CHEMICAL SPECIES

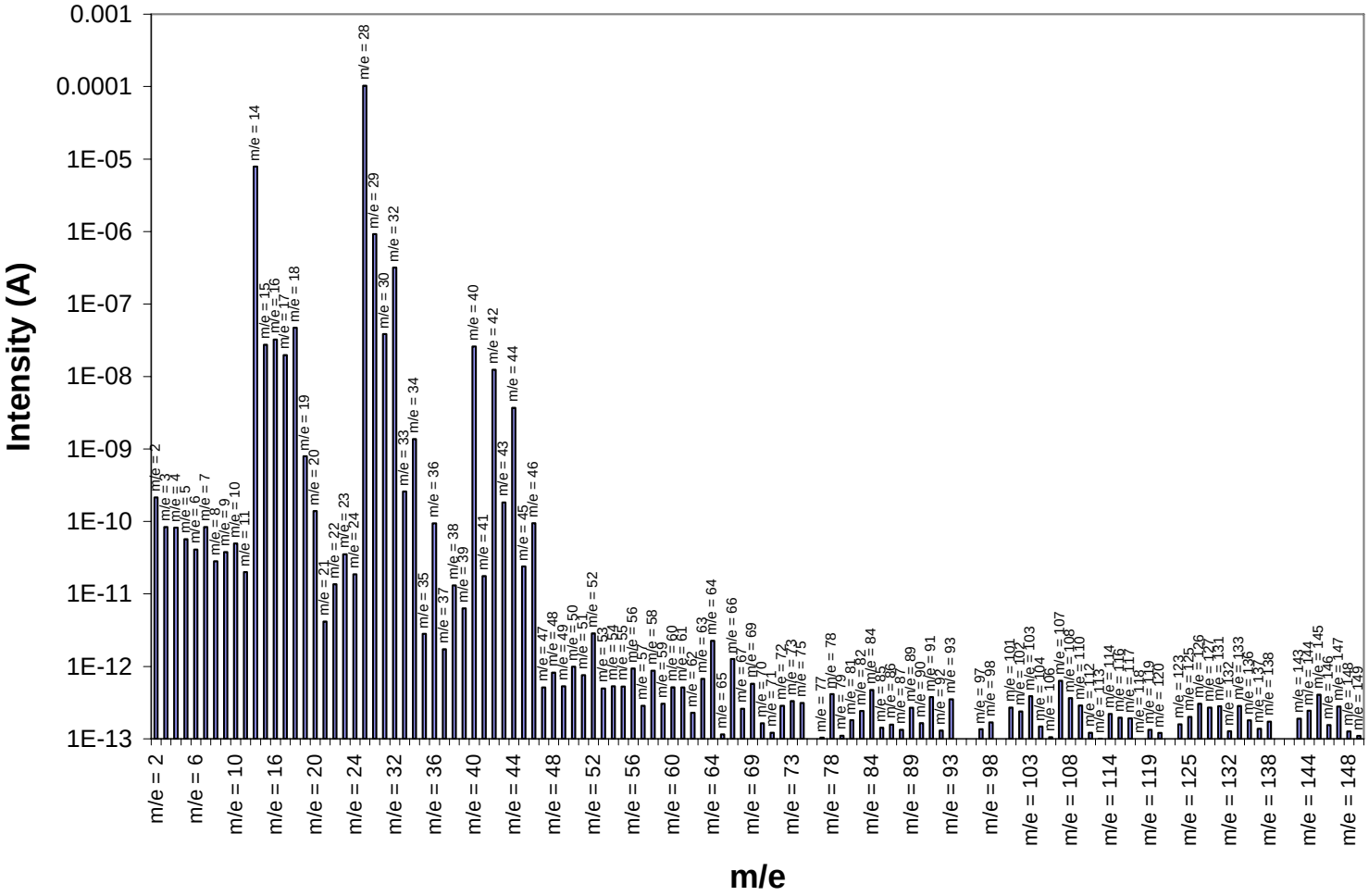

Figure B.1 – Overall relative abundance of trace MS peaks detected during heating of moisture-free $Q_8M_8^H$ (ie. sample B). The plot shows only MS peaks corresponding to masses with amu <150 and peak intensities > 10^{-13} A

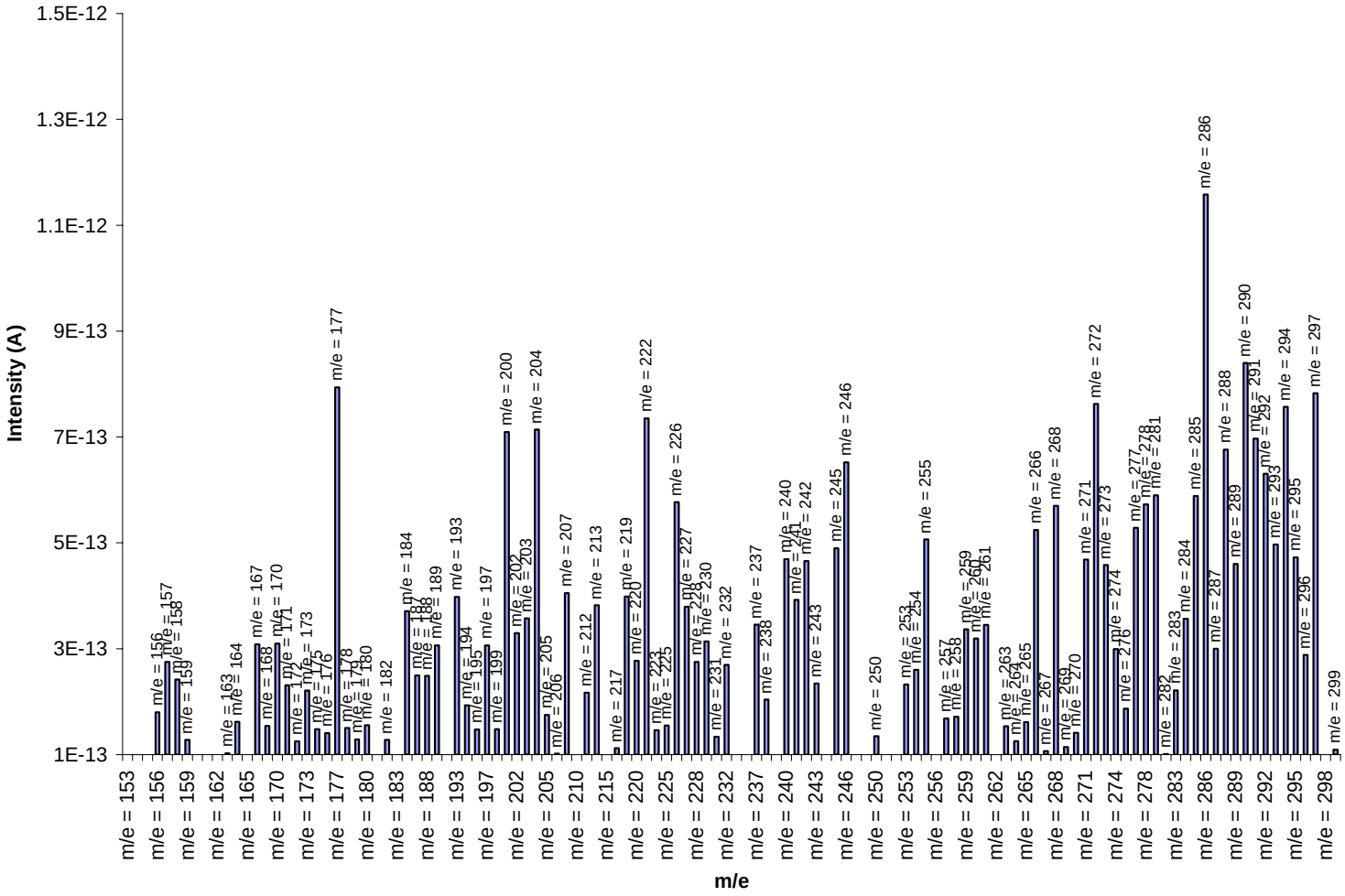

Figure B.2 – Overall relative abundance of trace MS peaks detected during heating of moisture-free $Q_8M_8^H$ (ie. sample B). The plot shows only MS peaks corresponding to masses with amu =150-300 and peak intensities > 10^{-13} A

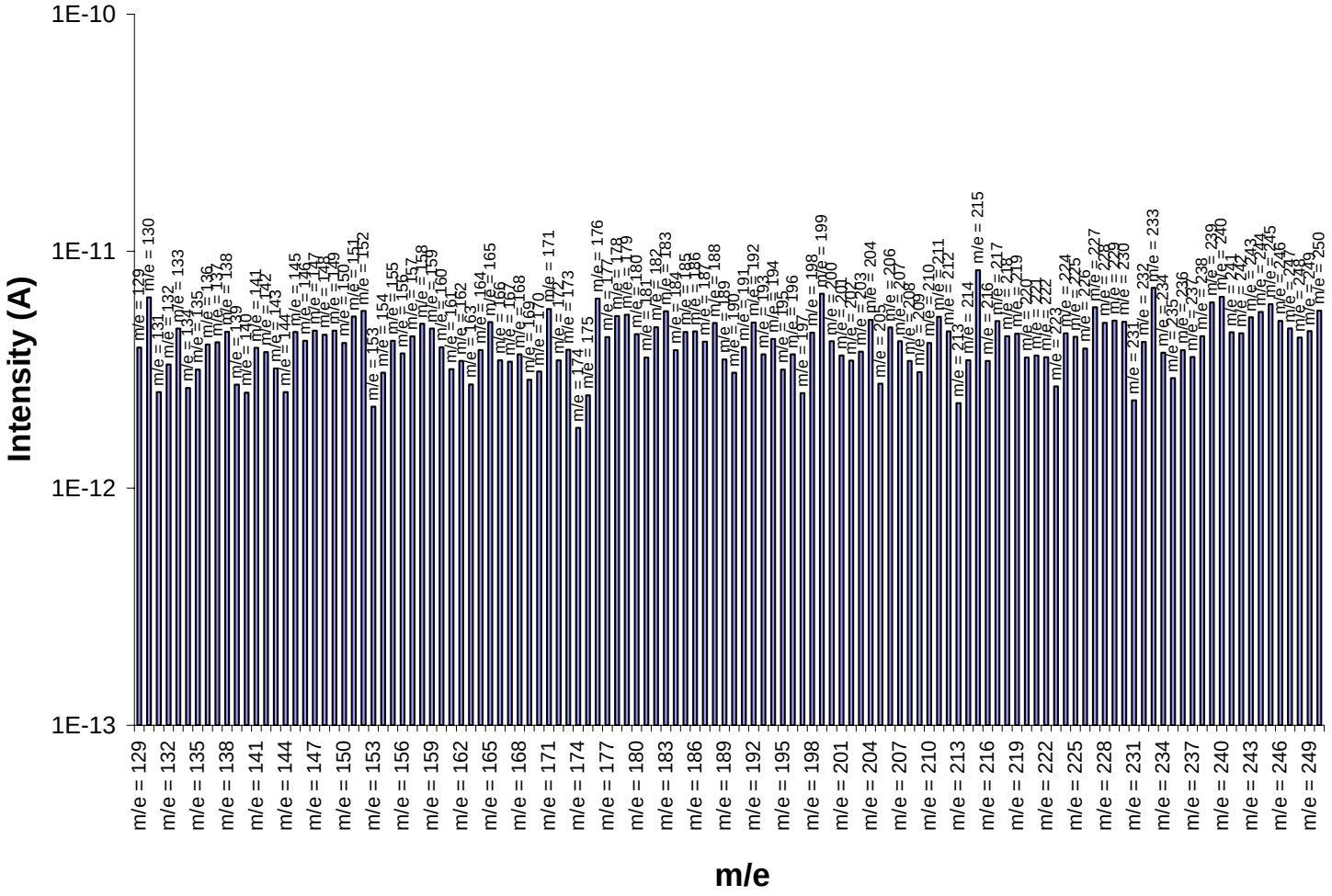

Figure B.3 - Overall relative abundance of MS peaks detected during heating of PDMSH. The plot shows only MS peaks corresponding to masses with amu = 129-250 and peak intensities > 10^{-13} A

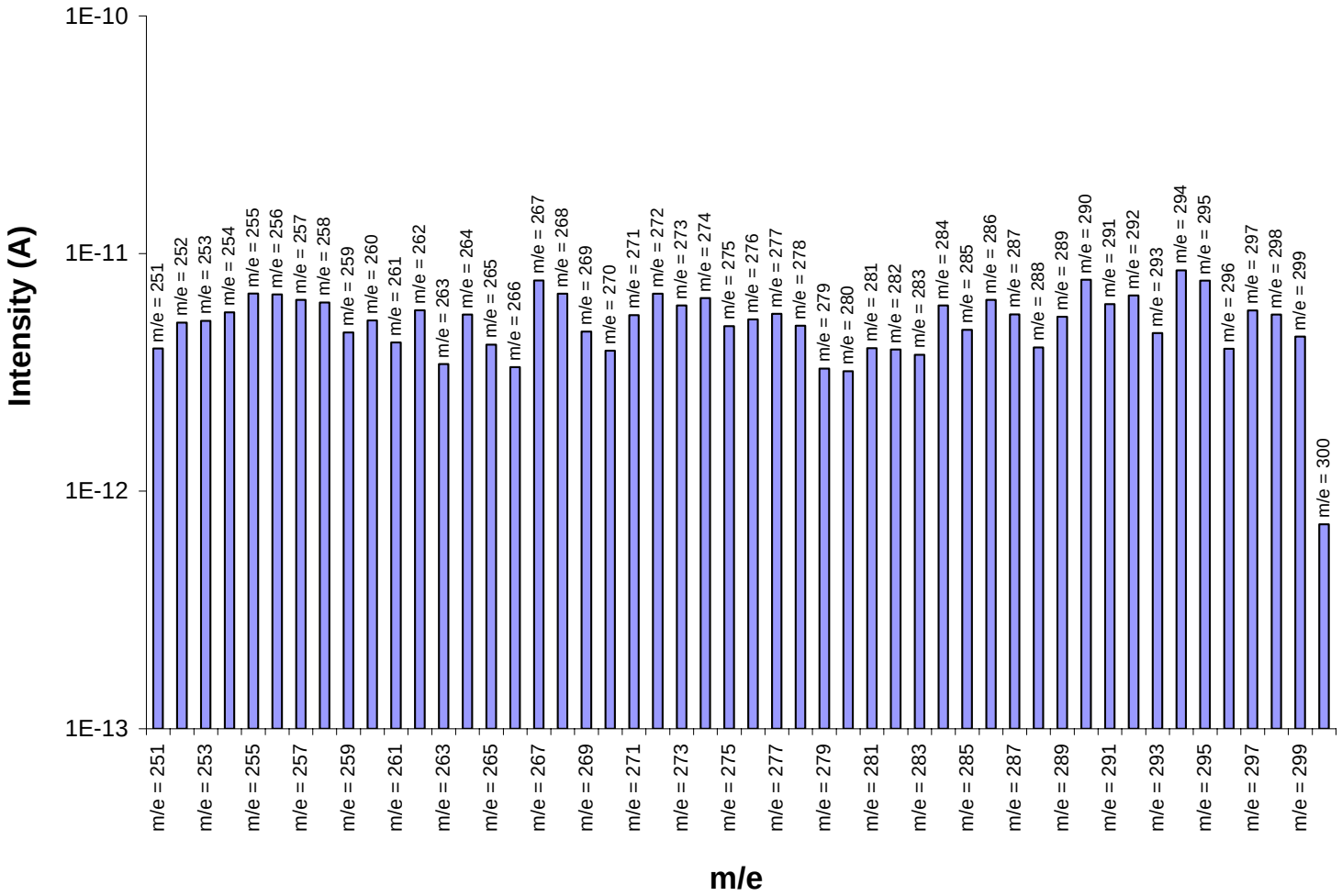

Figure B.4 - Overall relative abundance of MS peaks detected during heating of PDMSH. The plot shows only MS peaks corresponding to masses with amu = 251-300 and peak intensities > 10^{-13} A

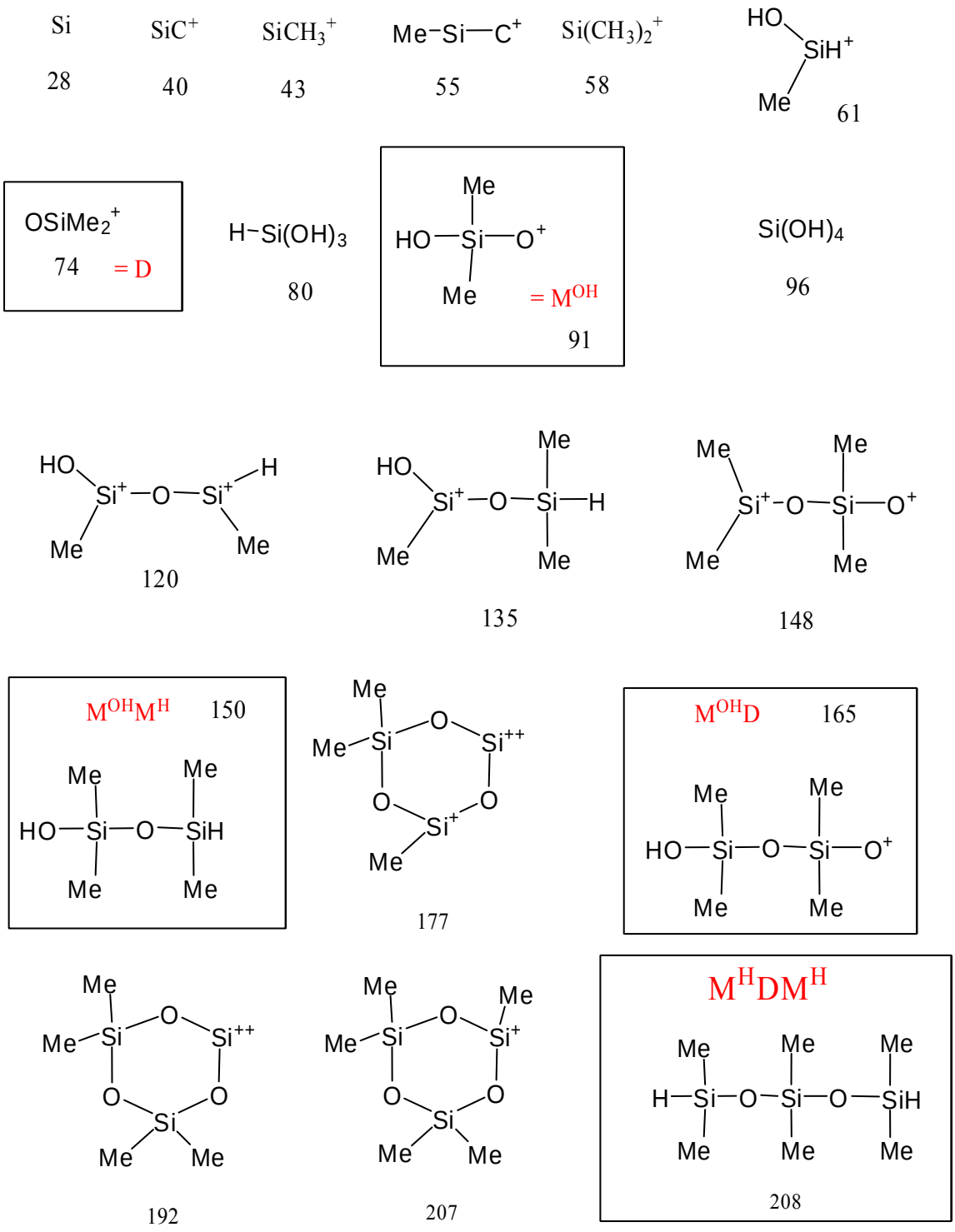

Figure B.5 – Volatile products detected by MS during heating of either $Q_8M_8^H$ or PDMSH for masses with amu = 28-208

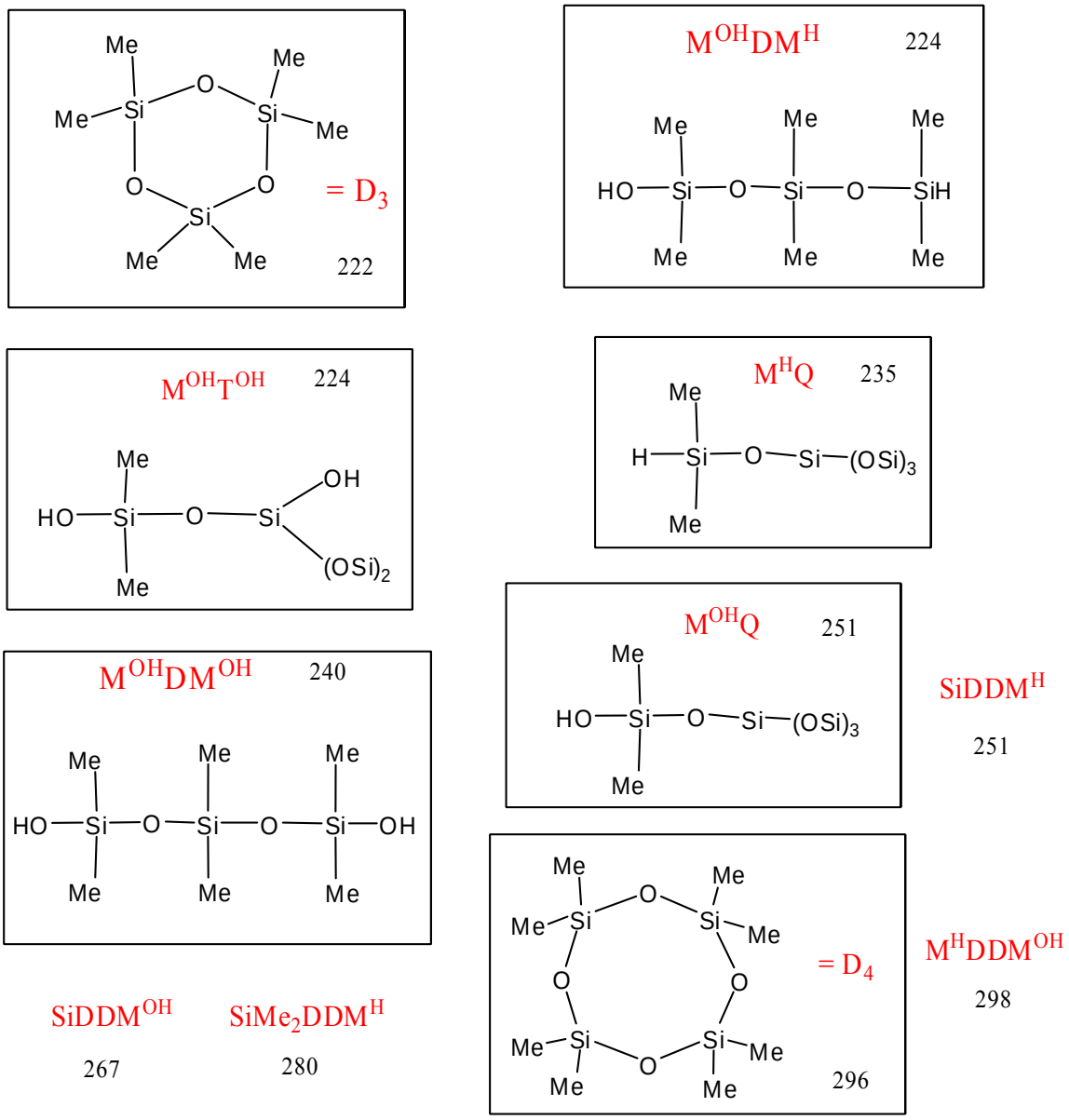

Figure B.6 – Volatile products detected by MS during heating of either $Q_8M_8^H$ or PDMSH for masses with amu = 222-298

APPENDIX C

MASS SPECTROMETRY DATA DECOMPOSITION OF NC1 AND NC2 NANOCOMPOSITES

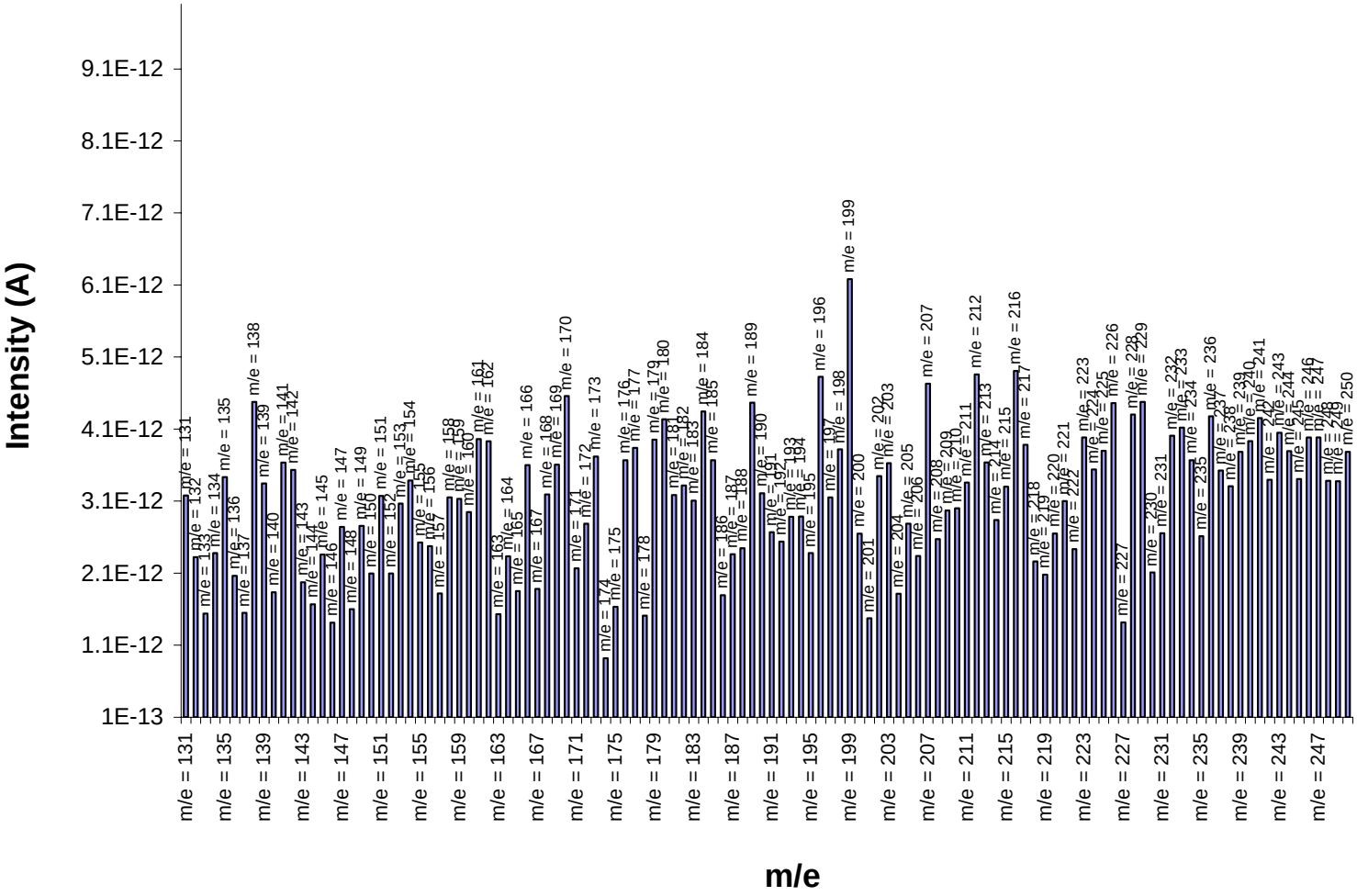

Figure C.1 – Overall relative abundance of trace MS peaks detected during heating of **NC1**. The plot shows only MS peaks corresponding to masses with amu = 129-250 and peak intensities > 10^{-13} A

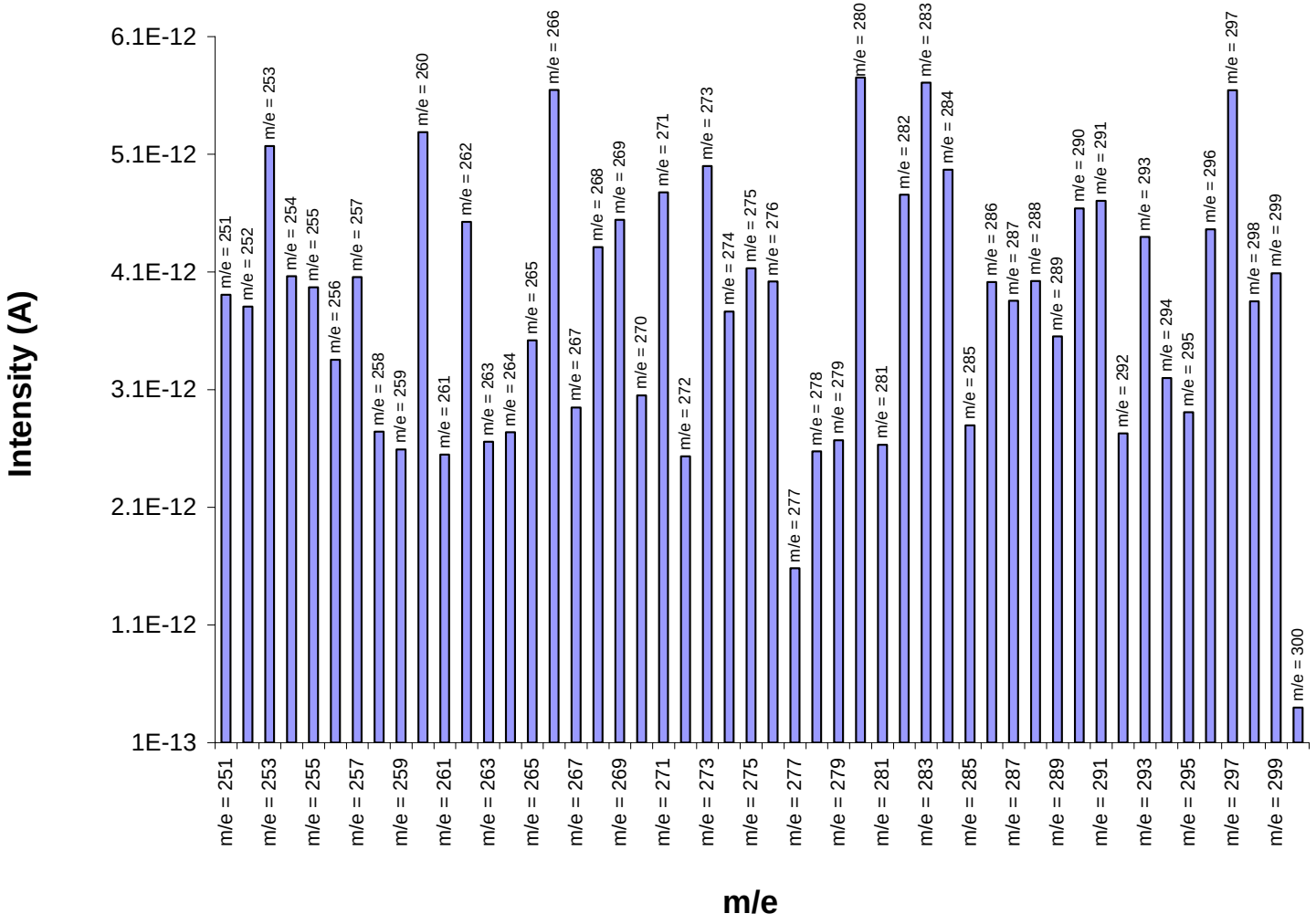

Figure C.2 – Overall relative abundance of trace MS peaks detected during heating of **NC1**. The plot shows only MS peaks corresponding to masses with amu = 251-300 and peak intensities > 10^{-13} A

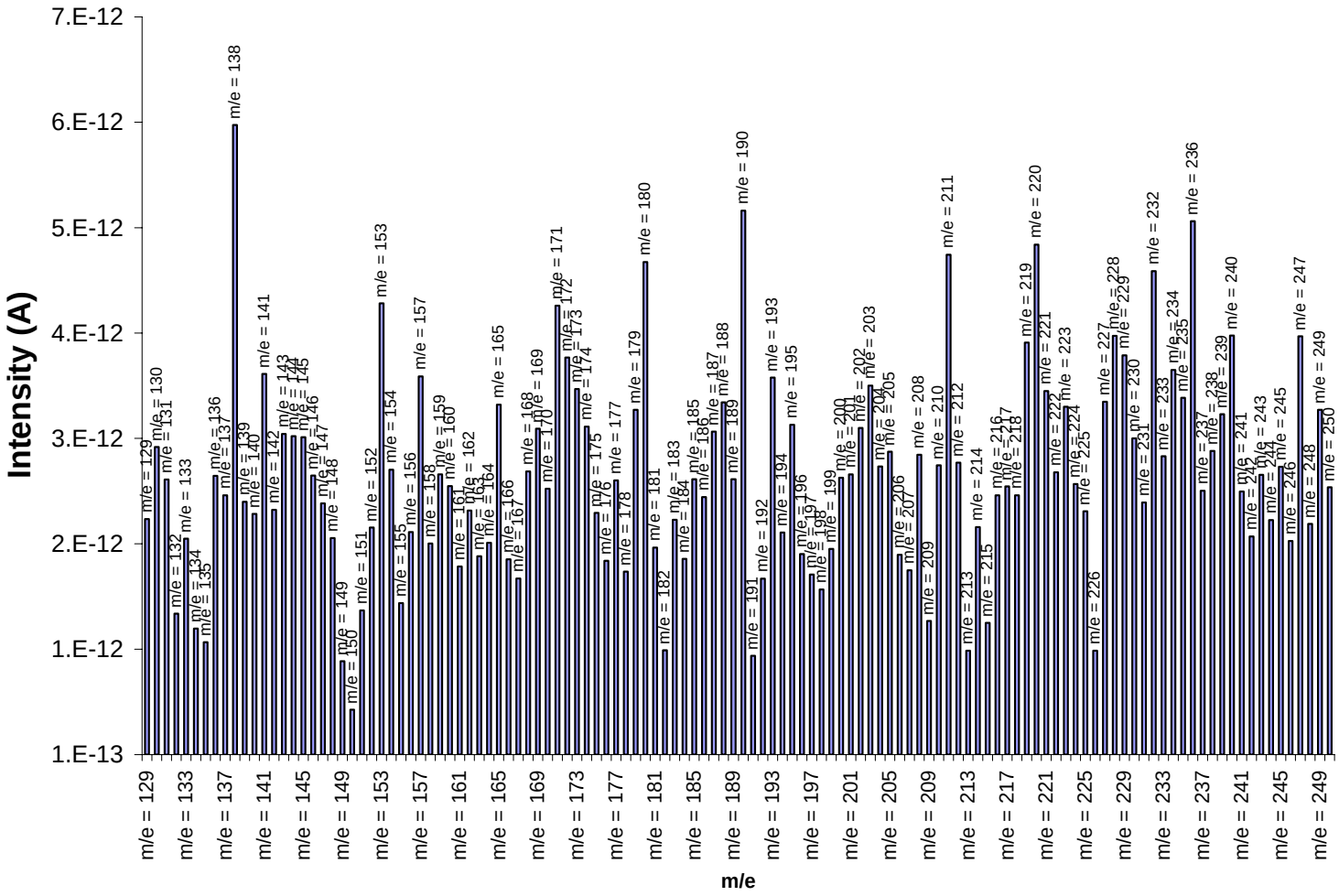

Figure C.3 – Overall relative abundance of MS peaks detected during heating of **NC2**. The plot shows only MS peaks corresponding to masses with amu = 129-250 and peak intensities > 10^{-13} A

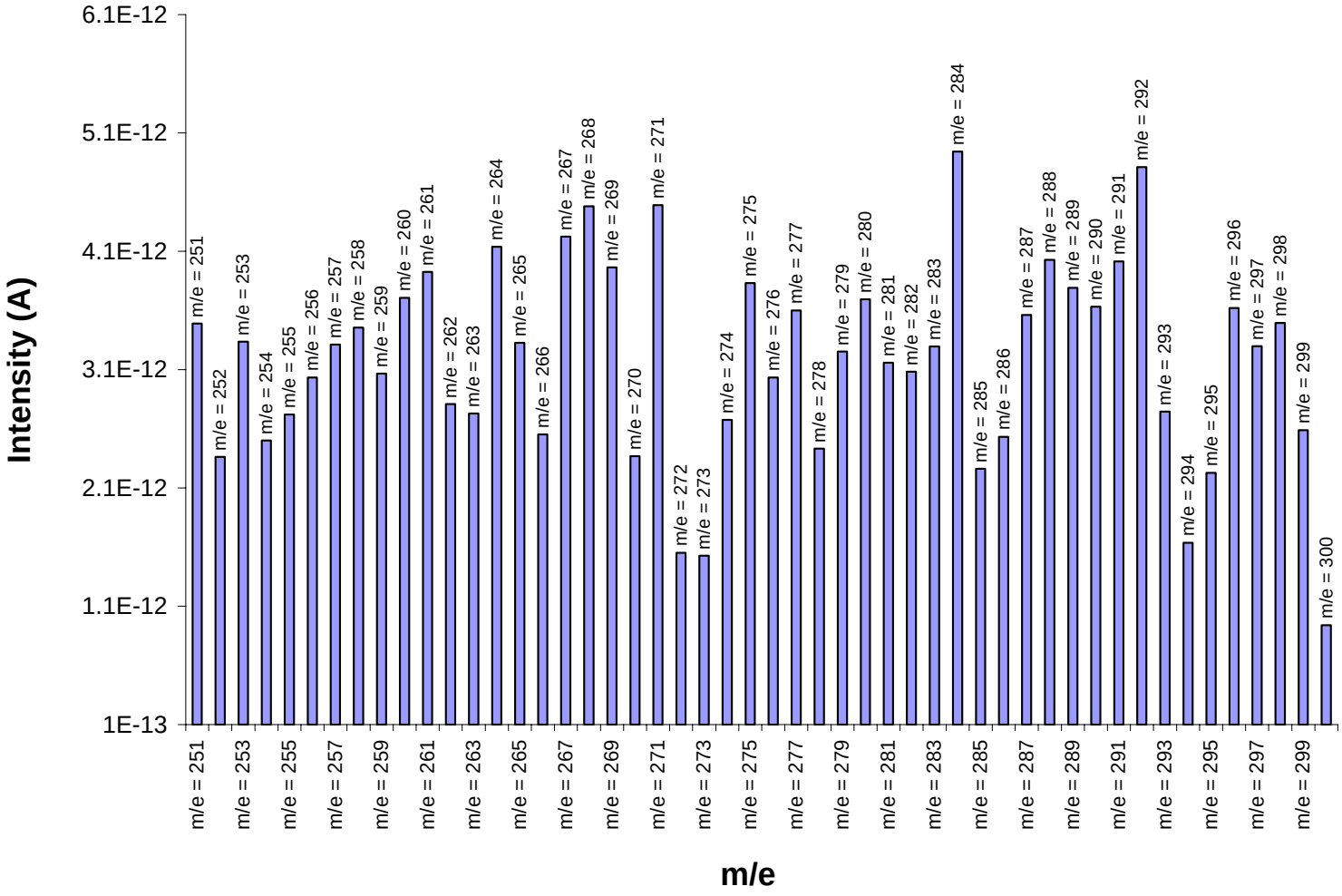

Figure C.4 – Overall relative abundance of MS peaks detected during heating of **NC2**. The plot shows only MS peaks corresponding to masses with amu = 251-300 and peak intensities > 10^{-13} A

REFERENCES

1. Abdallah, J., *The Fabrication of Direct-Write Waveguides via the glassy-state processing of porous films: UV-induced porosity and solvent-induced porosity*, in *Chemical Engineering*. 2007, Georgia Institute of Technology: Atlanta.

2. Abdallah, J., et al., *UV-induced porosity using photogenerated acids to catalyze the decomposition of sacrificial polymers templated in dielectric films.* Journal of Materials Chemistry, 2007. **17**: p. 873-885.

3. Maex, K., et al., *Low dielectric constant materials for microelectronics.* Journal of Applied Physics, 2003. **93**(11): p. 8793-8841.

4. SIA, *International Technology Roadmap for Semiconductors: 2003 Edition*. 2003, San Jose: Semiconductor Industry Association.

5. Tummala, R.R., *Fundamentals of microsystems packaging* 2001, New York: McGraw-Hill.

6. Clarke, M., *Applications Note MAL123: Introducing Low-k Dielectrics into Semiconductor Processing*, in *Applications Notes*. 2001, Mykrolis Corporation: Bedford, MA. p. 20.

7. Wong, C.P., *Polymers for electronic and photonic applications*. 1993, Boston: Academic Press.

8. Biswas, N., J.A. Lubgubah, and S. Gangopadhyay, *Electric Field and Temperature-Induced Removal of Moisture in Nanoporous Organosilicate Films.* Applied Physics Letters, 2004. **84**(21): p. 4254-4256.

9. Grill, A., et al., *Charecteristics of low-k and ultralow-k PECVD deposited SiCOH films*, in *Silicon Materials - Processing, Characterization, and Reliability (Mat. Res. Soc. Symp. Proc. Vol 716)*. 2002: San Francisco, CA.

10. Ryuzaki, D., T. Ishida, and T. Furusawa, *Time-Dependent Dielectric-Constant Increase Reliability Issue for Low Dielectric-Constant Materials.* J. Electrochem. Soc., 2003. **150**(12): p. F203-F205.

11. Bremmer, J.N., et al., *Rapid thermal processing of hydrogen silsesquioxane for low dielectric constant performance*, in *Low-Dielectric Constant Materials V (Materials Research Society Symposium Proceedings)*. 1999: San Francisco, CA, USA. p. 273-278.

12. Ferrari, A.C., et al., *Density, sp3 fraction, and cross-sectional structure of amorphous carbon films determined by x-ray reflectivity and electron-loss spectroscopy.* Physical Review B, 2000. **62**(16): p. 11089-11103.

13. Bremmer, J.N., et al., *cure of hydrogen silsesquioxane for intermetal dielectric applications*, in *Low-Dielectric Constant Materials III (Materials Research Society Symposium Proceedings)*. 1997: San Francisco, CA, USA. p. 37-44.

14. Liou, H.-C. and J. Pretzer, *Effect of curing temperature on the mechanical properties of hydrogen silsesquioxane thin films.* Thin Solid Films, 1998. **335**(1-2): p. 186-191.

15. Siew, Y.K., et al., *Thermal curing of hydrogen silsesquioxane.* Journal of the Electrochemical Society, 2000. **147**(1): p. 335-339.

16. Toivola, Y., J. Thurn, and R.F. Cook, *Structural, electrical, and mechanical properties development during curing of low-k hydrogen silsesquioxane films.* Journal of the Electrochemical Society, 2002. **149**(3): p. 9-17.

17. Yang, C.-C. and W.-C. Chen, *The structures and properties of hydrogen silsesquioxane (HSQ) films produced by thermal curing.* Journal of Materials Chemistry, 2002. **12**(4): p. 1138-1141.

18. Wu, Q. and K. Gleason, *Plasma-enhanced chemical vapor deposition of low-k dielectric films using methylsilane, dimethylsilane, and trimethylsilane precursors.* J. Vac. Sci. Technol. A, 2003. **21**(2): p. 388-393.

19. Liu, W.-C., et al., *The structural transformation and properties of spin-on poly(silsesquioxane) films by thermal curing.* Journal of Non-Crystalline Solids, 2002. **311**(3): p. 233-240.

20. Furusawa, T., et al., *Oxygen Plasma Resistance of Low-k Organosilica Glass Films.* Electrochemical and Solid State Letters, 2001. **4**(3): p. 31-34.

21. Lee, L.-H., W.-C. Chen, and W.-C. Liu, *Structural Control of Oligomeric Methyl Silsesquioxane Precursors and Their Thin-Film Properties.* J. Polymer Science: Part A: Polymer Chemistry, 2002. **40**: p. 1560-1571.

22. Wang, C.Y., et al., *Characterization of a Low-k Organic Spin-on-glass as an Intermetal Dielectric.* Surface and Interface Analysis, 1999. **28**: p. 97-100.

23. Lee, H.J., et al., *X-Ray Reflectivity and FTIR Measurements of N2 Plasma Effects on the Density Profile of Hydrogen Silsesquioxane Thin Films.* Journal of The Electrochemical Society, 2001. **148**(10): p. 195-199.

24. Gorman, B.P., et al., *Analytical TEM characterization of metal penetration and supercritical pore-sealing of ash-damaged porous low-k dielectrics*, in *Advanced Metallization Conference 2005 (AMC 2005) Proceedings*. 2006: Colorado Springs, CO, USA. p. 392-397.

25. Iacopi, F., et al., *Properties of porous HSQ-based films capped by plasma enhanced chemical vapor deposition dielectric layers.* Journal of Vacuum Science and Technology B: Microelectronics and Nanometer Structures, 2002. **20**: p. 109-115.

26. Jousseaume, V., et al., *Pore sealing of a porous dielectric by using a thin PECVD a-SiC:H conformal liner.* Journal of the Electrochemical Society, 2005. **152**(10): p. 156-161.

27. Lifshitz, N., W.Y.C. Lai, and G. Smolinsky, *Water-related degradation of contacts in the multilevel MOS IC with spin-on glasses as interlevel dielectrics.* IEEE Electron Device Letters, 1989. **10**(12): p. 562-564.

28. Padovani, A.M., et al., *Chemically bonded porogens in methylsilsesquioxane. I. Structure and bonding.* Journal of the Electrochemical Society, 2002. **149**(12): p. 161-170.

29. Padovani, A.M., et al., *Chemically bonded porogens in methylsilsesquioxane. II. Electrical, optical, and mechanical properties.* Journal of the Electrochemical Society, 2002. **149**(12): p. 171-180.

30. Padovani, A.M., S.A.B. Allen, and P.A. Kohl, *Templated nanoporous spin-on glass for high density interconnect applications*, in *2002 Proceedings of 8th International Advanced Packaging Materials Symposium*. 2002, Institute of Electrical and Electronics Engineers (IEEE), New York, NY, USA: Stone Mountain, GA, USA. p. 20-24.

31. Padovani, A.M., et al., *Porous methylsilsesquioxane for low-k dielectric applications.* Electrochemical and Solid-State Letters, 2001. **4**(11): p. 25-28.

32. Xu, J., et al., *Porosity in porous methyl-silsesquioxane (MSQ) films.* Applied Surface Science, 2002. **194**: p. 189-194.

33. Nahar, R.K., *Physical understanding of moisture induced degradation of nanoporous aluminum oxide thin films.* Journal of Vacuum Science & Technology, B: Microelectronics and Nanometer Structures, 2002. **20**(1): p. 382-385.

34. Murray, C., et al., *Comparison of techniques to characterise the density, porosity and elastic modulus of porous low-k SiO_2 xerogel films.* Microelectronic Engineering, 2002. **60**: p. 133-41.

35. Iacopi, F., et al. *Studies on XLK film characterization and integration in copper damascene processes*. in *Proceeding of Advanced Metallization Conference (AMC)*. 2000. held October 2-5 in San Diego, CA, United States and October 19-20 in Tokyo, Japan: Materials Research Society, Warrendale, Pa, USA.

36. Lee, H.-J., et al., *Structural comparison of hydrogen silsesquioxane based porous low-k thin films prepared with varying process conditions.* Chemistry of Materials, 2002. **14**(4): p. 1845-1852.

37. Baklanov, M.R., et al., *Comparative study of porous SOG films with different non-destructive instrumentation*, in *Proceedings of the IEEE 2001 International Interconnect Technology Conference*. 2001: Burlingame, CA, USA. p. 189-191.

38. Baklanov, M.R. and K.P. Mogilnikov, *Non-destructive characterisation of porous low-k dielectric films.* Microelectronic Engineering, 2002. **64**: p. 335-349.

39. Baklanov, M.R., K.P. Mogilnikov, and Y. Jin-Heong, *Ellipsometric porosimetry of porous low-k films with quasi-closed cavities*, in *Materials Research Society Proceedings*. 2004: San Francisco, CA, USA. p. 55-60.

40. Baklanov, M.R., et al., *Determination of pore size distribution in thin films by ellipsometric porosimetry.* Journal of Vacuum Science & Technology B (Microelectronics and Nanometer Structures), 2000. **18**(3): p. 1385-91.

41. Baklanov, M.R. and K.P. Mogilnmov, *Characterization of porous dielectric films by ellipsometric porosimetry.* Optica Applicata, 2000. **30**: p. 491-6.

42. Wang, J.H., et al., *Structural and electrical characteristics of low-dielectric constant porous hydrogen silsesquioxane for Cu metallization.* Journal of the Electrochemical Society, 2003. **150**(8): p. 141-146.

43. Iacopi, F., et al., *Factors affecting an efficient sealing of porous low-k dielectrics by physical vapor deposition Ta(N) thin films.* Journal of Applied Physics, 2002. **92**(3): p. 1548.

44. Shafer, M.W., et al., *Structural Observations of Porous Silica Gels*, in *Better Ceramics Through Chemistry II (Mater. Res. Soc. Symposium Proc. vol. 73)*. 1986, Materials Research Society: Palo Alto, CA.

45. Yu, S., et al., *The Effect of TEOS/MTES Ratio on the Structural and Dielectric Properties of Porous Silica Films.* Journal of The Electrochemical Society, 2003. **150**(5): p. 116-121.

46. Xu, Y., et al., *Synthesis and characterization of porous polymeric low dielectric constant films.* Journal of Electronic Materials, 2001. **30**(4): p. 309-313.

47. Wu, W.-l., et al., *Properties of nanoporous silica thin films determined by high-resolution x-ray reflectivity and small-angle scattering.* J. Appl. Phys., 2000. **87**(3): p. 1193-1200.

48. Sun, J.-N., et al., *How pore size and surface roughness affect diffusion barrier continuity on porous low-k films.* Journal of the Electrochemical Society, 2003. **150**(5): p. 97-101.

49. Donaton, R.A., et al., *Physical and electrical characterization of silsesquioxane-based ultra-low k dielectric films*, in *Proceedings of the IEEE 2000 International Interconnect Technology Conference (Cat. No.00EX407)*. 2000, IEEE: Piscatawy, NJ, USA. p. 93-5.

50. Hu, J.C., et al., *Self-organized nanomolecular films on low-dielectric constant porous methyl silsesquioxane at room temperature.* Journal of the Electrochemical Society, 2003. **150**(4): p. 61-66.

51. Yi, D.K. and D.-Y. Kim, *Novel approach to the fabrication of macroporous polymers and their use as a template for crystalling nanorings.* Nanoletters, 2002. **3**(2): p. 207-211.

52. Cai, Q., et al., *A novel porous cells scaffold made of polyactide-dextran blend combining phase-separation and particle-leaching techniques.* Biomaterials, 2002. **23**: p. 4483-4492.

53. Carter, K.R., et al., *Nanoporous polyimides derived from highly fluorinated polyimide/poly(propylene oxide) copolymers.* Chemistry of Materials, 2001. **13**(1): p. 213-21.

54. Hedrick, J.L., et al., *Templating nanoporosity in thin-film dielectric insulators.* Advanced Materials, 1998. **10**(13): p. 1049-1053.

55. Chae, K.H. and K.H. Sung, *A polymeric photobase generator containing oxime-urethane groups: Crosslinking reaction and application to negative photoresist.* Journal of Polymer Science, Part A: Polymer Chemistry, 2004. **42**(4): p. 975-984.

56. Frechet, J.M.J. and J.F. Cameron, *Photogenerated amines and diamines. Novel curing systems for thin film coatings*, in *Polymeric Materials Science and Engineering, Proceedings of the ACS Division of Polymeric Materials Science and Engineering*. 1991, American Chemical Society (ACS), Columbus, OH, USA: Atlanta, GA, USA. p. 55-56.

57. Winkle, M.R.a. and K.A. Graziano, *Acid-hardening positive photoresist using photochemical generation of base.* Journal of Photopolymer Science and Technology, 1990. **3**(3): p. 419-422.

58. Jin, C., et al., *Nanoporous silica as an ultralow-k dielectric.* MRS Bulletin, 1997. **22**(10): p. 39-42.

59. Jin, C., et al., *Deposition and characterization of porous silica xerogel films.* Materials Research Society Symposium Proceedings, 1997. **443**(Low-Dielectric Constant Materials II): p. 99-104.

60. Iler, R.K., *The chemistry of silica: solubility, polymerization, colloid and surface properties, and biochemistry*. 1979, New York: Wiley.

61. Suh, J.M., S.J. Bae, and B. Jeong, *Thermogelling multiblock poloxamer aqueous solutions with closed-loop sol-gel-sol transitions upon increasing pH.* Advanced Materials, 2005. **17**(1): p. 118-120.

62. Padovani, A., *Low Dielectric Constant Porous Spin-on Glass for Microelectronic Applications*, in *Chemical Engineering*. 2002, Georgia Institute of Technology: Atlanta. p. 182.

63. Yim, J.-H., et al., *Pore structure of modified cyclic silsesquioxane thin films made porous using a cyclodextrins-based porogen.* Journal of Physical Chemistry B, 2004. **108**(26): p. 8953-8959.

64. Labadie, J.W., et al., *Nanopore foams of high temperature polymers.* IEEE Transactions on Components, Hybrids, and Manufacturing Technology, 1992. **15**(6): p. 925-30.

65. Fan, W., et al., *Hierarchical nanofabrication of microporous crystals with ordered mesoporosity.* Nat Mater, 2008. **7**(12): p. 984-991.

66. Janssen, A., A. Koster, and J.P.d. Jong, *Three-Dimensional Transmission Electron Microscopic Observations of Mesopores in Dealuminated Zeolite Y.* Angewandte Chemie International Edition, 2001. **40**(6): p. 1102-1104.

67. Wang, L., et al., *High-temperature synthesis of stable ordered mesoporous silica materials using mesoporous carbon as a hard template.* Microporous and Mesoporous Materials, 2005. **86**(1-3): p. 81-88.

68. Miller, R.D. and J. Michl, *Polysilane high polymers.* Chemical Reviews, 1989. **89**(6): p. 1359-1410.

69. Mimura, S., et al., *Optical properties of organic-inorganic hybrid thin films containing polysilane segments prepared from polysilane-methacrylate copolymers.* Journal of Organometallic Chemistry, 2000. **611**(1-2): p. 40-44.

70. Miura, S., et al., *Photoinduced refractive index changes in organic polysilane-inorganic hybrid thin films.* Synthetic Metals, 2003. **137**: p. 1405-1406.

71. Nagayama, N., et al., *Refractive index modification due to the Uv-photodecomposition of polysilane and its application as phase mask.* Molecular Crystals and Liquid Crystals Science and Technology, Section A: Molecular Crystals and Liquid Crystals, 2000. **349**: p. 119-122.

72. Nakayama, Y., et al. *Photoinduced annihilation of σ bonds in amorphous poly(methylphenylsilane)*. 1996. Kobe, Japan: Elsevier.

73. Watanabe, A., et al., *Photodegradation of polysilanes studied by far-infrared spectroscopy.* Japanese Journal of Applied Physics, Part 1 (Regular Papers & Short Notes), 1994. **33**(7A): p. 4133-4.

74. Watanabe, A. and M. Matsuda, *Photodegradation of alkyl- and aryl-substituted polysilanes studied by flash photolysis.* Macromolecules, 1992. **25**(1): p. 484-488.

75. Matsukawa, K., et al., *Preparation and properties of organic-inorganic hybrid thin films containing polysilane segments from polysilane-methacrylate copolymers.* Chemistry Letters, 1999(10): p. 1073-1074.

76. Matsukawa, K., et al., *Preparation of photo-induced refractive index pattern using polysilane-silica hybrid thin films.* Journal of Photopolymer Science and Technology, 2004. **17**(1): p. 51-52.

77. Matsukawa, K. and Y. Matsuura, *Photo-induced optical and chemical properties of polysilane/inorganic nano-hybrids*, in *Organic/Inorganic Hybrid Materials-2004. (Materials Research Society Symposium Proceedings)*. 2005: Boston, MA, USA. p. 45-56.

78. Palik, E.D., *Handbook of optical constants*. 1998, San Diego: Academic Press.

79. Frechet, J.M., et al., *Design, Synthesis, and Study of Novel, Thermally Depolymerizable Polycarbonates.* J. Chem. Soc., Chem. Commun., 1985. **21**: p. 1514-1516.

80. Frechet, J.M.J., et al., *Thermally depolymerizable polycarbonates via acid-catalyzed thermolysis of allylic and benzylic polycarbonates: a new route to resist imaging.* Polymer Journal, 1987. **19**(1): p. 31-49.

81. Houlihan, F.M., F. Bouchard, and J.M. Frechet, *Thermally Depolymerizable Polycarbonates. 2. Synthesis of Novel Linear Tertiary Copolycarbonates by Phase-Transfer Catalysis.* Macromolecules, 1986. **19**(1): p. 13-19.

82. White, C., *Advanced Methods, Materials, and Devices for Microfluidics*, in *Chemical Engineering*. 2003, Georgia Institute of Technology: Atlanta.

83. White, C.E., A. Balogun, and C.L. Henderson, *Effects of the photoacid generator type on the imaging and thermal decomposition properties of photodefinable, thermally sacrificial poly(propylene carbonate) materials.* J. Appl. Polymer Science, 2006. **106**(1): p. 266-271.

84. White, C.E. and C.L. Henderson, *Development of improved photosensitive polycarbonate systems for the fabrication of microfluidic devices.* Journal of Vacuum Science & Technology, B: Microelectronics and Nanometer Structures, 2003. **21**(6): p. 2926-2930.

85. White, C.E. and C.L. Henderson. *Photosensitive co-polycarbonates for use as sacrificial materials in the fabrication of microfluidic and microelectromechanical devices*. in *Advances in Resist Technology and Processing XXI*. 2004. Santa Clara, California, USA: The International Society for Optical Engineering, Bellingham, United States.

86. Erickson, J. and S. Kahn, *Theoretical Studies of Thermal Syn Elimination Reactions. The Relative Rates of Ethyl Formate, Ethyl Xanthat, and Ethyl Phophinate Eliminations.* J. American Chemical Society, 1994. **116**: p. 6271-6276.

87. McNeill, I.C. and A. Rincon, *Degradation Studies of Some Polyesters and Polycarbonates -8. Bisphenol A Polycarbonate.* Polymer Degradation and Stability, 1991. **31**: p. 163-180.

88. Frechet, J.M.J., et al., *New Approach to Imaging Systems Incorporating Chemical Amplification: Synthesis and Preliminary Evaluation of Novel Resists Based on Tertiary Copolycarbonates.* J. Imaging Science, 1986. **30**(2): p. 59-64.

89. Jayachandran, J.P., et al., *Air-channel fabrication for microelectromechanical systems via sacrificial photosensitive polycarbonates.* Journal of Microelectromechanical Systems, 2003. **12**(2): p. 147-159.

90. Puglisi, C., et al., *MALDI-TOF Investigation of Polymer Degradation. Pyrolysis of Poly(bisphenol A carbonate).* Macromolecules, 1999. **32**: p. 8821-8828.

91. Taylor, R., G. Smith, and W. Wetzel, *Substituent Effects in Pyrolysis. V. A Correlation in the Pyrolysis of 1-Arylethyl Acetates.* J. American Chemical Society, 1962. **84**: p. 4817-4824.

92. Hurd, C.D. and F.H. Blunck, *The Pyrolysis of Esters.* Journal of the American Chemical Society, 1938. **60**(10): p. 2419-2425.

93. Lorentz, H.A., *The Theory of Electrons*. 1906, New York, USA: G.P. Stechert & Co.

94. Matsuura, Y., et al., *Preparation of porous titania thin films from polysilane-titania hybrid by UV irradiation.* Journal of Photopolymer Science and Technology, 2002. **15**(5): p. 761-4.

95. Su, K., et al., *Vinyl ether-modified poly(hydrogen silsesquioxanes) as dielectric materials.* J. Materials Chemistry, 2005. **15**: p. 4115-4124.

96. Zhong, B.M., H.; Iocopi, F.; Weidner, K.; Mailhouitre, S.; Moyer, E.; Bargeron, C.; Schalk, P.; Peck, A.; Hove, M.V.; Maex, K., *A new ultra-low K ILD material based on organic-inorganic hybrid resins*, in *Materials Research Society Symposium Proceedings*. 2002: San Francisco, CA, USA. p. 575-580.

97. Wyatt, P.J., *Light Scattering and the Absolute Characterization of Macromolecules.* Analytica Chimica Acta, 1993. **272**: p. 1-40.

98. Hua, Y., *Materials and Methods for Nanolithography using Scanning Thermal Cantilever Probes*, in *Chemical Engineering*. 2008, Georgia Institute of Technology: Atlanta.

99. Spreybroek, V., et al., *Ab Initio and Experimental Study on Thermally Degradable Polycarbonates: The effect of Substituents on the Reaction Rates.* J. American Chemical Society, 2001. **123**: p. 10650-10657.

100. Wedlake, M. and P. Kohl, *Thermal Decomposition Kinetics of Functionalized Polynorbornene.* J. Mater. Res., 2002. **17**(3): p. 632-640.

101. Oliver, W.C. and G.M. Pharr, *Improved technique for determining hardness and elastic modulus using load and displacement sensing indentation experiments.* Journal of Materials Research, 1992. **7**(6): p. 1564-1580.

102. Kohl, P.A., et al., *Low-k porous spin-on-glass*, in *Low-Dielectric Constant Materials V (Materials Research Society Symposium Proceedings)*. 1999: San Francisco, CA, USA. p. 55-61.

103. Maxwell-Garnett, J.C., *Colours in Metal Glasses, in Metallic Films, and in Metallic Solutions II.* Philosophical Transactions of the Royal Society of London. Series A, Containing Papers of a Mathematical or Physical Character, 1906. **205**: p. 237-288.

104. Choy, T.C., *Effective Medium Theory: Principles and Applications*. 1999, New York, USA: Oxford University Press USA.

105. Sathiarajy, T.S. and R. Thangarajz, *The experimental and calculated optical properties of Ni–Al_2O_3 coatings using effective medium theories.* J. Phys. D: Appl. Phys., 1997. **30**(5): p. 769–775.

106. Carter, K., et al., *Synthesis of Amine-Terminated Aliphatic Polycarbonate and Aliphatic Polyesters via $Al(Et)_2(OR)$ Initiated Polymerizations.* Polymer Preprints, 1996. **37**(1): p. 607-608.

107. Lee, C.-T., *Development and Advanced Characterization of Novel Chemically Amplified Resists for Next Generation Lithography*, in *School of Chemical and Biomolecular Engineering*. 2008, Georgia Institute of Technology: Atlanta. p. 276.

108. Lee, C.-T., et al., *Photosensitivity and line-edge roughness of novel polymer-bound PAG photoresists*, in *Advances in Resist Materials and Processing Technology XXIV (Proc. SPIE, vol. 6519: Part 1)*. 2007, SPIE: San Jose, CA, USA. p. 65191E1-65191E9.

109. Seidel, H., et al., *Anisotropic Etching of Crystalline Silicon in Alkaline Solutions: I. Orientation Dependence and Behavior of Passivation Layers.* J. Electrochem. Soc., 1990. **137**(11): p. 3612-3626.

110. Abis, L., et al., *Investigation of the Miscibility of Polycarbonate-Poly(ethyleneterephthalate) Blends: Solid-State 1H-NMR T1 Relaxation Time*

Measurements, Transmission Electron Microscopy, and Structure-Properties Relationship. J. Applied Polymer Science, 1994. **52**: p. 1431-1445.

111. Abu-Rous, M., E. Ingolic, and K.C. Schuster, *Visualisation of the Fibrillar and Pore Morphology of Cellulosic Fibres Applying Transmission Electron Microscopy.* Cellulose, 2006. **13**: p. 411-419.

112. Brown, G.M. and J.H. Butler, *New Method for the Characterization of Domain Morphology of Polymer Blends using Ruthenium Tetraoxide Staining and Low Voltage Scanning Electron Microscopy (LVSEM).* Polymer, 1997. **38**(15): p. 3937-3945.

113. Canilho, N., et al., *Real Space Imaging and Molecular Packing of Dendronized Polymer-Lipid Supramolecular Complexes.* Macromolecules, 2007. **40**: p. 7609-7616.

114. Chen, W., et al., *Mophological Characterization of PMMA/PAN Composite Particles in Nano to Submicro Size.* Macromol. Mater. Eng., 2005. **290**: p. 669-674.

115. Ferrer, G.G., et al., *Nanodomains in a Hydrophilic-Hydrophobic IPN Based on Poly(2-hydroxyethyl acrylate) and Poly(ethyl acrylate).* Macromolecular Nanotechnology, 2007. **43**: p. 3136-3145.

116. Hobbs, S.Y., M.E.J. Dekkers, and V.H. Watkins, *Effect of Interfacial Forces on Polymer Blend Morphologies.* Polymer, 1988. **29**: p. 1598-1602.

117. Hong, S., et al., *Morphology of Semicrystalline Block Copolymers: Polyethelyne-b-atactic-polypropylene.* Polymer, 2001. **42**: p. 5909-5914.

118. Hromadkova, J., F. Lednicky, and J. Kolarik, *Visualization of the Phase Structure of Selected Polycarbonate Blends using Various Preparation Techniques.* Polymer Testing, 1994. **13**: p. 461-478.

119. Jyo, Y., C. Nozaki, and M. Matsuo, *Electron Microscopy of Poly(vinyl chloride) and Ethylene-Vinyl Acetate Rubber Systems.* Macromolecules, 1971. **4**(4): p. 517-518.

120. Kato, K., *Osmium Tetraoxide Fixation of Rubber Latices.* Polymer Letters, 1966. **4**: p. 35-38.

121. Khandpur, A.K., C.W. Macosko, and F.S. Bates, *Transmission Electron Microscopy of Saturated Hydrocarbon Block Compolymers.* J. Polymer Science: Part B: Polymer Physics, 1995. **33**: p. 247-252.

122. Lednicky, F., J. Hromadkova, and J. Kolarik, *Phase Structure of Binary and Ternary Polycarbonate Blends.* Polymer Testing, 1999. **18**: p. 123-134.

123. Montezinos, D., B.G. Wells, and J.L. Burns, *The Use of Ruthenium in Hypochlorite as a Stain for Polymeric Materials.* J. Polymer Science: Polymer Letters Edition, 1985. **23**: p. 421-425.

124. Trent, J.S., J.I. Scheinbeim, and P.R. Couchman, *Ruthenium Tetraoxide Staining of Polymers for Electron Microscopy.* Macromolecules, 1983. **16**: p. 589-598.

125. Wang, Y., et al., *Interfacial Staining of a Phase-Separated Block Copolymer with Ruthenium Tetraoxide.* Macromolecules, 2007. **40**: p. 1594-1597.

126. Bethge, H. and J. Heydenreich, eds. *Electron Microscopy in Solid State Physics: Materials Science Monographs, 40*. 1987, Elsevier: Amsterdam. 596.

127. Bailey, W.J. and T. Endo, *Synthesis of Monomers that Expand on Polymerization. Synthesis and Polymerization of 3, 9-Dimethylene-1,5,7,11-Tetraoxaspiro[5.5] Undecane.* J. Polymer Science: Part A: Polymer Chemistry, 1976. **14**: p. 1735-1741.

128. Hino, T., N. Inoue, and T. Endo, *Cationic Copolymerization Behavior of Cyclic Ether Monomers with Norbornene-Containing Cyclic Carbonate or Spiro-Orthoether Structure.* J. Polymer Science: Part A: Polymer Chemistry, 2004. **42**: p. 5113-5120.

129. Murayama, M., F. Sanda, and T. Endo, *Anionic Ring-Opening Polymerization of a Cyclic Carbonate Having a Norbornene Structure with Amine Initiators.* Macromolecules, 1998. **31**(3): p. 919-923.

130. Nemoto, N., K. Kakimoto, and T. Endo, *Cationic Ring-Opening Polymerization of Monothiocarbonate with a Norbornene Group.* J. Polymer Science: Part A: Polymer Chemistry, 2002. **40**: p. 1698-1705.

131. Grutzner, T. and H. Hasse, *Solubility of Formaldehyde and Trioxane in Aqueous Solutions.* J. Chem. Eng. Data, 2004. **49**: p. 642-646.

132. Xamena, F.X.L.i., et al., *Formaldehyde Oligomerization on Silicalite: an FTIR and NMR studey.* Catalysis Letters, 2004. **95**(1-2): p. 51-55.

133. Culberson, C.F., J.H. Seward, and P.W. Jr., *2-Oxa-1,2-dihydrodicyclopentadiene.* J. American Chemical Society, 1960. **82**: p. 2541-2547.

134. Doyle, A.M., S.K. Shaikhutdinov, and H.J. Freund, *Alkene Chemistry on the Palladium Surface: Nanoparticles vs Single Crystals.* J. Catalysis, 2004. **223**: p. 444-453.

135. Craig, D., *The Rearrangment of endo-3,6-methylene-1,2,3,6-tetrahydro-cis-phthalic anhydride.* J. American Chemical Society, 1951. **73**: p. 4889-4892.

136. Lok, K., I. Jakovac, and J.B. Jones, *Enzymes in Organic Synthesis. 34. Preparations of Enantiomerically Pure Exo- and Endo-Bridged Bicyclic [2.2.1] and [2.2.2] Chiral Lactones via Stereospecific Horse Liver Alcohol Dehydrogenase Catalyzed Oxidations of Meso Diols.* J. American Chemical Society, 1985. **107**: p. 2521-2526.

137. Nelson, W.L., D.S. Freeman, and R. Sankar, *Bicyclic Amino Alcohols. The Isomeric 2-Dimethylaminomethyl-3-hydroxymethyl bicyclo [2.2.1] hept-5-enes.* J. Org. Chem., 1975. **40**(25): p. 3658-3664.

138. Cason, J., D.M. Lynch, and A. Weiss, *Hydride Reductions of Naphthalic Anhydrides.* J. Org. Chem., 1973. **38**(10): p. 1944-1947.

139. Nystrom, R.F. and W.G. Brown, *Reduction of Organic Compounds of Lithium Aluminum Hydride. I. Aldehydes, Ketones, Esters, Acid Chlorides, and Acid Anhydrides.* J. American Chemical Society, 1947. **69**: p. 1197-1199.

140. Nagao, Y., et al., *A new nonenzymatic chiral induction into prochiral meso compounds.* Tetrahedron, 1984. **40**(8): p. 1215-1223.

141. Chen, X., S.P. McCarthy, and R.A. Gross, *Synthesis, Characterization, and Epoxidation of an Aliphatic Polycarbonate from 2,2-(2-Pentene-1,5-diyl) trimethylene Carbonate (^{c}HTC) Ring-Opening Polymerization.* Macromolecules, 1997. **30**: p. 3470-3476.

142. Hovestadt, W., et al., *Ring-Opening Polymerization of 2,2-dimethyltrimethylene Carbonate, a Group Transfer or a Metal-free Anionic Polymerization?* Makromol. Chem., 1990. **11**: p. 271-278.

143. Keul, H., R. Buchler, and H. Hocker, *Anionic Ring-opening Polymerization of 2,2-dimethyltrimethylene Carbonate.* Makromol. Chem., 1986. **187**: p. 2579-2589.

144. Kihara, N. and T. Endo, *Synthesis and Properties of Poly(hydroxyurethane)s.* J. Polymer Science: Part A: Polymer Chemistry, 1993. **31**: p. 2765-2773.

145. Kricheldorf, H.R. and B. Weegen-Schulz, *Polymers of Carbonic Acid. XIV. High Molecular Weight Pol(trimethylene carbonate) by Ring-Opening Polymerization with Butyltin Chlorides as Initiators.* J. Polymer Science: Part A: Polymer Chemistry, 1995. **33**: p. 2193-2201.

146. Kricheldorf, H.R. and B. Weegen-Shulz, *Polymers of Carbonic Acid. 11. Reactions and Polymerizations of Aliphatic Cyclocarbonates with Boron Halogenides.* Macromolecules, 1993. **26**: p. 5991-5998.

147. Kuhling, S., H. Keul, and H. Hocker, *Polymers from 2-allyloxymethyl-2-ethyltrimethylene Carbonate and Copolymers with 2,2-dimethyltrimethylene Carbonate Obtained by Anionic Ring-Opening Polymerization.* Makromol. Chem., 1990. **191**: p. 1611-1622.

148. Takata, T., M. Igarashi, and T. Endo, *Synthesis and Cationic Ring-Opening Polymerization of a Cyclic Carbonate, 5-Methylene-1,3-dioxan-2-one.* J. Polymer Science: Part A: Polymer Chemistry, 1991. **29**: p. 781-784.

149. Takata, T., H. Matsuoka, and T. Endo, *Synthesis and Anionic Ring-Opening Polymerization of a Novel Aromatic Cyclic Carbonate Having Binaphthyl Structure.* Chemistry Letters, 1991. **12**: p. 2091-2094.

150. Rokicki, G., *Aliphatic Cyclic Carbonates and Spiroorthocarbonates as Monomers.* Progress in Polymer Science, 2000. **25**: p. 259-342.

151. Takata, T. and T. Endo, *Recent Advances in the Development of Expanding Monomers: Synthesis, Polymerization and Volume Change.* Progress in Polymer Science, 1993. **18**: p. 839-870.

152. Ariga, T., T. Takata, and T. Endo, *Alkyl Halide-Initiated Cationic Polymerization of Cyclic Carbonate.* J. Polymer Science: Part A: Polymer Chemistry, 1993. **31**: p. 581-584.

153. Ariga, T., T. Takata, and T. Endo, *Cationic Ring-Opening Polymerization of Cyclic Carbonates with Alkyl Halides to Yield Polycarbonate without the Ether Unit by Suppression of Elimination of Carbon Dioxide.* Macromolecules, 1997. **30**: p. 737-744.

154. Kricheldorf, H., J. Jenssen, and I. Kreiser-Saunders, *Polymerization of Trimethylene Carbonate (1,3-dioxan-2-one) with Complexation Catalysts.* Makromol. Chem., 1991. **192**: p. 2391-2399.

155. Kricheldorf, H.R. and J. Jenssen, *Polylactones. 16. Cationic Polymerization of Trimethylene Carbonate and other Cyclic Carbonates.* J. Macromol. Sci. Chem., 1989. **A26**(4): p. 631-644.

156. Kricheldorf, H.R. and J. Jenssen, *Polymers of Carbonic Acid -2. Synthesis and Polymerization of 2,2-Dihydroxybiphenyl Carbonate (4,5,6,7-Dibenzo-2-oxo-1,3-dioxacycloheptane).* Eur. Polym. J., 1989. **25**(12): p. 1273-1279.

157. Sanda, F., T. Fueki, and T. Endo, *Cationic Ring-Opening Polymerization of an Exomethylene Group Carrying Cyclic Carbonate. Pseudo-Living Polymerization of 5-Methylene-1,3-dioxan-2-one by the Assistance of the Exomethylene Group.* Macromolecules, 1999. **32**: p. 4220-4224.

158. Takata, T., et al., *Unusual Ring-Opening Polymerization of a Spiro Orthocarbonate Containing Norbornene Moiety.* Macromolecules, 1989. **22**: p. 3188-3190.

159. Kuhling, S., et al., *Polymerization of 5,5-(Bicyclo [2.2.1] hept-2-en-5,5-ylidene)-1,3-dioxan-2-one and Copolymerization with 5,5-Dimethyl-1,3-dioxan-2-one.* Macromolecules, 1991. **24**(15): p. 4229-4235.

160. Acemoglu, M., et al., *Poly(ethylene carbonate)s, part I: Synthesis and Structural Effects on Biodegradation.* J. Controlled Release, 1997. **49**: p. 263-276.

161. Darensbourg, D. and M. Holtcamp, *Catalysts for the Reactions of Epoxides and Carbon Dioxide.* Coordination Chemistry Reviews, 1996. **153**: p. 155-174.

162. Lukaszczyk, J., et al., *Synthesis of Functional Polycarbonates by Copolymerization of Carbon Dioxide with Allyl Glycidyl Ether.* Macromol. Rapid Commun., 2000. **21**: p. 754-757.

163. Ree, M., et al., *New Copolymerization Process Leading to Poly(propylene carbonate) with a Highly Enhanced Yield from Carbon Dioxide and Propylene Oxide.* J. Polymer Science: Part A: Polymer Chemistry, 1999. **37**: p. 1863-1876.

164. Tan, C.-S. and T.-J. Hsu, *Alternating Copolymerization of Carbon Dioxide and Propylene Oxide with a Rare-Earth-Metal Coordination Catalyst.* Macromolecules, 1997. **30**: p. 3147-3150.

165. Mang, S., et al., *Copolymerization of CO_2 and 1,2-Cyclohexene Oxide using a CO_2-Soluble Chromium Porphyrin Catalyst.* Macromolecules, 2000. **33**: p. 303-308.

166. Jung, J.H., M. Ree, and T. Chang, *Copolymerization of Carbon Dioxide and Propylene Oxide Using an Aluminum Porphyrin System and its Components.* J. Polymer Science: Part A: Polymer Chemistry, 1999. **37**: p. 3329-3336.

167. Frechet, J., et al., *Design and synthesis of novel allylic and benzylic copolycarbonates susceptible to acidolytic or thermolytic depolymerization.* Makrmol. Chem. Rapid Commun., 1986. **7**: p. 121-126.

168. Hua, Y. and C.L. Henderson, *Photodefinable thermally sacrificial polymers and processes for microelectronics and MEMS fabrication.* PMSE Preprints, 2004. **94**: p. 825-826.

169. Hua, Y., et al., *Nanolithography in thermally sacrificial polymers using nanoscale thermal probes*, in *Advances in Resist Technology and Processing XXIII*. 2006, SPIE: San Jose, CA, USA. p. 61531G1-G7.

170. Kadokawa, J.-i., et al., *Direct Polycondensation of Carbon Dioxide with Xylylene Glycols: a New Method for the Synthesis of Polycarbonates.* Macromol. Rapid Commun., 1998. **19**: p. 657-660.

171. Wang, L.S., et al., *Preparation and Cytotoxicity of Novel Aliphatic Polycarbonate Synthesized from Dihydroxyacetone.* Chinese Chemical Letters, 2005. **16**(5): p. 572-574.

172. Chung, M.-K., et al., *Regioselective Silylation of Sugars through Palladium Nanoparticle-Catalyzed Silane Alcoholysis.* J. American Chemical Society, 2002. **124**: p. 10508-10518.

173. Field, L., et al., *Cationic Iridium(I) Complexes as Catalysts for the Alcoholysis of Silanes.* Organometallics, 2003. **22**: p. 2387-2395.

174. Foston, M., *Cyclic, Tethered and Nanoparticulate Silicones for Material Modification*, in *Polymer, Textile, and Fiber Engineering*. 2008, Georgia Institute of Technology: Atlanta. p. 272.

175. Wang, M., Q. Zhang, and K. Wooley, *Silyl Ether-Coupled Poly(epsilon-caprolactone)s with Stepwise Hydrolytic Degradation Profiles.* Biomacromolecules, 2008. **2**(4): p. 1206-1213.

176. Blackwell, J., et al., *B(C6F5)3-Catalyzed Silation of Alcohols: A Mild, General Method for Synthesis of Silyl Ethers.* J. Org. Chem., 1999. **64**: p. 4887-4892.

177. Ito, H., A. Watanabe, and M. Sawamura, *Verstatile Dehydrogenative Alcohol Silylation Catalyzed by Cu(I)-Phosphine Complex.* Organic Letters, 2005. **7**(9): p. 1869-1871.

178. Auner, N. and J. Weis, eds. *Organosilicon Chemistry I: from Molecules to Materials*. Vol. 1. 1994, VCH: Weinheim ;. 226.

179. Brook, M.A., *Silicon in Organic, Organometallic, and Polymer chemistry* 2000, New York John Wiley & Sons.

180. Frechet, J.M., et al., *Poly(p-terbutoxycarbonyloxystyrene): a Convenient Precursor to p-hydroxystryrene Resins.* Polymer, 1983. **24**: p. 995-1000.

181. Patai, S. and Z. Rappoport, eds. *The Chemistry of Organic Silicon Compounds*. Part 2 ed. Vol. 1. 1989, John Wiley & Sons: New York.

182. Rappoport, Z. and Y. Apeloig, eds. *The Chemistry of Organic Silicon Compounds*. Part 2 ed. Vol. 2. 1998, John Wiley & Sons: New York. 2830.

183. Sommer, L.H., *Stereochemistry, Mechanism and Silicon; an Introduction to the Dynamic Stereochemistry and Reaction Mechanisms of Silicon Centers*. McGraw-Hill series in advanced chemistry. 1965, New York: McGraw-Hill

184. Devaux, J., et al., *19F N.M.R. End-group Analysis of a Poly(aryl ether ether ketone) (PEEK).* Polymer, 1989. **30**(1): p. 161-164.

185. Brandrup, J., E.H. Immergut, and E.A. Grulke, eds. *Polymer Handbook*. Fourth ed. 1999, John Wiley & Sons, Inc.: New York. 2336.

186. Arai, T., et al., *Excluded-Volume Effects on the Hydrodynamic Radius of Oligo- and Polystyrenes in Dilute Solution.* Macromolecules, 1995. **28**(10): p. 3609-3616.

187. Mandema, W. and H. Zeldenrust, *Diffusion of Polystyrene in Tetrahydrofuran.* Polymer, 1977. **18**: p. 835-839.

188. Park, S., et al., *Light Scattering Study on Polymer Chain Conformation: Polystyrene in Good Solvents.* Bull. Korean Chem. Soc., 1991. **12**(6): p. 682-685.

189. Venkataswamy, K., A.M. Jamieson, and R.G. Petschek, *Static and dynamic properties of polystyrene in good solvents: ethylbenzene and tetrahydrofuran.* Macromolecules, 1986. **19**(1): p. 124-133.

190. Yamada, M., et al., *Excluded-Volume Effects on the Mean-Square Radius of Gyration of Oligo- and Polyisobutylenes in Dilute Solution.* Macromolecules, 1997. **30**: p. 7166-7170.

191. Appelt, B. and G. Meyerhoff, *Characterization of Polystyrenes of Extremely High Molecular Weights.* Macromolecules, 1980. **13**(3): p. 657-662.

192. Bhatt, M. and A.M. Jamieson, *Dynamic light scattering studies of polystyrene in tetrahydrofuran at intermediate scattering vectors.* Macromolecules, 1988. **21**(10): p. 3015-3022.

193. Jackson, C., Y.-J. Chen, and J.W. Mays, *Size exclusion chromatography with multiple detectors: Solution properties of linear chains of varying flexibility in tetrahydrofuran.* Journal of Applied Polymer Science, 1996. **61**(5): p. 865-874.

194. Meyerhoff, G. and B. Appelt, *A Low Shear Viscometer with Automated Recording and Application to High Molecular Weight Polystyrene Solutions.* Macromolecules, 1979. **12**(5): p. 968-971.

195. Egorov, A.A., *Theory of Waveguide Light Scattering in an Integrated Optical Waveguide in the Presence of Noise.* Radiophysics and Quantum Electronics, 2005. **48**(1): p. 57-67.

196. Hattori, H., et al., *Scattering characteristics of crystallites in fluoride optical fibers.* Applied Optics, 1987. **26**(13): p. 2683-2687.

197. Li, H. and K.E. Torrance, *An experimental study of the correlation between surface roughness and light scattering for rough metallic surfaces*, in *Proceedings of SPIE Vol. 5878 (Advanced Characterization Techniques for Optics, Semiconductors, and Nanotechnologies II)*. 2005, SPIE, Bellingham, WA.

198. Walter, D.J. and J. Houghton, *Attenuation in Thin Film Optical Waveguides due to Roughness-Induced Mode Coupling.* Thin Solid Films, 1978. **52**: p. 461-476.

199. Yegorov, A.A., *Use of waveguide light scattering for precision measurements of the statistical parameters of irregularities of integrated optical waveguide materials.* Optical Engineering, 2005. **44**(1): p. 14601-1-10.

200. Shirai, M. and M. Tsunooka, *Photoacid and photobase generators: chemistry and applications to polymeric materials.* Progress in Polymer Science, 1996. **21**(1): p. 1-45.

201. Pappas, S.P., et al., *Photoinitiation of Cationic Polymerization. IV. Direct and Sensitized Photolysis of Aryl Iodonium and Sulfonium Salts.* Polymer Photochemistry, 1984. **5**: p. 1-22.

202. Fouassier, J.P., D. Burr, and J.V. Crivello, *Photochemistry and photopolymerization activity of diaryliodonium salts.* Journal of Macromolecular Science - Pure and Applied Chemistry, 1994. **A31**(6): p. 677-701.

203. Harkness, B.R., K. Takeuchi, and M. Tachikawa, *Demonstration of a directly photopatternable spin-on-glass based on hydrogen silsesquioxane and photobase generators.* Macromolecules, 1998. **31**(15): p. 4798-4805.

204. Harkness, B.R., K. Takeuchi, and M. Tachikawa, *Photopatternable thin films from silyl hydride containing silicone resins and photobase generators.* Polymers for Advanced Technologies, 1999. **10**(11): p. 669-677.

205. Shea, K.J. and D.A. Loy, *A Mechanistic Investigation of Gelation. The Sol-Gel Polymerization of Precursors to Bridged Polysilsesquioxanes.* Acc. Chem. Res., 2001. **34**(9): p. 707-716.

206. Feher, F.J., K.J. Weller, and J.J. Schwab, *Reactions of Hydrogensilsesquioxanes and Chlorosilsesquioxanes with Phosphoranes.* Organometallics, 1995. **14**: p. 2009-2017.

207. Lattimer, R., *Pyrolysis Field Ionization Mass Spectrometry of Hydrocarbon Polymers.* J. Analytical and Applied Physics, 1997. **39**: p. 115-127.

208. Gomory, A., et al., *Mass Spectrometric and MNDO Study of Electron Impact Induced Fragmentation of some Norbornane- and Norbornene-Condensed Pyrimidinones and Oxazinones.* International Journal of Mass Spectrometry and Ion Process, 1991. **107**(2): p. 225-246.

209. Lenz, T. and J. Vaughan, *Computer-Based Molecular Mechanics Techniques for Accurate Prediction of Thermodynamic Properties of Chemically Reactive Systems.* Chemical Engineering Science, 1990. **45**(7): p. 1755-1763.

210. Harrison, P.G., *Silicate cages: precursors to new materials.* Journal of Organometallic Chemistry, 1997. **542**(2): p. 141-183.

211. Agaskar, P., *Synthesis of Functionalized Sperosilicates: Novel Polyhedral Polyreactive Oligomers.* Synthesis and Reactivity in Inorganic and Metal-organic Chemistry, 1990. **20**(4): p. 483-493.

212. Agaskar, P., *New Synthetic Route to the Hydridospherosiloxanes O_h-$H_8Si_8O_{12}$ and D_{5h}-$H_{10}Si_{10}O_{15}$.* Inorganic Chemistry, 1991. **30**: p. 2707-2708.

213. Auner, N., et al., *Chemistry of Hydrogen-Octasilsesquioxane: Preparation and Characterization of Octasilsesquioxane-Containing Polymers.* Chemistry of Materials, 2000. **12**: p. 3402-3418.

214. Bassindale, A. and T. Gentle, *Siloxane and Hydrocarbon Octopus Molecules with Silsesquioxane Cores.* J. Materials Chemistry, 1993. **3**(12): p. 1319-1325.

215. Crivello, J.V. and D. Bi, *Regioselective Hydrosilation. II. The Synthesis of Silicon-Hydrogen Functional Compounds.* J. Polymer Science: Part A: Polymer Chemistry, 1993. **31**: p. 2729-2737.

216. Crivello, J.V., B. Yang, and W.-G. Kim, *Chemoselective Hydrosilations. I. Synthesis and Photopolymerization of 1-Propenyl Ether Functionalized Siloxanes.* J. Polymer Science: Part A: Polymer Chemistry, 1995. **33**: p. 2415-2423.

217. Daum, J., *Novel Networks by the Polymerization of Cyclic Siloxanes*. 2005, University of Akron: Akron. p. 139.

218. Frye, C. and W. Collins, *The Oligomeric Silsesquioxanes, $(HSiO_{3/2})_n$.* J. American Chemical Society, 1970. **92**: p. 5586-5588.

219. Hasegawa, I., *Co-Hydrolysis Products of Tetraethoxyl silane and Methyltriethoxysilane in the Presence of Tetramethylammonium Ions: Part 2.* J. Sol-Gel Science and Technology, 1994. **2**: p. 127-130.

220. Hasegawa, I. and S. Motojima, *Dimethylvinylsilylation of Si8O208- silicate anion in methanol solutions of tetramethylammonium silicate.* J. Organometallic Chemistry, 1992. **441**: p. 373-380.

221. Herren, D., H. Burgy, and G. Calzaferri, *New Synthetic Route to Polyhedral Organylsilsesquioxanes.* Helvetica Chimica Acta, 1991. **74**: p. 24-26.

222. Mattori, M., et al., *Studies on the Trapping and Detrapping Transition States of Atomic Hydrogen in Octasilsesquioxane using the Density Functional Theory B3LYP Method.* J. Phys. Chem. A, 2000. **104**: p. 10868-10872.

223. Miravet, J. and J. Frechet, *New Hyperbranched Poly(siloxysilanes) from AB_2, AB_4, AB_6 Monomers: Variation of the Branching Pattern and End-*

Functionalization. Polymeric Materials Science and Engineering, 1997. **77**: p. 141-142.

224. Nyman, M.D., S.B. Desu, and C.H. Peng, *T_8-hydridospherosiloxanes: Novel Precursors for SiO_2 Thin Films. 1. Precursor Characterization and Preliminary CVD.* Chem. Mater., 1993. **5**: p. 1636-1640.

225. Pan, J., W. Lau, and C.S. Lee, *Preparation of HALS by Hydrosilylation of Vinyl Monomers Containing Hindered Amine.* J. Polymer Science: Part A: Polymer Chemistry, 1994. **32**: p. 997-1000.

226. Schwab, J. and J. Lichtenhan, *Polyhedral Oligomeric Silsesquioxane (POSS)-Based Polymers.* Applied Organometallic Chemistry, 1998. **12**: p. 707-713.

227. Sellinger, A. and R. Laine, *Silsesquioxanes as Synthetic Platforms. 3 Photocurable, Liquid Epoxides as Inorganic/Organic Hybrid Precursors.* Chem. Mater., 1996. **8**: p. 1592-1593.

228. Shockey, E., et al., *Functionalized Polyhedral Oligosilsesquioxane (POSS) Macromers: New Graftable POSS Hydride, POSS alpha-Olefin, POSS Epoxy, and POSS Chlorosilane Macromers and POSS Siloxane Triblocks.* Applied Organometallic Chemistry, 1999. **13**: p. 311-327.

229. Tsuchida, A., et al., *Ethene and Propene Copolymers Containing Silsesquioxane Side Groups.* Macromolecules, 1997. **30**(2818-2824).

230. Voronkov, M. and V. Lavrent'yev, *Polyhedral Oligosilsesquioxanes and their Homo Derivatives.* Topics in Current Chemistry, 1982. **102**: p. 199-236.

231. Zhang, C. and R. Laine, *Hydrosilylation of Allyl Alcohol with [HSiMe2OSiO1.5]8 Octa(3-hydroxypropyldimethylsiloxy)octasilsesquioxane and its Octamethacrylate Derivative as Potential Precursors to Hybrid Nanocomposites.* J. American Chemical Society, 2000. **122**: p. 6979-6988.

232. Agaskar, P.A. and W.G. Klemperer, *A New Route to Trimethylsilylated Spherosilicates: Synthesis and Structure of [Si12018](OSiMe3)12, D3h-[Si14O21](OSiMe3)14, and C2v-[Si14O21](OSiMe3)14.* J. American Chemical Society, 1987. **109**: p. 5554-5556.

233. Li, G., et al., *Polyhedral Oligomeric Silsesquioxane (POSS) Polymers and Copolymers: A Review.* J. Inorganic and Organometallic Polymers, 2001. **11**(3): p. 123-154.

234. Kim, S.M., et al. *Experimental and theoretical study of structure-dielectric property relationships for polysilsesquioxanes*. in *Low-Dielectric Constant Materials IV (Mat. Res. Soc. Symp. Proc., vol 115)*. 1998. San Francisco, CA: Materials Research Society, Warrendale, Pennsylvania.

235. Harrison, P. and C. Hall, *Preparation and Characterization of Octasilsesquioxane Cage Monomers.* Main Group Metal Chemistry, 1997. **20**(8): p. 515-529.

236. West, R., *Cyclic organosilicon compounds. II. Ring size and reactivity in the alkali-catalyzed hydrolysis of silanes.* Journal of the American Chemical Society, 1954. **76**: p. 6015-17.

237. Simonyi, E., et al., *Characterization of Spin-on Glasses by Microindentation*, in *Low Dielectric Constant Materials IV: (Mater. Res. Soc. Symp. Proc. Vol. 511)*. 1998: San Francisco, CA. p. 157-163.

238. Cameron, J.F. and J.M.J. Frechet, *Photogeneration of organic bases from o-nitrobenzyl-derived carbamates.* Journal of the American Chemical Society, 1991. **113**(11): p. 4303-4313.

239. Lee, S.K., et al., *Photolithographic Micropatterning of an Electroluminescent Polymer Using Photobase Generator.* Macromolecules, 2003. **36**(24): p. 9252-9256.

240. Matuszczak, S., et al., *Photogenerated amines and their use in the design of a positive-tone resist material based on electrophilic aromatic substitution.* Journal of Materials Chemistry, 1991. **1**(6): p. 1045-50.

241. Epling, G.A. and M.E. Walker, *A new photochemically removable protecting group for amines.* Tetrahedron Letters, 1982. **23**(38): p. 3843-3846.

242. Loy, D.A., et al., *Effect of pH on the gelation time of hexylene-bridged polysilsesquioxanes.* Chemistry of Materials, 2004. **16**(11): p. 2041-2043.

243. Tagawa, S., et al., *Radiation and photochemistry of onium salt acid generators in chemically amplified resists*, in *Advances in Resist Technology and Processing XVII*, F.M. Houlihan, Editor. 2000, Society of Photo-Optical Instrumentation Engineers, Bellingham, WA, USA: Santa Clara, CA, USA. p. 204-213.

244. Dektar, J.L. and N.P. Hacker, *Photochemistry of triarylsulfonium salts.* Journal of the American Chemical Society, 1990. **112**(16): p. 6004-15.

245. Rikowski, E. and H. Marsmann, *Cage-rearrangement of Silsesquioxanes.* Polyhedron, 1997. **16**(9): p. 3357-3361.

246. Laine, R., et al., *Polyfunctional Cubic Silsesquioxanes as Building Blocks for Organic/Inorganic Hybrids.* Applied Organometallic Chemistry, 1998. **12**: p. 715-723.

247. Haddad, T., et al., *Polydimethylsilanes Modified with Polyhedral Oligomeric Silsesqioxanes: From Viscous Oils to Thermoplastics.* Polymer Preprints, 1998. **39**(1): p. 611-612.

248. Zhou, G. and J. Smid, *Hydrosilylation of m-TMI: New Siloxane Based Aliphatic Polyisocyanates.* J. Polymer Science: Part A: Polymer Chemistry, 1991. **29**: p. 1097-1105.

249. Mabry, J., M. Runyon, and W. Weber, *Poly(silyl ether)s by Ruthenium-Catalyzed Hydrosilylation Polymerization of Aliphatic omega-Dimethylsiloxy Ketones and Copolymerization of Aliphatic alpha,omega-Diketones with alpha,omega-Dihydridooligodimethylsiloxanes.* Macromolecules, 2002. **35**: p. 2207-2211.

250. Leeuwen, P.W.N.M.v., *Homogeneous Catalysis*. 2004, Dordrecht: Kluwer Academic Publishers.

251. Marciniec, B., ed. *Comprehensive Handbook on Hydrosilylation*. 1992, Pergamon Press: Oxford. 754.

252. Chalk, A.J. and J.F. Harrod, *Homogenous Catalysis. II. The Mechanism of the Hydrosilation of Olefins Catalyzed by Group VIII Metal Complexes.* J. American Chemical Society, 1965. **87**(1): p. 16-21.

253. Gentle, T. and A. Bassindale, *Effect of Catalyst on Regioselectivity and Vinyl/H Exchange on Silicon in the Hydrosilylation of Vinyl-Siloxanes by T_8 Hydrogen Silsesquioxane.* J. Inorganic and Organometallic Polymers, 1995. **5**(3): p. 281-294.

254. Markovic, E., et al., *Poly(ethylene glycol)-Octafunctionalized Polyhedral Oligomeric Silsesquioxane: Synthesis and Thermal Analysis.* Macromolecules, 2007. **40**: p. 2694-2701.

255. Fu, B., A. Lee, and T. Haddad, *Styrene-Butadiene-Styrene Triblock Copolymers Modified with Polyhedral Oligomeric Silsesquioxanes.* Macromolecules, 2004. **37**: p. 5211-5218.

256. Kim, S.H., et al., *Synthesis and Properties of Allyl-Terminated and Silicon-Containing Polycarbonates.* Macromolecules, 1999. **32**: p. 6363-6366.

257. Kobayashi, T., T. Hayashi, and M. Tanaka, *Synthesis of Highly Heat-Resistant Soluble Polymers through Hydrosilylation Polymerization between Octakis(hydridosilsesquioxane) and Diynes.* Chemistry Letters, 1998: p. 763-764.

258. Nakayama, Y., et al., *Photoinduced annihilation of sigma bonds in amorphous poly(methylphenylsilane).* J. Non-Cryst. Solids, 1996. **198-200**: p. 657-660.

259. Collins, T. *Online Manual for the 'ImageJ for Microscopy' bundle*. Date of last update: 2008. Available from: http://www.macbiophotonics.ca/imagej/.(Date Accessed: March 20, 2009)

260. Rasband, W. *ImageJ: Image Processing and Analysis in Java*. Date of last update: 2004. Available from: http://rsbweb.nih.gov/ij/index.html. (Date Accessed: March 20, 2009)